

See discussions, stats, and author profiles for this publication at: <https://www.researchgate.net/publication/268559957>

# Frisbee(TM) Aerodynamics

Conference Paper · June 2002

DOI: 10.2514/6.2002-3150

---

CITATIONS  
18

READS  
11,818

---

2 authors:



Jonny Potts  
Sheffield Hallam University

18 PUBLICATIONS 106 CITATIONS

[SEE PROFILE](#)



William James Crowther  
The University of Manchester

91 PUBLICATIONS 1,239 CITATIONS

[SEE PROFILE](#)

# **Disc-wing Aerodynamics**

A thesis submitted to The University of Manchester for the degree of  
Doctor of Philosophy  
in the Faculty of Engineering & Physical Sciences.

2005

Jonathan Potts  
School of Mechanical, Aerospace & Civil Engineering

<b>Contents</b>	<b>Page</b>
<b>Title Page</b>	1
<b>Contents</b>	2
<b>List of Figures</b>	6
<b>Abstract</b>	19
<b>Declaration &amp; Copyright</b>	21
<b>Acknowledgements</b>	22
<b>The Author</b>	24
<b>Nomenclature</b>	25
<b>Chapter 1 Introduction</b>	<b>28</b>
1.1 <b>Opening Statements</b>	28
1.2 <b>Definitions</b>	28
1.3 <b>Thesis Aims &amp; Objectives</b>	29
1.4 <b>Thesis Outline</b>	30
<b>Chapter 2 Theoretical Background</b>	<b>31</b>
2.1 <b>Disc-wing Geometric Parameters</b>	31
2.2 <b>Aerodynamic Coefficients</b>	32
2.3 <b>Lift &amp; Drag Characteristics of Low Aspect Ratio Wings</b>	34
2.4 <b>Trim &amp; Stability of Tailless Flight Vehicles</b>	36
2.5 <b>Flight Dynamics of a Spin-stabilised Disc-wing</b>	39
2.5.1   Non-dimensional Roll Time Constant	41
<b>Chapter 3 Literature Review</b>	<b>44</b>
3.1 <b>Opening Statements</b>	44
3.2 <b>Aerodynamics of the Circular Planform</b>	44
3.2.1   Frisbee	44
3.2.2   Discus	47
3.2.3   Coin-like Cylinders	48
3.2.4   Analysis on Span Effectiveness Factor	49
3.3 <b>Flight Dynamics of Spin-stabilised Disc-wings</b>	50
3.3.1   Frisbee	50

3.3.2 Wind Tunnels	55
<b>Chapter 4 Experimental Facilities &amp; Techniques</b>	<b>57</b>
<b>4.1 Wind Tunnels</b>	<b>57</b>
4.1.1 Goldstein Laboratory	57
4.1.2 Project Tunnel	57
4.1.3 9' × 7' Tunnel	57
<b>4.2 Apparatus</b>	<b>57</b>
4.2.1 Rigs	58
4.2.2 Disc-wing Models	58
<b>4.3 Data Acquisition</b>	<b>59</b>
4.3.1 Load data	59
4.3.2 Surface Pressure Data	59
4.3.3 Flow Visualisation	60
4.3.3.1 Surface paint	60
4.3.3.2 Smoke wire	60
<b>4.4 Wind Tunnel Corrections</b>	<b>61</b>
<b>Chapter 5 Experimental Results</b>	<b>63</b>
<b>5.1 Load Data</b>	<b>63</b>
5.1.1 Non-spinning Case	63
5.1.1.1 Baseline force & moment data	63
5.1.1.2 Reynolds number effects	64
5.1.1.3 Comparison with theory	64
5.1.1.4 Comparison with data from the literature	65
5.1.2 Spinning Disc	68
5.1.3 Basic Geometry Comparisons	69
5.1.3.1 Camber	69
5.1.3.2 Cavity	70
<b>5.2 Surface Pressure Data</b>	<b>70</b>
5.2.1 Overview	70
5.2.2 Discussion of Results at Typical Flight AoA (5°)	71
5.2.3 Effect of AoA on Pressure Distributions	72
5.2.4 Effect of Reynolds number	74

5.2.5	Loads Comparison: Integrated Pressure Data	75
<b>5.3</b>	<b>Surface Flow Visualisation</b>	76
5.3.1	Surface Flow Patterns	76
5.3.1.1	Typical flight angle of attack ( $5^\circ$ )	76
5.3.1.2	Range of attack angles ( $0^\circ$ to $30^\circ$ )	77
5.3.2	Comparison with Pressure Data	79
<b>5.4</b>	<b>Smoke Wire Flow Visualisation</b>	81
5.4.1	Centre-line Visualisation	81
5.4.2	Wake Visualisation	82
5.4.3	Visualisation of the Effect of Spin	83
<b>Chapter 6</b>	<b>Flow Topology</b>	86
<b>6.1</b>	<b>Typical Flight Angle of Attack (<math>10^\circ</math>)</b>	86
<b>6.2</b>	<b>Range of Attack Angles (<math>0^\circ</math> to <math>45^\circ</math>)</b>	87
<b>Chapter 7</b>	<b>Disc-wing Flightpath Simulation</b>	89
<b>7.1</b>	<b>Flight Equations of Motion</b>	89
<b>7.2</b>	<b>Simulation Implementation</b>	93
<b>7.3</b>	<b>Results from Numerical Experiments</b>	94
7.3.1	Comparison with Experimental Data	94
7.3.2	Analysis of a Typical Frisbee Trajectory	94
7.3.3	Effect of Varying Launch Condition	96
7.3.4	Frisbee Flight Control	97
<b>Chapter 8</b>	<b>Conclusions</b>	99
<b>References</b>		102
<b>Figures</b>		113
<b>Appendices</b>		208
<b>Appendix A History of the Frisbee</b>		209
<b>A.1</b>	<b>Introduction</b>	209
<b>A.2</b>	<b>Wham-O's Frisbee™ Disc</b>	209
<b>A.3</b>	<b>Professional Sport Disc Development</b>	210

<b>Appendix B Disc-wing Aircraft R&amp;D</b>	<b>211</b>
<b>B.1 Introduction</b>	<b>211</b>
<b>B.2 Literature Review: In Brief</b>	<b>211</b>
<b>B.3 History of the Circular Planform</b>	<b>213</b>
B.3.1 Chance-Vought XF-5U-1	213
B.3.2 Avro's Special Projects Group	213
B.3.3 Lenticular Re-entry Vehicle	214
B.3.4 Self-suspended Flare for Special Ordnance	215
<b>Appendix C Blockage Corrections &amp; Analysis</b>	<b>216</b>
<b>C.1 Maskell's Blockage Correction</b>	<b>216</b>
<b>C.2 Analysis</b>	<b>218</b>

## List of Figures

	Page
Figure 2.1 Cross-sectional frisbee-like disc-wing profile.	114
Figure 2.2 Relationship between the <i>Lift &amp; Drag</i> and the Axial <i>X</i> & Normal <i>Z</i> forces. The <i>Side</i> force (not shown here) is identical for both systems, directed out of the page.	115
Figure 2.3 Definition of reference locations for longitudinal forces and moments acting on a tailless flight vehicle.	116
Figure 2.4 Illustration of longitudinal stability and trim characteristics of a tailless vehicle for permutations of camber and static margin.	117
Figure 2.5 Comparison of the aerodynamic centre location as a function of angle of attack for a Frisbee and a circular planform wing with a non-axisymmetric airfoil cross-section.	118
Figure 2.6 (a) Disc-wing flight dynamics. (b) Schematic of body fixed axes.	119
Figure 3.1 Comparison of aerodynamic load data for circular planform wings, derived from various sources found in the literature, with chordwise cross-sections as seen to the right of the figure.	120
Figure 4.1 Wind tunnel support strut fixed to balance beam above wind tunnel working section (left), pressure lines (capillary tubing) connected to pressure transducer (right middle) via a scanivalve (right).	121
Figure 4.2 Wind tunnel control room.	122
Figure 4.3 L-shaped support strut and disc-wing mounted vertically at 0° incidence.	123

Figure 4.4 Surface paint flow visualisation rig configuration, the disc is horizontal at zero incidence. The disc is mounted on a central axle, which is fixed to a horizontal crossbar, two vertical struts either side of the balance beam support the crossbar, the incidence arm is connected to control the angle of attack. Rig designed by Ali (1998). 124

Figure 4.5 Smoke wire flow visualisation rig configurations: (a) Motor driven axle connected to centre of vertical test model allows visualisation of spinning disc, up to 24Hz. (b) Geared down motor driven axle connected to rim of test model allows visualisation of the full central flow field cross-section of a non-spinning disc. 125

Figure 4.6 Cross-sectional disc profiles. (a) Frisbee-like (b) Intermediate (c) Flatplate. 126

Figure 4.7 Wind tunnel configuration to measure interference and tare effects, the disc was mounted on a dummy support (left). The dummy strut was a mirror image of the measuring strut (right) and held the disc in the correct position (on the balance centre) but not connected to the balance itself. The measuring strut was set with the axle tip (centre) at around 3mm from the disc, without touching, and was fixed to the balance. 127

Figure 4.8 Comparison of the disc test model and the support strut at zero spin rate,  $AoA = -10^\circ$  to  $30^\circ$ ,  $V_\infty = 20\text{m/s}$ ,  $Re = 3.78 \times 10^5$ . 128

Figure 4.9 L-shaped rig configuration, to measure the surface pressure distribution. The capillary tubes were carefully wound around the support strut. 129

Figure 4.10 (a) The pressure tappings in the surface of the disc-wing test models were positioned on a spiral curve. (b) The spiral curve of points was stepped at  $12^\circ$  increments, by yawing the model, to achieve full coverage of the disc-wing surface. That is a polar grid array of 571 points on each surface, upper and cavity. 130

Figure 4.11 Schematic of (a) smoke wire and oil supply system, (b) the oil feeder device. 131

Figure 5.1 Load Characteristics at zero spin rate, AoA =  $-10^{\circ}$  to  $30^{\circ}$ ,  $V_{\infty} = 20$ m/s,  $Re = 3.78 \times 10^5$ . 132

Figure 5.2 Load Characteristics at zero spin rate, AoA =  $-10^{\circ}$  to  $50^{\circ}$ ,  $V_{\infty} = 20$ m/s,  $Re = 3.78 \times 10^5$ . 133

Figure 5.3 Load Characteristics at zero spin rate, AoA =  $-100^{\circ}$  to  $100^{\circ}$ ,  $V_{\infty} = 20$ m/s,  $Re = 3.78 \times 10^5$ . 134

Figure 5.4 Effect of Reynolds number at zero spin rate, AoA =  $-10^{\circ}$  to  $30^{\circ}$ . 135  
Tunnel speed varied to achieve different Re ( $V_{\infty} = 6, 10, 15, 20, 25$ m/s).

Figure 5.5 Further load characteristics at zero spin rate, AoA =  $-10^{\circ}$  to  $30^{\circ}$ ,  $V_{\infty} = 20$ m/s,  $Re = 3.78 \times 10^5$ . 136

Figure 5.6 Comparison of the present experimental data to circular planform wings, both theoretical and experimental. 137

Figure 5.7 Comparison of the present experimental data to Frisbee-like circular planform wings from the literature. 138

Figure 5.8 Comparison of the present experimental data to a similar Frisbee-like circular planform wing. 139

Figure 5.9 Comparison of the present experimental data to a variety of circular planform wings, with chordwise cross-sections as seen below. 140

Figure 5.10 Lift coefficient: Comparison of the present experimental data to that found in the literature for similar circular planform wings, with chordwise cross-sections as seen to the right of the figure. 141

Figure 5.11 Drag coefficient: Comparison of the present experimental data to  
that found in the literature for similar circular planform wings, with chordwise  
cross-sections as seen to the right of the figure. 142

Figure 5.12 Pitching moment coefficient: Comparison of the present  
experimental data to that found in the literature for similar circular planform  
wings, with chordwise cross-sections as seen to the right of the figure. 143

Figure 5.13 Load characteristics at various advance ratios,  $\text{AdvR} = 0$  to 1,  $\text{AoA} = -10^\circ$  to  $30^\circ$ ,  $V_\infty = 20\text{m/s}$ ,  $\text{Re} = 3.78 \times 10^5$ . 144

Figure 5.14 Load characteristics (detail) at various advance ratios,  $\text{AdvR} = 0$  to 1,  $\text{AoA} = -10^\circ$  to  $30^\circ$ ,  $V_\infty = 20\text{m/s}$ ,  $\text{Re} = 3.78 \times 10^5$ . 145

Figure 5.15 Effect of spin on the Lift Coefficient: Comparison set of spin rates  
(0, 4, 8, 16, 24Hz) tested at various flow speeds ( $V_\infty = 6, 10, 15, 20\text{m/s}$ ),  $\text{AoA} = -10^\circ$  to  $30^\circ$ . 146

Figure 5.16 Effect of spin on the Drag Coefficient: Comparison set of spin rates  
(0, 4, 8, 16, 24Hz) tested at various flow speeds ( $V_\infty = 6, 10, 15, 20\text{m/s}$ ),  $\text{AoA} = -10^\circ$  to  $30^\circ$ . 147

Figure 5.17 Effect of spin on the Side Force Coefficient: Comparison set of spin  
rates (0, 4, 8, 16, 24Hz) tested at various flow speeds ( $V_\infty = 6, 10, 15, 20\text{m/s}$ ),  
 $\text{AoA} = -10^\circ$  to  $30^\circ$ . 148

Figure 5.18 Effect of spin on the Pitching Moment Coefficient: Comparison set  
of spin rates (0, 4, 8, 16, 24Hz) tested at various flow speeds ( $V_\infty = 6, 10, 15,$   
 $20\text{m/s}$ ),  $\text{AoA} = -10^\circ$  to  $30^\circ$ . 149

Figure 5.19 Effect of spin on the Rolling Moment Coefficient: Comparison set  
of spin rates (0, 4, 8, 16, 24Hz) tested at various flow speeds ( $V_\infty = 6, 10, 15,$   
 $20\text{m/s}$ ),  $\text{AoA} = -10^\circ$  to  $30^\circ$ . 150

Figure 5.20 Effect of Advance Ratio at 0° AoA for various Reynolds numbers, tunnel speed varied to achieve different Re ( $V_\infty = 6, 10, 15, 20$ m/s), AdvR = 0 up to 3.5, each curve utilises a consistent range of spin rates (0 to 31Hz). 151

Figure 5.21 Comparison of disc-wings with various thicknesses achieved by modifying the rim height to increase the cavity depth, with chordwise cross-sections as seen below,  $t_h / c = 0.01$  to  $0.16$ . 152

Figure 5.22 Comparison of the baseline (hollow) Frisbee configuration to a cavity filled (solid) disc-wing geometry. 153

Figure 5.23 2D flat surface colour weighted contour plot of pressure coefficients  $C_p$  derived from measurements of the 3D upper surface pressure distribution of a non-spinning disc-wing, taken over the entire surface, not over half the disc and mirrored to the other side, flow direction from top to bottom, AoA = 5°,  $V_\infty = 15$ m/s,  $Re = 2.84 \times 10^5$ . 154

Figure 5.24 2D flat surface colour weighted contour plot of pressure coefficients  $C_p$  derived from measurements of the 3D cavity surface pressure distribution of a non-spinning disc-wing, taken over the entire surface, not over half the disc and mirrored to the other side, flow direction from top to bottom, AoA = 5°,  $V_\infty = 15$ m/s,  $Re = 2.84 \times 10^5$ . 155

Figure 5.25 2D flat surface colour weighted contour plot of pressure coefficients  $C_p$  derived from measurements of the 3D upper (a) & cavity (b) surface pressure distribution of a non-spinning disc-wing, taken over the entire surface, not over half the disc and mirrored to the other side, flow direction from top to bottom, AoA = 5°,  $V_\infty = 15$ m/s,  $Re = 2.84 \times 10^5$ . 156

Figure 5.26 Central cross-sectional pressure profile at the half span station. Pressure coefficients  $C_p$  derived from measurements of the 3D surface pressure distribution of a non-spinning disc-wing. Non-dimensional disc geometry shown below pressure plot, leading edge on the left of the figure. Unbroken line - upper surface, dashed line - lower surface, AoA = 5°,  $V_\infty = 15$ m/s,  $Re = 2.84 \times 10^5$ . 157

Figure 5.27 Central cross-sectional pressure profile at the half chord station, 158  
pressure coefficients  $C_p$  derived from measurements of the 3D surface pressure  
distribution of a non-spinning disc-wing. Non-dimensional disc geometry shown  
below pressure plot, port wing tip on the left of the figure. Unbroken line - upper  
surface, dashed line - lower surface,  $AoA = 5^\circ$ ,  $V_\infty = 15m/s$ ,  $Re = 2.84 \times 10^5$ .

Figure 5.28 2D flat surface colour weighted contour plots of pressure 159  
coefficients  $C_p$  for a range of  $AoA$ , derived from measurements of the 3D upper  
surface pressure distribution of a non-spinning disc-wing, taken over the entire  
surface, not over half the disc and mirrored to the other side, flow direction from  
top to bottom,  $AoA = -10^\circ$  to  $30^\circ$ ,  $V_\infty = 20m/s$ ,  $Re = 3.78 \times 10^5$ .

Figure 5.29 2D flat surface colour weighted contour plots of pressure 160  
coefficients  $C_p$  for a range of  $AoA$ , derived from measurements of the 3D cavity  
surface pressure distribution of a non-spinning disc-wing, taken over the entire  
surface, not over half the disc and mirrored to the other side, flow direction from  
top to bottom,  $AoA = -10^\circ$  to  $30^\circ$ ,  $V_\infty = 20m/s$ ,  $Re = 3.78 \times 10^5$ .

Figure 5.30 Central cross-sectional pressure profiles at the half span station, 161  
for a range of  $AoA$ . Pressure coefficients  $C_p$  were derived from measurements of the  
3D surface pressure distribution of a non-spinning disc-wing. Non-dimensional  
disc geometry shown below pressure plot, leading edge on the left of the figure.  
Unbroken line - upper surface, dashed line - lower surface,  $AoA = -10^\circ$  to  $30^\circ$ ,  
 $V_\infty = 20m/s$ ,  $Re = 3.78 \times 10^5$ .

Figure 5.31 Central cross-sectional pressure profiles at the half span station, 162  
for a range of  $AoA$ . Pressure coefficients  $C_p$  were derived from measurements of the  
3D surface pressure distribution of a non-spinning disc-wing. Non-dimensional  
disc geometry shown below pressure plot, leading edge on the left of the figure.  
Unbroken line - upper surface, dashed line - lower surface,  $AoA = -10^\circ$  to  $30^\circ$ ,  
 $V_\infty = 20m/s$ ,  $Re = 3.78 \times 10^5$ .

Figure 5.32 Cross-sectional pressure profiles at various span stations (a) 1/2 b, (b) 3/8 b, (c) 1/4 b (d) 1/8 b. Pressure coefficients  $C_p$  were derived from measurements of the 3D surface pressure distribution of a non-spinning disc-wing. Non-dimensional disc cross-section shown below pressure plot, leading edge on the left of the figure. Unbroken line - upper surface, dashed line - lower surface,  $AoA = 5^\circ$ ,  $V_\infty = 15\text{m/s}$ ,  $Re = 2.84 \times 10^5$ . 163

Figure 5.33 Cross-sectional pressure profiles at various span/chord stations (i) 1/2 b, (ii) 3/8 b, (iii) 1/4 b, (iv) 1/8 b, (v) 1/2 c and a range of AoA. Pressure coefficients  $C_p$  were derived from measurements of the 3D surface pressure distribution of a non-spinning disc-wing. Non-dimensional disc cross-section shown below pressure plot (e), leading edge (i, ii, iii, iv) and port wing-tip (v) on the left of each plot. Unbroken line - upper surface, dashed line - lower surface,  $AoA = -10^\circ$  to  $30^\circ$ ,  $V_\infty = 20\text{m/s}$ ,  $Re = 3.78 \times 10^5$ . 164

Figure 5.34 2D flat surface colour weighted contour plots of pressure coefficients  $C_p$  for a range of Re, derived from measurements of the 3D upper surface pressure distribution of a non-spinning disc-wing, taken over the entire surface, not over half the disc and mirrored to the other side, flow direction from top to bottom,  $AoA = 5^\circ$ ,  $V_\infty = 6$  to  $20\text{m/s}$ ,  $Re = 1.13$  to  $3.78 \times 10^5$ . 165

Figure 5.35 2D flat surface colour weighted contour plots of pressure coefficients  $C_p$  for a range of Re, derived from measurements of the 3D cavity surface pressure distribution of a non-spinning disc-wing, taken over the entire surface, not over half the disc and mirrored to the other side, flow direction from top to bottom,  $AoA = 5^\circ$ ,  $V_\infty = 6$  to  $20\text{m/s}$ ,  $Re = 1.13$  to  $3.78 \times 10^5$ . 166

Figure 5.36 Central cross-sectional pressure profiles at the half span station, for a range of Re. Pressure coefficients  $C_p$  were derived from measurements of the 3D surface pressure distribution of a non-spinning disc-wing. Non-dimensional disc geometry shown below pressure plot, leading edge on the left of the figure. Unbroken line - upper surface, dashed line - lower surface,  $AoA = 5^\circ$ ,  $V_\infty = 6$  to  $20\text{m/s}$ ,  $Re = 1.13$  to  $3.78 \times 10^5$ . 167

Figure 5.37 Pressure load characteristics, integrated from the pressure data over the 3D disc-wing geometry, and a comparison to the load measurements, taken from the wind tunnel balance, AoA = -10° to 30°,  $V_\infty = 20\text{m/s}$ ,  $\text{Re} = 3.78 \times 10^5$ . 168

Figure 5.38 Upper surface paint patterns for a non-spinning disc-wing, flow direction from top to bottom, AoA = 5°,  $V_\infty = 15\text{m/s}$ ,  $\text{Re} = 2.84 \times 10^5$ . 169

Figure 5.39 Lower (cavity) surface paint patterns for a non-spinning disc-wing, flow direction from top to bottom, AoA = 5°,  $V_\infty = 15\text{m/s}$ ,  $\text{Re} = 2.84 \times 10^5$ . 170

Figure 5.40 Upper (a) and Lower (cavity) (b) surface paint patterns for a non-spinning disc-wing, including superimposed labels to aid the explanation of surface flow features, flow direction from top to bottom, AoA = 5°,  $V_\infty = 15\text{m/s}$ ,  $\text{Re} = 2.84 \times 10^5$ . 171

Figure 5.41 Upper surface paint patterns for a non-spinning disc-wing, over a range of AoA, flow direction from top to bottom, AoA = 0° to 30°,  $V_\infty = 15\text{m/s}$ ,  $\text{Re} = 2.84 \times 10^5$ . 172

Figure 5.42 Lower (cavity) surface paint patterns for a non-spinning disc-wing, over a range of AoA, flow direction from top to bottom, AoA = 0° to 30°,  $V_\infty = 15\text{m/s}$ ,  $\text{Re} = 2.84 \times 10^5$ . 173

Figure 5.43 Upper surface paint patterns (detail) for a non-spinning disc-wing, depicting boundary layer reattachment features, flow direction from top to bottom, (a) Straight line reattachment (half disc) at 20° AoA, (b) Nodal point reattachment at 30° AoA.  $V_\infty = 15\text{m/s}$ ,  $\text{Re} = 2.84 \times 10^5$ . 174

Figure 5.44 Half surface comparison plot: 3D pressure surface colour weighted contour plots of pressure coefficients  $C_p$  derived from measurements of the upper (a) & lower (cavity) (b) surface pressure distribution over a non-spinning disc-wing, superimposed onto the half surface flow visualisation images, flow direction from top to bottom, AoA = 5°,  $V_\infty = 15\text{m/s}$ ,  $\text{Re} = 2.84 \times 10^5$ . 175

Figure 5.45 Comparison plot: Central cross-sectional, upper surface pressure profile at the half span station, superimposed onto a half surface paint flow visualisation image. Leading edge on the left of the figure. Pressure coefficients  $C_p$  derived from measurements of the upper surface pressure distribution over a non-spinning disc-wing. Separation ( $S_1$ ,  $S_2$ ) and reattachment ( $R_1$ ) lines are marked on for comparison, flow direction from left to right,  $AoA = 5^\circ$ ,  $V_\infty = 15\text{m/s}$ ,  $Re = 2.84 \times 10^5$ . 176

Figure 5.46 Half surface comparison plot: 3D pressure surface colour weighted contour plots of pressure coefficients  $C_p$  derived from measurements of the upper surface pressure distribution over a non-spinning disc-wing, superimposed onto the half surface flow visualisation images, over a range of  $AoA$ , flow direction from top to bottom,  $AoA = 0^\circ$  to  $30^\circ$ ,  $V_\infty = 15\text{m/s}$  (flow vis) &  $20\text{m/s}$  (pressure),  $Re = 2.84 \times 10^5$  &  $3.78 \times 10^5$ . 177

Figure 5.47 Half surface comparison plot: 3D pressure surface colour weighted contour plots of pressure coefficients  $C_p$  derived from measurements of the lower surface pressure distribution over a non-spinning disc-wing, superimposed onto the half surface flow visualisation images, over a range of  $AoA$ , flow direction from top to bottom,  $AoA = 0^\circ$  to  $30^\circ$ ,  $V_\infty = 15\text{m/s}$  (flow vis) &  $20\text{m/s}$  (pressure),  $Re = 2.84 \times 10^5$  &  $3.78 \times 10^5$ . 178

Figure 5.48 Central cross-section of the flow field over a non-spinning disc-wing, for a range of  $AoA$ , flow direction from right to left. An electrically heated wire vaporised oil to create smoke, visualising the flow field when illuminated.  $AoA = 0^\circ$  to  $50^\circ$ ,  $V_\infty = 3\text{m/s}$ ,  $Re = 5.67 \times 10^4$ . 179

Figure 5.49 Central cross-section of the leading edge separation bubble over a disc-wing, for a range of  $AoA$ , flow direction from right to left. An electrically heated wire vaporised oil to create smoke, visualising the separation bubble when illuminated by a laser light sheet.  $AoA = 0^\circ$  to  $30^\circ$ ,  $AdvR = 0.7$ ,  $V_\infty = 3\text{m/s}$ ,  $Re = 5.67 \times 10^4$ . 180

Figure 5.50 Central cross-section of the separated shear layer and cavity flow over a non-spinning disc-wing, for a range of AoA, flow direction from left to right. An electrically heated wire vaporised oil to create smoke, visualising the cavity flow when illuminated by a laser light sheet. AoA = 0° to 30°,  $V_\infty = 3\text{m/s}$ ,  $\text{Re} = 5.67 \times 10^4$ .

181

Figure 5.51 Visualisation of the wake, downwash and trailing vortex structures downstream of a non-spinning disc-wing, for a range of AoA. An electrically heated wire vaporised oil to create smoke, visualising the flow field when illuminated by ambient lighting (i) or a laser light sheet (ii). The camera was placed downstream of the disc model, flow direction is out of the page. The wake cross-sections (ii) were taken at a distance of one diameter from the trailing edge, AoA = 0° to 10°,  $V_\infty = 3\text{m/s}$ ,  $\text{Re} = 5.67 \times 10^4$ .

182

Figure 5.52 Visualisation of the wake, downwash and trailing vortex structures extending to just over five diameters downstream from the trailing edge of a non-spinning disc-wing, for a range of AoA. An electrically heated wire vaporised oil to create smoke, visualising the flow field when illuminated, flow direction from right to left, AoA = 0°, 5° & 10°,  $V_\infty = 3\text{m/s}$ ,  $\text{Re} = 5.67 \times 10^4$ .

183

Figure 5.53 Cross-sectional slices through the wake, downwash and trailing vortex structures. Each slice was located aft of a non-spinning disc-wing at a range of positions, up to two chord lengths downstream from the trailing edge. An electrically heated wire vaporised oil to create smoke, visualising the flow field when illuminated by a laser light sheet, flow direction is out of the page.  $x/c = 0$  to 2, AoA = 10°,  $V_\infty = 3\text{m/s}$ ,  $\text{Re} = 5.67 \times 10^4$ .

184

Figure 5.54 Visualisation of flow structures over the upper surface planform including the separation bubble and wake over a disc-wing, for various AoA and advance ratios. An electrically heated wire vaporised oil to create smoke, visualising the flow field when illuminated, flow direction from top to bottom.

185

i)  $\text{AdvR} = 0 \& 0.9$ , AoA = 0°,  $V_\infty = 1.5\text{m/s}$ ,  $\text{Re} = 2.84 \times 10^4$ ,

ii)  $\text{AdvR} = 0 \& 0.7$ , AoA = 5°,  $V_\infty = 3\text{m/s}$ ,  $\text{Re} = 5.67 \times 10^4$ .

b) Spinning Disc: Advancing side on left of figure, retreating side on the right.

Figure 5.55 Cross-sectional slices through the wake, downwash and trailing vortex structures at various spin rates. Each slice was located aft of a disc-wing model at a couple of positions, up to two chord lengths downstream of the trailing edge. An electrically heated wire vaporised oil to create smoke, visualising the flow field when illuminated by a laser light sheet, flow direction is out of the page. Advancing side on the left of the figure, retreating side on the right.  $x/c = 1 \& 2$ ,  $AdvR = 0, 0.7 \& 1.6$ ,  $AoA = 10^\circ$ ,  $V_\infty = 3m/s$ ,  $Re = 5.67 \times 10^4$ . 186

Figure 5.56 Cross-sectional slices through the wake, downwash and trailing vortex structures at various advance ratios including opposite spin directions. Each slice was located aft of a disc-wing model at a range of positions, up to two chord lengths downstream from the trailing edge. An electrically heated wire vaporised oil to create smoke, visualising the flow field using laser light sheet illumination, flow direction is out of the page.  $x/c = 0$  to  $2$ ,  $AdvR = -0.7, 0 \& 0.7$ ,  $AoA = 5^\circ$ ,  $V_\infty = 3m/s$ ,  $Re = 5.67 \times 10^4$ . i) Advancing side on the left of the figure, retreating side on the right. iii) Advancing side on the right of the figure, retreating side on the left. 187

Figure 6.1 Two-dimensional central cross-sectional flow topology for a non-rotating disc-wing at  $10^\circ$  AoA. The proposed topology is based upon the flow visualisation, depicting many of the flow structures, namely the separation bubble, cavity flow and turbulent wake. Flow direction from right to left. 188

Figure 6.2 Three-dimensional flow topology for a non-rotating disc-wing at  $10^\circ$  AoA. The proposed topology is based upon the flow visualisation, depicting many of the flow structures, namely the separation bubble and trailing vortices. Flow direction from right to left. 189

Figure 6.3 Two-dimensional central cross-sectional flow topology for a non-rotating disc-wing for a range of AoA. Each proposed topology is based upon the flow visualisation, depicting many of the flow structures, namely the separation bubble, cavity flow and turbulent wake. Flow direction from right to left,  $AoA = 0^\circ$  to  $30^\circ$ . 190

Figure 6.4 Two-dimensional central cross-sectional flow topology for a non-rotating disc-wing at 45° AoA, pre- (a) and post-stall (b). Each proposed topology is based upon the flow visualisation, depicting many of the flow structures, namely the separation bubble and turbulent wake. Flow direction from right to left, AoA = 0° to 30°. 191

Figure 7.1 Additional axes systems used for the disc-wing simulation. 192  
(a) Zero sideslip body axes (xyz)<sub>3</sub>. (b) Relative wind axes (xyz)<sub>4</sub>.

Figure 7.2 Comparison of simulated results (no dots) with experimental time histories (dots) from flight tests (flight f2302; Hummel, 2003), for an identical set of initial conditions, given below. 193

Figure 7.3 Trajectory plots and parameter time histories for a simulated Frisbee flight path. Solid lines correspond to results from using the full non-linear aerodynamic model. Grey lines correspond to results from using a linear approximation. 194

Figure 7.4 Comparison of the Frisbee-like disc-wing wind tunnel data to the linear approximations for use in the simulation. The alpha dependent aerodynamic coefficients are governed by the equations beneath each respective figure, linear derivatives given also. Angle of attack range given in radians, AoA = -0.2 to 0.6 rads. 195

Figure 7.5 Effect of launch conditions (advance ratio) on disc-wing XZ and XY trajectories. The time interval between each data point is 0.2 seconds. 196

$$\phi_L = 0^\circ, \theta_L = 0^\circ, \psi_L = 0^\circ, \alpha_L = 0^\circ, V_L = 19 \text{ m/s}, AdvR = 0 \text{ to } 8.$$

Figure 7.6 Effect of launch conditions (pitch angle) on disc-wing XZ and XY trajectories. The time interval between each data point is 0.2 seconds. 197

$$\phi_L = 0^\circ, \theta_L = 0^\circ \text{ to } 90^\circ, \psi_L = 0^\circ, \alpha_L = 0^\circ, V_L = 19 \text{ m/s}, AdvR = 1.1.$$

Figure 7.7 Range as a function of launch pitch angle. 198

Figure 7.8 Flight duration as a function of launch pitch angle. 199

Figure 7.9 Effect of launch conditions (angle of attack) on disc-wing XZ and XY trajectories. The time interval between each data point is 0.2 seconds. 200

$$\phi_L = 0^\circ, \theta_L = 0^\circ, \psi_L = 0^\circ, \alpha_L = 0^\circ \text{ to } 90^\circ, V_L = 19 \text{ m/s}, AdvR = 0.5.$$

Figure 7.10 Effect of launch conditions (roll angle) on disc-wing XZ and XY trajectories. The time interval between each data point is 0.2 seconds. 201

$$\phi_L = 0^\circ \text{ to } 90^\circ, \theta_L = 0^\circ, \psi_L = 0^\circ, \alpha_L = 0^\circ, V_L = 19 \text{ m/s}, AdvR = 0.5.$$

Figure 7.11 Disc landing position (XY location at which Z=0) as a function of launch roll angle. Re-plotted from data in Fig. 57.8a. 202

Figure 7.12 Trajectory plots and parameter time histories for a simulated spiral turn manoeuvre obtained using a constant rolling moment control input. 203

$$\phi_L = -45^\circ, \theta_L = -30^\circ, \psi_L = 0^\circ, \alpha_L = 5^\circ, V_L = 13.5 \text{ m/s}, C_{Lcontrol} = 0.1, AdvR = 0.5.$$

Figure 7.13 Trajectory plots and parameter time histories for a simulated spiral roll manoeuvre obtained using a constant pitching moment control input. 204

$$\phi_L = -0^\circ, \theta_L = -20^\circ, \psi_L = 0^\circ, \alpha_L = -3^\circ, V_L = 19 \text{ m/s}, C_{Mcontrol} = 0.2, AdvR = 0.34.$$

Figure C.1 (a) Uncorrected lift data taken in the wind tunnel  $C_{Lu}^2$  plotted against uncorrected drag data  $C_{Du}$ , equation of the best fit line given. 205

(b) Disc-wing drag analysis for a lifting wing, after Maskell (Fig. 8, 1965).

(c) Uncorrected wind tunnel data  $C_{Lu}^2$  plotted against  $C_{Du}$ , for the negative AoA range, equation of the best fit line given.

Figure C.2 Corrected and uncorrected drag results for various AoA ranges. 206

(a) AoA  $-10^\circ$  to  $30^\circ$ , (b) AoA  $-10^\circ$  to  $50^\circ$ , (c) AoA  $-100^\circ$  to  $100^\circ$ .

Figure C.3 Experimentally measured open face bluff body drag coefficients for various disc planform configurations (Potts & Crowther, 2002), compared to similar shapes detailed in White (1999) and Stilley & Carstens (1971), AoA =  $+90^\circ$  or  $-90^\circ$ . 207

## **Abstract**

### **The University of Manchester**

Abstract of Thesis submitted by **Jonathan Potts** for the Degree of **Doctor of Philosophy** and entitled **Disc-wing Aerodynamics**

Month and Year of submission: **March 2005**

Disc-wings are a class of un-powered, axi-symmetric flight vehicles that use spin to achieve acceptably stable flight characteristics. Examples of commonly encountered disc-wings include the Frisbee sports disc, the athletics discus and the clay pigeon. Historically, it appears that most disc-wing designs have been based on trial and error approaches. The main aim of the present work is to develop a theory of flight for spin-stabilised disc-wings that can be used to inform the process of their design. This theory of flight is based both on theoretical analysis and experimental data.

It is shown from a simple trim and stability analysis that a disc-wing with positive camber will trim at a positive angle of attack. However, for most axi-symmetric cross-sectional shapes, the aerodynamic centre is ahead of the centre of the disc (which by definition is the disc centre of gravity). Hence, the static margin is negative and the disc is unstable in pitch.

In practice, a disc-wing must be spun in order to fly successfully. The imparted angular momentum due to the spin means that, through precessional effects, the destabilising pitching moments tend to result in a rolling motion rather than a pitching motion. Thus, without spin, a disc-wing would tumble soon after release. With spin however, the disc-wing will not tumble, instead it tends to exhibit a relatively benign roll to the left or right, depending on the spin direction.

The aerodynamic characteristics of various disc-wing geometries based around a Frisbee sports disc are investigated through a series of wind tunnel experiments on a spinning and non-spinning disc. It is shown that the basic lift and drag characteristics are consistent with those expected for a finite wing of the same aspect ratio. The pitching moment characteristic is key to understanding the resulting disc dynamics. A comparison of pitching moment curves is given, for a number of different cross-

sectional profiles, some tested as part of the present work and some taken from data found in the literature. It is shown that the Frisbee cross-section is unique in that the pitching moment is zero at around  $9^{\circ}$  angle of attack, approximately coincident with the angle attack for best lift to drag ratio, and that the disc is approximately neutrally stable in this region. It is these characteristics that enable a typical Frisbee to fly successfully. Spin has almost negligible effect on aerodynamic forces and moments.

Force and moment data is supported by surface pressure data, and by on and off surface flow visualisation. Surface pressure data shows that the aerodynamic centre of the Frisbee cross-section is shifted aft by the presence of an aft pressure peak that is not present on other cross-section shapes. The aft pressure peak is a function of both the upper surface geometry and the presence of the cavity on the under surface of the disc. Flow visualisation and pressure data are used to propose a model of disc-wing flow topology that is dependant on the angle of attack and includes leading edge separation and reattachment, recirculating cavity flow and a pair of trailing vortices.

To understand further disc-wing flight dynamics and the effect of aerodynamic characteristics, a six-degree of freedom disc-wing simulation model was developed using Matlab. The simulation is validated against published Frisbee trajectory data obtained from free-flight experiments. Flight profiles are also discussed for a number of different launch conditions consistent with a range of typical Frisbee throws. The simulation is also used to demonstrate that with control moments from suitable control effectors, it is possible to generate a number of proscribed manoeuvres, including a spiral turn and a spiral roll.

## **Declaration**

No portion of the work referred to in the thesis has been submitted in support of an application for another degree or qualification of this or any other university or other institute of learning.

## **Copyright**

Copyright in text of this thesis rests with the author. Copies (by any process) either in full, or of extracts, may be made only in accordance with instructions given by the author and lodged in the John Rylands University Library of Manchester. Details may be obtained from the Librarian. This page must form part of any such copies made. Further copies (by any process) of copies made in accordance with such instructions may not be made without the permission (in writing) of the Author.

The ownership of any intellectual property rights which may be described in this thesis is vested in the University of Manchester, subject to any prior agreement to the contrary, and may be made available for use by third parties without the written permission of the University, which will prescribe the terms and conditions of any such agreement.

Further information on the conditions under which disclosures and exploitation may take place is available from the Head of the School of Mechanical, Aerospace & Civil Engineering.

## Acknowledgements

Bill Crowther, PhD Supervisor. Thankyou so much for pondering over Frisbee<sup>TM</sup> flight in the first place, thus providing the opportunity for me to enjoy contemplating with you. Supporting me in frequent international conference visits, even against your better judgement, has made my research programme a much more exciting and challenging experience. Your patience and perseverance have truly been tested to the end.

My time at the Goldstein Lab. has been a wonderful experience, the friendly working environment far outweighed the daily noise pollution. David Smith, apart from being an all round electronics genius, has offered me his ear whenever I needed it, his pastoral care has been spot on, you are such a good man! His wife Carole is an extension to the support the Smiths have collectively provided to students and staff at the Lab. and beyond. Andrew Kennaugh is the font of all knowledge and all that is City, if you can't find a reference get Andrew on the case. The dynamic speed with which the technicians fabricate equipment, constantly foregoing tea-breaks to meet tight deadlines, will forever astound. Dave Mould constructed the marvellously versatile wind tunnel rig and disc-wing model, it could not have worked out any better. Thanks for putting up with, 'Is it ready yet?' first thing in the morning.

The breadth of knowledge I have acquired during these few years can primarily be attributed to the mentoring of Andrew Crook. His unselfish servant attitude is worked out practically through his brief you, show you, leave you approach. I miss many things about him, particularly his constant banging on about how nature has been doing fluid mechanics for thousands of years but none more so than his friendship. Just one more Ahmedia before I leave...

I have had the pleasure of making many friends on my travels in the USA. In particular I would like to thank Peter Lissaman for making himself available throughout my research, you always seem to be two steps ahead of me. My American friends have always made me feel extremely welcome, none more so than at UC Davis. Mont Hubbard & Sarah Hummel have cleared their schedule more than once to accommodate my somewhat impromptu visits.

I must acknowledge the disc-wing related experimental work of Wajid Ali, Martin Stone and Carlos Martin-Henry, undergraduate students at the University of Manchester. All have now successfully graduated on the Aerospace Engineering course.

This research was funded by the Engineering and Physical Sciences Research Council (EPSRC), award reference number 98317373. International Travel Grants, primarily to present papers at various international conferences in the USA, were secured through multiple applications and an extensive search for relevant awarding bodies: EPSRC, RAcEng, RAeS & IoP.

---

I cannot capture the gratitude I have for my parents John & Maxine Potts in brief. Their unceasing support in every way possible has ensured that I can work this thing out to the end. Along with my sister Kate, they have provided the immovable standard on which my life is based.

How could I forget the constant banter, “Eeh-ya Jonneh, put d’keckle on an’ make me a brew before ah brake yer jaw, d’yer get meh” from the infamous Manc brothers Phil an’ar kid Paul Stapleton. You have livened up my evenings and weekends with never-ending inner city comedy. Mary & Adge Bennett have treated me like one of their own.

Thanks to Graham & Veronica Dawson I have been able to find refuge from my work in Staly-vegas, claiming them there hills as my own. I have especially enjoyed the many late nights I’ve spent with your son David, over a wee dram.

## The Author

Master of Mathematics (MMath) in Combined Mathematics, awarded 2:1 with honours. Jonathan Potts studied mathematics as an undergraduate at the University of Manchester, U.K. (1994-98) gaining experience in a varied cross-section of the discipline, with special interest in applied mathematics. A grounding in fluid mechanics followed including research project work on Ocean Waves, Boomerangs and Tornado-like Vortices. Written reports contain a review of the scientific literature base, original work includes an experiment on the bath-tub vortex and an analytical model of triangular boomerang dynamics.

He chose to continue his education at the University of Manchester as a postgraduate in the Division of Aerospace Engineering (1998-2002), based at their experimental fluids and aerodynamics facility, the Goldstein Research Laboratory. He investigated the aerodynamics of a spin-stabilised axi-symmetric circular wing configuration i.e. disc-wing and conducted a feasibility assessment of appropriate flow control methodologies. Dissemination activities include the presentation of state of the art knowledge, from the disc-wing research initiative, at international conferences including AIAA ASM&E (Reno, Nevada, USA), aerospace engineering institutions including invited seminars at USC & UC Davis, CA and briefed interested professionals at AeroVironment Inc.

# Nomenclature

$a$	Lift curve slope, finite wing
$a_0$	Lift curve slope, infinite wing
$AdvR$	Advance ratio ( $r c / 2V_\infty$ )
AoA	Angle of attack ( $^\circ$ )
AR	Aspect ratio
$c$	Disc-wing chord & diameter (m)
$C_{Drag}$	Drag coefficient
$C_{Do}$	Profile drag coefficient
cg	Centre of gravity
$C_{Lift}$	Lift coefficient
$C_M$	Pitching moment coefficient (about $c/2$ )
cp	Centre of pressure
$C_p$	Pressure coefficient
$C_L$	Rolling moment coefficient
$C_Y$	Side force coefficient
$H$	Angular momentum ( $\text{kg m}^2 \text{s}$ )
$I$	Moment of inertia ( $\text{kg m}^2$ )
$e$	Span efficiency factor
<i>Lift</i>	Lift (N)
LE	Leading edge
$L$	Rolling moment (Nm)
$M$	Pitching moment (Nm)
$m$	Mass of disc-wing (kg)
$N$	Yawing moment (Nm)
$Re$	Reynolds number
$S$	Surface planform area ( $\text{m}^2$ )
$t_h$	Disc thickness (m)
TE	Trailing edge
$x$	Displacement vector, along roll axis (m)
$y$	Displacement vector, along pitch axis (m)
$z$	Displacement vector, along yaw axis (m)
$g$	Acceleration due to gravity ( $\text{ms}^{-2}$ )

$p$	Rate of roll ( $\text{rad s}^{-1}$ )
$q$	Rate of pitch ( $\text{rad s}^{-1}$ )
$r$	Rate of yaw ( $\text{rad s}^{-1}$ )
$q_\infty$	Dynamic pressure ( $\frac{1}{2} \rho_\infty V_\infty^2$ )
$V_\infty$	Freestream/wind velocity ( $\text{ms}^{-1}$ )
$\alpha$	Geometric angle of attack ( $^\circ$ )
$\alpha_0$	Zero lift angle of attack ( $^\circ$ )
$\pi$	Circle circumference/diameter ratio ( $\sim 3.14$ )
$\rho_\infty$	Density of air ( $\text{kg m}^{-3}$ )

One night I dreamed I was walking  
Along the beach with the Lord.  
Many scenes from my life flashed across the sky.  
In each scene I noticed footprints in the sand.  
Sometimes there were two sets of footprints.  
Other times there were one set of footprints.  
This bothered me because I noticed that  
During the low periods of my life when I was  
Suffering from anguish, sorrow, or defeat,  
I could see only one set of footprints,  
So I said to the Lord, "You promised me,  
Lord, that if I followed You,  
You would walk with me always.  
But I noticed that during the most trying periods  
Of my life there have only been  
One set of prints in the sand.  
Why, When I have needed You most,  
You have not been there for me?"  
The Lord replied,  
"The times when you have seen only one set of footprints  
Is when I carried you."

**Footprints in the Sand**  
**by Mary Stevenson**  
**081122 – 060199**

# Chapter 1 Introduction

## 1.1 Opening Statements

It is the Frisbee<sup>1</sup> sports disc that has inspired this study. The ability of such a simple shape to glide so successfully over short distances has amazed many over its short history. With a minimum of practice a novice can extract maximum enjoyment from throwing, catching and observing the simple glider design, oblivious to the complex aerodynamics securing such stable flight characteristics.

The flying disc is the more generic term used to describe what is most famously known as the Frisbee disc. That is a throwing implement with circular planform, typically launched with a specific backhand motion to impart velocity and spin to the disc in flight. The sports disc is therefore a flying gyroscope, with similar dynamics to a boomerang but vastly different aerodynamics. A history of the Frisbee disc is outlined in Appendix A.

The original goal of the work presented in this thesis was to develop a controllable flight vehicle based on the principles of a Frisbee sports disc. Flow control technologies were to be used to provide control forces and moments and a suitable flight control system developed. However, soon after starting the work, it became clear that, firstly, the basic aerodynamics and flight dynamics of a disc wing were more complex than initially thought, and that, secondly, the available literature on disc wing aerodynamics was sparse and rather inconclusive. In light of this, the original study was refocused on obtaining a comprehensive aerodynamic data set for the Frisbee sports disc and developing a sound theoretical framework for understanding how the aerodynamics influences the vehicle flight dynamics.

## 1.2 Definitions

For the present work, a ‘disc-wing’ is defined as wing with circular planform and axial symmetry. Axial symmetry is important because it means that the disc-wing has no preferred angular orientation for flight, and hence can be spin-stabilised. Note that this

---

<sup>1</sup> Frisbee is used to define the axisymmetric aerodynamic shape of the generic flying disc-wing model tested in this study, for ease of description and understanding. Frisbee, frisbee-like and disc are used interchangeably throughout the thesis and should be taken to have the same meaning. Frisbee™ is a registered trademark of Wham-O Inc.

disc-wing definition includes objects such as the Frisbee and discus, but excludes aircraft with non-axisymmetric circular planforms such as the Black Widow MAV or Chance-Vought XF-5U-1 (see Appendix B) that fly at a fixed angular orientation to the free stream.

Aerodynamics is principally the study of the motion of air around a body and the forces and moments that arise on the body as result of the air motion. Within the present study, of particular interest are the lift, drag and pitching moments acting on a disc-wing at various angles of attack to the oncoming wind. Furthermore, to understand the mechanism by which forces and moments are generated, it is necessary to measure the pressure distribution over the surface of the disc-wing and to identify the associated flow topology through on and off surface flow visualisation experiments.

Flight dynamics is concerned with understanding how a body moves under the influence of aerodynamic, gravitational and propulsive forces. Spin-stabilised disc-wings offer an interesting challenge to flight dynamics in that the response of the disc to moments is dominated by gyroscopic precession. It is the effect of precession that causes the familiar roll of a sports disc along its flight path. The cross-sectional profile of a disc-wing has a strong influence on the rate at which the disc rolls. It turns out that the shape of Frisbee is such that the roll rate is minimised, however there was no experimental evidence at the outset of the present work to show why this was the case.

The principle tool of study in the present work is the wind tunnel. The wind tunnel works on the simple premise that the aerodynamic forces and moments acting on a body moving through still air are the same as the aerodynamic forces and moments acting on a stationary body in an air stream moving at the same velocity as the original body. However, from an experimental point of view, it is far more convenient to move the air and keep the body stationary than it is to move the body and keep the air stationary.

### **1.3 Thesis Aims & Objectives**

#### **Aim**

To develop a theory of flight for spin-stabilised disc-wings based on theoretical analysis and experimental data.

## **Objectives**

1. To provide context and motivation for experimental work through introductory remarks and a review the existing disc-wing literature.
2. To provide a basic theoretical context for understanding the aerodynamic and flight dynamic characteristics of a disc-wing.
3. To present, describe and discuss wind tunnel results and to propose a flow topology consistent with the experimental data.
4. To describe the development of a disc-wing dynamic simulation programme based on wind tunnel data and to present and describe simulated trajectory results obtained.

## **1.4 Thesis Outline**

Chapter 2 presents a theoretical analysis of the geometric, aerodynamic and flight dynamic parameters relevant to disc-wings and Chapter 3 provides a review of the disc-wing literature. The apparatus and techniques used to perform the experimental work are described in Chapter 4, with experimental work and proposed flow topology presented and discussed in Chapters 5 and 6, respectively. Chapter 7 introduces the disc-wing dynamic simulation programme and presents results for a range of simulated trajectories. Finally, Chapter 8 summarises the overall conclusions from the work.

## Chapter 2 Theoretical background

### Summary

This chapter presents a theoretical analysis of key aspects of disc wing geometry, aerodynamics and flight dynamics. Section 2.1 provides a derivation of aerodynamically relevant disc-wing geometric parameters. Section 2.2 develops a simple aerodynamic model for the lift and drag characteristics of a disc wing based on finite wing theory and basic drag estimation. Section 2.3 considers the impact of pitching moment characteristics on the trim and stability of generic tailless flight vehicles and establishes the pitching moment design requirements for a successful disc-wing. Finally, section 2.4 examines the fundamental dynamics of disc wing flight and identifies a non-dimensional roll rate parameter that characterises disc-wing trajectories.

### 2.1 Disc-wing Geometric Parameters

The basic disc-wing geometry is defined by its diameter. The root chord  $c$ , located at the mid-span station, is identical to the diameter  $d$  of the circular planform and is therefore taken as the characteristic length for a disc-wing. This allows the definition of the disc-wing reference area,

$$S = \pi \frac{d^2}{4} . \quad (2.1)$$

By definition, the aspect ratio of a circular planform is given by,

$$AR = \frac{b^2}{S} \quad (2.2)$$

where  $b$  is the wing span at the mid-chord station, such that  $b = c = d$ . Therefore for the circular planform,

$$AR = \frac{4}{\pi} \sim 1.27 . \quad (2.3)$$

The thickness to chord ratio  $t_h/c$  is defined using the root chord  $c$ . The thickness  $t_h$  is defined as the perpendicular distance of the disc-wing rim tip above the flat central plate, see Fig. 2.1. This is really a non-dimensional measure of the amount of maximum camber, used here for ease of comparison between disc-wing shapes within the literature. Typically a Frisbee has thickness to chord ratio of around,

$$\frac{t_h}{c} \sim 0.15 \quad . \quad (2.4)$$

The mean chord  $\bar{c}$  for the disc planform is given by,

$$\bar{c} = \frac{\pi c}{4} \quad (2.5)$$

The mean aerodynamic chord  $mac$ , which is the chord weighted chord, is calculated using,

$$mac = \frac{2}{S} \int_0^{\frac{\pi}{2}} c_y^2 dy \quad . \quad (2.6)$$

where  $c_y$  is the chord length at the relevant span station  $y$  and  $b$  is the wing span. Using cylindrical polar coordinates to define the chord at each span station the integral in equation (2.2) becomes,

$$mac = -\frac{4b}{\pi} \int_{\pi/2}^0 \sin^3 \theta d\theta \quad . \quad (2.7)$$

Therefore the mean aerodynamic chord for the circular planform is,

$$mac = \frac{8b}{3\pi} \sim 0.85c \quad . \quad (2.8)$$

## 2.2 Aerodynamic coefficients

It is necessary to define the aerodynamics forces in terms of dimensionless coefficients. This is achieved by normalising the aerodynamic forces by the dynamic pressure  $q_\infty$  and the surface planform area  $S$ . The aerodynamic Drag, Side Force and Lift are therefore defined as,

$$\begin{aligned} C_{Drag} &= \frac{Drag}{q_\infty S} \\ C_{Side} &= \frac{Side}{q_\infty S} \\ C_{Lift} &= \frac{Lift}{q_\infty S} \end{aligned} \quad (2.9)$$

respectively. Similarly the aerodynamic moments are normalised by the characteristic length  $c$  also such that the aerodynamic Rolling, Pitching and Yawing moments are defined as,

$$\begin{aligned} C_L &= \frac{L}{q_\infty S c} \\ C_M &= \frac{M}{q_\infty S c} \\ C_N &= \frac{N}{q_\infty S c} \end{aligned} \quad (2.10)$$

respectively. The Axial, Side and Normal forces are defined here also given by,

$$\begin{aligned} C_X &= \frac{X}{q_\infty S} \\ C_Y &= \frac{Y}{q_\infty S} \\ C_Z &= \frac{Z}{q_\infty S} \end{aligned} \quad (2.11)$$

respectively. The Axial, Side and Normal forces are the aerodynamic force components along the body fixed axes  $x, y, z$  (see Fig. 2.2) and are related to the Lift, Drag and Side force by,

$$\begin{aligned} X &= \text{Lift} \cdot \sin \alpha - \text{Drag} \cdot \cos \alpha \\ Y &= \text{Side} \\ Z &= -\text{Lift} \cdot \cos \alpha - \text{Drag} \cdot \sin \alpha \end{aligned} \quad (2.12)$$

where  $\alpha$  is the geometric angle of attack.

Pressure is made dimensionless using pressure coefficient  $C_p$  defined as,

$$C_p = \frac{p_w - p_\infty}{q_\infty} \quad (2.13)$$

where  $p_w$  is the pressure on the disc-wing surface,  $p_\infty$  is the total free-stream pressure and  $q_\infty$  the dynamic pressure defined by,

$$q_\infty = \frac{1}{2} \rho_\infty V_\infty^2 \quad (2.14)$$

where  $\rho_\infty$  is the air density and  $V_\infty$  the free-stream flow speed.

### 2.3 Lift & Drag Characteristics of Low Aspect Ratio Wings

The lift and drag characteristics of a disc-wing can be determined theoretically using finite wing theory or lifting line theory (Anderson, 1991). However, it is noted that finite wing theory is conventionally restricted to aspect ratios greater than 2, whereas disc-wings have an aspect ratio of 1.27, see equation 2.3. The application of this theory to the disc-wing is intended therefore only as a first approximation, offering an insightful starting point.

As a first approximation, it is reasonable to use the lift curve slope for an infinite wing defined by,

$$a_o = 2\pi \quad . \quad (2.15)$$

It can be shown using an analysis of induced velocity (Anderson, 1991) that the lift curve slope of a finite span wing is reduced compared to that of an infinite wing with the same cross section,

$$a = \frac{a_o}{1 + (a_o/\pi eAR)} \quad (2.16)$$

where  $a_o$  is the lift curve slope of the infinite wing,  $a$  is the lift curve slope of the finite wing and  $e$  is the span effectiveness factor.

By definition, the aspect ratio of a circular planform is  $4/\pi$ , see equation 2.3. Defining  $a_o$  as  $2\pi$  from equation (2.15) and  $e$  as 1 as a first approximation, substitution of these values into (2.16) yields a theoretical value of the lift curve slope of a disc-wing,

$$a = \frac{2\pi}{1 + \pi/2} \sim 2.44 \quad . \quad (2.17)$$

Due to the positive camber of a disc-wing the theoretical lift curve is given by,

$$C_L = a(\alpha - \alpha_o) \quad (2.18)$$

where  $\alpha_o$  is the zero lift angle of attack. From experiment the value for  $\alpha_o$  was taken to be  $-2^\circ$  such that,

$$C_L = 2.44\alpha + 0.085 \quad . \quad (2.19)$$

The aerodynamic drag generated by the disc-wing can be modelled as the sum of profile drag  $C_{Do}$  and induced drag using the familiar drag polar equation,

$$C_D = C_{Do} + \frac{C_L^2}{\pi e AR} \quad . \quad (2.20)$$

Due to the bluff nature of practical disc-wing cross-sectional shapes, an estimate of the disc profile drag coefficient can be made by modelling the disc as a sphere of the same frontal area as the disc. The profile drag coefficient can then be obtained by scaling according to the ratio of frontal (subscript  $f$ ) to planform (subscript  $p$ ) areas,

$$C_{Do} = C_{Dp} = \frac{S_f}{S} C_{Df} \quad . \quad (2.21)$$

The frontal area of the disc can be approximated from the disc centre-line thickness to chord ratio,

$$S_f = t_h c \quad (2.22)$$

and the planform area  $S$  is given in equation (2.1). Substituting (2.1) & (2.22) into (2.21) then gives,

$$C_{Do} = \frac{4t_h}{\pi c} C_{Df} \quad . \quad (2.23)$$

The drag coefficient of a sphere in turbulent flow  $C_{Df}$  based on the frontal area is approximately 0.5 and the centre line thickness to chord ratio of a typical Frisbee is approximately 0.15, see equation (2.4). Substitution of these values in equation (2.23) gives,

$$C_{Do} = 0.0955 \approx 0.1 \quad . \quad (2.24)$$

The induced drag component at a given angle of attack can be estimated from known geometric parameters and the lift coefficient from equation (2.19). Substituting these values into equation (2.20) gives a drag polar equation,

$$C_D = 0.1 + 0.25 C_L^2 . \quad (2.25)$$

Finally, the drag curve can be written in terms of  $\alpha$  by substituting equation (2.19) into (2.25) such that,

$$C_D = 0.1 + 1.5(\alpha + 0.035)^2 . \quad (2.26)$$

Theoretical results derived in this section are compared to experimental results in Chapter 5.

## 2.4 Trim & Stability of Tailless Flight Vehicles

A number of requirements need to be met in order for a vehicle to achieve recognisably successful flight. The two most fundamental of these are that:

1. The vehicle should be able to generate a lift force at least equal to its weight.
2. The vehicle should be able to achieve and vary aerodynamic balance such that orientation of the vehicle with respect to the free stream can be controlled.

If sustained flight is required, then a further condition is that:

3. The vehicle should be able to generate a thrust force at least equal to the drag force.

Lastly, for ‘passive’ flight vehicles without an automatic flight control system or human pilot:

4. The vehicle should be aerodynamically stable such that when disturbed, it returns to its original balanced state, set by condition 2 above.

Most conventional flight vehicles satisfy condition 1 using a primary aerodynamic surface for generating lift (a wing), and conditions 2 and 4 using a secondary aerodynamic surface (horizontal stabiliser). Whilst the provision of a horizontal

stabiliser, in the form of a tailplane or foreplane, is often beneficial to the overall design, it is not a necessary condition for balance and stability.

The disc-wing is an example of a wider class of tailless flight vehicles including hang gliders and delta winged aircraft that use a single aerodynamic surface to both generate lift, and provide balance and stability.

The longitudinal forces and moments acting on a generic tailless aircraft are shown in Fig. 2.3. In keeping with linear airfoil theory (Anderson, 1991), the forces and moments are modelled as a lift force, *Lift*, and zero lift pitching moment,  $M_o$ , acting at the aerodynamic centre of the section.

For a 2D airfoil section at low speeds and small angles of attack (attached, incompressible flow), the zero lift pitching moment is constant and the aerodynamic centre is located at approximately a quarter chord back from the leading edge. The zero lift pitching moment is negative for positively cambered sections and positive for negatively cambered sections.

Taking moments about the centre of gravity of the tailless configuration the following moment balance equation is obtained,

$$M_{cg} = M_o - Lift(x_{ac} - x_{cg}) . \quad (2.27)$$

Non-dimensionalising, (2.27) becomes,

$$C_{M_{cg}} = C_{M_o} - C_{Lift} k_n \quad (2.28)$$

where  $k_n$  is the static margin, defined as,

$$k_n = \left( \frac{x_{ac} - x_{cg}}{c} \right) . \quad (2.29)$$

The system is balanced (trimmed) when  $C_{M_{cg}} = 0$ . The lift coefficient for trim is therefore given by,

$$C_{Lift_{trim}} = \frac{C_{M_o}}{k_n} . \quad (2.30)$$

In order to meet the first condition for flight above,  $C_{Lift_{trim}}$  must be greater than zero.

This is achieved if both  $C_{M_o}$  and  $k_n$  are positive or if both  $C_{M_o}$  and  $k_n$  are negative.

For stability (fourth condition for flight), the change in moment about the centre of gravity with increase in lift coefficient must be negative i.e.,

$$\frac{\partial C_{M_{cg}}}{\partial C_{Lift}} < 0 . \quad (2.31)$$

Differentiating (2.28) gives,

$$\frac{\partial C_{M_{cg}}}{\partial C_{Lift}} = -k_n , \quad (2.32)$$

thus for stability,  $k_n$  must be positive.

Combining results from (2.30) and (2.32), it can be concluded that a stable configuration requires a positive  $C_{M_o}$  for balance, whereas an unstable configuration requires a negative  $C_{M_o}$  for balance. This implies that a stable configuration should have negative camber and an unstable configuration positive camber.

To illustrate the effects of camber and static margin on the stability and trim of a tailless flight vehicle, Fig. 2.4 compares the pitching moment characteristics with angle of attack for the four possible permutations of camber and static margin. It is assumed that lift is directly proportional to angle of attack.

For a stable tailless aircraft  $C_{M_o}$  must be positive to provide balance and hence the wing must have negative camber. This configuration is shown in Fig. 2.4b. For a disc-wing, the centre of gravity must be at the centre of the disc and in practice the aerodynamic centre will always be ahead of this point, therefore the static margin will always be

negative. Thus to balance a disc-wing  $C_{M_0}$  must also be negative, i.e. the camber must be positive. This configuration is shown in Fig. 2.4c.

Fig. 2.5 shows the aerodynamic centre location as a function of angle of attack for both a Frisbee disc and a non-axisymmetric circular planform wing with an aerofoil cross section (Zimmerman, 1935). Over the angle of attack range  $0^\circ$  to  $10^\circ$  the aerodynamic centre of the Frisbee is just ahead of the half chord point of the disc, giving a static margin of approximately zero and thus neutral pitch stability. For the circular planform wing with an airfoil cross-section, however, the aerodynamic centre is at approximately quarter chord, resulting in a large negative static margin and hence negative stability.

An explanation of the reason why the Frisbee cross-sectional shape results in a favourable pitching moment characteristic compared to other cross-sectional profiles is provided in Chapter 6, and forms an important outcome of the work presented in this thesis.

## 2.5 Flight Dynamics of a Spin-stabilised Disc-wing

The most distinctive feature of disc-wing flight compared to the flight of other projectiles or aircraft is the tendency for disc-wings to roll about their direction of motion. As an illustration consider Fig. 2.6a. For a frisbee-like shape at typical flight angles of attack, if the centre of pressure (cp) of the disc-wing is ahead of the centre of the disc i.e. ahead of the cg. This results in an untrimmed nose up pitching moment. If the disc is rotating, gyroscopic effects dictate that this pitching moment  $M$  results in a precessional rolling rate,  $p$ . Using the conventional body fixed axes definition (Fig. 2.6b), for a disc rotating in the direction of positive yaw  $r$  then a positive pitching moment will generate roll rate.

The purpose of this section is to derive a non-dimensional roll rate parameter based on the disc's physical properties and launch conditions that can be used to predict the approximate flight behaviour of the disc. The starting point for the analysis is the standard set of equations describing the motion of an aircraft with six degrees of freedom (Nelson, 1998). Assuming a horizontal flightpath, equilibrium of forces and negligible yawing moment (a reasonable assumption based on experimental results), the motion of the disc is governed by the rolling moment and pitching moment equations,

$$L = I_x \dot{p} - I_{xz} \dot{r} + qr(I_z - I_y) - I_{xz} pq \quad (2.33)$$

$$M = I_y \dot{q} - rp(I_x - I_z) - I_{xz}(p^2 - r^2) . \quad (2.34)$$

Now for a uniform axisymmetric circular disc,

$$I_x = I_y = \frac{1}{2} I_z \quad \text{and} \quad I_{xz} = 0 \quad (2.35)$$

reducing equations (2.33) and (2.34) to,

$$L = I_x \dot{p} + \frac{1}{2} qr I_z \quad (2.36)$$

$$M = I_y \dot{q} - \frac{1}{2} rp I_z . \quad (2.37)$$

Due to the rapid spin of the disc (Hess, 1975) it can be assumed that the angular motion of the disc is unaccelerated thus,

$$\dot{p} \ll qr \quad \text{and} \quad \dot{q} \ll rp . \quad (2.38)$$

Therefore equations (2.36) and (2.37) can be written,

$$q = \frac{2L}{rI_z} \quad (2.39)$$

$$p = -\frac{2M}{rI_z} . \quad (2.40)$$

These equations express the fundamental effect of gyroscopic precession on the dynamics of a disc-wing. i.e. for a positive spin rate, a positive rolling moment causes pitch up and a positive pitching moment causes a roll left wing down. Since the aerodynamic rolling moment on a symmetrical disc is very small (see Chapter 5), the precessional pitch rate is negligible. However, the pitching moment acting on a disc-wing may be quite large and hence the roll rate can be significant. The tendency of a disc to roll in flight is anecdotally known as the “turnover effect” (Schuurmans, 1990).

### 2.5.1 Non-dimensional Roll Time Constant

It is proposed that non-dimensionalised disc-wing trajectories from similar starting conditions will be nominally similar if the non-dimensional roll rate is similar.

For the present analysis, the non-dimensional time and non-dimensional distance are given by equations (2.41) and (2.42) respectively, where  $t$  is dimensional time and  $\ell$  is dimensional length,

$$\hat{t} = \frac{t g}{V_\infty} \quad (2.41)$$

$$\hat{\ell} = \frac{\ell g}{V_\infty^2} . \quad (2.42)$$

The non-dimensional disc roll rate is thus obtained as follows,

$$\hat{p} = \frac{p V}{g} = -\frac{2MV_\infty}{rI_z g} . \quad (2.43)$$

Using equation (2.28) and assuming that  $M_o$  for the disc is zero, the disc pitching moment can be approximated as,

$$M = -k_n C_{Lift} q_\infty S c . \quad (2.44)$$

The mass moment of inertia  $I_z$  of the disc about the z-axis will depend on the mass distribution. To put the moment of inertia into context, it is useful to consider the equation,

$$I_z = m k_{zz}^2 \quad (2.45)$$

where  $k_{zz}$  is the radius of gyration.

Values of  $k_{zz}$  for various disc-wing shapes become larger when the weight is removed towards the circumference. Firstly, consider a circular cylinder with negligible height which has radius of gyration  $k_{zz} = (c/2)\sqrt{2} \sim 0.71(c/2)$ . Secondly, as the mass is redistributed towards the circumference  $k_{zz}$  increases, a typical value for a Frisbee-like

disc-wing is  $k_{zz} = 0.86(c/2)$  (Hubbard & Hummel, 2002). Lastly, for the theoretical case of a flying ring with the total mass distributed evenly at the outside radius  $k_{zz} = 1(c/2)$ .

For the present analysis, however, it is assumed that the disc is a uniform circular cylinder of negligible height for which,

$$I_z = \frac{1}{8}mc^2 \quad (2.46)$$

where  $m$  is the overall mass of the disc.

Substituting equations (2.44) and (2.46) into (2.43), the following result is obtained,

$$\hat{p} = \frac{16k_n C_{Lift} q_\infty S V_\infty}{mg rc} . \quad (2.47)$$

Given that for the condition  $Lift = Weight$ ,

$$C_{Lift} = \frac{mg}{q_\infty S} \quad (2.48)$$

and that,

$$AdvR = \frac{rc}{2V_\infty} \quad (2.49)$$

equation (2.47) simplifies to,

$$\hat{p} = \frac{8k_n}{AdvR} . \quad (2.50)$$

Equation (2.50) states that the non-dimensional roll rate of a disc-wing in unaccelerated horizontal flight is proportional to the ratio of static margin to the advance ratio. Thus roll rate is minimised when:

1. The aerodynamic centre of the disc is closest to the centre of the disc (minimum  $k_n$ ) i.e. a well designed disc.
2. The disc is launched with a high spin rate compared to the forward velocity (high advance ratio).

Both these conditions above are consistent with everyday experience of Frisbee throwing. The effect of varying  $\hat{p}$  on the flight path of a disc-wing is investigated numerically in Chapter 7.

# Chapter 3 Literature Review

## Summary

*This chapter provides a review of the disc-wing aerodynamics and flight dynamics literature. The review is split into two sections: the first on the aerodynamic characteristics of circular planform wings and the second on the flight dynamic characteristics. The first section includes aerodynamic data from both spin-stabilised (axisymmetric) and non-spin-stabilised (axisymmetric) disc-wings. The second section discusses the dynamics of spin-stabilised discs only, focusing on the Frisbee and discus.*

### 3.1 Opening Statements

The flying sports disc is of fundamental interest to the aerodynamicist, however the peripheral nature of such a shape to mainstream aeronautical applications has ensured it has largely escaped scientific scrutiny. As such, the literature base detailing the aerodynamics of circular planform wings is patchy, with much of the key work often in obscure sources and unpublished reports.

### 3.2 Aerodynamics of Circular Planform Wings

This section provides a descriptive review of the aerodynamics literature for circular planform wings. A quantitative comparison of results from the various sources is included later as part of the discussion of experimental results from the present work in Chapter 5.

#### 3.2.1 Frisbee

Arguably the first scientific study into disc-wing aerodynamics resulted from a U.S. Navy project considering the development of a self-suspended flare. The proposed flare was essentially a spin-stabilised axi-symmetric flying disc (Stilley, 1972; Stilley & Carstens, 1972). Familiar shapes such as the Frisbee, clay pigeon & right circular cylinders were tested in the wind tunnel alongside various flare configurations. Test results were obtained for a non-spinning frisbee-like model (hollow) and published as typical plots of axial, normal and pitching moment coefficients against angle of attack. The load measurements were far from rigorous, data points were few, enough just to capture the general trends. The drawback of barely sufficient data is that it leaves the reader wondering what happens between data points, particularly in the vicinity of the

aerodynamic stall. The normal curve for the frisbee-like model is linear below the stall at around  $35^\circ$  AoA and the pitching moment, taken about the semi-chord position, is linear with positive gradient trimmed just above  $10^\circ$  AoA.

The effect of the cavity provided a large change in nose down pitching moment, when comparing the solid (cavity filled) and hollow flares. The effect of spin on the aerodynamic loads was investigated on a right circular cylinder ( $t_h \ll c$ ) and found to be negligible, for the purposes of their work. Their technique for the measurement of ‘Magnus’ aerodynamic loads was a complicated test model support structure. The present author offers the suggestion that their side sting mount approach introduces large interference effects particularly at high angles of attack, to account for the premature onset of aerodynamic stall. They concluded that the accurate measurement of aerodynamic loads due to spin was problematic, recommended as an area for further investigation. Aerodynamic damping measurements for the Frisbee (hollow) were considered very small, in comparison to other conventional and unconventional bodies, with a pitch damping coefficient of around 0.5 for the positive angle of attack range.

Lazzara et al (1980) described a project to develop a wind tunnel balance and measure the aerodynamic loads acting on a Frisbee-like flying disc. Lift and drag results were presented for various flow speeds and spin rates over a narrow angle of attack range ( $0^\circ$  to  $10^\circ$ ). They concluded that spin generates a small lift component, although this may be a simple result of experimental accuracies.

Ali (1998), in an undergraduate project at the University of Manchester, measured lift, drag and pitching moment of a spinning Frisbee over a range of angles of attack and spin rates. This study was a precursor to the present study, providing a useful starting point for the design of a wind tunnel mounting rig for a spinning disc, see Fig. 4.4.

Mitchell (1999), as part of his Masters thesis at the University of Nevada, measured lift and drag for three non-spinning disc-wing configurations at various flow speeds. The results were plotted for each AoA ( $-20^\circ$  to  $20^\circ$ ) separately in the form of  $L/D$  ratio against  $Re$ . The vastly different curves were attributed to the varying camber and contour of each disc-wing. These graphs suggest that all three discs were strongly Reynolds number dependent, over the entire range of angles and flow speeds tested. The present research findings however are quite the opposite, the aerodynamic loads

were found to be Reynolds number independent, for the (more comprehensive) range of flow speeds tested. Flow visualisation using tuft and smoke techniques enabled the observation of the upwash ahead of the leading edge, the downwash aft of the trailing edge and the existence of trailing edge vortices, although the images included in the report are merely clear enough to see their existence and nothing more. The flow over the upper surface was described to be completely attached throughout whereas the lower (concaved) surface was entirely detached and separated. The effect of spin was deemed to have no effect on the development or location of boundary layer flow structures. Although the above statements regarding flow visualisation are perhaps correct for low angles of attack the present research offers discussion and evidence to suggest otherwise. The upper surface flow includes a separation bubble, the cavity shear layer reattaches to the cavity at low angles of attack ( $5^\circ$ ) and although the broad flow structures over the spinning disc are similar they are far from identical to the non-spinning case. Most worthy of note here, is that the near surface flow direction within the separation bubble, on the spinning disc, is dominated by the movement of the surface at that locality.

Higuchi et al (2000) investigated the flow over a similar disc-wing (golf disc) to that tested in the present study, using smoke wire flow visualisation and PIV (particle image velocimetry) measurements. A laser light sheet was used to illuminate various flow structures including trailing vortices, the separation bubble and upper & lower (cavity) surface streamwise flow cross-sections, both on spinning and non-spinning discs. At high angles of attack ( $30^\circ$ ) the separated shear layer was reported to be forced downwards by the strong trailing vortex pair, which is consistent with the findings of the present study. Vortex strength was calculated from PIV results. When compared to the non-spinning baseline case, the vortex strength remained unchanged for a spinning disc at a low angle of attack ( $5^\circ$ ) but decreased at a higher AoA ( $15^\circ$ ). A reduction in circulation was stated to cause the loss of vortex strength, attributed to the separation bubble becoming larger with spin. Enhanced lift at low AoA ( $5^\circ$ ) and reduced lift at higher AoA ( $15^\circ$ ) is described as being due to the effect of spin, based on observations of the wake. Load measurements from the present research, for an equivalent Reynolds number (10m/s), confirm that the lift enhancement, as a result of spin, decreases with increased AoA, Fig 5.15b. At no point is the lift reduced however, although the shape of the golf disc is slightly different to the disc tested in the present study and as such, it is possible that the two shapes exhibit contrasting aerodynamic loads. The reduced

strength of the two trailing vortices with spin is attributed quite rightly to the change in effective camber on advancing and receding surfaces. This paper also incorporated flow visualisation results, proposing a flow topology for a flat disc at incidence. Their wind tunnel model comprised a right circular cylinder with rounded edges, similar to the ‘coin-like’ cylinders studied by Zdravkovich et al (1998).

Yasuda (1999) measured the lift and drag characteristics of a recreational sports disc, analogous to the one tested in the present study, and a flat plate disc also. The wind tunnel results were taken for various flow speeds & spin rates but were consistently lower than the measurements taken in the present study, across the board, for both the cambered disc (see Figs 5.10, 5.11) & the flat plate also. Systematic balance errors or coefficient calculation errors could account for this. Both spin and roughness strips (ridges) were found to have no effect on the load measurements.

Nakamura & Fukamachi (1991) visualised the flow past a Frisbee using the smoke wire method. The observations are as follows: A horizontal plane of smoke filaments, aligned with the upper surface of the disc, shows a symmetric wake for the non-spinning case. A vertical smoke grid downstream of the disc shows a pair of trailing vortices formed behind the disc, the effect of spin causes an asymmetric wake. They concluded that the spinning disc strengthened the trailing vortex pair thereby enhancing the downwash. Although an asymmetric downwash is commonly observed in the wake of a spinning disc, the Advance Ratio ( $\text{AdvR} = 2.26$ ) was not matched to that which would be typical in flight, i.e.  $\text{AdvR} < 1$ . The present study has shown that the lift increases with high  $\text{AdvR} (>> 1)$  at low Re numbers (see Fig. 5.15a), which confirms this conclusion. However, with increased Re number, equivalent to typical free-flight conditions, the  $\text{AdvR}$  is more weakly dependent upon spin. This suggests that the vortex strength enhancement is dependent upon  $\text{AdvR}$ . However this was overlooked due to the study being limited to a single test case for a spinning disc.

### 3.2.2 Discus

Independent studies by Ganslen (1964) and Tutjowitsch (1976) measured the lift & drag characteristics for the discus from field athletics. Ganslen’s (1964) load data (lift and drag) shows variation with velocity i.e. Reynolds number change, especially at high AoA ( $30^\circ$  to  $50^\circ$ ). His smoke flow visualisation (flow speed 18 m/s) depicts the discus

flow field both in planform and cross-section at various AoA including the trailing vortices, separation bubble and deep stall flow structures.

Kentzer & Hromas (1958) measured the pitching moment, in addition to the aerodynamic forces. The effect of spin on the aerodynamic loads has also measured although the presented spin rate (2.5 rev/sec) is well below that for typical discus throws, 5 to 8 rev/sec (Ganslen, 1964). The effect of spin does not change the lift and drag curves except to prolong the stall ( $24^\circ$ ) by at least  $4^\circ$ .

Much of the load data in the available reports present measurements which agree only in their general characteristics. The researchers disagree on stall AoA, there are discrepancies in lift curve slope and the form of the drag curve also. It is interesting to see the decrease in drag at stall measured by both Kentzer & Hromas (1958) and Tutjowitsch (1976) however Ganslen (1964) does not report any such thing. None of the above investigators have presented a thorough study of the effect of spin on the aerodynamic loads over a range of typical flight speeds. The only offering being from Kentzer & Hromas (1958) who presented the lift, drag and pitching moment for one speed and one non-zero spin rate only.

No-one to the knowledge of the author, has measured the spin dependent aerodynamic rolling moment, yawing moment and side force. There is a need for a more definitive aerodynamic study of the discus to corroborate the present experimental work currently available on the subject.

### **3.2.3 Coin-like Cylinders**

In related work, Zdravkovich et al (1998) studied the aerodynamics of what he called ‘coin-like cylinders’. These have a thickness to chord ratio  $t_h/c \ll 1$ , where the thickness  $t_h$  is the cylinder height and the chord  $c$  is the diameter of the cylinder. A talcum powder-paraffin film was applied to the cylinder surface to visualise the surface flow. With its planform parallel to the free stream, the flow over the cylinder revealed surface patterns which are similar to those observed during the present experimental work, namely a semi-circular separation line and straight line reattachment. This gave an insight into the interaction of flow structures over the cylinder and allowed the specification of the flow topology. Unfortunately the study was limited to  $0^\circ$  angle of attack and as such has limited relevance in the context of the present study.

### 3.2.4 Analysis on Span Effectiveness factor

As a way of evaluating the relevant aerodynamic load data, within the literature, for circular planform wings, a graph of  $C_D$  against  $C_L^2$  was plotted in Figure 3.1. The aerodynamic load data for various circular wing shapes are compared to the present disc-wing measurements in Figures 5.5 to 5.12 and discussed in full in Chapter 5. However, the graph in Figure 3.1 is considered here as a way of analysing the Span Effectiveness factor  $e$  for circular planforms. The Span Effectiveness or Span Efficiency factor  $e$  is a measure of the drag induced by a finite wing, the theoretical maximum being  $e = 1$  for an elliptical lift distribution which yields minimum induced drag, Anderson (1991). The curves plotted in Figure 3.1 are for a variety of different geometries with chordwise cross-sections as seen in the key next to the figure. These geometries are sports implements (reviewed in section 3.2) and circular wings from aerospace applications (reviewed in appendix B).

To understand the similarities between various circular wing shapes, the gradient of respective curves are compared by means of the span efficiency factor. Applying equation 2.20, the gradient of each curve in Figure 3.1 is given by  $(\pi e AR)^{-1}$  and the AR is identical for every wing with circular planform. Therefore the AR is  $4/\pi$  and the gradient is given by  $0.25 e^{-1}$ . Taking the gradient of the experimental curves in Figure 3.1 we can calculate the span effectiveness  $e$ .

The values of  $e$  for the circular planform geometries compared in Figure 3.1 vary between 0.5 and 0.8. The graph shows Frisbee-like wings with approximately the same span effectiveness  $e \sim 0.8$ , namely Stilley & Carstens (1972) and Ali (1998), however Zimmersmans (1935) planar wing also has similar gradient or in other words  $e \sim 0.8$ . The graph also shows Frisbee-like wings with contrasting gradients, namely Stilley & Carstens (1972) and Yasuda (1999) have span effectiveness  $e \sim 0.8$  and 0.6, respectively. However, recall that the measurements Yasuda (1999) took are expected to have systematic errors, which would account for the lower span efficiency here,  $e \sim 0.6$ . There are also examples of similar planar wings with approximately the same span effectiveness  $e \sim 0.5$ , namely Greif & Tolhurst (1963) and Tutjowitsch (1976).

In general, the curves for Frisbee-like wings have similar magnitudes and similar span effectiveness  $e \sim 0.8$ , see Figure 3.1. However, circular planar wings with thin cross-section also have similar span effectiveness to the Frisbee-like wings,  $e \sim 0.8$ . Circular

planar wings with thick cross-section have much lower span effectiveness,  $e \sim 0.5$ . The Frisbee-like shape therefore has large span effectiveness, relative to other circular wings of identical aspect ratio, within the literature. The Frisbee-like shape therefore has similar induced drag to a thin circular wing, such as the Zimmerman (1935) Clark Y, but lower induced drag than thick solid wings, such as the discus. This is an indicator of the inherent flow structures created over a circular wing, namely trailing vortices in close proximity which induce a strong central downwash with associated spanwise lift distribution and thus span efficiency factor. However, the fact that thicker circular wings have lower span efficiency suggests that the presence of the cavity on the Frisbee-like shape, returns lower induced drag back down to a value similar to planar wings. However, even though they both have a similar span efficiency factor, the spanwise lift distribution for Frisbee-like and planar circular wings could well be different.

### **3.3 Flight Dynamics of Spin-stabilised Disc-wings**

#### **3.3.1 Frisbee**

Katz (1968) developed a simplified mathematical model of a rotating flying disc treating the spin as an independent parameter. Firstly, considering linear aerodynamic moments alone, the derivation of classical stability criteria was given, including steady state results. A non-linear model was derived by adding lift, drag and gravity forces, so that typical flight trajectory solutions could be calculated numerically. From the stability analysis, the increased spin rate was shown to [spin-] stabilise the motion towards a constant precession rate condition. This work is sketchily written and difficult to follow with no formalised conclusions. The flight trajectories are largely two-dimensional and difficult to visualise with scant information on what is being presented in the figures.

Lissaman (1994) considered the dynamics of a spinning oblate spheroid including mathematical stability analysis. The development of a characteristic dynamics matrix from the equations of motion and subsequent decomposition into dynamic groups enabled the modes of the dynamic motion to be determined from the roots of the characteristic equation. A formal dynamic analysis approach enabled the interpretation of the dynamic modes with specific reference to the flying sports disc. Numerical results for a Frisbee disc, with launch parameters chosen carefully to match a realistic throw release, were analysed and compared to Stilley & Carstens (1972) data. The dynamic

modes for both discs were found to be quite similar, their behaviour supported by actual flight tests (Stilley & Carstens, 1972).

Revisiting disc flight dynamics, Lissaman (1998) presented the linearised equations of motion and discussed various numerical codes used to solve them. However problems arose when attempting to integrate the flight equations, it was noted that very small time steps were required to maintain convergence which suggests more computational power was needed. Lissaman (1999) also described the aerodynamics at zero spin rate & non-zero spin, the gyroscopic dynamics and both the longitudinal & lateral flight trajectory. Much of the discussion was based on wind tunnel results from the early data collected for present study. An approximate solution of the longitudinal and lateral trajectories was described but not presented, aerodynamic coefficients were taken from the present research. The spin dependent rolling moment was described to be caused by the delayed separation on the retreating side and earlier separation on the advancing side which makes the spanwise lift distribution asymmetric. However, the local surface moves across the flow on the leading edge of a spinning disc, directly along the arced separation rather than advancing or retreating. Therefore it is not possible to treat the fluidic generation of the rolling moment so simplistically, the rolling moment is generated by a unique combination of interacting flow structures over an axisymmetric body with a rotational slip condition. Latterly, Lissaman (2001; 2003a; 2003b) considered the maximum range of a flying disc compared to other well understood projectiles, mainly spheres.

Hummel & Hubbard (2000; 2001; 2002; 2003; 2004) analysed both the Frisbee throw and flight, from throw biomechanics through the development of a numerical flightpath simulation, even to the extent of identifying aerodynamic coefficients from free-flight tests. Hubbard & Hummel (2000) developed a 5dof simulation and demonstrated basic Frisbee flight trajectories successfully. Hummel (2003) compared simulated trajectories to experimental flight path data (f2302), as in the present study (Fig. 7.3), to validate the simulation.

The simulation included a (linearised) dynamic model for the identification of parameters from flight tests (Hubbard & Hummel, 2002). Free-flight experiments accurately tracked the position of a Frisbee in three dimensions using high-speed video cameras. Linear approximations to aerodynamic coefficients were derived from the

flight data and compared reasonably well to wind tunnel data from the present study, a comparison is given in Figure 5.7.

Estimation of parameters from flight tests is significantly more challenging than wind tunnel testing and there is considerable scatter in the results obtained. Furthermore, it is only possible to obtain parameters linearised around a nominal flight condition. That said, the only experimental data currently available on the rate damping derivatives (Hummel & Hubbard, 2000; 2002) is from flight tests, meaning the technique provides an important input for simulation work.

The biomechanics of Frisbee throwing (Hubbard & Hummel, 2001) provides useful information on the range of launch conditions (altitude, velocity and spin rate) physically possible and, coupled with the use of simulation, allows their optimisation for specific performance goals.

With maturity this study has the potential to accurately simulate the Frisbee throw and resulting flight trajectory, with the power to yield the optimal throwing technique for various purposes, such as maximum range. It could also be used to analyse the throwing technique of specific athletes. In presented work however, the simulation did not progress much further than the validation and the biomechanics model was not taken far enough to couple the two.

Pozzy (2001) investigated the correlation of throw speed with range by clocking the disc release speed at launch, from a professional field of disc golf players, with a radar gun. The range was plotted against launch speed on a scatter graph and a best fit line drawn to show the correlation. Although it is no great surprise that the range increases with higher release speeds, this is a useful resource for the comparison of simulated predictions. Lissaman (2003b) recently considered the 2D flight dynamics to find the upper bounds for maximum range via an optimisation procedure. The solutions were plotted alongside field results (Pozzy, 2001) and found to have reasonable agreement. In both cases the dependence of range on velocity was modelled with a straight line, in spite of the quadratic dependence of the launch speed on the range. Lissaman (2003b) noted that this was due to energy dissipation by drag at high velocities which reduced the favourable effects of lift. It is helpful to bare in mind that the golf throw data was collected in various locations, wind conditions and topology. This could explain the

cluster of scattered points that represented long range achieved for moderate launch speed, which was attributed to throwing technique (Pozzy, 2001).

Cotroneo (1980) analysed biomechanic and aerodynamic aspects of disc flight from throw observations. The study was focussed on the comparison of back-hand and side-arm (fore-hand) throwing technique for maximum distance, including a biomechanic analysis of the athlete subjects with contrasting throw actions yet exceptional range. Minimal wind tunnel test results for a Frisbee without the concentric rings [that forced boundary layer transition] on the upper disc surface, reduced the optimum release angle of attack and improved the lift to drag ratio. Release velocities were correlated with range to confirm that initial velocity is the most important factor affecting the maximum distance thrown. Both back-hand and sidearm throwers could achieve approximately the same range. Pozzy (2002) also investigated the throwing technique, analysing high-speed camera footage of disc golf professionals' launch strategy.

Recently, Lorenz (2004) began to investigate the free-flight dynamics of a Frisbee via measurements from onboard instrumentation. A varied array of real-time data was recorded in flight from pressure sensors, accelerometers, an infra-red sensor, and a magnetometer mounted within the cavity of a Frisbee and uploaded to a computer post flight. The flight trajectory was recorded using a conventional video recorder, digitised and converted into physical distance. The body attitude was calculated from data taken with the various sensors and velocity computed from the video record. The aerodynamic force coefficients could then be calculated from the instantaneous accelerations and the pitching moment from the precessional roll rate, which was derived from the attitude record. The aerodynamic loads were compared to the wind tunnel data of the present study and were in agreement. However, only two points were plotted on each graph of lift, drag and pitching moment and as such were merely only verification that the instrumentation was providing realistic data. The discrepancy between the free-flight load data and the wind tunnel data, of the present study, was at times large in drag and pitching moment but still well within the vicinity of the wind tunnel data to profess a successful correlation. The ongoing research by Lorenz, using this onboard instrumentation methodology, is potentially an extremely useful way of gathering aerodynamic data in free-flight or even within the wind tunnel environment. Future work is proposed to determine the effect of spin on the separation and measure the surface pressure distribution on a spinning disc.

Danowsky & Cohanim (2002) sought to develop a computer model that predicted aerodynamic parameters and use these to simulate free-flight trajectories, which was a similar study to that of Hubbard & Hummel (2000). Instead of deriving parameters from free-flight experiments, they used potential flow theory that was slightly modified to account for the spin.

A wind tunnel balance was constructed from a combination of load cells to give 3dof, set in two positions one which picked up Lift, Drag & Pitching Moment and the other Lift, Side Force & Rolling Moment. A golf disc (Frisbee) was fixed to the balance via a motor driven axle, at  $0^\circ$  angle of attack, to test at various flow and spin rate combinations. The flexibility of the plastic disc particularly at the centre meant that it deformed during high wing loading, observed most dramatically at zero spin but also causing a nose-down orientation for the spinning disc. The solitary angle of attack test case, deformity of the test model and the omission of matched advance ratios over the flow rate test range, limit the accuracy of the data. Smoke wire flow visualisation was used to record the port and starboard sidewash angles from the spinning disc.

Potential flow theory was applied to a virtual disc geometry, similar to that tested in the wind tunnel, to predict aerodynamic parameters. The vortex lattice method was applied to the disc, accounting for spin by the use of a slip boundary condition. The sidewash angles were plotted against advance ratio and were deemed to be dependent parameters, however their plots show two scattered arrays which suggested independence. These angles were required by the computer code to specify the trailing edge. Steady state solutions were obtained iteratively using a wake evolution methodology from which aerodynamic forces could be computed. Simulated flow visualisations based on the wake solutions show the presence of trailing vortices.

The inputs to the flightpath model were derived from the zero angle of attack case alone and as such the accuracy of the trajectories is somewhat dubious. Never-the-less, for high spin rates the plotted trajectories modelled the gyroscopic roll stiffness, the disc held its orientation in a much straighter lateral flightpath. The effect of the bank angle launch condition was also illustrated.

The accuracy of the results obtained during this research is questionable, however this is due to the sheer breadth of the subject matter and analysis techniques employed here, in a short period of time. The wind tunnel tests and the potential flow solutions were limited to the zero angle of attack, which restricted the derivation of aerodynamic inputs solely from this single orientation. The application of potential flow and wake evolution to the Frisbee has, to the knowledge of the author, never been done before. It is a shame that they didn't have time go into more depth.

Tuck & Lazauskas (2004) applied a general lifting surface computer code to the circular planform, in order to compare lift and pitching moment to semi-analytical solutions. Expanded solutions to include axisymmetric discs modelled a simple Frisbee-like profile closely. A combination of these solutions were then used to outline another set of axisymmetric cross-sectional profile solutions that eliminated the pitching moment entirely but as a result drastically reduced the lift too. Eliminating the pitching moment is a highly desirable property of flying discs as it eliminates precessional roll. It is good to keep in mind however, that these solutions are theoretical and as such do not model turbulent and separated flow regimes which dominate the flow over a flying disc in air.

### **3.3.2 Discus**

The earliest study of discus flight (Taylor, 1932) was initiated by the Intercollegiate Associations of Amateur Athletics of America (ICAAA) in response to a puzzling question posed by discus throwers who noticed that they could achieve greater distances when throwing into a headwind. Taylor (1932) investigated this observation using wind tunnel tests and a flight path simulation to offer practical guidelines for intelligent throwing in a prevailing wind. The wind tunnel data and details of the mathematical analysis were not published however, only results of predicted (2DOF) longitudinal flight-paths based on a variation in ambient wind velocity. The model predicted the optimum attitude ( $35^\circ$  to the horizontal) and angle of attack ( $0^\circ$ ) given to the discus at launch to achieve maximum range, for still (no wind) conditions. Using the no wind case as a baseline, Taylor's (1932) calculations suggested that a headwind increased the range whereas a tailwind decreased the range.

As the discus is released for an efficient throw in still air, it is oriented to maximise lift and minimise drag in the climb portion of the flight (Frohlich, 1981). Investigators roughly agree that optimal release angles are around  $30^\circ$  attitude and  $-10^\circ$  AoA

(Bartlett's Table 1, 1992). Although this results in negative lift during the initial portion of flight (Ganslen, 1964; Frohlich, 1981), the discus makes use of the low drag, negative AoA range to minimise deceleration over the climb portion of the flight. The initial upward momentum on release, projects the discus away from the ground and it isn't until the discus reaches the zero lift AoA ( $0^\circ$ ) that there is any aerodynamic lift contribution. The discus generates lift throughout the middle portion of the flight at highest elevation, with a higher rate of deceleration due to the increased drag at high AoA. As the discus descends during the latter portion of the flight, the drag approaches a maximum further retarding the speed as the discus flight path approaches vertical back to ground. A negative AoA at launch is arguably impractical (Samozwetow, 1960) as it limits the speed and stability given to the discus on release. However, Terauds (1978) reported a launch AoA range of  $-10.5^\circ$  to  $-27.5^\circ$  for elite male discus throwing athletes, which supports the calculated optimum AoA values reported in the literature.

Contrary to the common assumption that the discus attitude is constant throughout the flight, small aerodynamic moments will cause the disc to pitch and roll. Samozwetow (1960) reported the roll left wing tip down and subsequent banked left turn towards the end of the discus flight, caused by the (nose up) pitching moment. As the discus rolls the AoA is reduced, Hubbard (1989) suggested that this may cause a favourable change in pitch attitude gaining aerodynamic advantage in flight. Tutjowitsch (1976) claimed the discus bank angle could be ignored given high spin rates. However Soong's (1976) simulation predicted the range to be spin dependent (Soong's figure 5a, 1976) for typical and atypical discus throw spin rates, from 4 up to 740 rev/sec. Voigt (1972) also reported an increase in range with increased spin rate, based on flight test observations.

# **Chapter 4 Experimental Facilities and Techniques**

## **Summary**

*This chapter presents the experimental facilities, apparatus, data acquisition techniques and wind tunnel corrections. Section 4.1 outlines the wind tunnel facilities. Section 4.2 describes the apparatus constructed to mount the disc-wing models in the wind tunnel and the various models themselves. Section 4.3 outlines the techniques used to acquire aerodynamic load & pressure data, and also includes the flow visualisation methodologies. Section 4.4 discusses the blockage corrections applied to the drag data.*

### **4.1 Wind Tunnels**

#### **4.1.1 Goldstein Laboratory**

The Disc-wing wind tunnel research was carried out at the Goldstein Laboratory, a self-contained experimental fluids and aeronautics facility located at Barton Aerodrome, approximately 8 miles from the primary University of Manchester Campus. Established in 1946 by Sidney Goldstein as part of the Mathematics Department the Fluid Motion Laboratory later became the Goldstein Aeronautical Engineering Laboratory, now as part of the Department of Aeronautical Engineering.

#### **4.1.2 Project Tunnel**

The primary low speed wind tunnel used for this research was an open-circuit blow down tunnel with a test section of  $0.9 \times 1.1\text{m}$ , a top speed of  $50\text{m/s}$  and turbulence level of 0.5%. The tunnel is fitted with a six-component balance above the working section and a pressure transducer with scanivalve measurement system, see Fig. 4.1. Outputs are fed via a digital converter to a computer located in the control room (Fig. 4.2), all measurement equipment was operated from here. The balance had  $360^\circ$  yaw control and an incidence arm with  $\pm 30^\circ$  range.

#### **4.1.3 9' $\times$ 7' Tunnel**

A second low speed wind tunnel had a closed-circuit with a test section of  $2.1 \times 2.7\text{m}$  (9'  $\times$  7'), a top speed of  $70\text{m/s}$  and a turbulence level of 0.1%. This was used for the smoke wire experiments due to the superior flow quality at low speeds.

## 4.2 Apparatus

### 4.2.1 Rigs

A number of metal frames were used to mount the disc-wing in the wind tunnel in various configurations. The first (Fig. 4.3) was an L shaped arm with the disc mounted vertically on a horizontal axle supported by a vertical strut. The disc was mounted, with its planform vertical, on a motor driven axle to test at various spin rates, the disc's centre of mass remained at the balance centre at all times.

The second rig was used for surface paint flow visualisation and held the disc in the horizontal plane (Fig. 4.4). It consisted of two vertical struts connected to a horizontal crosspiece. In the centre of the horizontal bar, an axle was mounted vertically, at zero incidence, on which the disc could be spun with its planform horizontal. Incidence was adjusted using an incidence arm.

The first support strut was also adapted for use in the 9' × 7' tunnel (Fig. 4.5a). This was necessary for the smoke wire flow visualisation work as the flow quality in this wind tunnel was superb. Modified parts were designed to fit the versatile L-shaped strut, including a geared down motor (for fine incidence control) and side sting mounted disc (Fig. 4.5b), for the purpose of visualising the full central flow field cross-section of a non-spinning disc.

### 4.2.2 Disc-wing Models

The geometry of the disc-wing used for the majority of experiments was based on that of a Floater<sup>TM</sup> sports disc manufactured by Dynamic Discs<sup>TM</sup>. The half cross-sectional profile can be seen in Fig. 2.1, with the axis of symmetry vertical and on the left of the figure.

The model used for spinning and non-spinning load measurements was machined from aluminium and dynamically balanced by hand. Commercially available plastic discs were adapted for taking surface pressure measurements and flow visualisation studies.

Other test models were a flat plate disc and a semi flat plate disc i.e. an intermediate disc-wing model between the flat plate and the Frisbee. Both were formed from flat aluminium sheet to the profiles shown in Fig. 4.6.

## 4.3 Data Acquisition

### 4.3.1 Load Data

The load measurements for the disc-wing were taken using a six component overhead balance in the  $0.9 \times 1.1\text{m}$  wind tunnel. The disc-wing was tested over a range of Reynolds numbers from  $1.13 \times 10^5$  to  $3.78 \times 10^5$ , corresponding to a speed range of 6m/s to 20m/s, with an angle of attack range from  $-100^\circ$  to as much as  $100^\circ$  and spin rates up to 24Hz or 1440rpm.

The aerodynamic forces acting on the rig and disc induced mechanical moments due to the off-centre lone strut configuration. This had a significant effect on the pitching and rolling moment measurements. Taking measurements of the moments caused by the static loading of the strut at the centre of the balance, these mechanical components were removed.

Interference and tare effects due to the strut were measured with the disc mounted on a dummy support, Fig. 4.7. The dummy strut was a mirror image of the measuring strut and held the disc in the correct position, on the balance centre. The aerodynamic loads acting on the wind tunnel support strut (including interference effects from the dummy strut mounted disc) are presented in Fig. 4.8 alongside results for the test model itself.

### 4.3.2 Surface Pressure Data

Two pressure tapped disc models were fabricated, one for upper surface pressures, the other for lower surface pressures. The necessary pressure tubing used for surface pressure measurement, connected the pressure tappings to the scanivalve. The capillary tubes were carefully wound around the L shaped rig, as shown in Fig. 4.9, to limit interference. The tappings were arranged in a curved line (Fig. 4.10a) to both facilitate the manufacturing process and reduce boundary layer interference effects on down stream tappings. The pressure across the entire disc surface was measured by yawing the model at  $12^\circ$  increments to achieve effective coverage (Fig. 4.10b) providing 1200 measurements in total, for each set of conditions. Tests were performed at 20m/s through an AoA range of  $-10^\circ$  to  $30^\circ$  and at  $5^\circ$  for velocities 6, 10, 15 & 20m/s.

### **4.3.3 Flow Visualisation**

#### **4.3.3.1 Surface paint**

A film of fluorescent paint, made up of a mix of two parts kerosene to one part fluorescent powder, was applied liberally to the surface of the disc. The disc was then mounted in the wind tunnel at the required angle of attack and the tunnel run until the kerosene had evaporated. Streak lines in the resulting surface patterns indicate the time-averaged orientation of the surface flow direction and reveal important surface flow structures, such as separation lines. Flow patterns were photographed outside the wind tunnel under ultra-violet rich light. Note that for the flow visualisation studies, the disc was mounted in the horizontal plane to minimise the effects of gravity on the surface flow patterns. The surface oil flow technique is, by its nature, only suitable for the non-spinning disc.

#### **4.3.3.2 Smoke wire**

There are many methods for generating smoke filaments such as the smoke wire, smoke wand and smoke rake. The smoke wire technique was chosen for this investigation as it could provide many thin smoke filaments, ideal for the visualisation of a complex 3D flow such as this. The smoke is generated by the resistive heating of a wire causing the vaporisation of oil droplets. As the flow passes the wire it creates a smoke filled wake behind it. With a small diameter wire (0.1mm) and at low speeds (<2m/s) the wake is laminar, producing clearly defined smoke filaments. The most rewarding results from the smoke wire technique are achieved by a careful balance of flow speed, electrical power and oil supply. As with any other flow visualisation technique the captured images are only as good as the camera and lighting equipment.

A vertical wire was mounted upstream of the disc with a pressurised oil reservoir connected allowing continuous feed (Fig. 4.11). The nichrome flat wire (0.1×0.4mm rectangular cross-section) was electrically heated causing the oil to vaporise producing smoke filaments. The wire was aligned with the flow so that the narrow edge pointed upstream, this limited the turbulence generated behind the wire. A number of models were constructed so that the disc-wing could be mounted in both the vertical and horizontal planes. This allowed the wire to remain vertical and therefore continuous smoke filaments could be generated due to the gravity oil feed system. The disc was tested at a maximum flow speed of 3m/s and 0° to 50° incidence. At speeds greater than 3m/s smoke filaments from the wire became turbulent.

An oil feed system (Fig. 4.11a) was set up on the wind tunnel to provide a continuous supply to the smoke wire. A regulated cylinder filled with compressed nitrogen pressurised an oil reservoir to 10psi, this was held above the tunnel. The reservoir pressure forced the oil to flow along the capillary tubing and dripped oil onto the smoke wire through the feeder device (Fig. 4.11b). The oil feeder was a simple and effective device that dripped oil onto the wire through a narrow bore steel tube, this also provided a contact for the power supply. The wire was electrically heated by a power supply connected at each end and the base of the wire was weighted to keep it taut.

The flow field cross-sections were illuminated using 1000 watt halogen spot lamps positioned on opposite sides of the disc. The cross-sections of the separation and vortex structures were illuminated using a laser light sheet. The laser beam was transmitted through a fibre optic cable and a cylindrical lens split the beam into a light sheet of 4mm thickness. The air-cooled, argon-ion laser was operated at 200mW intensity. Footage of the smoke was captured by a video camera operating at various shutter speeds and individual images were transferred to a computer via a frame grabber card. For optimum image definition and contrast, Ondina oil was chosen as it generates clearly visible smoke filaments.

#### **4.4 Wind Tunnel Corrections**

Many methods of correcting for blockage effects were considered but the one which seemed most applicable and gave reasonable results is Maskell's separated flow blockage correction. The complexity of the flow over a disc-wing has demanded a careful analysis to realistically represent the true drag of the disc. The two definitive flow 'states' for a disc-wing at incidence are pre- and post-stall which are dominated by induced and separated drag respectively. Physically this corresponds to the transition from a pre-stall flow state dominated by large trailing vortices to a post-stall state with a large closed separation bubble aft of the disc (Fail et al, Fig. 6a, 1957).

The unconventional shape of the disc-wing has meant that the classical blockage correction methods proposed by Maskell among others must be applied intelligently to represent realistically the true drag appropriately.

The experiments were conducted in a wind tunnel with an octagonal test section with height 0.9m, width 1.1m and cross sectional area  $S_{wt} = 0.9\text{m}^2$ . The disc-wing model and wake cause the flow to accelerate around the obstruction due to the confinement of an enclosed working section. This tends to introduce an error in the drag measurements but can be removed by applying a blockage correction. The blockage is dependent upon the flow regime, in the case of the disc-wing the blockage is negligible at low AoA (around  $0^\circ$ ) and significant at higher AoA (above  $30^\circ$ , say).

Full details of how Maskell's blockage correction was applied to the drag results taken in the wind tunnel is outlined in Appendix C, both corrected and uncorrected  $C_D$  curves for the full range of AoA are shown in Figure C.2.

It was deemed more reasonable to leave the lift and pitching moment data uncorrected than to misrepresent the lift and pitching moment curves through the inappropriate application of standardised wind tunnel correction methods, developed primarily for higher aspect ratio wings. The drag correction however was considered to represent the flow physics appropriately and the resulting post-stall drag data agrees closely with high AoA results found in the literature (Stilley & Carstens, 1971; 1972; White, 1999).

# Chapter 5 Experimental Results

## Summary

*This chapter presents the wind tunnel based experimental work, including force & moment characteristics, surface pressure data and flow visualisation results. Section 5.1 is split into three main sections: section 5.1.1 presents the baseline load characteristics for the non-spinning disc-wing configuration and outlines test results of basic geometry variations to illustrate why the Frisbee-like shape is so stable. Section 5.1.2 compares and contrasts the present load data with a representative low aspect ratio (disc) wing based on finite wing theory and similar disc-wings found in the literature. Section 5.1.3 considers the effect of spin on the aerodynamics for various Reynolds numbers and advance ratios. Section 5.2 outlines the surface pressure data for the non-spinning disc, including colour contour plots, cross-sectional profiles, effect of Reynolds number and a comparison of aerodynamic coefficients integrated from the pressure data to those directly measured in the wind tunnel. Section 5.3 presents flow visualisation images taken using surface paint and smoke wire techniques, to provide information for a description of the flow physics.*

## 5.1 Load Data

### 5.1.1 Non-spinning Case

#### 5.1.1.1 Baseline force and moment data

Force and moment coefficient data for the non-spinning disc for a range of angle of attack scales is shown in Figs. 5.1 to 5.5. A number of important observations can be made from these data:

- The angle of attack for zero lift is approximately  $-3^\circ$ .
- The best lift to drag ratio is approximately 3, and occurs at around  $7^\circ$  AoA.
- The lift curve is approximately linear ( $C_{L\alpha} \sim 0.05$  per degree) up to the stall, which occurs at around  $45^\circ$  AoA. The flow is separated even at zero AoA and the term ‘stall’ is therefore somewhat unconventionally used here to describe the change from partially separated to fully separated flow.

- The stall is associated with a steep decrease in lift, drag and pitching moment.
- The minimum profile drag  $C_{D_0}$  is 0.085 at the zero lift AoA,  $-3^\circ$ .
- The side force and rolling moment are negligible over the whole AoA range, as would be expected for a rotationally symmetric disc.
- The slope of the pitching moment (about the centre of gravity) is generally positive, indicating negative pitch stability. However, between  $0^\circ$  to  $10^\circ$  AoA, the positive gradient, and hence instability, is much reduced.
- A (unstable) trim point exists at approximately  $8^\circ$  AoA, meaning the angle at which the pitching moment is zero.
- Since the disc is asymmetric in the  $xy$  plane, force and moment characteristics are dissimilar at positive and negative incidences. In particular, a less clearly defined stall is not present at negative incidences. This is due to the differing leading edge geometry presented to the flow.
- The span efficiency  $e$  was found to be 0.83.

#### 5.1.1.2 Reynolds number effects

Lift, drag and pitching moment data from  $-10^\circ$  to  $30^\circ$  AoA at a range of Reynolds numbers corresponding to a speed range from 6 to 25m/s are shown in Fig. 5.4. For the speed range tested the force and moment coefficients are approximately independent of Reynolds number, however a slightly more significant change is noticeable in the pitching moment compared to the force coefficients.

#### 5.1.1.3 Comparison with theory

A comparison of experimental lift and drag data for a sports disc with that predicted from finite wing theory as outlined in section 2.3 is shown in Fig. 5.6. The figure also includes data for a non-axisymmetric circular planform wing with a Clark Y cross section. The following observations have been made:

##### *Lift curves*

- The lift curve slope of the Zimmerman wing is almost identical to that predicted from theory ( $\sim 0.041$  per degree).

- The sports disc lift curve slope is on average slightly greater than expected from theory ( $\sim 0.049$  per degree).

### *Drag polars*

- The zero lift drag coefficient calculated for the disc-wing ( $\sim 0.1$ ) is almost identical to the experimental value.
- The zero lift drag coefficient of the Zimmerman wing is approximately a factor of 5 less than for the Frisbee-like sports disc. This performance increase is due to the streamlining of the trailing edge, which is impractical for an axisymmetric cross section.
- The second derivatives of the Zimmerman and theoretical drag curves are similar, indicating that the lift dependent drag coefficients are similar.
- The second derivative of the sports disc drag curves is greater than that for the theoretical curve, indicating that the lift dependent drag coefficients for the sports disc are greater than that predicted from theory. Note, however, that the theoretical drag polar is calculated from the theoretical lift curve slope. If the theoretical drag polar is calculated from the actual lift curve slope the agreement in lift dependent drag coefficients is much closer. Also, note that using a span efficiency value  $e$  ( $= 0.83$ ) derived from experiment (Fig. 5.5d) did not make any appreciable difference, theoretical curves were therefore calculated using the first approximation  $e = 1$ .

#### 5.1.1.4 Comparison with data from the literature

##### *Comparison with other Frisbee-like geometries*

A comparison of the aerodynamic loads to data from the literature is shown in Fig. 5.7, for Frisbee-like disc-wing geometries with cross-sectional profiles similar to that of Fig. 2.1. The data is derived from three wind tunnel experiments (Stilley & Carstens, 1972; Ali, 1998; Yasuda, 1999) and a free-flight experiment (Hubbard & Hummel, 2002). Hubbard & Hummel's coefficients were estimated from multiple short flights of a flying sports disc (<20m range), similar to the disc-wing used in the present study.

The lift curves (Fig. 5.7a) all have a negative zero lift AoA and similar gradients. The drag curves are all approximately parabolic (Fig. 5.7b) with good agreement for the

profile drag but some disparity for the lift dependent drag coefficient. This is to be expected as a result of the small variation in the lift curve slopes.

The pitching moment curves (Fig. 5.7c) are all of similar form, with a region of reduced slope between 0 and 10° AoA. However, there is a negative pitching moment offset in the data of Stilley & Carstens (1972) at low AoA and a positive offset in the data of Ali (1998) at a higher AoA. It is not clear whether these are genuine differences or discrepancies due to experimental methods used.

A comparison of the data from the present study to that of Stilley & Carstens over an AoA range of -30 to +90 is shown in Fig. 5.8. The most noticeable difference is that the Stilley & Carstens disc stalls at around 30° AoA whereas the disc in the present study stalls at 45°, leading to large differences in forces and moments between 30° and 45° AoA. Notice also that the severity of the stall for the Potts & Crowther disc is much greater than that for the Stilley & Carstens disc. Once both discs have stalled, however, the data is once again in reasonable agreement. It is believed that the differences in the stall data between the two discs is attributable to difference in leading edge profile and differences in tunnel mounting arrangement (Stilley & Carstens mounted their disc from the side, which would interfere with the rollup of the leading edge vortex on one side).

#### *Comparison of circular planforms with non Frisbee-like profiles*

A comparison of the present data to that found in the literature for non-Frisbee-like circular planform geometries is shown in Fig. 5.9. The data set plotted here is derived from many experiments working at very different Reynolds numbers up to  $3.3 \times 10^6$  (Demele & Brownson, 1961). Note that these disc-wings are all axi-symmetric apart from the Zimmerman disc.

The Discus (Tutjowitsch, 1976), from field athletics, has zero camber and therefore zero lift at zero AoA (Fig. 5.9a). The Avrocar shape (Greif & Tolhurst, 1963) and the Clark Y disc-wing (Zimmerman, 1935) are both positively cambered and the lift curves are offset compared to the Discus (Fig. 5.9a).

The sharp rim streamlined geometry (Greif, Kelly & Tolhurst, 1960) was shown to have negative lift up to around 2° AoA. The central raised platform geometry suggests that this shape should have positive camber and positive lift at zero AoA. Their wind tunnel apparatus (Greif, Kelly & Tolhurst, 1960) included a single L-shaped strut, similar to that used in the present study, centrally attached through the raised platform. The strut

diameter was around half that of the raised platform diameter. Therefore the most likely explanation for a zero lift measurement at  $2^\circ$  AoA is strut interference over the upper surface raised platform.

The re-entry geometry (Demele & Brownson, 1961) has negative camber and a lift curve with positive zero lift AoA, at around  $3^\circ$ .

The Discus has half the profile drag ( $C_{D0} \sim 0.04$ ) of the Frisbee-like shape (Fig. 5.9b). However, the more streamlined sharp-rimmed disc (Greif, Kelly & Tolhurst, 1960) is unexpectedly much larger ( $C_{D0} \sim 0.12$ ), again the most likely situation is that the strut interference has added an error into the drag measurements, as previously reasoned. It is also surprising that the drag measurements for the Avrocar shape (Greif & Tolhurst, 1963) and the re-entry geometry (Demele & Brownson, 1961) are so different, even the profile drag ( $C_{D0} \sim 0.06$  &  $C_{D0} < 0.01$ , respectively).

The pitching moment curves (Fig. 5.9c) fall into three sets: Firstly, the Frisbee-like disc has minimum gradient (0.001 per degree) over the typical flight AoA range ( $0^\circ$  to  $10^\circ$ ) and trim AoA at  $9^\circ$ . Secondly, Greif & Tolhurst's (1963), Greif, Kelly & Tolhurst's (1960) and Zimmerman's (1935) disc geometries overlay one another and have steeper gradient (0.008 per degree) and trim AoA at around  $3^\circ$ . Thirdly, Kentzer & Hromas' (1958) Discus and Demele & Brownson's (1961) geometry overlay each other with even steeper gradient (0.01 per degree) and a trim AoA at  $0^\circ$  or just above.

For the typical flight angle of attack range ( $0^\circ$  to  $10^\circ$ ), the negatively cambered re-entry disc (Demele & Brownson, 1961) has the highest nose up pitching moment, followed by the Discus (Kentzer & Hromas, 1958) but has approximately the same gradient and magnitude. For the positively cambered discs (Zimmermen, 1935; Greif, Kelly & Tolhurst, 1960; Greif & Tolhurst, 1963) the nose up (overlaying) pitching moment curves decrease in magnitude and in gradient slightly also, all have a zero pitching moment trim condition at  $3^\circ$  AoA. As the cavity is introduced i.e. Frisbee-like disc-wing, the pitching moment gradient decreases, becoming almost zero but slightly positive with a higher trim condition at  $9^\circ$  AoA. So from negative (Demele & Brownson, 1961), through zero (Kentzer & Hromas, 1958) to positive camber (Zimmerman, 1935; Greif, Kelly & Tolhurst, 1960; Greif & Tolhurst, 1963) and the introduction of a cavity (Frisbee-like shape), the pitching moment curve has decreasing gradient & magnitude and increasing trim AoA (Fig. 5.9c).

All the data described so far, found in the literature, is plotted on large-scale graphs for easy comparison (Figs 5.10 to 5.12).

### 5.1.2 Force and Moment Data for a Spinning Disc

Force and moment data for a disc at various spin rates (0, 4, 8, 16 & 24Hz) and free stream speeds (6, 10, 15 & 20m/s) is shown in Figs 5.13 to 5.19. Note that an advance ratio of 1 corresponds to the maximum value expected for a typical hand launch of a sports disc. Spin direction is clockwise when viewed from above.

The first figure (5.13) shows data for a speed of 20m/s plotted at a similar scale to that shown for previous non-spinning cases. A number of conclusions can be drawn from this data:

- For advance ratios up to 1, the change in lift and drag is small compared to the changes due to variations in AoA.
- Increasing advance ratio generates an increasing side force increment. This increment is independent of angle of attack over the range presented. The sign of the side force increment is consistent with the sign of the Magnus force generated on a spinning cylinder with cross flow.
- There are small changes in pitching moment and rolling moment between  $0^\circ$  and  $10^\circ$  AoA due to the effects of spin. The changes are consistent with negative changes in  $C_{Mo}$  and  $C_{Ro}$ , however it is not clear why the spin causes these changes, although some evidence is provided by the off surface flow visualisation of the spinning disc discussed later.

For reference, the side force, rolling moment and pitching moment results discussed above are shown at increased y-axis scale in Fig. 5.14.

To investigate the effect of higher advance ratios, the tests presented in Fig. 5.13 were repeated at the same spin rates but reduced free stream speeds, Figs 5.15 to 5.19. The most important result from these tests is that at sufficiently high advance ratios ( $>1$ ), there is a significant increase lift (e.g.  $\Delta C_L$  of 0.5). It is speculated that this is due to spin-induced radial flow components on the upper and cavity surfaces of the disc.

From a dimensional perspective, it is expected that force and moment coefficient data taken at different spin rates and free stream speeds should collapse if plotted against the advance ratio. To investigate this, data was obtained at a fixed angle of attack ( $0^\circ$ ) by varying advance ratio for a number of different speeds, Fig. 5.20. From this figure it is apparent that the correlation with advance ratio is in good agreement for the lift, drag, pitching moment and rolling moment. Although the correlation for side force is not apparent here (Fig. 5.20c), re-plotting side force against spin rate clearly shows that the curves overlay one another. This suggests that the side force is independent of Re number and dependent upon spin rate, for reasons that are at present unclear.

The spin dependent rolling moment (Fig. 5.20e) curves show a good correlation with advance ratio. This suggests that the asymmetric lift generation over the spinning disc is consistent across appropriately matched flow conditions. The errors observed on the lowest Reynolds number ( $\text{Re} = 1.13 \times 10^5$ )  $C_R$  curve at rapid spin rates and low flow speeds, are likely to be caused by the vibration transmitted to the balance at resonant (spin) frequencies, particularly at  $\text{AdvR} \sim 2 \& 3$ .

### 5.1.3 Basic Geometry Comparisons

#### 5.1.3.1 Camber

Force and moment data for various discs with increased camber (or cavity depth) are presented in Fig. 5.21, cross-sectional profiles of the various axisymmetric discs are provided in a key below the figure. The dimensions of three of the discs are given on Fig. 4.6, the thickness of the fourth test model was extended using a thin annular ring fixed inside the rim of the disc, protruding at a fixed height above the lip.

Using the frisbee-like configuration as the baseline case ( $t_h/c = 0.14$ ), the reduced drag and increased lift of the intermediate shape ( $t_h/c = 0.06$ ) suggests superior performance but the larger (nose up) pitching moment would give stronger roll divergence, above  $3^\circ$  AoA. This would cause the disc to roll, bank and sideslip away from the initial flight direction more strongly than the frisbee-like disc. The minimum thickness of the flat plate disc ( $t_h/c = 0.01$ ) ensures that the profile drag is very low,  $C_{Do} = 0.015$  at  $0^\circ$  AoA, but the pitching moment is even larger (stronger roll), than the more cambered shapes tested. The disc with increased rim height ( $t_h/c = 0.16$ ) was shown to have a relatively moderate (but not small) nose up pitching moment over the typical flight angle of attack

range. The frisbee-like geometry therefore, has a unique small nose down pitching moment for typical flight angles of attack that is lost for both increased and reduced camber.

#### 5.1.3.2 Cavity

The aerodynamic loads acting on the frisbee-like configuration (hollow cavity) are compared to the cavity filled variant (solid) in Fig. 5.22. The upper surface is identical for both discs, the only difference being the cavity geometry. The lift curve slope of the solid disc is much lower ( $\sim 0.03$  per degree) than for the hollow shape. The drag of the solid shape is roughly half that of the frisbee-like disc, the profile drag is much lower,  $C_{D_0} \sim 0.047$ . The pitching moment gradient of the solid geometry is much steeper and nose up, above  $2^\circ$  AoA. The large contrast in load measurements is primarily caused by the inside cavity rim, of the hollow configuration, being presented to the incident flow. This increases both the lift & drag and provides a large nose down pitching moment increment, reducing the pitching moment slope close to zero. The frisbee-like (hollow) geometry therefore, has a unique small nose down pitching moment for typical flight angles of attack that is lost for the cavity filled (solid) variant.

## 5.2 Surface Pressure Data

### 5.2.1 Overview

The surface pressure distribution on a non-rotating disc-wing was investigated over an angle of attack range and at various flow speeds. The data is presented as colour weighted contour plots of pressure coefficients  $C_p$  and cross-sectional profiles for both the upper and lower (cavity) surfaces. The colour contour plots are generated directly from the pressure data, the pressure profiles are taken from a fine grid of points 1/2 mm apart interpolated from the pressure data.

The following outlines the surface pressure distribution for a typical angle of attack and contrasts the variation over an AoA range. The effect of Reynolds number on the pressure distribution is discussed and the load data integrated from the pressure data is compared to the directly measured aerodynamic load data.

The pressure data plotted in Fig. 5.23 and thereafter takes the 3D surface pressure distribution and creates a 2D surface, with the 2D radial distance equal to the 3D surface distance. This has the effect of stretching the data at the edges of the disc compared to the true view of the surface when viewed from above. Note also that whilst all pressure distributions are nominally symmetric about the  $xz$  plane, data was taken over the entire surface of disc, not over half the disc and mirrored.

### 5.2.2 Discussion of Results at Typical Flight Angle of Attack ( $5^\circ$ )

The upper & lower surface pressure distributions at  $Re = 2.84 \times 10^5$ , equivalent to a flow speed of 15m/s and AoA =  $5^\circ$  are shown in Figs 5.23 to 5.27.

The highest pressure region (A), Fig. 5.25a, occurs on the leading edge upper surface with a low pressure crescent region (B) aft of this region. The central part of the disc shows pressure recovery (C). The low pressure band (D) on the trailing edge rim is associated with trailing vortices and bluff body effects. Low pressure (F) is seen within the cavity (Fig. 5.25b) except inside the trailing edge rim (G).

The central cross-sectional pressure profile at the half span station is shown in Fig. 5.26, leading edge on the left of the figure. The upper surface is shown by the unbroken line, the lower surface curve is dashed. The cross-sectional disc geometry is also shown to relate the location of pressure peaks to the disc surface. The high (positive) pressure coefficient on the leading edge is shown by the spike at zero chord ( $C_p \rightarrow 1$ ), positive pressure axis down. The lowest pressure region at around tenth chord ( $C_p \sim -1.25$ ) and secondary peak thereafter produce a large suction on the leading edge. The pressure recovery on the upper surface is the same pressure as in the cavity ( $C_p \sim -0.25$ ) through the central portion (0.3c to 0.6c). The high pressure trough in the cavity ( $C_p \sim 0.3$ ) and the upper surface low pressure peak ( $C_p \sim -0.8$ ) are shown on the trailing edge. It is clear that the main contributions to the lift are from the low pressure peak on the leading edge and the large pressure difference on the trailing edge. The spikes in the cavity surface data at  $x/c \sim 0.05$  &  $0.95$  are due to the presence of the vertical surface at this location.

The pressure profile at the half chord station is shown in Fig. 5.27, port wing tip on the left of the figure. The symmetry of the profile is evident, the only pressure difference visible at the wing tips. Much of the upper and lower surface is set at a consistent low pressure ( $C_p = -0.3$ ).

### 5.2.3 Effect of Angle of Attack on Pressure Distributions

The variation in surface pressure distribution with angle of attack is shown in Figs 5.28 to 5.31, for  $Re = 2.84 \times 10^5$  and  $AoA = -10^\circ$  to  $30^\circ$ .

The pressure of the upper surface distribution (Fig. 5.28) can be seen to decrease, as a whole, with increased angle of attack. The high pressure region (red) on the leading edge becomes narrower and moves progressively forward with increased AoA. The low pressure region aft of the leading edge high pressure region (yellow, Fig. 5.28a; blue/green, Fig. 5.28e) grows with AoA, extending downstream and decreasing in pressure magnitude ( $C_p \sim -1$ , Fig. 5.28c;  $C_p \sim -2.5$ , Fig. 5.28i). The central pressure recovery region (orange, Fig. 5.28a; yellow, Fig. 5.28e) decreases in pressure slightly with AoA. Above  $10^\circ$  AoA the pressure recovery region reduces in size and moves downstream locating aft of the disc centre at around  $x/c = 0.7$ . The low pressure band on the trailing edge (green, Fig. 5.28a; green, Fig. 5.28e) curves upstream near the wing tips at  $-10^\circ$  AoA, becoming a figure of eight formation at  $0^\circ$ . Low pressure spots develop on the wing tips (blue, Fig. 5.28e) by  $10^\circ$  AoA, growing in size and moving upstream with increasing AoA. A pressure recovery region is visible on the trailing edge rim, which decreases in pressure with AoA (orange, Fig. 5.28a; yellow, Fig. 5.28i).

The pressure of the cavity surface distribution (Fig. 5.29) can be seen to increase, as a whole, with increased angle of attack. The disc cavity exhibits low pressure over much of the lower surface (green, Fig. 5.29a; yellow, Fig. 5.29c) for low AoA. The high pressure region on the trailing edge rim (orange, Fig. 5.29a; red, Fig. 5.29e) grows in size as the cavity becomes more exposed at increased AoA. At high AoA a higher pressure region develops just ahead of the disc centre (red, Fig. 5.29h; dark red, Fig. 5.29i). At  $30^\circ$  the isolated high pressure region (dark red, Fig. 5.29i) just ahead of the centre approaches a  $C_p$  of 1, it decreases thereafter until the approach to the trailing edge where the steep rim surface forces compression and the  $C_p$  approaches 1 again.

The central cross-sectional pressure profiles at the half span station are shown in Fig. 5.30, for various AoA at  $10^\circ$  intervals. Considering firstly the upper surface, from an AoA of  $-10^\circ$  the low pressure peak on the leading edge increases in magnitude with AoA ( $C_p \sim -0.5$  at  $-10^\circ$  AoA;  $C_p \sim -2.5$  at  $30^\circ$ ) and moves towards the leading edge. However, at  $20^\circ$  AoA the initial low pressure peak decreases in magnitude slightly from

$10^\circ$  ( $C_p \sim -1.5$  at  $10^\circ$  AoA;  $C_p \sim -1.3$  at  $20^\circ$ ) but the secondary peak becomes elongated ( $20^\circ$  AoA) moving further downstream. The central higher pressure trough increases in magnitude slightly with AoA ( $C_p \sim -0.1$  at  $-10^\circ$  AoA;  $C_p \sim -0.3$  at  $10^\circ$ ) and shifts downstream aft of the disc centre ( $x/c \sim 0.7$ ,  $20^\circ$  AoA) for higher AoA. The low pressure peak on the trailing edge increases in magnitude with AoA ( $C_p \sim -0.7$  at  $-10^\circ$  AoA;  $C_p \sim -1.3$  at  $30^\circ$ ) but remains located at around  $x/c = 0.9$ .

Secondly, considering the lower surface (Fig. 5.30), the low pressure over much of the surface becomes higher with increased AoA ( $C_p \sim -0.7$  at  $-10^\circ$  AoA;  $C_p \sim 0.6$  at  $30^\circ$ ,  $x/c = 0.5$ ). The high pressure trough within the trailing edge cavity becomes higher with AoA ( $C_p \sim -0.2$  at  $-10^\circ$  AoA,  $C_p \sim 1$  at  $30^\circ$ ;  $x/c = 0.95$ ) and another high pressure trough develops at around  $x/c = 0.3$  for high AoA ( $C_p \sim 0.9$  at  $30^\circ$  AoA).

A high pressure spike is seen on the leading edge, for both the upper and lower surfaces, at all AoA tested (Fig. 5.30 & 5.31).

The central cross-sectional pressure profiles at the half span station are shown in Fig. 5.31, for various AoA at  $5^\circ$  intervals. The data presented here (Fig. 5.31) allows the comparison of a greater number of attack angles and the gradual transition with increasing AoA is more evident. The lower surface curve shows lower pressure (overall) than the upper surface at  $-10^\circ$  AoA. Overall, the upper and lower surface pressure becomes lower and higher, respectively, with increased AoA.

The cross-sectional pressure profiles at various span stations are shown in Fig. 5.32, for  $5^\circ$  AoA. The cross-sectional slice through the disc, shown below each plot, is at the respective span position to relate the location of pressure peaks to the disc surface. A full description of the pressure profile at the half span station (Fig. 5.32a) is given previously with reference to Fig. 5.26. At further outboard stations the profile is broadly similar, almost identical at the  $3/8$  span position (Fig. 5.32b). The magnitude of the low pressure (double) peak on the leading edge decreases in magnitude towards the wing tips ( $C_p \sim -1.2$  at  $3/8$  b station;  $C_p \sim -0.8$  at  $1/8$  b station). The low pressure peak on the trailing edge increases in magnitude ( $C_p \sim -0.7$  at  $1/2$  b station;  $C_p \sim -1.3$  at  $1/8$  b station) at outboard stations becoming more of a spike at the  $1/8$  span position (Fig. 5.32d). The lower surface remains at a constantly low pressure ( $C_p \sim -0.25$ ), for all span stations, aft of the high pressure spike except towards the trailing edge. The high

pressure trough just upstream of the trailing edge, inside the cavity rim, is at a consistent maximum pressure for all span stations ( $C_p \sim 0.3$ ) except 1/8 b ( $C_p \sim -0.2$ ).

A grid of cross-sectional pressure profiles at various span/chord stations and various AoA are shown in Fig. 5.33, to give a more complete set of pressure profiles for comparison. Many of the profiles and trends have previously been described with reference to Figs 5.30 to 5.32. Just to comment on the variation with AoA at the 1/2 chord station (Fig. 5.33v), the symmetry is evident at low AoA (-10° to 10°) but the upper surface pressure profile becomes asymmetric at higher AoA (20° & 30°). The constant low pressure over the central portion of the upper surface increases in magnitude slightly for increasing AoA (-10° to 10°), increasing further for higher AoA (20°, Fig. 5.33d,v) and developing a central trough at 30° (Fig. 5.33e,v). The low pressure (upper surface) increases in magnitude towards the wing tips ( $x/b = 0$  & 1) for all AoA ( $C_p \sim -0.5$ , Fig. 5.33a,v;  $C_p \sim -1.5$ , Fig. 5.33d,v). The constant low pressure over the central portion of the lower surface becomes high pressure for increasing AoA ( $C_p \sim -0.6$  at  $x/c = 0.5$ , Fig. 5.33a,v;  $C_p \sim 0.6$  at  $x/c = 0.5$ , Fig. 5.33e,v). The pressure drops sharply at the wing tips (lower surface) for high AoA (10° to 30°, Fig. 5.33v).

#### **5.2.4 Effect of Reynolds number on pressure distributions**

The variation in surface pressure distribution with Reynolds number is shown in Figs 5.34 to 5.36, for AoA = 5°,  $Re = 1.13$  to  $3.78 \times 10^5$  equivalent to  $V_\infty = 6$  to 20m/s.

The pressure surface distributions presented in Figs 5.34 & 5.35 are at first glance identical but there are small differences. The low pressure crescent aft of the leading edge (blue, Fig. 5.34) narrows with increased Re, the downstream edge moves upstream. The magnitude of this low pressure region increases, as does that of the low pressure band on the trailing edge (blue, Fig. 5.34a; dark blue, Fig. 5.34d). The pressure distribution within the cavity is unaffected by Re (Fig. 5.35).

The central cross-section profiles (Fig. 5.36) show that the upper surface low pressure double peak aft of the leading edge narrows but increases in magnitude with increased Re. The primary low pressure peak location remains at  $x/c \sim 0.1$  for all Re tested, whereas the secondary peak moves upstream ( $Re = 1.13 \times 10^5$  at  $x/c \sim 0.3$ ;  $Re = 2.84 \times 10^5$  at  $x/c \sim 0.2$ ). The low pressure peak on the trailing edge increases in magnitude

( $C_p \sim -0.6$ ,  $Re = 1.13 \times 10^5$ ;  $C_p \sim -0.9$ ,  $Re = 3.78 \times 10^5$ ) but remains at  $x/c \sim 0.9$ . The lower surface pressure profiles overlay one another for all Re tested.

### 5.2.5 Loads Comparison: Integrated Pressure Data and Balance Measurements

Pressure load characteristics were integrated from the pressure data over the 3D disc-wing geometry. The disc was divided into a 3D grid of flat surfaces, each was a trapezium (isosceles trapezoid) with a central pressure tapping. The grid was generated by splitting the disc into 60 axisymmetric segments  $6^\circ$  apart, each segment divided further into 39 trapezium surfaces, from the centre of the upper surface (tapping 1) along the profile around the rim and lip (tapping 20) onto the lower surface and back to the disc centre (tapping 39) within the cavity. The pressure over each trapezium surface was assumed constant and equal to the pressure at each corresponding tapping. The incident pressure produced a small force ( $10^{-3}$  N) at the tapping position, acting in the direction perpendicular to the surface. Each force was resolved to the vertical and horizontal directions and appropriate contributions were summed to calculate total values for the aerodynamic pressure normal and axial forces. The normal and axial forces were then resolved to account for AoA and therefore calculate the pressure lift and drag (Fig. 5.37a&b). The pitching moment calculation took account of the perpendicular distance of each vertical and horizontal force from the y-axis (side force axis, see Fig. 2.6b), which was located at  $(x/c, z/t) = (1/2, 1/2)$ . Appropriate moment contributions were summed to calculate the aerodynamic pressure pitching moment (Fig. 5.37c).

The integrated pressure data is compared to the load measurements, taken from the wind tunnel balance, in Fig. 5.37 for  $AoA = -10^\circ$  to  $30^\circ$ ,  $V_\infty = 20\text{m/s}$ ,  $Re = 3.78 \times 10^5$ . The pressure lift curve closely follows the total lift curve (Fig. 5.37a), but has slightly less lift for the low AoA range, the zero pressure lift AoA at around  $-1^\circ$ . The profile pressure drag (0.035) is less than half that of the total profile drag (0.085) at  $-3^\circ$  AoA, the drag curves (Fig. 5.37b) converge at higher AoA approaching  $30^\circ$ . The pressure pitching moment curve is similar in form to the total pitching moment curve (Fig. 5.37c), negative (nose down) pitching moment at low AoA ( $< 15^\circ$ ), zero pitching moment from  $15^\circ$  to  $20^\circ$  and positive (nose up) pitching moment for higher AoA (above  $20^\circ$ ). The

entire pressure moment curve is well below (nose down increment) the total pitching moment curve for all AoA.

The aerodynamic loads are a combined result of the pressures and shear stresses, acting locally on the disc model surface, generated by a crossflow. The integrated pressure data does not account for the shear stress loading component, causing discrepancies between the curves presented in Fig. 5.34. The shear stress acting on the leading edge upper surface, due to accelerating flow, causes local lift & drag which in turn drives a nose up pitching moment. This explains the slightly higher lift and much larger drag & pitching moment curves plotted from the balance data. The reattachment of the shear layer to the upper surface will also contribute a drag force due to the downstream shear stress. Added to the aforementioned sources of shear stress is inside the trailing edge cavity rim at higher angles of attack, which provides nose down pitching moment. This explains the large pitching moment discrepancy above 15° AoA.

## 5.3 Surface Flow Visualisation

### 5.3.1 Surface Flow Patterns

#### 5.3.1.1 Typical flight angle of attack (5°)

The surface paint patterns for a non-spinning disc-wing are shown for both the upper (Fig. 5.38) & cavity (lower) surfaces (Fig. 5.39) at a typical flight angle of attack (5°) and a flow speed of 15m/s, equivalent to a Reynolds number of  $2.84 \times 10^5$ .

A description of the surface flow is given with reference to Fig. 5.40, which superimposes labels onto the surface flow patterns taken of Figs 5.38 & 5.39 to aid the explanation of the surface flow features.

The upper surface pattern (Fig. 5.40a) shows that the surface flow direction is from the leading edge towards  $L_1$ . This is indicated by the streak lines within region A. The boundary layer separates from the surface at an arc of near constant radius ( $L_1$ ), followed by reattachment at a line of similar geometry ( $L_2$ ). The boundary layer remains attached throughout region C and then separates at  $L_3$ . The initial separation and subsequent reattachment at the leading edge forms a separation bubble in region B. At the trailing edge, a similar reversed surface flow pattern is observed within region D, as fluid is drawn towards the stagnation line at  $L_3$ . The two points  $V_1, V_2$  at symmetrical

positions are separation nodes formed by the detachment of the trailing vortices from the bluff body surface. Streak lines in the vicinity of  $V_1$  and  $V_2$  suggest that fluid from the separation bubble and from beneath the cavity feeds into these vortices.

The cavity surface pattern (Fig. 5.40b) indicates that the boundary layer separates off the leading edge lip and reattaches on the inside of the trailing edge rim leaving a stagnation line (which cannot be seen on Fig. 5.40b). The shear layer encloses a reversed flow region (F) from the trailing edge towards the stagnation line  $L_4$  and a ‘dead air’ (or weakly circulating) pocket (E) aft of the leading edge rim. It is worth noting that the line  $L_4$  which defines the boundary between the reversed flow (F) and dead air pocket (E) is straight.

### 5.3.1.2 Range of angles of attack ( $0^\circ$ to $30^\circ$ )

A description of the variation in surface paint patterns with AoA follows with reference to Figs 5.41 & 5.42. Firstly a polar coordinate system is defined for quantitative demarcation of surface flow features; if the centre of the disc-wing is  $(0, \theta_p)$  using polar coordinates  $(r_p, \theta_p)$ ,  $r_p$  defined as the radial position and  $\theta_p$  the angular component. Take positive  $\theta_p$  in the positive yaw direction ( $0 \leq \theta_p < 2\pi$ ) and the point  $(c/2, 0)$  central on the leading edge, where  $c$  is the chord length i.e.  $c/2$  the disc radius.

On the upper surface (Fig. 5.41) at  $0^\circ$  AoA, the flow separates at a line (arc) of constant radius, which crosses the body fixed roll axis at  $(0.8c/2, 0)$ . For increased AoA, at  $5^\circ$  the flow separates at the same position  $(0.8c/2, 0)$ , again with reference to the roll axis, gradually moving upstream with increased AoA to  $(0.95c/2, 0)$  at  $30^\circ$ . The separated boundary layer can be seen to reattach for the full AoA range  $0^\circ$  to  $30^\circ$  depicted in Fig. 5.41.

The surface patterns indicate that the reattachment line, is an arc of constant radius from  $0^\circ$  to  $10^\circ$  AoA moving downstream from  $(0.5c/2, 0)$  at  $0^\circ$  to  $(0.4c/2, 0)$  at  $10^\circ$ . Between  $10^\circ$  and  $20^\circ$  AoA the reattachment line transitions to a straight line (perpendicular to the roll axis) but it is difficult to see this on Fig. 5.41. A close up of the reattachment is given for  $20^\circ$  AoA on Fig 5.43a, crossing the roll axis at  $(0.1c/2, 0)$ . The arrows show the flow direction away from the stagnation line.

The reattachment line shifts further downstream to a position of  $(0.2c/2, \pi)$  at  $25^\circ$ , before returning upstream to a central position of  $(0, \pi)$  at  $30^\circ$  AoA. For  $25^\circ$  to  $30^\circ$  AoA the straight reattachment line narrows, transitioning to a nodal point, see Fig. 5.41f&g. A close up of the nodal reattachment is shown for  $30^\circ$  AoA in Fig 5.43b. The radial outflow on the surface, from this point, has left an uneven pattern suggesting unsteady effects as the reattachment of the boundary layer dictates the surface flow in this locality.

For increasing angle of attack therefore the reattachment line is initially an arc of constant radius ( $0^\circ$  to  $10^\circ$ ) which transitions to a straight line ( $10^\circ$  to  $20^\circ$ ) and then narrows in width to become a nodal point or focus of reattachment ( $20^\circ$  to  $30^\circ$ ).

The separation line on the trailing edge of the disc-wing crosses the roll axis at a position of  $(0.8c/2, \pi)$  at  $0^\circ$  AoA. For increased angle of attack the separation line does not move much, merely shifting slightly downstream to  $(0.9c/2, \pi)$  at  $30^\circ$  AoA. At low AoA ( $0^\circ$  to  $10^\circ$ ) the trailing edge separation line exists between two nodal points which are clearly visible in Figs 5.41a,b&c, also labeled  $V_1$  &  $V_2$  on Fig. 5.40a. The flow in close vicinity to these nodal points is a complex interaction of the bluff body wake, separated boundary layer and, at high enough AoA, trailing vortices also. As the AoA increases further, these nodes change in form and location moving upstream towards the wing tips. As the reattachment line transitions from an arc to a straight line ( $10^\circ$  to  $20^\circ$ ) the separation nodes become increasingly dominated by the detachment of trailing vortices. The positions of these nodes are  $(0.8c/2, 5\pi/6)$  &  $(0.8c/2, 7\pi/6)$  at  $0^\circ$  AoA, moving through  $(c/2, 2\pi/3)$  &  $(c/2, 4\pi/3)$  at  $15^\circ$  to  $(c/2, \pi/2)$  &  $(c/2, 3\pi/2)$  at  $30^\circ$ .

Within the cavity at low AoA (Fig. 5.42), the shear layer that separates off the leading edge reattaches to the surface inside the trailing edge rim. At  $0^\circ$  AoA, the reversed flow beneath the shear layer generates two spiral nodes which are located at  $(0.7c/2, \pi/5)$  and  $(0.7c/2, 9\pi/5)$ . A half annulus shaped dead air region can be seen ahead of the spiral nodes (Fig. 5.42a).

Thereafter the straight-line stagnation (as labelled  $L_4$  in Fig. 5.40b) becomes the most obvious feature within the cavity paint patterns, caused by the reversed flow beneath the shear layer and the dead air enclosed behind the leading edge rim, for  $5^\circ$  to  $10^\circ$  AoA. The straight stagnation line is perpendicular to the roll axis, crossing the axis at  $(0.2c/2, 0)$ . Between  $10^\circ$  &  $15^\circ$ , the shear layer reattachment line moves upstream, off

the inside surface of the trailing edge rim. The reattachment is located centrally (0,0) at  $15^\circ$  and is probably better described as a nodal point than a line. The streak line patterns indicate that the near surface flow is towards the trailing edge from the reattachment. The paint patterns also suggest that reversed flow occurs from the reattachment towards the dead air stagnation line. This encloses a recirculating bubble, beneath the shear layer. As the AoA increases the reattachment line moves further upstream, crossing the roll axis at  $(0.5c/2,0)$  for  $30^\circ$  (Fig. 5.42g). Evidence for reversed flow ahead of the reattachment is present in the paint patterns up to the highest AoA tested using surface paints,  $30^\circ$ . This reversed flow suggests that a recirculating bubble is present at  $15^\circ$  and above. As the reattachment moves upstream the bubble moves with it. This pushes the dead air pocket stagnation line towards the leading edge until the bubble is directly behind the leading edge and the dead air pocket disappears.

It is also worth noting that on the downstream half of the cavity, particularly for higher AoA ( $20^\circ$  to  $30^\circ$ ), the streak lines aft of the reattachment can be seen to converge on the centre line. This is due to the convergence of fluid as the rim narrows towards the trailing edge.

### 5.3.2 Comparison of Surface Flow Visualisation with Pressure Data

The comparison images of Fig. 5.44 are the half surface 3D pressure distribution, viewed perpendicular to the surface planform, superimposed onto the half surface paint flow visualisation images, at  $5^\circ$  AoA. The separation line, on the upper surface (Fig. 5.44a), is shown to be just aft of the lowest pressure (dark blue) region on the leading edge. The boundary layer reattachment is responsible for the pressure recovery thereafter (green). The trailing edge separation and nodes correspond to the low pressure (blue) band and are similar in form. The high pressure region (orange) on the trailing edge, within the cavity (Fig. 5.44b), corresponds to where the separated boundary layer reattaches inside the rim. The rest of the pressure cavity shows suction (green). The straight surface paint line (Fig. 5.44b) defining the dead air boundary is not visible in the pressure data.

The central cross-sectional pressure profile for the upper surface is compared to the surface paint flow distribution in Fig. 5.45, with the chord wise positions of the separation and reattachment lines marked on, for  $5^\circ$  AoA. It is clear that the separation

bubble corresponds to the double low pressure peak close to the leading edge. The separation line ( $S_1$ ) is positioned just after the highest (low pressure) peak, and the flow separates due to an unfavourable (adverse) pressure gradient. The pressure recovery at the reattachment line ( $R_1$ ) and throughout the central portion of the upper surface is due to the reattachment of the boundary layer. Another suction peak occurs approaching the trailing edge separation line ( $S_2$ ), again the boundary layer separates under the influence of an adverse pressure gradient.

The comparison images of Fig. 5.46 & 5.47 are the half surface 3D pressure distributions, viewed perpendicular to the surface planform, superimposed onto the half surface paint flow visualisation images, for a range of AoA ( $0^\circ$  to  $30^\circ$ ). The direct comparison of paint patterns with the pressure distribution (Figs 5.46 & 5.47) in this case is over two flow speeds. The surface paint flow visualisation patterns were taken for a flow speed of 15m/s whereas the pressure data was taken at 20m/s. Although the flow features have been shown to have slightly different boundaries at various Reynolds numbers (see Fig. 5.34 to 5.36), this is perfectly valid for the purpose of deriving relevant information to further define the flow characteristics over an AoA range ( $0^\circ$  to  $30^\circ$ ).

It can be seen that the upper surface paint patterns are similar in form to the pressure colour contour plots, see Fig. 5.46. At low AoA ( $0^\circ$  to  $10^\circ$ ) the low pressure region (green / blue) on the leading edge coincides well with the crescent shaped surface pattern formed by the separation bubble. The leading edge separation line is consistently just aft of the highest pressure peak for all AoA, similarly for the trailing edge separation line, the boundary layer always separating from the surface under the influence of an adverse pressure gradient. As the boundary layer reattachment line moves downstream with increased AoA, the pressure recovery region (yellow / orange) narrows in the streamwise direction. For high AoA ( $25^\circ$  to  $30^\circ$ ), note that the nodal point of reattachment coincides with the upstream boundary of the pressure recovery region, located aft of the disc centre. The lower pressure band on the trailing edge exists for all AoA ( $0^\circ$  to  $30^\circ$ ) and corresponds to the trailing edge separation line. The low pressure regions (dark blue) on the wing-tips correspond to the complex surface paint patterns formed by bluff body effects and the detachment of trailing vortices. These low pressure regions grow larger with increased AoA, merging into the low pressure region generated by the separation bubble, at higher AoA ( $25^\circ$  to  $30^\circ$ ). It is difficult to see from Fig. 5.46 how these low pressure regions relate to the bluff body effects on the suction

side of the disc. The detachment of trailing vortices with increased AoA is accompanied by low pressure, which becomes increasingly dominant at the wing-tips for increased AoA. Note that for  $30^\circ$  AoA the clearly visible surface paint node of trailing vortex detachment (Fig. 5.46g) on the wing-tip coincides with low pressure.

The similarities between the lower surface paint patterns and the pressure colour contour plots (Fig. 5.47) are less obvious than for the upper surface. The high pressure at the trailing edge ( $0^\circ$ , orange) moves gradually upstream with increased AoA but there is no obvious pressure feature, which coincides with the stagnation line, and spiral node features in the surface paint patterns for low AoA ( $0^\circ$  to  $10^\circ$ ). At  $15^\circ$  the shear layer reattaches just ahead of the centre, pressure recovery is observed aft of the nodal point of reattachment. The pressure recovery remains bounded by the location of the reattachment as it moves upstream with increasing AoA ( $15^\circ$  to  $30^\circ$ ). At  $30^\circ$  the isolated high pressure region (dark red) directly aft of the reattachment approaches a  $C_p$  of 1, it decreases thereafter until the approach to the trailing edge where the steep rim surface forces compression and the  $C_p$  approaches 1 again.

## 5.4 Smoke Wire Flow Visualisation

### 5.4.1 Centre-line Visualisation

The central cross-sectional profiles of the disc-wing flow field are shown in Figs 5.48 to 5.50 at various AoA ( $0^\circ$  to  $50^\circ$ ) and a flow speed of 3m/s, equivalent to a Reynolds number of  $5.67 \times 10^4$ .

The flow field over a non-rotating disc-wing at various AoA ( $0^\circ$  to  $50^\circ$ ) are shown in Fig. 5.48. At  $0^\circ$  AoA (Fig. 5.48a) the flow field shows straight smoke filaments, which are relatively undisturbed from their horizontal free-stream position, except for the turbulent bluff body wake. As the AoA increases to  $10^\circ$  &  $20^\circ$  the filaments show upward deflection upstream of the leading edge and subsequent downwash aft of the trailing edge. At  $30^\circ$  &  $40^\circ$  AoA the steep curvature of the filaments above the upper surface are particularly apparent (Fig. 5.48d,e) as is the vortex shedding off the trailing edge in the wake of the disc. The separation bubble is visible as a dark region close to the leading edge, the smoke was not entrained into the structure but the separated shear layer outlines the shape in shadow. The shear layer reattaches to the surface on the centre line throughout the range  $0^\circ$  to  $40^\circ$  AoA. Stall occurs at  $45^\circ$  (see Fig. 5.2)

creating a much broader wake and shedding larger vortex structures, see Fig. 5.48f with the wing in deep stall.

The central cross-section of the separation bubble at various AoA ( $0^\circ$  to  $30^\circ$ ) is shown in Fig. 5.49. The laminar separation forms a distinct shear layer and the unsteady reattachment entrains smoke into the bubble. The separated shear layer is seen to become unstable due to a similar process to the Kelvin-Helmholtz instability for inviscid flows, according to linear stability theory. The shear layer rolls up into one or more laminar structures before becoming turbulent. The separation bubble forms even at  $0^\circ$  AoA (Fig. 5.49a), the thickness of the bubble structure enlarges with increased AoA. It is possible to see the reattachment of the shear layer in Fig. 5.49a where a slug flattens out on the surface and reaches into the separation bubble. Whilst observing the separation bubble in the wind tunnel the reattachment was seen to dance on the surface in an unsteady manner. Note the upwash angle of the fluid upstream of the leading edge.

The central cross-section of the cavity flow for various AoA ( $0^\circ$  to  $30^\circ$ ) are shown in Fig. 5.50, illuminated by a laser light sheet. The laminar separation on the leading edge lip forms a distinct shear layer (Fig. 5.50a&b), which becomes unstable (Kelvin-Helmholtz instability) rolling up into one or more laminar structures before becoming turbulent. The turbulent recirculation within the cavity stems from the trailing edge rim at low AoA ( $0^\circ$  &  $10^\circ$ ) with reversed flow observed beneath the shear layer (Fig. 5.42). For increased AoA ( $20^\circ$  to  $30^\circ$ ) the shear layer reattaches ahead of the disc centre (Fig. 5.50d). Unstable turbulent structures are shed with regular frequency from the separation bubble (Fig. 5.50c).

#### 5.4.2 Wake Visualisation

The bluff body wake, downwash and trailing vortex structures downstream of a non-spinning disc-wing are shown Fig. 5.51, for the low AoA range ( $0^\circ$  to  $10^\circ$ ). The ambient illumination in Fig. 5.51i shows the downwash generated in the wake of the disc-wing. The strong central downwash and the form of the trailing vortices becomes apparent with increased AoA from  $0^\circ$  through  $10^\circ$  (Fig. 5.51a,b&c). The laser light sheet illumination in Fig. 5.51ii shows the wake cross-section at one chord length downstream of the disc trailing edge. Fig. 5.51aii shows the unsteady bluff body wake at  $0^\circ$  AoA. The structure of the trailing vortices has begun to develop at  $5^\circ$  AoA (Fig. 5.51bii), the

turbulence generated by the bluff body still visible. Note the close vicinity of the trailing vortex pair due to the low aspect ratio, as the AoA increases the central downwash develops and stronger rotation is given to the trailing vortices. At 10° AoA the vortex structures are more clearly defined (Fig. 5.51cii). The comparison of these two methods of illumination enable the reader to better understand how the wake cross-sections relate to the disc-wing model.

The bluff body wake, downwash and trailing vortex structures extending downstream from a non-spinning disc-wing are shown Fig. 5.52, for the low AoA range (0° to 10°). Note the symmetry in the wake. The ambient illumination used for Fig. 5.52a shows the turbulent bluff body wake at 0° AoA to just over five chord lengths downstream from the disc trailing edge. The trailing vortices become more clearly defined with increased AoA, from 0° through 10° (Fig. 5.52a,b&c). Fig. 5.52b is a transitional stage of trailing vortex development, the bluff body wake is still evident but the trailing vortices begin to take shape (see Fig. 5.51b also). The trailing vortex pair is established at 10° AoA (Fig. 5.52c). The inboard edge of the trailing vortices is clearly defined in Fig. 5.52c by two symmetrical white lines, which narrow with distance downstream. The strong central downwash exists between these two lines with the trailing vortices either side. Close behind the trailing edge the smoke is entrained into the trailing vortex structures and the wake seems narrower than the disc itself (Fig. 5.52c). This is deceptive however: At the trailing edge, these white lines define the inboard edge of the trailing vortex detachment from the disc surface. The outboard edge of the wake and vortex detachment is bounded at the wing tips.

Cross-sectional slices through the wake at a range of positions downstream of a non-spinning disc-wing at 10° AoA are shown in Fig. 5.53. The laser light sheet illuminates turbulence at the trailing edge ( $x/c = 0$ , Fig. 5.53a) and the curvature on either side of the disc, indicates central downwash. With distance downstream, the central downwash forces the turbulent bluff body wake lower and the form of the trailing vortices becomes clearer as more smoke is entrained into the vortices.

### 5.4.3 Visualisation of the Effect of Spin

The flow structures on the upper surface of a spinning disc-wing ( $\text{AdvR} = 0, 0.7 \& 0.9$ ) at 0° & 5° AoA are shown in Fig. 5.54. At 0° AoA, the separation bubble is clearly

identifiable for the non-spinning case (Fig. 5.54ai), note the symmetry particularly in the wake. For the spinning case (Fig. 5.54bii) the form of the separation bubble is largely unchanged, however the bubble shifts slightly towards the leading edge on the advancing side (left of the figure) but remains unchanged on the retreating side. Also, the fluid within the bubble is curved around the disc with the local surface and is mostly shed from the retreating side. The wake becomes asymmetric and is deflected slightly towards the advancing side. At  $5^\circ$  AoA, the turbulence in the near surface reattached flow is clearly visible at this higher Reynolds number (Fig. 5.54ii,  $Re = 5.67 \times 10^4$ ). For the non-spinning case (Fig. 5.54bi), the smoke is entrained into the separation bubble within the central corridor (inboard) only. However, for the spinning case (Fig. 5.54bii), the boundary reattachment is visualised further outboard on the advancing disc surface (Fig. 5.54bii, left hand side) forces the smoke layer to feed into the separation bubble. The moving surface (due to spin) can also be seen to deflect the smoke filaments within the separated shear layer (Fig. 5.54b) in the spin direction, when compared to the non-spinning case (Fig. 5.54a). For  $5^\circ$  AoA also, the wake becomes asymmetric and is deflected slightly towards the advancing side (Fig. 5.54bii).

Cross-sectional slices through the wake, central downwash and trailing vortex structures downstream of a spinning disc-wing ( $AdvR = 0, 0.7 \& 1.6$ ) at  $10^\circ$  AoA, are shown in Fig. 5.55. The symmetrical vortices (Fig. 5.55i), illuminated by a laser light sheet, for the non-spinning disc become asymmetric with increased rotation (Fig. 5.55ii&iii). The advancing side of the disc, on the left side of each image, inhibits the near surface flow (for non-zero advance ratio, Fig. 5.55ii&iii) and retards the downwash on that side inhibiting the vorticity given to the trailing vortex. Whereas the retreating side of the disc, on the right hand side of each image, aides the near surface flow (for non-zero advance ratio, Fig. 5.55ii&iii) and augments the downwash on that side enhancing the vorticity given to the trailing vortex. This deforms the trailing vortex detached from the advancing side into a more unsteady bluff body structure, which is also raised slightly higher than the undisturbed trailing vortex detached from the retreating side. Note the similarity between the deformation of the trailing vortex detached from the advancing side at the two downstream positions shown in Fig. 5.55a&b.

Cross-sectional slices through the wake, central downwash and trailing vortex structures at a range of positions downstream of a spinning disc-wing (including opposite spin directions,  $AdvR = 0.7, 0 \& -0.7$ ) at  $5^\circ$  AoA, are shown in Fig. 5.56. At the trailing edge, a marked downwash cusp is observed aft of the retreating side of the disc (Fig.

5.56ai, right hand side), which is not present for the non-spinning case (Fig. 5.56a<sup>ii</sup>). If this localised downwash is tracked downstream (Fig. 5.56ia-g), the initially small downwash cusp (Fig. 5.56ai) develops into enhanced downwash aft of the retreating side (Fig. 5.56ib-d, right hand side), compared to that downstream of the advancing side. The form of the trailing vortices starts to become apparent at one chord length downstream (Fig. 5.56e). The enhanced downwash aft of the retreating side sweeps into the trailing vortex thus enhancing its rotation (Fig. 5.56e&f). Two chord lengths downstream, the trailing vortices at 5° (Fig. 5.56gi) show asymmetry similar to that at 10° (Fig. 5.55bii). Namely, the trailing vortex aft of the advancing side is raised slightly higher than the trailing vortex aft of the retreating side (Fig. 5.56gi). The retarded downwash aft of the advancing side is also observed in Fig. 5.56i, compared to the non-spinning case (Fig. 5.56ii), at each respective downstream station. The slightly raised trailing vortex aft of the advancing side is attributed to this retarded downwash, which also inhibits the rotation given to the vortex on that side. The wake downstream of a disc with reversed rotation ( $\text{AdvR} = -0.7$ ) is shown in Fig. 5.56iii. The same wake characteristics are depicted here, the enhanced downwash now on the left of each image, due to the opposite direction of disc rotation. There is a good level of symmetry between Figs 5.56i and 5.56iii, taking into account the turbulent and unsteady nature of the bluff body wake at 5° AoA.

# Chapter 6 Flow Topology

## Summary

*This chapter proposes a flow topology to define the non-spinning disc-wing flow physics in both two and three dimensions. Section 6.1 presents the 2D mid-span flow field cross-section and 3D flow structures topologically for a typical flight angle of attack (10°). Section 6.2 illustrates the variation in mid-span flow field with angle of attack (0° to 30°) including pre- and post-stall topologies (+/- 45°).*

### 6.1 Typical Flight Angle of Attack (10°)

The proposed topology of the flow over a non-rotating disc-wing is given based upon the flow visualisation. The two-dimensional central flow cross-section at 10° AoA shown in Fig. 6.1 depicts many of the flow structures that have been previously discussed, namely separation bubble, cavity flow and turbulent wake. With flow from right to left, first of all note the upwash ahead of the leading edge, then the boundary layer separates off the upper surface reattaching shortly thereafter creating a recirculating bubble. Further downstream the reattached boundary layer separates from the upper surface on the trailing edge, this separated shear layer contributes to the wake which has downwash angle slightly greater than the AoA. Within the cavity, the shear layer that separates off the leading edge lip reattaches on the inside of the trailing edge rim, reversed flow occurs beneath the shear layer towards the leading edge. The fluid flowing towards the leading edge (reversed flow) within the cavity is restricted from flowing further forward by the stagnant air pocket in the lee of the leading edge rim. This stagnant air aft of the leading edge is denoted by the weakly moving arrow heads on Fig. 6.1. The straight stagnation line in the cavity surface paint patterns (Fig. 5.40b) marks the boundary between the reversed flow and the stagnant air, within the cavity. This boundary is depicted in the topology (Fig. 6.1) as a separation line. On the tip of the trailing edge rim, the boundary layer separates from the surface, contributing to the vortices shed into the wake.

The three-dimensional flow topology at 10° AoA is shown in Fig. 6.2 and depicts the structure of the separation bubble and trailing vortices, flow from right to left. The separation bubble forms a crescent like shape, the arced separation and reattachment lines are clearly marked. The arrows show the direction of the separated shear layer

flow. Three cross-sectional slices through the structure show the recirculation / roll-up of fluid within the bubble. The trailing vortices are in close proximity to each other, these drive a strong central downwash between the pair. Their rotation is in the conventional sense for a typical wing section at positive AoA, the vortex trailing from the port wing-tip has clockwise rotation (when viewed from downstream) whereas the starboard trailing vortex rotates counter clockwise. Note the entrainment of fluid into the vortices from the upper surface boundary layer and also from within the cavity.

## 6.2 Range of Attack Angles (0° to 45°)

The two-dimensional central flow cross-sections for a range of AoA are shown in Figs 6.3 & 6.4, flow from right to left. At 0° AoA the separation bubble is small (Fig. 6.3a), the shear layer beneath the disc covers the entire cavity. Reversed flow above the cavity shear layer occurs centrally for almost the entire length of the cavity. The leading edge rim forces the central reversed flow to split, deflected towards the wing tips. This deflection provided the rotation to generate two stagnation points either side of the mid-span, these spiral nodes were visualised in the surface paint patterns (Fig. 5.42a). Separation occurs on the trailing edge, the separated shear layers influence the structure of the bluff body wake.

With increased AoA the separation bubble on the upper surface becomes enlarged, reattachment occurs further downstream. Also, the shear layer separating off the leading edge lip reattaches further upstream and the wake downwash angle increases.

At 10° AoA the separation bubble enlarges slightly (Fig. 6.3b), the shear layer beneath the disc still covers the entire cavity. Reversed flow above the cavity shear layer occurs centrally for only half the length of the cavity, as the dead air pocket grows larger.

At 20° AoA the upper surface separation bubble enlarges further (Fig. 6.3c), as the reattachment line moves further downstream. The cavity shear layer now reattaches at the half chord position, a recirculating bubble is enclosed beneath the shear layer, downstream from the dead air pocket. Within the cavity, the reattached boundary layer remains attached throughout the inside of the trailing edge rim, separating off the lip.

At 30° AoA the upper surface separation bubble enlarges further still (Fig. 6.3d). The cavity shear layer now reattaches at the quarter chord position enclosing the

recirculating bubble directly behind the leading edge rim. The dead air pocket no longer exists, eliminated by the bubble.

The flow topology for both pre- and post-stall regimes at  $45^\circ$  AoA are shown in Fig. 6.4. Pre-stall (Fig. 6.4a) the upper surface separation bubble is now enlarged to the extent of being oversized. It is the strong central downwash, driven by the trailing vortices, that sustains the separation bubble up to such an extreme upper limit AoA. The separated shear layer is forced back onto the surface aft of the disc centre. The cavity recirculating bubble does not exist at such a high AoA, instead the boundary layer is attached to the cavity surface following the profile. The pre-stall wake is narrow, not much thicker than the disc itself.

Post-stall (Fig. 6.4b) the separated shear layer on the upper surface no longer reattaches but becomes unstable rolling up into vortex structures shed into the wake. Similarly, the shear layer separated from the trailing edge lip sheds large vortex structures. A representation of the reversed flow towards the disc upper surface, within the wake, is also added to Fig. 6.4b. This reversed flow will create a central nodal reattachment point on the upper surface, similar to that illustrated in the surface paint visualisations at  $30^\circ$  AoA, see Fig. 5.41 & 5.43b. The post-stall wake is much thicker, approximately the width of the disc chord. The flow within the cavity remains largely unchanged.

Aerodynamic stall appears in the load data (Fig 5.2) and the wake flow visualisations (Fig. 5.48), at  $45^\circ$  AoA as illustrated in the flow topology (Fig. 6.4). Note that, this is not consistent with Stilley & Carstens (1972) experiments. The author offers the suggestion that the complicated side sting support structure (Stilley & Carstens, Fig. 3, 1972) accounts for the premature onset of aerodynamic stall, just above  $30^\circ$  AoA. The interference effects caused by the sting (connected to the rim at one of the wingtips) on the test model are particularly intrusive at high angles of attack. The sting directly blocks the fluidic generation of the natural roll up of the trailing vortex on the strut side of the disc. This weakens the trailing vortex pair and in turn reduces the strength of central downwash. The partially separated flow regime therefore breaks down at just above  $30^\circ$  AoA, the trailing vortex pair unable to drive the shear layer back to the surface.

# Chapter 7 Disc-wing Flightpath Simulation

## Summary

This chapter presents a six-degree of freedom disc-wing simulation model developed using Matlab. Section 7.1 outlines the flight equations of motion of a rigid flight vehicle in three-dimensions. The computer simulation is validated against published Frisbee trajectory data obtained from free-flight experiments. Flight profiles are discussed for a number of different launch conditions consistent with a range of typical Frisbee throws. The simulation is also used to demonstrate that with control moments from suitable control effectors, it is possible to generate a number of proscribed flight manoeuvres.

### 7.1 Flight Equations of Motion

The disc-wing simulation is based on the standard equations of motion of a rigid flight vehicle in three dimensions (Etkin & Reid, 1982). For convenience, four separate axes systems are used:

1. Earth axes,  $(xyz)_1$
2. Body axes,  $(xyz)_2$
3. Zero sideslip body axes,  $(xyz)_3$
4. Relative wind axes,  $(xyz)_4$

The earth axes and body axes are the conventional axes used for aircraft stability and control. The zero sideslip body axes are obtained by rotating the body axes through  $-\beta_2$ , Fig. 7.1a. The relative wind axes are then obtained by rotating the zero sideslip body axes through  $-\alpha_3$ , Fig. 7.1b.

The transformation matrix required to change forces and velocities between coordinate systems is defined as,

$$\mathbf{T}_a(\phi, \theta, \psi) = \begin{bmatrix} \cos \theta \cos \psi & \sin \phi \sin \theta \cos \psi - \cos \phi \sin \psi & \cos \phi \sin \theta \cos \psi + \sin \phi \sin \psi \\ \cos \theta \sin \psi & \sin \phi \sin \theta \sin \psi + \cos \phi \cos \psi & \cos \phi \sin \theta \sin \psi - \sin \phi \cos \psi \\ -\sin \theta & \sin \phi \cos \theta & \cos \phi \cos \theta \end{bmatrix} \quad (7.1)$$

where  $\phi$ ,  $\theta$  and  $\psi$  are the roll, pitch and yaw angles through which the axes system is rotated (in the order yaw, pitch, roll). The transformation of angular rates about different axes systems requires a further matrix,

$$\mathbf{T}_r(\phi, \theta, \psi) = \begin{bmatrix} 1 & \sin \phi \tan \theta & \cos \phi \tan \theta \\ 0 & \cos \phi & -\sin \phi \\ 0 & \sin \phi \sec \theta & \cos \phi \sec \theta \end{bmatrix} \quad (7.2)$$

where once again,  $\phi$ ,  $\theta$  and  $\psi$  are the roll, pitch and yaw angles through which the axes system is rotated.

To simplify presentation, a notation system is adopted whereby,

$$(xyz)_2 = \mathbf{T}_{a_{12}}(xyz)_1, (xyz)_3 = \mathbf{T}_{a_{23}}(xyz)_2, (xyz)_4 = \mathbf{T}_{a_{34}}(xyz)_3 \quad (7.3)$$

and

$$\mathbf{T}_{a_{12}} = \mathbf{T}_a(\phi, \theta, \psi), \mathbf{T}_{a_{23}} = \mathbf{T}_a(0, 0, -\beta_2), \mathbf{T}_{a_{34}} = \mathbf{T}_a(0, -\alpha_3, 0) . \quad (7.4)$$

The position and orientation of the disc wing is defined by a position vector  $\mathbf{x}$  and attitude vector  $\boldsymbol{\theta}$ . Using standard aircraft notation,

$$\mathbf{x}_1 = [X \ Y \ Z]^T, \quad \boldsymbol{\theta}_1 = [\phi \ \theta \ \psi]^T \quad (7.5)$$

and

$$\dot{\mathbf{x}}_2 = [u \ v \ w]^T, \quad \dot{\boldsymbol{\theta}}_2 = [p \ q \ r]^T . \quad (7.6)$$

Furthermore, using the transformations defined above,

$$\dot{\mathbf{x}}_2 = \mathbf{T}_{a_{12}} \dot{\mathbf{x}}_1, \quad \dot{\boldsymbol{\theta}}_2 = \mathbf{T}_{r_{12}} \dot{\boldsymbol{\theta}}_1 . \quad (7.7)$$

The dynamics of the system is governed by Newton's second law, which using the notation defined by Etkin and Reid can be conveniently expressed as,

$$\ddot{\mathbf{x}}_2 = \frac{\mathbf{F}_2}{m} - \tilde{\boldsymbol{\omega}} \dot{\mathbf{x}}_2 \quad (7.8)$$

$$\ddot{\theta}_2 = \mathbf{I}^{-1} \mathbf{M}_2 - \tilde{\omega} \dot{\theta}_2 \quad (7.9)$$

where  $\mathbf{F}_2$  and  $\mathbf{M}_2$  are the body axes force and moment vectors acting on the disc,  $m$  is the disc mass,  $\mathbf{I}$  is the disc moment of inertia matrix defined as,

$$\mathbf{I} = \begin{bmatrix} I_x & 0 & 0 \\ 0 & I_y & 0 \\ 0 & 0 & I_z \end{bmatrix} = \begin{bmatrix} \frac{1}{2}I_z & 0 & 0 \\ 0 & \frac{1}{2}I_z & 0 \\ 0 & 0 & I_z \end{bmatrix} \quad (7.10)$$

and

$$\tilde{\omega} = \begin{bmatrix} 0 & -r & q \\ r & 0 & -p \\ -q & p & 0 \end{bmatrix} \quad (7.11)$$

The principle task in solving equations (7.8) & (7.9) is now that of obtaining the aerodynamic forces and moments acting on the disc wing as a function of its velocity, aerodynamic attitude and rate. The approach adopted is as follows:

Firstly, calculate the sideslip angle of the disc within the body axes system,

$$\beta_2 = \tan^{-1} \left( \frac{\dot{x}_2(2)}{\dot{x}_2(1)} \right) . \quad (7.12)$$

Next, calculate the disc velocity in the zero sideslip body axes system,

$$\dot{\mathbf{x}}_3 = \mathbf{T}_{a_{23}} \dot{\mathbf{x}}_2 . \quad (7.13)$$

Using this result, the true angle of attack of the disc can be calculated as follows,

$$\alpha_3 = \tan^{-1} \left( \frac{\dot{x}_3(3)}{\dot{x}_3(1)} \right) \quad (7.14)$$

with the orientation of the relative wind axes given by,

$$\dot{\mathbf{x}}_4 = \mathbf{T}_{a_{34}} \dot{\mathbf{x}}_3 . \quad (7.15)$$

The aerodynamic force and moment coefficients can now be obtained either from linear aerodynamic derivatives (Hubbard & Hummel, 2000), or as in the present case, a mixture of linear derivatives for the rate terms and look up table results based on wind tunnel experiments for the steady terms. The complete set of force and moment coefficients used is as follows,

$$C_{Drag} = C_{Drag}(\alpha) \quad (7.16)$$

$$C_{Lift} = C_{Lift}(\alpha) \quad (7.17)$$

$$C_{Side} = C_{Yr}(r_3, |\dot{\mathbf{x}}_4|) \quad (7.18)$$

$$C_L = C_{L_p} \frac{p_4 c}{2|\dot{\mathbf{x}}_4|} \quad (7.19)$$

$$C_M = C_M(\alpha) + C_{M_q} \frac{q_4 c}{2|\dot{\mathbf{x}}_4|} \quad (7.20)$$

$$C_N = C_{N_r} \frac{r_4 c}{2|\dot{\mathbf{x}}_4|} \quad (7.21)$$

The dimensional forces and moments acting on the disc are then given by,

$$\mathbf{F}_4 = q_\infty S \mathbf{C}_F \quad (7.22)$$

and,

$$\mathbf{M}_4 = \mathbf{M}_2 = q_\infty S c \mathbf{C}_M \quad (7.23)$$

where,

$$\mathbf{C}_F = [-C_{Drag} \ C_{Side} \ -C_{Lift}] \ , \quad (7.24)$$

$$\mathbf{C}_M = [C_L \ C_M \ C_N] \quad (7.25)$$

and,

$$q_\infty = \frac{1}{2} \rho_\infty |\dot{\mathbf{x}}_1|^2 \ . \quad (7.26)$$

The forces and moments now have to be resolved back in to body axes. This is achieved as follows,

$$\mathbf{F}_{2(aero)} = \mathbf{T}_{a_{23}}' \mathbf{T}_{a_{34}}' \mathbf{F}_4 \quad (7.27)$$

$$\mathbf{M}_2 = \mathbf{T}_{r_{23}}' \mathbf{T}_{r_{34}}' \mathbf{M}_4 \ . \quad (7.28)$$

Finally, gravitational forces have to be added,

$$\mathbf{F}_2 = \mathbf{F}_{2_{(aero)}} + \mathbf{T}_{a_{12}} m\mathbf{g} \quad (7.29)$$

where,

$$\mathbf{g} = [0 \quad 0 \quad g]^T . \quad (7.30)$$

Note that gravitational moments are zero since the moment reference point is the centre of gravity.

Equations (7.8) & (7.9) can now be integrated to give, via suitable axes transformation, the earth axes position and orientation as required.

## 7.2 Simulation Implementation

In implementing the mathematical model developed in section 7.1, a choice has to be made as to how disc angular momentum is represented in equation (7.9). There are two options: firstly, the body fixed coordinate system can be fixed to the disc such that it rotates with disc, or secondly, the body fixed coordinated system can be fixed only to the disc yaw and pitch axes, i.e. in such a manner that it does change orientation as the disc spins. In the first case, the angular momentum of the disc is included implicitly in the angular momentum equation. However, in the second case, the angular momentum of the disc must be calculated separately from the spin rate, and its effect added as an extra term in equation (7.9). The advantage of the second method over the first is that it reduces the computation time by a factor of approximately 5 over the first method, however, higher order dynamics of any wobble at the beginning of the motion may not be modelled correctly.

A number of numerical experiments based on typical launch conditions were performed to evaluate the impact of the angular momentum model on the simulation output. It was found that results were identical when plotted at reasonable scales (e.g. maximum error magnitudes less than 0.1% of full scale deflection). A further related issue concerns modelling of disc yaw damping  $N_r$ , which leads to disc spin-down during flight. Numerical experiments showed that the spin rate reduced by approximately 3% during a typical 4 second flight, based on a value of  $N_r$  from Hummel & Hubbard (2002). However, the impact of the spin-down on the disc trajectory was, once again, not visible

on graphs plotted at sensible scale. For these reasons, unless otherwise stated, the results presented in this thesis are for a disc rotating at constant speed (no spin-down), and with non-rotating body axes.

The disc-wing mathematical model was implemented using Matlab 5.3 running on a 233 mHz Pentium PC. Equations of motion were solved numerically using the ODE23s solver in Matlab, with relative and absolute error tolerance set to the default values of  $1 \times 10^{-3}$  and  $1 \times 10^{-6}$ , respectively. Typical simulation run times were of the order of 3 minutes for a 5 second flight (non-rotating body axes). Run time increased with increasing advance ratio.

The simulation was thoroughly debugged using a series of numerical experiments based on initial conditions for which the output trajectory could be easily predicted from simple physics. These experiments were designed to show that the implementation of the mathematical model was physically sound for all combinations of attitude and angle of attack. Example tests included horizontal release at zero forward speed, horizontal/vertical launch at zero angle of attack, launch at  $\pm 90^\circ$  angle of attack, etc.

## 7.3 Results from Numerical Experiments

### 7.3.1 Comparison with experimental data

A comparison between an experimental Frisbee trajectory from Hummel (2003) and a simulated trajectory from the same initial conditions is presented in Fig. 7.2. The results are qualitatively similar, however, the velocity magnitude for the simulated data shows a rapid decrease immediately following launch that is not present in the experimental data. This deceleration is caused by wobble of the disc following launch, which causes an oscillation in angle of attack of amplitude  $15^\circ$  and hence increase in drag. The author of the experimental study reported that there was significant disc wobble during the initial part of the trajectory presented, however, this was the best data available. Unfortunately there is a lack of detailed published data on Frisbee trajectories and there is a clear need for further experimental data to provide a fuller validation of the simulation.

### 7.3.2 Analysis of a typical Frisbee trajectory

Trajectory plots and flight parameter time histories for a typical Frisbee trajectory are shown in Fig. 7.3. The disc is launched at a pitch attitude of  $15^\circ$  in the XZ plane

$(\phi_L = 0^\circ, \theta_L = 15^\circ, \psi_L = 0^\circ)$  with a velocity of magnitude 15m/s aligned with the attitude vector, such that  $u = 15, v = 0, w = 0$  m/s and the angle of attack is zero. The disc is spinning at 5 revs/sec in a clockwise direction when viewed from above ( $r$  positive). The total flight time is 4 seconds, with discs shown in the trajectory plots every 0.2 seconds. Discs are drawn eight times their actual size. Non-spinning body axes are used, with constant spin rate. Black lines represent results from using the full non-linear aerodynamic model for the steady derivatives, grey lines represent results from using linearised derivatives.

The full non-linear aerodynamic model case will be discussed first. The trajectory planform view (Fig. 7.3a) shows the classic ‘S’ shaped flight profile associated with Frisbee flight in which the disc first turns one way, then turns the opposite way. This ‘S’ shaped profile arises from the relationship between pitching moment and angle of attack for the disc (Fig. 7.4c). At the start of the flight, with angle of attack close to zero, the pitching moment is negative. For a positive spin rate, this leads to a positive roll rate due to precessional effects (equation 39) and hence an increasingly positive roll attitude (Fig. 7.3c). As the flight progresses to around 2 seconds, the pitch attitude remains roughly constant (Fig. 7.3g), however the angle of attack is steadily increasing (Fig. 7.3e) due to the increase vertical velocity of the disc. When the angle of attack becomes greater than  $9^\circ$ , the pitching moment reverses sign and becomes positive, leading to a negative roll rate and hence an increasingly negative roll attitude. At around 3 seconds, the speed has reached a minimum point of around 4.5m/s, the angle of attack has reached a maximum point of around  $40^\circ$ , and the disc is banked at an angle of around  $-15^\circ$ . The disc then turns sharply to the left with the angle of attack decreasing and the absolute attitude increasing (Fig. 7.3f). Note that the advance ratio varies from 0.3 at the beginning of the flight to around 1 at 3 seconds due to changes in the disc speed over this period.

Focusing now on the linear aerodynamic case (grey lines and symbols), it can be seen that behaviour similar to the non-linear case is obtained initially, however, the rate of trajectory divergence increases appreciably after 2 seconds. This is due to larger differences in the aerodynamic models at increased angles of attack. The linear fit model diverges considerably from the wind tunnel pitching moment data (Fig. 7.4) for angles of attack greater than  $10^\circ$ , as previously noted.

### 7.3.3 Effect of Varying Launch Condition

Figs 7.5 to 7.8 show Frisbee trajectories in the XZ and XY planes for various launch initial conditions. The default initial condition is a launch attitude of  $\phi_L, \theta_L, \psi_L = [0\ 0\ 0]^\circ$  and body axis velocity  $u, v, w = [19\ 0\ 0]$  m/s. Changes from these default conditions are indicated on each graph. The time interval between each data point is 0.2 seconds.

The effect of varying advance ratio at launch (obtained by varying spin rate, initial velocity held constant at 19m/s) is shown in Fig. 7.5a&b. The non-dimensional analysis presented in section 2.5.1 predicts that the non-dimensional roll rate of the disc increases with decreasing advance ratio, and the results in Fig. 7.5a qualitatively support this. At high advance ratios much greater than 1, the disc follows an almost straight path in the XY plane along the X axis. As the advance ratio decreases to around 0.4, the disc increasingly turns to the right, however the vertical motion is not much affected. At an advance ratio of 0.1, the increasingly positive roll attitude of the disc leads to an increasing rate of descent as the disc ‘slips’ out of the turn. Finally, at an advance ratio of 0, i.e. a non-spinning disc, the disc pitches leading edge down immediately after launch and descends with a tumbling motion in the vertical plane.

The next set of data (Fig. 7.6a&b) shows the effect of varying launch attitude. The XZ data (Fig. 7.6a) shows the classic ‘boomerang’ effect by which a disc can be made to return to the thrower if launched with sufficient pitch attitude. For the present case, a velocity reversal occurs for a launch pitch attitude of greater than  $30^\circ$ . Note that the data for this test was obtained at a high advance ratio of 1.1, so that the disc roll rate was minimised, and there is little lateral displacement in the XY plane (Fig. 7.6b). The relationships between launch pitch angle and maximum range is plotted in Fig. 7.7, and between launch pitch angle and maximum duration in Fig. 7.8. These results shows that, based on the present simulation, the launch pitch angle for maximum range is approximately  $10^\circ$  and the launch pitch angle for maximum duration is approximately  $20^\circ$ . Note that range is much more sensitive to launch angle than is duration.

The effect of launch angle of attack for a horizontally launched disc is shown in Figs. 7.9a&b. At zero angle of attack, the resulting trajectory is very similar to the zero launch attitude case in Fig. 7.5b, however, there is a slight difference due to the  $+3^\circ$  offset of the aerodynamic angle of attack compared to the geometric angle of attack for

the disc (see Fig. 7.4a). As the launch angle of attack is increased to  $60^\circ$ , the behaviour is qualitatively similar to the effect of launch attitude, though both the range and duration are much reduced due to the effects of increased drag in the initial part of the flight. At a launch angle of attack of  $90^\circ$ , i.e. the disc is pitched to  $90^\circ$  and launched horizontally, the disc decelerates rapidly, immediately following a descending flight path, as would be expected. Note that the angle of attack tests were performed with an advance ratio of 0.5, and hence the lateral dispersion in the results is greater than in Fig. 7.6b.

The effect of launch roll attitude on the trajectory of a disc launched at zero angle of attack and a pitch attitude of  $20^\circ$  is shown in Figs. 7.10a&b. At zero roll attitude, the disc proscribes the classic ‘S’ shaped flight path. This is more pronounced than the ‘S’ profile shown in Fig. 4 since the advance ratio in the present case is reduced. By introducing a negative roll angle at launch, the initial curvature to the right is corrected, and an approximately straight initial flight path is achieved for a roll angle around  $-7^\circ$ .

Of particular interest is the relationship between the landing spot of the disc, i.e. the XY location of the disc when  $Z = 0$ , and the launch roll angle, Fig. 7.11. Notice that the disc landing point follows an ‘S’ shaped locus starting on the left hand side of the X axis (from the point of view of a person standing at the launch point) and moving to the right hand side as the launch roll angle is changed from  $-30^\circ$  to  $+30^\circ$ . The locus is offset in that the landing point for zero roll angle is approximately 8m to the right of the X axis. A landing closest to the X axis is achieved for an initial roll angle of approximately  $-6^\circ$ .

### 7.3.4 Frisbee Flight Control

The original purpose of the work presented in this paper was to investigate the possibility of developing a steerable projectile based on a spin-stabilised disc-wing. For completeness, two examples of trajectories with fixed control inputs are discussed: firstly a downward spiral turn and secondly a spiral roll.

Trajectory plots and parameter time histories for the spiral turn are shown in Fig. 7.12. The turn is set up by launching the disc at an initial bank angle of  $-45^\circ$  and a pitch attitude of  $-30^\circ$ , and by applying a constant control input rolling moment. From Fig. 7.12 it can be seen that after about 2 seconds the turn reaches approximately steady conditions, with an angle of attack of around  $15^\circ$ , an absolute attitude of around  $30^\circ$ , and

a speed of around 7m/s. Note that if the drag is set to zero, it is possible to launch the disc with a zero pitch attitude and a constant speed horizontal turn is achieved.

Trajectory plots and parameter time histories for the spiral roll are shown in Fig. 7.13. In this case, the manoeuvre is set up by launching the disc at a pitch attitude of  $-20^\circ$  and an angle of attack of  $-3^\circ$ , and by applying a constant pitching moment control input. Note that the trajectory is such that the angle of attack remains constant at  $-3^\circ$ , which is the angle of attack for zero lift. Since the angle of attack is constant, the lift to drag ratio of the disc is constant and hence the angle of the flight path in the XZ plane is constant, despite the velocity reducing.

## Chapter 8 Conclusions

1. The disc-wing is a class of tailless, longitudinally unstable flight vehicles that is inertially stabilised using spin. The disc-wing is most commonly encountered as the Frisbee sports disc.
2. Due to precessional effects, out of balance pitching moments result in a rolling motion of the disc as it flies. This behaviour results in the commonly observed ‘drop off’ behaviour of sports discs, especially towards the end of its flight.
3. The aerodynamic lift and drag characteristics of a sports disc are in keeping with what would be expected for a finite wing with low aspect ratio. That is, a relatively shallow lift curve, linear up to high angles of attack ( $45^\circ$ ) and a drag characteristic reasonably approximated by a component dependent on the square of the lift (induced drag) and non lift dependent component (profile drag at zero lift).
4. The pitching moment characteristic of a successful sports disc is unique in that the trim angle of attack ( $\sim 9^\circ$ ) is approximately coincident with the angle of attack for best lift to drag ratio ( $\sim 7^\circ$ ), and that the static margin in this region is least positive ( $\sim 0$ ), i.e. least unstable. For other cross-sectional profiles, e.g. Frisbee-like but with reduced rim height, stability is strongly negative for all flight angles of attack.
5. Surface pressure data shows that at typical flight angles of attack, the Frisbee-like profile has a leading edge suction peak similar to that found on conventional airfoil sections, but also a second suction peak towards the aft of the section. This, coupled with increased positive pressure in the cavity at the rear of the section, is consistent with the afterwards shift of the aerodynamic centre implied by the pitching moment results (conclusion 4).
6. At flight angles of attack, the flow around a sports disc typically exhibits a crescent shaped separation bubble a short distance down stream of the leading edge, lower surface leading edge separation and subsequent recirculation in the forward half of the cavity, and a turbulent wake like flow from the aft rim. Further aft, the wake flow is dominated by the presence of the roll up of the trailing vortex pair. At higher angles of attack, the wake vortex pair is stabilised by the separating leading edge

flow, delaying the stall to approximately  $45^\circ$ . Post-stall, the disc acts effectively as a bluff body, with an associated turbulent wake.

7. Spin has very little effect on the aerodynamic forces and moments acting on a disc-wing at typical flight advance ratios ( $\sim 1$ ). The largest effect is on the rolling moment, off surface flow visualisation shows that this is consistent with asymmetries in the leading edge separation bubble and vortex wake.
8. A six degree of freedom mathematical model of a rotating disc-wing has been derived and a simplified analysis used to make predictions of the disc pitch and roll rate in response to aerodynamic moments. A non-dimensional analysis of the roll rate equation has shown that non-dimensional disc trajectories will be fundamentally similar if a parameter based on the ratio of the disc static margin to the disc advance ratio is similar.
9. The disc-wing mathematical model has been implemented successfully in Matlab, and it has been shown that simulation can be simplified (and hence speeded up) with no significant loss of accuracy by using a body axis coordinate system that does not rotate with the disc. The simulation has been validated against a single experimental trajectory and reasonable agreement achieved. However more experimental flight test data is needed to provide a more comprehensive validation data base.
10. A comparison has been made between results for a typical throw trajectory based on using a nonlinear aerodynamic model for steady terms and a model based on linear derivatives. The results are qualitatively similar, though differences increase for parts of the trajectory where the angle of attack is above around  $10^\circ$  due to inaccuracies in the linear pitching moment approximation.
11. The effect of a range of launch conditions has been investigated numerically. It is shown that:
  - A high advance ratio (i.e. high disc spin rate) leads to straighter trajectories in the XY plane, as would be expected.
  - The launch pitch angles for maximum range and maximum duration with  $\phi_L = 0$  are  $10^\circ$  and  $20^\circ$  respectively.
  - The effect of launch angle of attack is qualitatively similar to the effect of launch pitch attitude for angles of attack less than  $60^\circ$ . At higher angles of attack, increased drag at launch leads to greatly reduced range and duration.

- The locus of disc landing position as a function of launch roll angle for the typical launch pitch angle of  $20^\circ$  has been shown to be an ‘S’ shape curve, with the locus crossing the X axis for a roll angle of  $-6^\circ$ .
12. Finally, it has been shown that with appropriate initial conditions and appropriate control moment input, it is feasible to explore hypothetical disc-wing manoeuvres such as a spiral turn and a spiral roll.

## **References**

Ali W., Aerodynamics of Rotating Disc Wings, Division of Aerospace Engineering, The Manchester School of Engineering, University of Manchester, UK, April 1998.

Anderson J.D., Fundamentals of Aerodynamics, 2<sup>nd</sup> Ed., McGraw-Hill, New York, 1991.

Asai M. & Yamamoto M., Frisbee-The Flow About a Frisbee, J. Japan Soc. Flu. Mech., Vol. 17, No. 1, 1998 (in Japanese).

Atsumi S., Pressure Distribution on a Wing with Circular Plan Form, J. Aeronautical Sci., pp. 499-501, 1937.

Author Unknown, The Goldstein Aeronautical Engineering Research Laboratory, Aero. Report No. 9100, School of Aeronautical Eng., University of Manchester, U.K., 1991.

Barger V. & Olsson M., Classical Mechanics: A Modern Perspective, McGraw-Hill, New York, 1973.

Barlow J.B., Rae Jr. W.H. & Pope A., Low Speed Wind Tunnel Testing (3<sup>rd</sup> Ed.), John Wiley & Sons, New York, USA, 1999.

Bartlett R.M., The Biomechanics of the Discus Throw: A Review, J. Sports Sci., Vol. 10, pp. 467-510, 1992.

Bauer S.X.S., An Aerodynamic Assessment of Micro-Drag Generators (MDGs), AIAA 98-2621, 16<sup>th</sup> AIAA Applied Aero. Conf., Albuquerque, NM, June 1998.

Borger J., Identified Flying Object, G2 Supplement, The Guardian, UK, 13 Sept. 2001, pp 1-3,8,9.

Cook N., Review Supplement (Extract from: The Hunt for Zero Point), The Mail on Sunday, UK, 12 Aug. 2001, pp 43-46.

Cook N., The Hunt for Zero Point, Century, London, U.K. Sept. 2001.

Cook W. L., Summary of Lift and Lift/Cruise Fan Powered Lift Concept Technology, NASA Ames Research Center, NASA-CR-177619, Aug. 1993.

Cooper I., Dalzell D. & Silverman E., Flight of the Discus, Report: E.Sc. 472, Div. Eng. Sci., Purdue University, Layfayette, Indiana, USA, May 1959.

Cooper K.R. (Ed.) et al, Closed-Test-Section Wind Tunnel Blockage Corrections for Road Vehicles, SAE Special Report SP-1176, Soc. Auto. Eng. Inc., Warrendale, PA, USA, 1996.

Cotroneo P.W., Biomechanical and Aerodynamical Aspects of the Backhand and Sidearm Frisbee-Disc Throws for Distance, MS Thesis, Faculty of Phys. Ed., Cal. State Univ., Hayward, June 1980.

Crook A. & Wood N.J., Measurements and Visualisations of Synthetic Jets, AIAA 2001-0145, 39<sup>th</sup> Aero. Sci. Meet & Exhibit, Reno, NV, Jan. 2001.

Danowsky B. & Cohanim B., Analysis of a Flying Disc, Senior Project Report No. SP-S02-006-R-BPD, Iowa State University, Iowa, USA, 26<sup>th</sup> April 2002.

Deckert W. H., The Lift-Fan Powered-Lift Aircraft Concept Lessons Learned, NASA Ames Research Center, NASA CR-177616, Sept. 1993.

Demele F.A. & Brownson J.J., Subsonic Longitudinal Aerodynamic Characteristics of Disks with Elliptic Cross Sections and Thickness-Diameter Ratios from 0.225 to 0.325., NASA Ames Research Center, NASA TM-X-556, May 1961.

Demele F.A. & Lazzeroni F. A., Effects of Control Surfaces on the Aerodynamic Characteristics of a Disk Reentry Shape at Large Angles of Attack and a Mach Number of 3.5, NASA Ames Research Center, NASA TM-X-576, Aug. 1961.

Fail R., Lawford L.A. & Eyre R.C.W., Low-Speed Experiments on the Wake Characteristics of Flat Plates Normal to an Air Stream, ARC R&M No. 3120, June 1957.

Frohlich C., Aerodynamic Effects on Discus Flight, Am. J. Physics, Vol. 49, pp. 1125-32, 1981.

Frost J.C.M. & Earl T.D., The Circular Wing in Forward Flight, Section from the paper: Flow Phenomena of the Focused Annular Jet, Symposium on Ground Effect Phenomena, Dept. Aero. Eng., Princeton University, Oct. 1959.

Ganslen R.V., Aerodynamic Factors which Influence Discus Flight, Unpublished Research Report, University of Arkansas, Arkansas, USA, 1958.

Ganslen R.V., Aerodynamic Forces in Discus Flight, Scholastic Coach, Vol. XXVIII, Pages 44 & 77, 1959.

Ganslen R.V., Aerodynamic and Mechanical Forces in Discus Flight, Athletic J., Vol. 44, Pages 50, 52, 68 & 88-89, 1964.

Gerloff M., The Discus Body and its Application to V/STOL Aircraft and Space Vehicles, Aero/Space Engineering, Jan. 1960, pp. 51-56.

Glaskin M., Torque It Up (Frontiers - Emerging Technologies), New Scientist, 2 Feb 2002.

Goto Y., Hiramoto R., Higuchi H. & Meisel I., Vortical Flows Past Cambered Flying Disks, JSASS 38<sup>th</sup> Aircraft Symposium, Sendai, Japan, Oct. 2000.

Grasmeyer J.M. & Keenon, Development of the Black Widow Micro Air Vehicle, AIAA 2001-0127, 39th Aero. Sci. Meet & Exhibit, Reno, NV, USA, Jan. 2001.

Greif R.K., Kelly M.W. & Tolhurst Jr. W. H., Wind-tunnel Tests of a Circular Wing with Annular Nozzle in Proximity to the Ground, NASA Ames Research Center, NASA TN-D-317, May 1960.

Greif R.K., Tolhurst Jr. W. H., Large-scale Wind-tunnel Tests of a Circular Plan-form Aircraft with a Peripheral Jet for Lift, Thrust and Control, NASA Ames Research Center, NASA TN-D-1432, Feb. 1963.

Grosjean C., Lee G., Hong W., Tai Y.C. & Ho C.M., Micro Balloon Actuators for Aerodynamic Control, 11th Ann. Int. Workshop on MEMS, Heidelberg, Germany, pp. 166-171, Jan. 1998.

Harrison T., Wood N.J. & Zhong S., Turbulent Separation Control Using Vortex Generators, RAeS Aerodynamics Research Conference Proc., London, UK, Apr. 2001.

Headrick E.E., Flying Saucer, Patent Application, Ser. No. 3359678, Patented 23<sup>rd</sup> Dec 1976.

Higuchi H., Goto Y., Hiramoto R. & Meisel I., Rotating Flying Disks and Formation of Trailing Vortices, AIAA 2000-4001, 18th AIAA Applied Aero. Conf., Denver, CO, USA, Aug. 2000.

Hubbard M., The Throwing Events in Track and Field, Chapter 6: Biomechanics of Sport (edited by Vaughan C.L.), pp. 213-38, CRC Press, Boca Raton, Florida, USA, 1989.

Hubbard M. & Hummel S., Simulation of Frisbee Flight, 5<sup>th</sup> Conf. on Mathematics and Computers in Sport, G. Cohen (Ed.), University of Technology, Sydney, Australia, June 2000.

Hummel S. & Hubbard M., A Musculoskeletal Model for the Backhand Frisbee Throw, 8<sup>th</sup> International Symposium on Computer Simulation in Biomechanics, Politecnico di Milano, Milan, Italy, July 2001.

Hummel S. & Hubbard M., Identification of Frisbee Aerodynamic Coefficients using Flight Data, 4<sup>th</sup> International Conference on the Engineering of Sport, Kyoto, Japan, Sept. 2002.

Hummel S.A., Frisbee Flight Simulation and Throw Biomechanics, Masters Thesis, University of California, Davis, California, USA, 2003.

Hummel S. & Hubbard M., Implications of Frisbee Dynamics and Aerodynamics on Possible Flight Patterns, 5<sup>th</sup> International Conference on the Engineering of Sport, Davis, California, USA, Sept. 2004.

Johnson S.E.D., FRISBEE A Practitioner's Manual and Definitive Treatise, Workman Publishing Co., New York, USA, 1975.

Katz P., The Free Flight of a Rotating Disc, pp. 150-155, Isreal J. Tech., Vol. 6, No. 1-2, 1968.

Kentzer C.P. & Hromas L.A., Letter to: Mr. Willis B.E. (Unpublished Research Report), School Aero. Eng., Purdue University, Layfayette, Indiana, USA, 2<sup>nd</sup> July 1958.

Keyes J.W., Aerodynamic Characteristics of Lenticular and Elliptic Configurations at a Mach Number of 6, NASA Langley Research Center, NASA TN-D-2606, Aug. 1965.

Laslett M., Boomlab, MSc Thesis, Aston University, Birmingham, UK, 1997.

Lazzara S., Schweitzer C. & Toscano, J., Design and Testing of a Frisbee Wind Tunnel Balance, Unpublished Report, Code: Engin 12, Brown University, Advisor: Prof. Karlson S.K.F., May 1980.

Lazzeroni F. A., Experimental Investigation of a Disk-shaped Reentry Configuration at Transonic and Low Supersonic Speeds: NASA Ames Research Center, NASA TM-X-652, May 1962.

Lissaman P.B.S., Stability and Dynamics of a Spinning Oblate Spheriod, Unpublished Document, 2<sup>nd</sup> Dec. 1994.

Lissaman P.B.S., The Meaning of Lift, AIAA 96-0161, 34<sup>th</sup> Aero. Sci. Meet & Exhibit, Reno, NV, Jan. 1996.

Lissaman P.B.S., Disc Flight Dynamics, Unpublished Document, 29<sup>th</sup> Dec. 1998.

Lissaman P.B.S., Disc Flight Description, Unpublished Document, University of Southern California, 12<sup>th</sup> Jan. 1999.

Lissaman P.B.S., Private Communication (with Hubbard M.), 2000.

Lissaman P.B.S., Range of a Free Disc, Unpublished Document, 4<sup>th</sup> Jan. 2001.

Lissaman P.B.S., Physics of the Far Flung Frisbee, Unpublished Document, 11<sup>th</sup> Dec. 2003.

Lissaman P.B.S., Upper Bounds on Range of a Free Disc, Unpublished Document, 19<sup>th</sup> Dec. 2003.

Lorenz R.D., Flying Saucers, New Scientist, pp. 40-1, 19<sup>th</sup> June 2004.

Lorenz R.D., Flight and Attitude Dynamics Measurements of an Instrumented Frisbee, pp. 738-48, Meas. Sci. Tech., Vol. 16, 11<sup>th</sup> Feb. 2005.

Martin-Henry C., Disc-wing Flow Visualisation, Division of Aerospace Engineering, The Manchester School of Engineering, University of Manchester, UK, April 2000.

Maskell E.C., A Theory of the Blockage Effects on Bluff Bodies and Stalled Wings in a Closed Wind Tunnel, ARC R&M No. 3400 Nov. 1965.

Meisel I., Struktur der Umstromung einer angestellten Scheibe, Diplomarbeit, Universitat Karlsruhe, 2000 (in German).

Mitchell T.L., The Aerodynamic Response of Airborne Discs, MS Thesis, University of Nevada, Las Vegas, NV, USA, 1999.

Murray D.C., The Avro VZ-9 Experimental Aircraft – Lessons Learned, AIAA-90-3237-CP, 1990.

Nakamura Y. & Fukamachi N., Visualisation of Flow Past a Frisbee, Fluid Dyn. Res., v7, pp31-35, 1991

Peterson H., Calculation of Self-Suspended Flare Trajectories, Denver Research Institute, NAD/Crane RDTR No. 193, AD731866, 16 Sept. 1971.

Potts J., Stabilising the Spin, Unmanned Vehicles Magazine, Shephard Press, Aug. 2001.

Potts J.R. & Crowther W.J., The Flow Over a Rotating Disc-wing, RAeS Aerodynamics Research Conference, London, UK, April 2000.

Potts J.R. & Crowther W.J., Visualisation of the Flow Over a Disc-wing, Proc. of the Ninth International Symposium on Flow Visualization, Edinburgh, Scotland, UK, Aug. 2000.

Potts J.R. & Crowther W.J., Flight Control of a Spin Stabilised Axi-symmetric Disc-wing, AIAA 2001-0253, 39th Aero. Sci. Meet & Exhibit, Reno, NV, USA, Jan. 2001.

Potts J.R. & Crowther W.J., Application of Flow Control to a Disc-wing UAV, 16<sup>th</sup> UAV Systems Conference, Bristol, UK, April 2001.

Potts J.R. & Crowther W.J., Disc-wing UAV: A Feasibility Study in Aerodynamics & Control, CEAS Aerospace Aerodynamics Research Conference, Cambridge, UK, 10<sup>th</sup> - 13<sup>th</sup> June 2002.

*Also presented orally as:*

Potts J.R. & Crowther W.J., Aerodynamics and Control of a Spin-stabilised Disc-wing, Session 136-APA-16: CEAS Aerospace Aerodynamics Conference Highlights (Invited), 41st AIAA Aero. Sci. Meet & Exhibit, Reno, NV, USA, Jan. 2003.

Potts J.R. & Crowther W.J., Frisbee<sup>TM</sup> Aerodynamics, AIAA 2002-3150, 20<sup>th</sup> Applied Aero. Conf. & Exhibit, St. Louis, MI, USA, 24<sup>th</sup> - 26<sup>th</sup> June 2002.

Pozzy T., Getting More Distance - How Important Is Disc Speed, Disc Golf World News, No. 57, Spring 2001.

Pozzy T., Getting More Distance - How The Pros Do It, Disc Golf World News, No. 60, Winter 2002.

Reed R. D., Lister D. & Huntley J. D., Wingless Flight: The Lifting Body Story, NASA Dryden Flight Research Center, NASA SP-4220, 1997.

Rose B., Flying Saucers – Avro's Secrets, Air Pictorial, May 2001, pp 342-7.

Saltzman E. J., Wang K.C. & Iliff K. W., Flight-determined Subsonic Lift and Drag Characteristics of Seven Lifting-body and Wing-body Reentry Vehicle Configurations with Truncated Bases, AIAA-99-0383, 37<sup>th</sup> AIAA Aerospace Sciences Meeting and Exhibit, Reno, Nevada, USA, Jan. 1999.

Samozwetow A., Diskus und Wind, Der Leichtathletik Trainer, Vol. 2, Pages 407-10, 1970.

Schuurmans M., Flight of the Frisbee, New Scientist, 28<sup>th</sup> July 1990, pp 37-40.

Soong T.C., The Dynamics of the Discus Throw, J. Appl. Mech., Vol. 98, pp. 531-6, 1976.

Spearman M. L. & Braswell D.O., Aerodynamics of a Sphere and an Oblate Spheroid for Mach Numbers from 0.6 to 10.5 including the Effect of Test Conditions, NASA Langley Research Center, NASA TM-109016, Aug. 1993.

Spearman M. L., Supersonic Aerodynamic Characteristics of some Reentry Concepts for Angles of Attack up to 90 degrees, AIAA-85-1795, 12<sup>th</sup> AIAA Atmospheric Flight Vehicles Conference, Snowmass, CO, USA Aug. 1985.

Spearman M. L., Supersonic Aerodynamic Characteristics of Some Reentry Concepts for Angles of Attack up to 90 degrees, NASA Langley Research Center, NASA-TM-87645, Nov. 1985.

Stilley G.D. & Carstens D.L., Adaptation of Frisbee Flight Principle to Delivery of Special Ordnance, AIAA Paper No. 72-982, 1972.

Stilley G.D., Aerodynamic Analysis of the Self-Suspended Flare, Honeywell Inc., NAD/Crane RDTR No.199, AD740117, 23 Feb. 1972.

Stone M., Compact Disc Frisbee Aerodynamics, Division of Aerospace Engineering, The Manchester School of Engineering, University of Manchester, UK, April 1999.

Taylor J.A., Behaviour of the Discus in Flight, Athletic J., Vol. 12, pp. 9-10 & 44-7, 1932.

Terauds J., Technical Analysis of the Discus, Scholastic Coach, Vol. 47, Pages 98, 100, 104, 166, 1978.

Tobak M. & Peake D.J., Topology of Three Dimensional Separated Flows, Ann. Rev. Fluid Mech., v14, pp61-85, 1982.

Tuck E.O. & Lazauskas L., Lifting Surfaces with Circular Planforms, 19th International Workshop on Water Waves and Floating Bodies, Cortona, Italy, 28-31 April 2004.  
(to appear in Journal of Ship Research, 2005).

Tutjowitsch V.N., Theorie der Sportlichen Wurfe Teil 1, Leistungssport, Vol. 7, pp. 1-161, 1976.

Voigt H., Wirkungen der Luftkrafte auf die Flugweite beim Diskuswerf, Der Leibeserziehung, Vol. 21, Pages 319-26, 1972.

Wagner R., American Combat Planes (3<sup>rd</sup> Ed.), Doubleday & Co., Garden City, New York, USA, 1982.

Ware G. M., Investigation of the Low-Subsonic Aerodynamic Characteristics of a Model of a Modified Lenticular Reentry Configuration, NASA Langley Research Center, NASA TM-X-756, Dec 1962.

Washabaugh P.D., Bernal L.P., Najafi K. et al, An Approach Toward Wafer Integrated Micro Air Vehicle, 15<sup>th</sup> International UAV Systems Conf., Bristol, U.K., Apr. 2000.

White F.M., Fluid Mechanics (4<sup>th</sup> Ed.), McGraw-Hill, Singapore, 1999.

Wilson J., Roswell Plus 50, Popular Mechanics, July 1997.

Wilson J., America's Nuclear Flying Saucer, Popular Mechanics, Nov. 2000.

Yasuda K., Flight- and Aerodynamic Characteristics of a Flying Disk, Japanese Soc. Aero. Space Sci., Vol. 47, No. 547, pp 16-22, 1999 (in Japanese).

Zdravkovich M.M., Flaherty A.J., Pahle M.G. & Skelhorne I.A., Some Aerodynamic Aspects of Coin-like Cylinders, JFM, v360, pp73-84, 1998.

Zimmerman C.H., Characteristics of Clark Y Airfoils of Small Aspect Ratios, NACA Langley Memorial Aeronautical Laboratory, NACA-TR-431, 1932.

Zimmerman C.H., Aerodynamic Characteristics of Several Airfoils of Low Aspect Ratio, NACA Langley Memorial Aeronautical Laboratory, NACA-TN-539, Aug. 1935.

## **Figures**

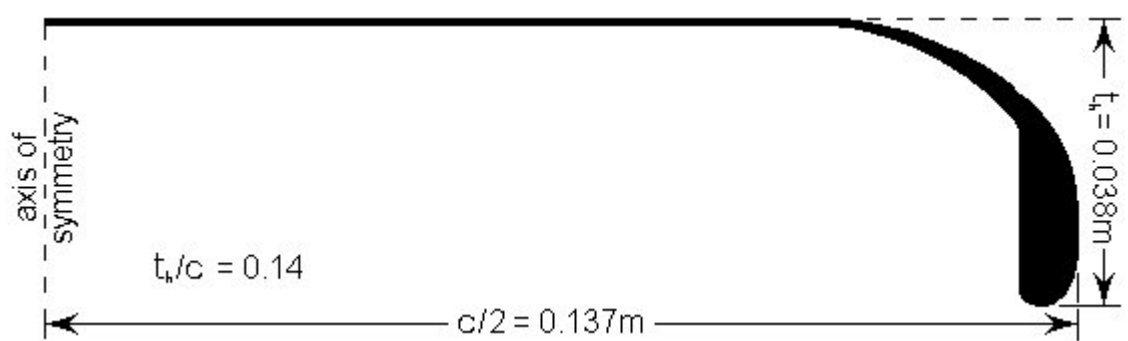


Figure 2.1 Cross-sectional frisbee-like disc-wing profile.

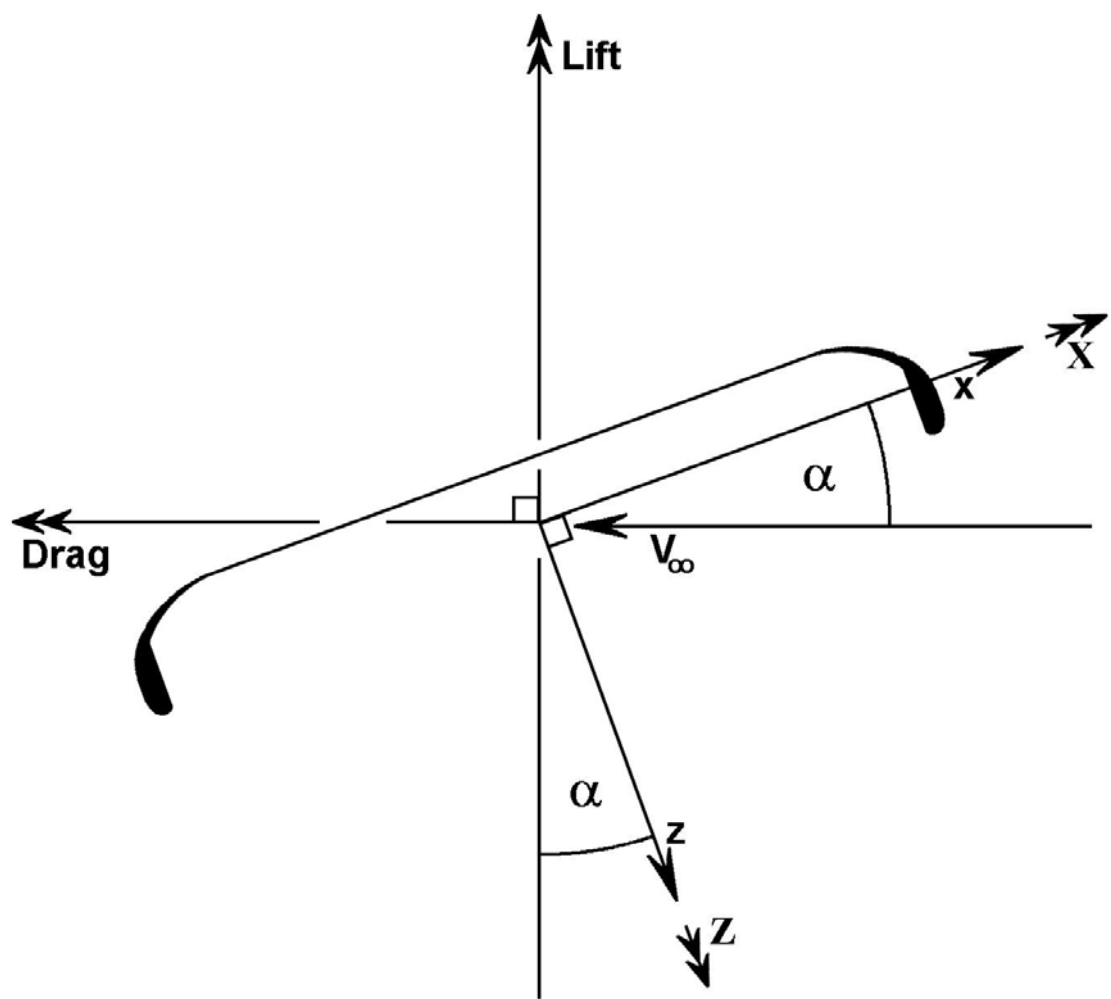


Figure 2.2 Relationship between the *Lift & Drag* and the Axial  $X$  & Normal  $Z$  forces.

The *Side* force (not shown here) is identical for both systems,  
directed out of the page.

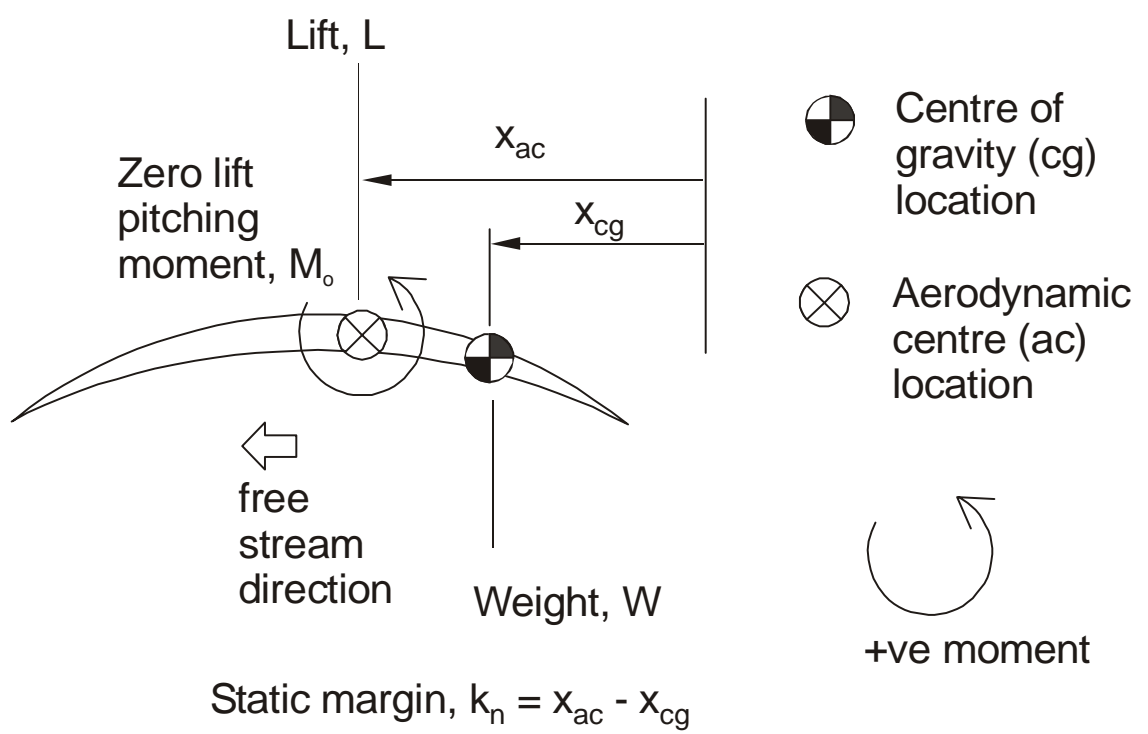
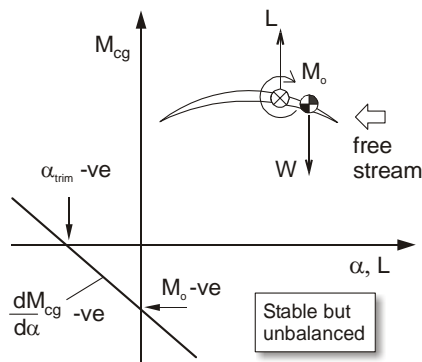
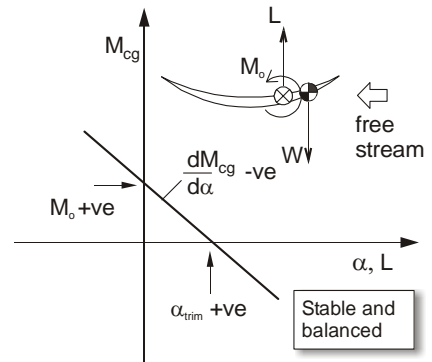


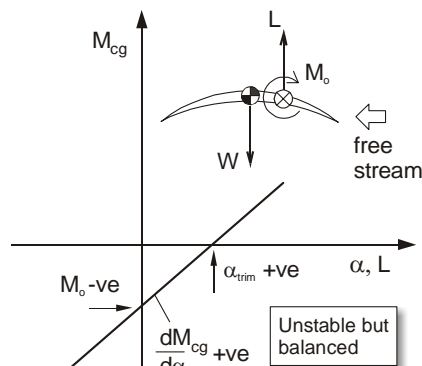
Figure 2.3 Definition of reference locations for longitudinal forces and moments acting a tailless flight vehicle.



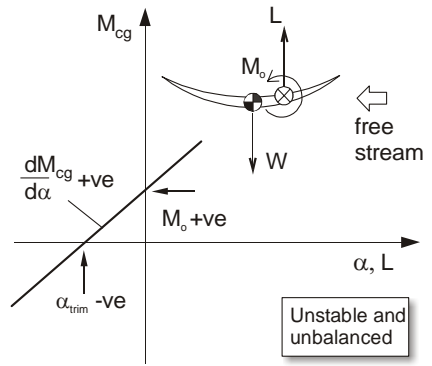
a) Positively camber, positive static margin



b) Negative camber, positive static margin



c) Positive camber, negative static margin



d) Negative camber, negative static margin

Figure 2.4 Illustration of longitudinal stability and trim characteristics of a tailless flight vehicle for permutations of camber and static margin.

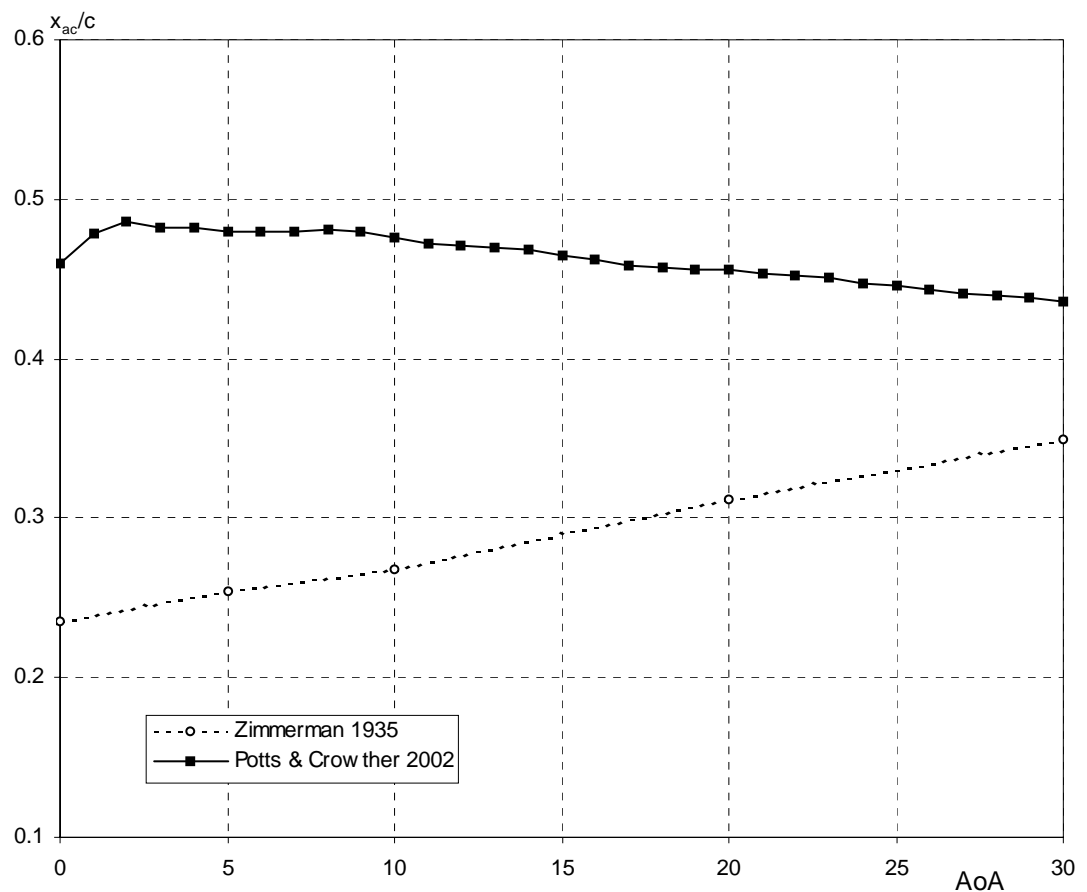


Figure 2.5 Comparison of the aerodynamic centre location as a function of angle of attack for a Frisbee (Potts & Crowther, 2002) and a circular planform wing with a non-axisymmetric airfoil cross-section (Zimmerman, 1935).



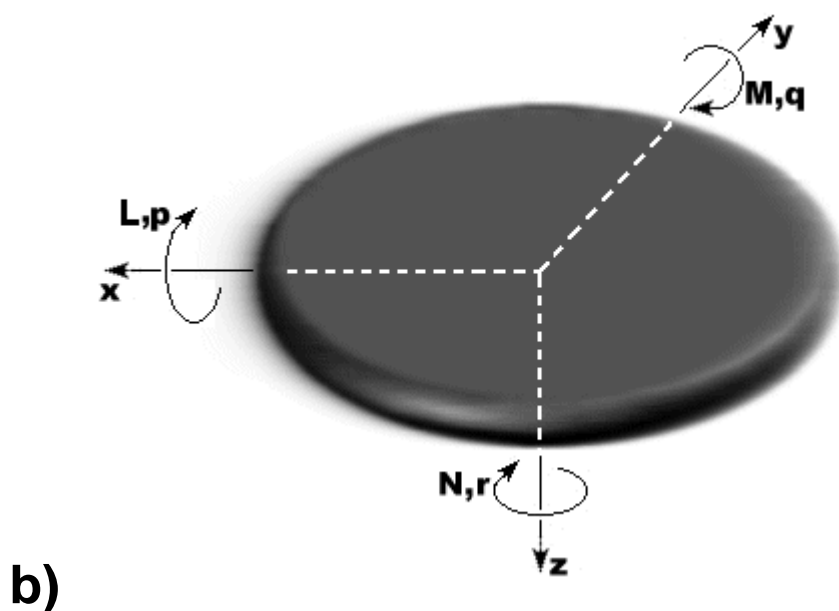
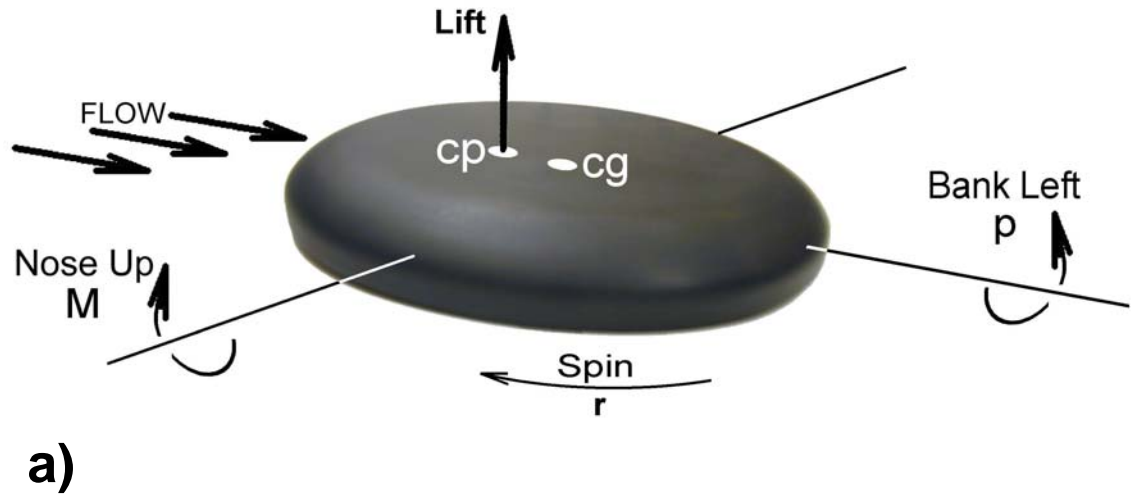


Figure 2.6 (a) Disc-wing flight dynamics. (b) Schematic diagram of body fixed axes.

N.B. for a conventional aircraft the nose would point in the positive x-direction.

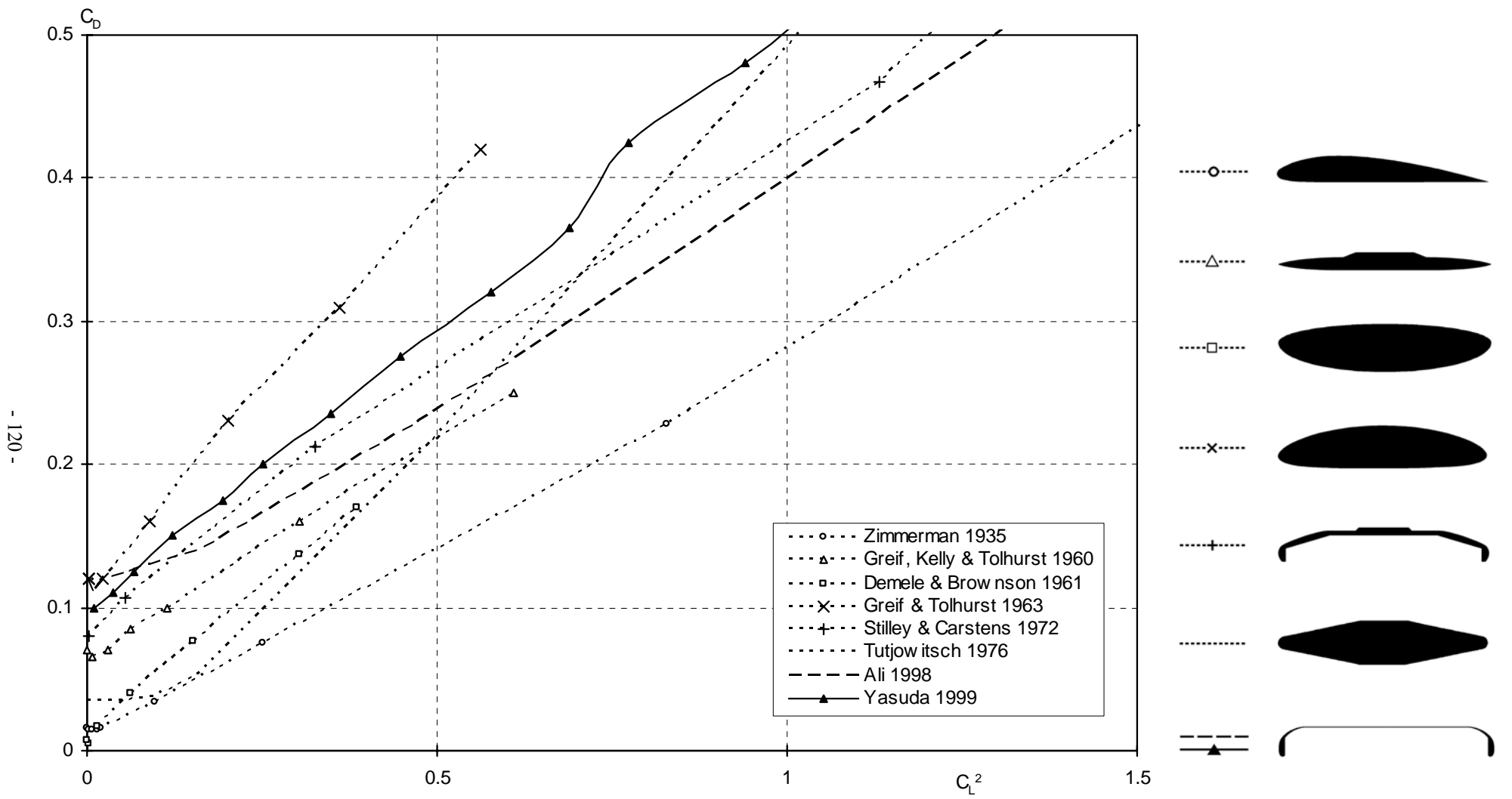


Figure 3.1 Comparison of aerodynamic load data for circular planform wings, derived from various sources found in the literature, with chordwise cross-sections as seen to the right of the figure.

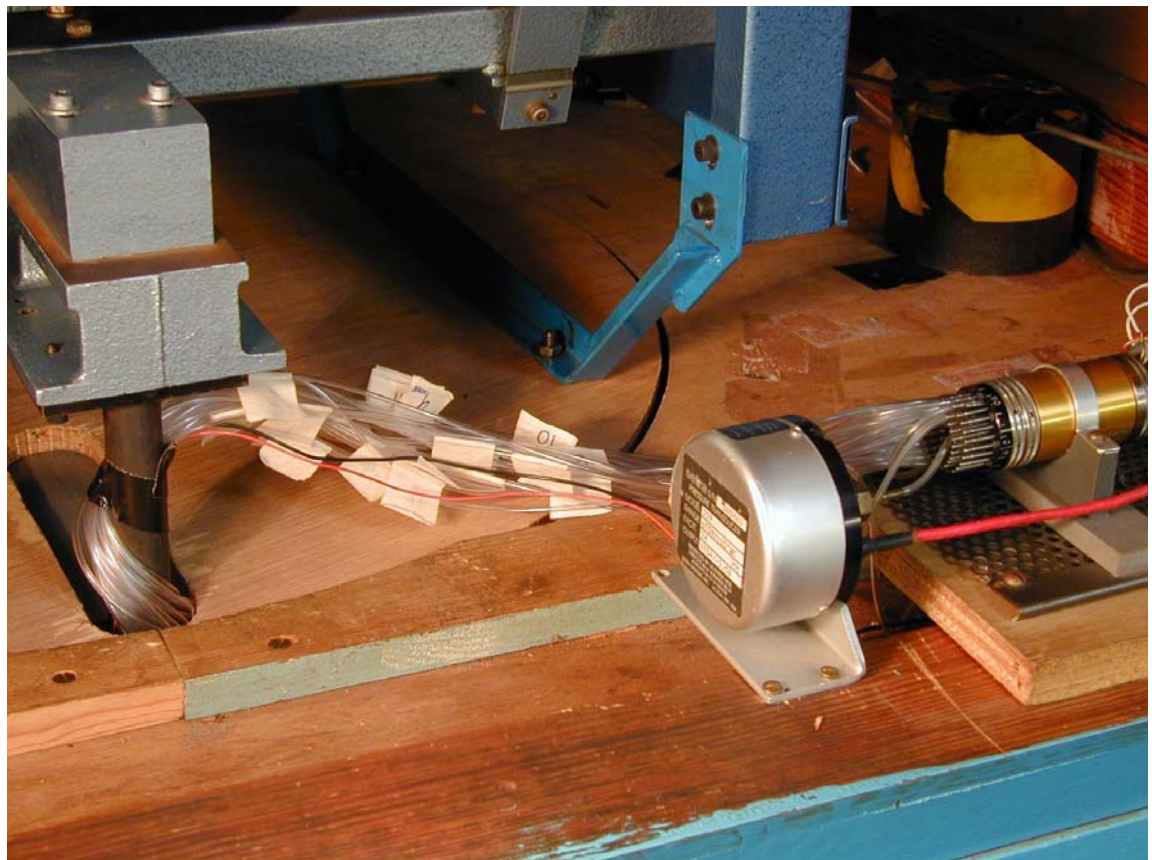


Figure 4.1 Wind tunnel support strut fixed to balance beam above wind tunnel working section (left), pressure lines (capillary tubing) connected to pressure transducer (right middle) via a scanivalve (right).



Figure 4.2 Wind tunnel control room. Equipment listed as follows:

1. Betz pressure manometer (top left) sitting on top of the
2. Yaw & incidence controller (below 1),
3. Power supply for motor (above 2),
4. Flow speed controller (above 3),
5. Scanivalve stepper control (right of 3),
6. Wind tunnel computer including raw data visual display (right of 5),
7. Data processing computer with pressure contour plot displayed (right of 6).

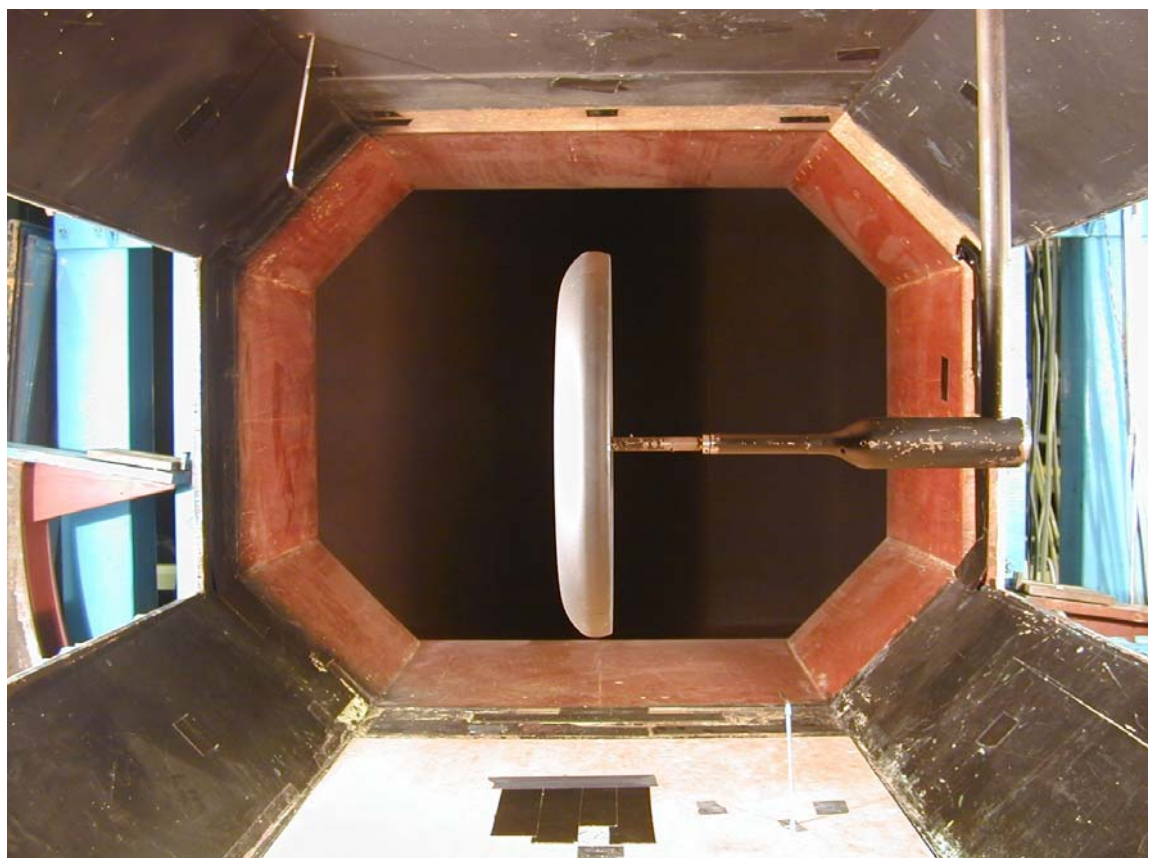


Figure 4.3 L-shaped support strut and disc-wing mounted vertically at  $0^\circ$  incidence.

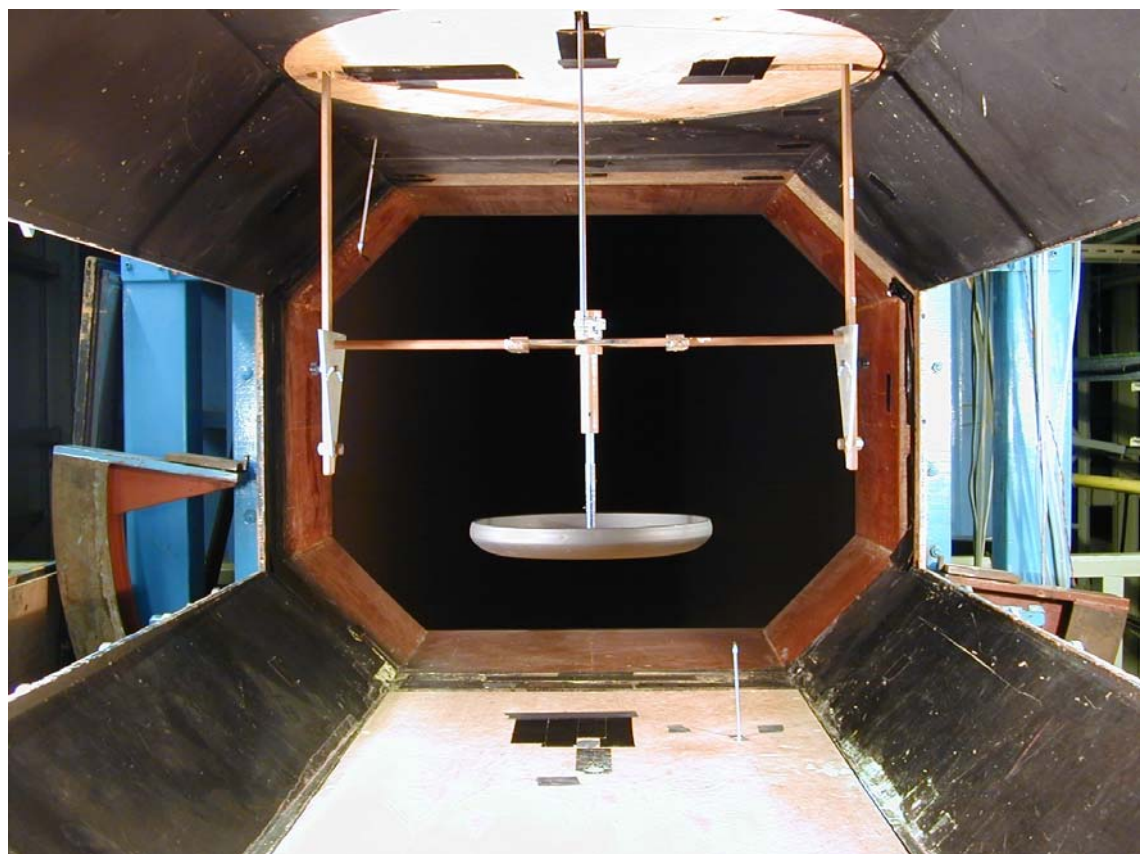
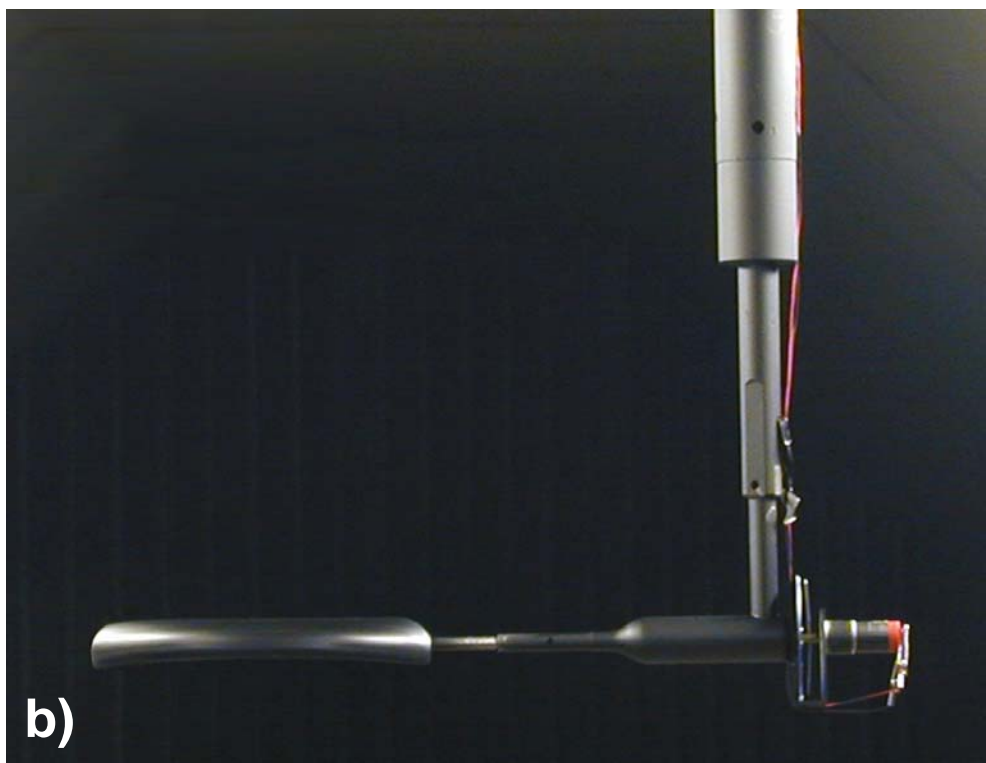


Figure 4.4 Surface paint flow visualisation rig configuration, the disc is horizontal at zero incidence. The disc is mounted on a central axle, which is fixed to a horizontal crossbar, two vertical struts either side of the balance beam support the crossbar, the incidence arm is connected to control the angle of attack. Rig designed by Ali (1998).



a)



b)

Figure 4.5 Smoke wire flow visualisation rig configurations: (a) Motor driven axle connected to centre of vertical test model allows visualisation of spinning disc, up to 24Hz. (b) Geared down motor driven axle connected to rim of test model allows visualisation of the full central flow field cross-section of a non-spinning disc.

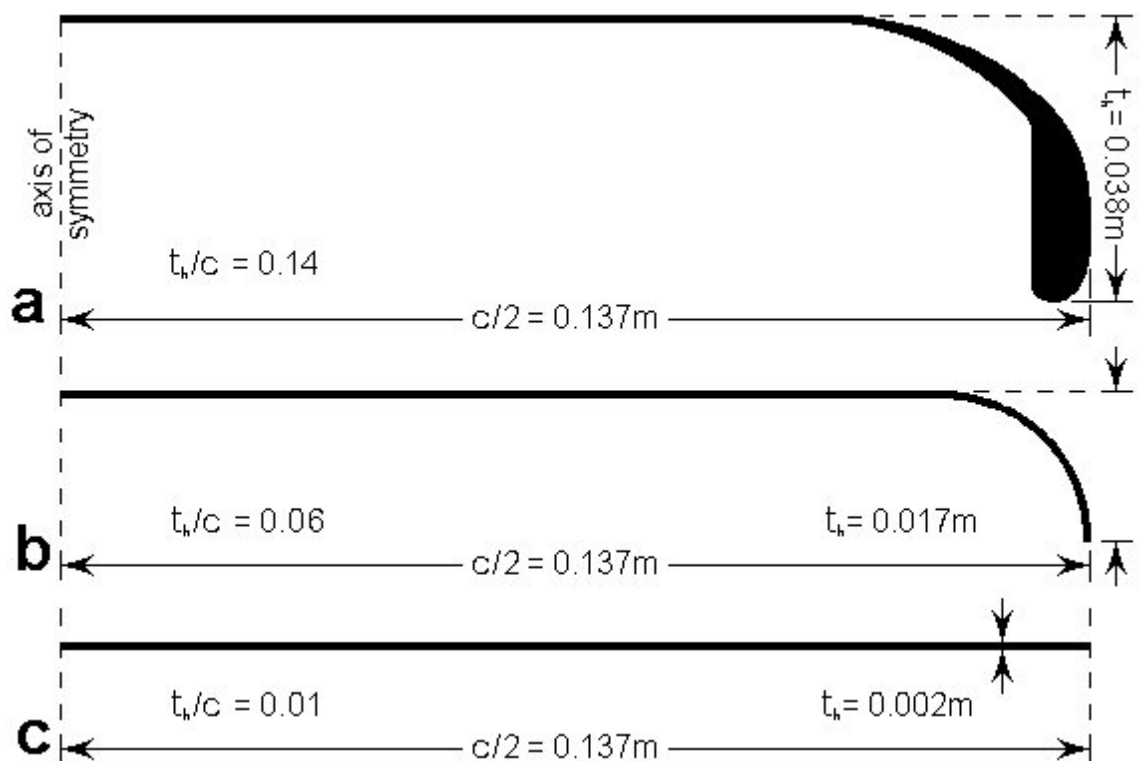


Figure 4.6 Cross-sectional disc-wing profiles.

(a) Frisbee-like (b) Intermediate (c) Flat Plate.

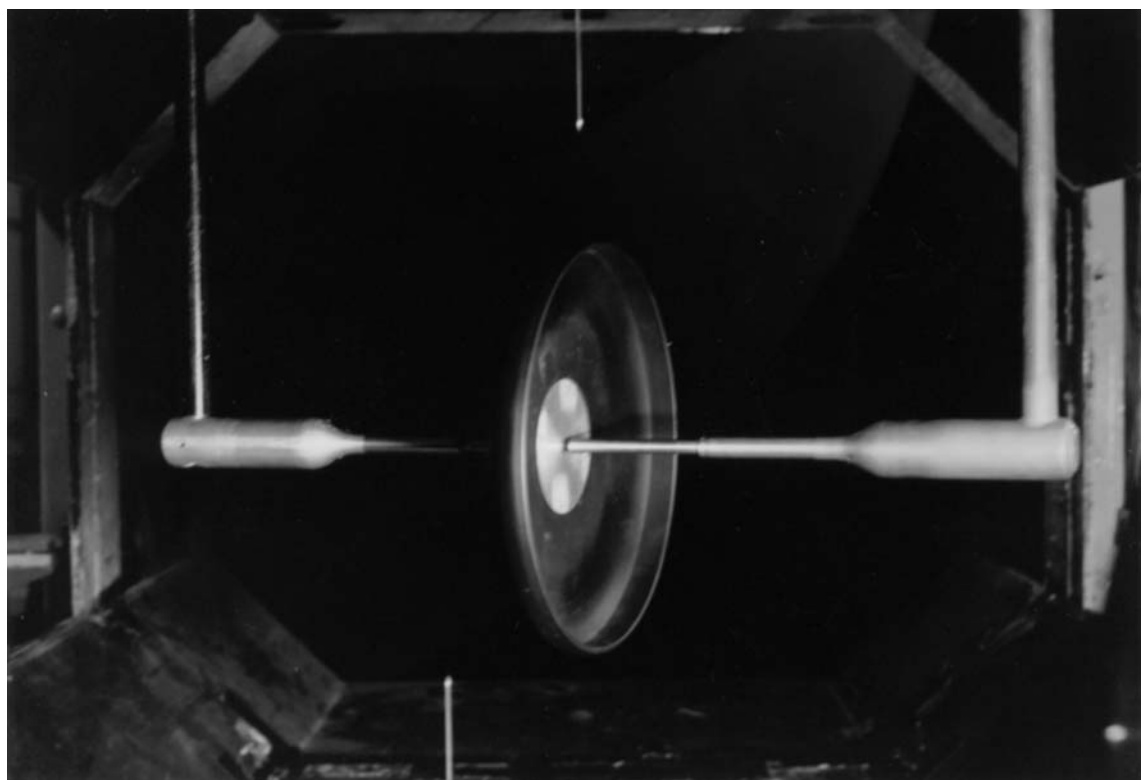
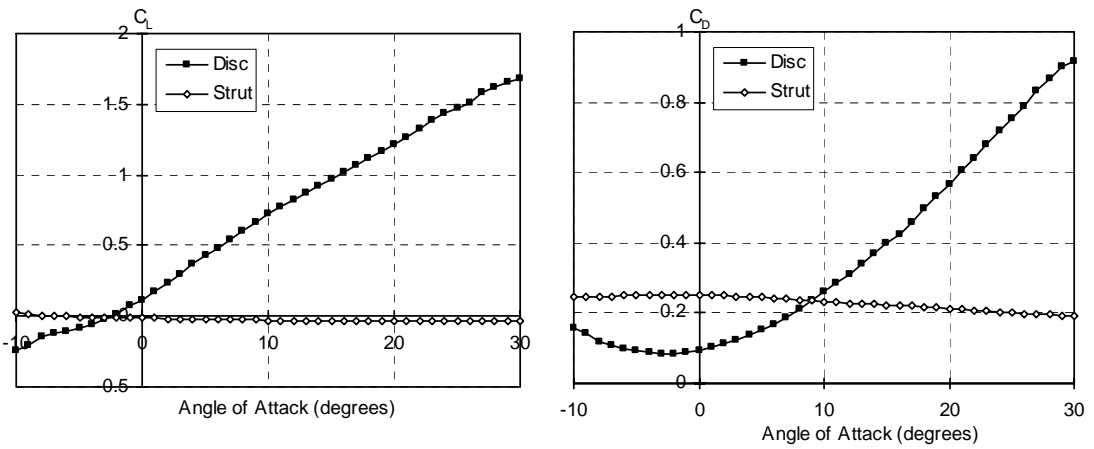
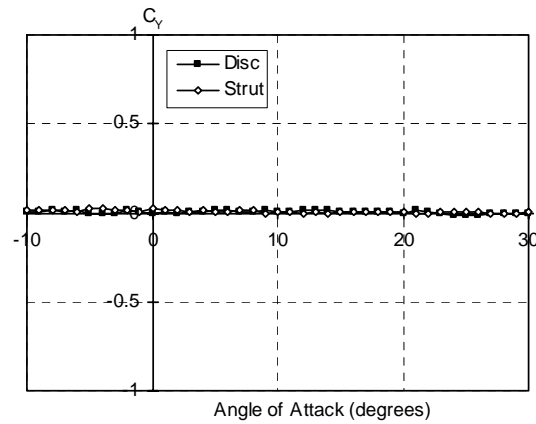


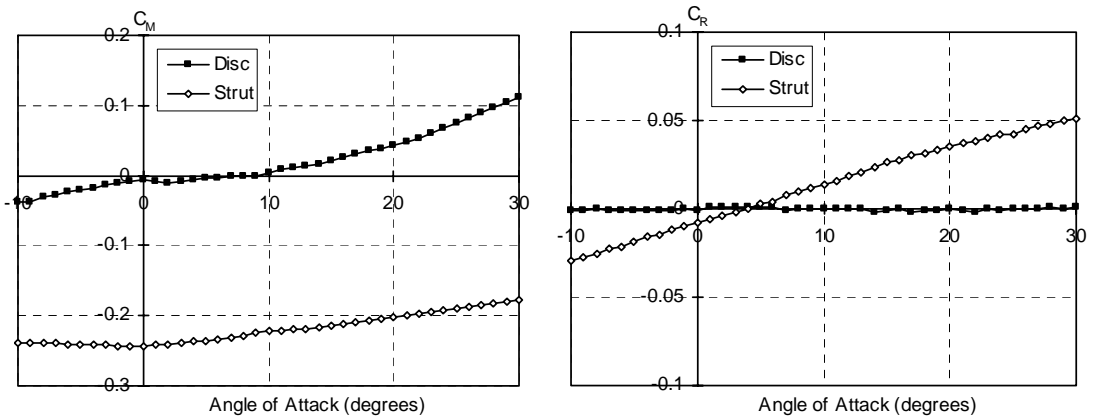
Figure 4.7 Wind tunnel configuration to measure interference and tare effects, the disc was mounted on a dummy support (left). The dummy strut was a mirror image of the measuring strut (right) and held the disc in the correct position (on the balance centre) but not connected to the balance itself. The measuring strut was set with the axle tip (centre) at around 3mm from the disc, without touching, and was fixed to the balance.



(a) Lift coefficient. (b) Drag coefficient.



(c) Side force coefficient.



(d) Pitching moment coefficient. (e) Rolling moment coefficient.

Figure 4.8 Comparison of the disc test model and the support strut at zero spin rate,  
 $\text{AoA} = -10^\circ$  to  $30^\circ$ ,  $V_\infty = 20\text{m/s}$ ,  $\text{Re} = 3.78 \times 10^5$ .

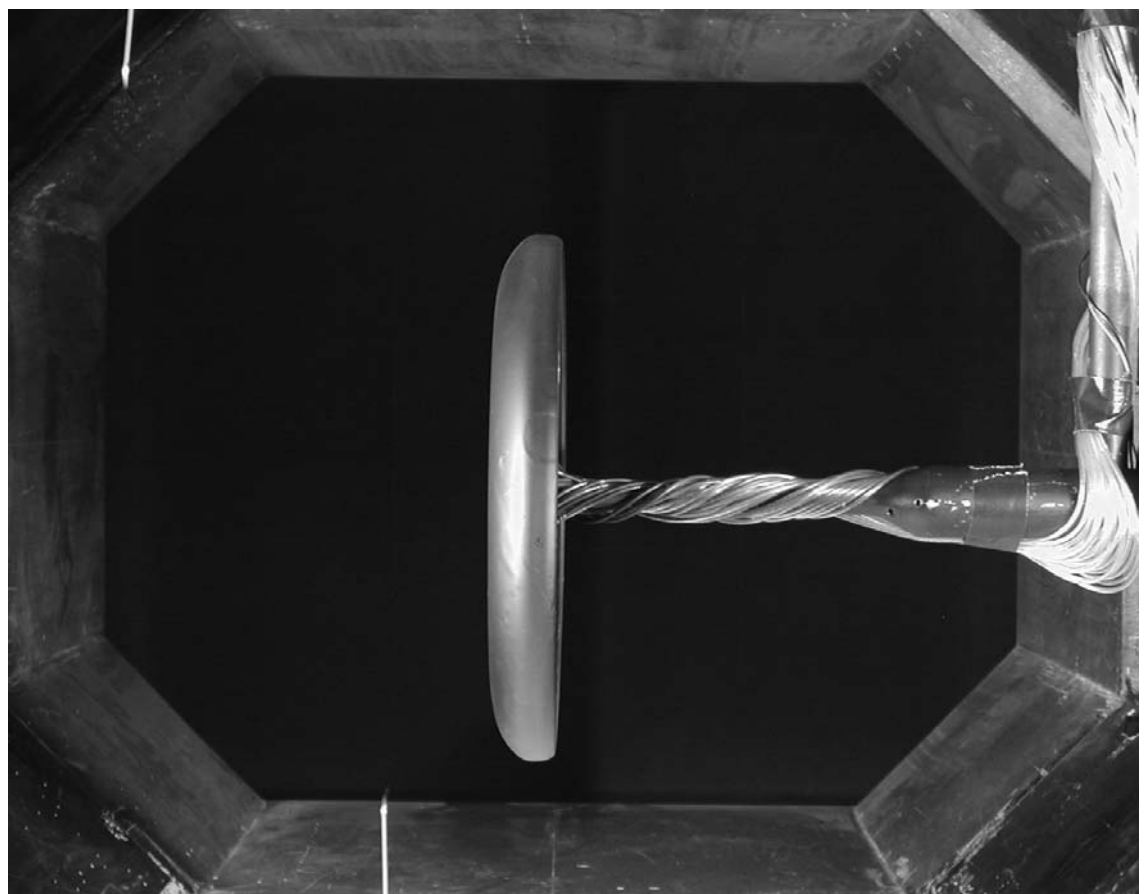


Figure 4.9 L-shaped rig configuration, to measure the surface pressure distribution.

The capillary tubes were carefully wound around the support strut.

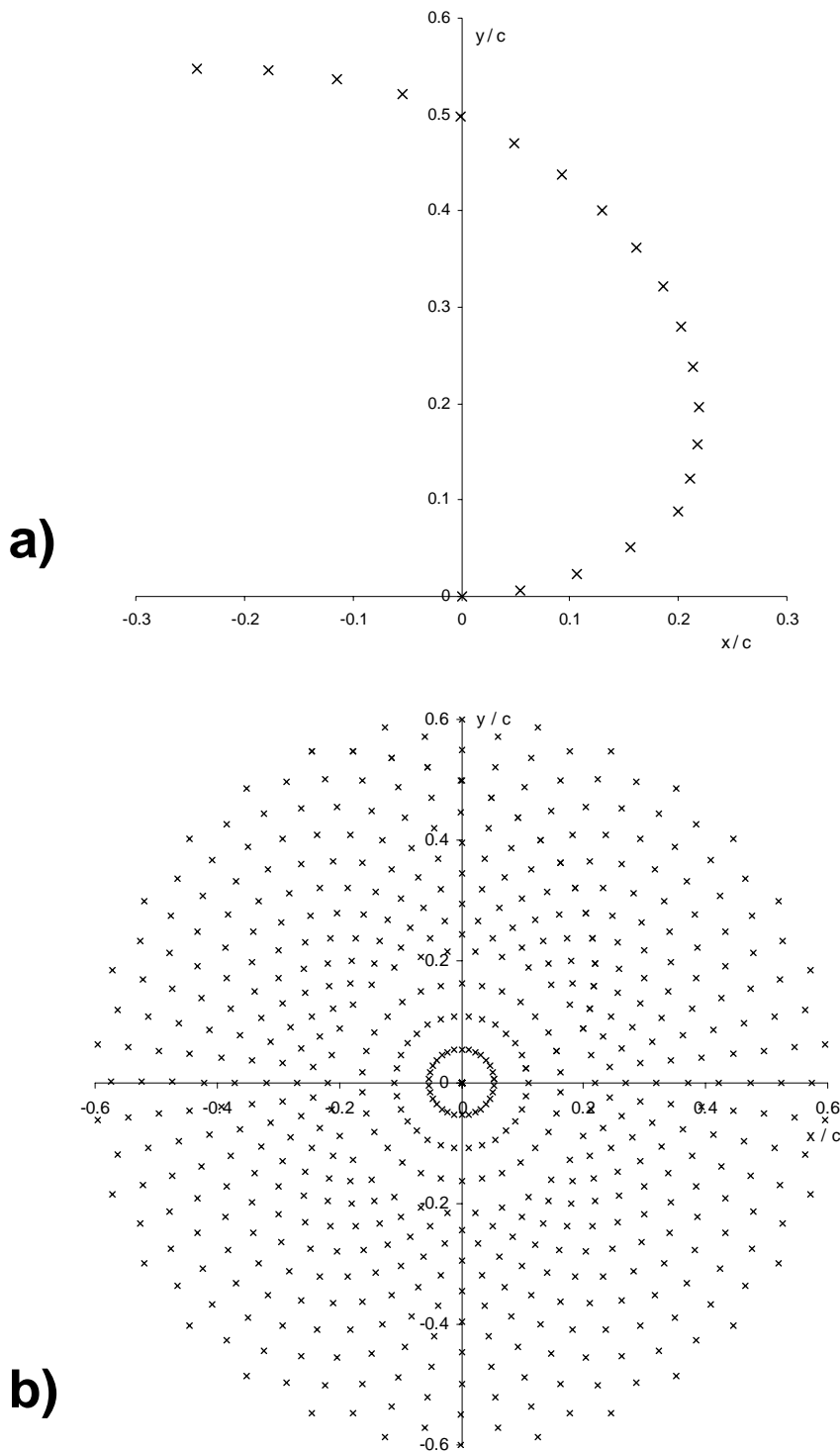


Figure 4.10 (a) The pressure tappings in the surface of the disc-wing test models were positioned on a spiral curve. (b) The spiral curve of points was stepped at  $12^\circ$  increments, by yawing the model, to achieve full coverage of the disc-wing surface. That is a polar grid array of 571 points on each surface, upper and cavity.

The non-dimensional position (normalised by the chord  $c$ ) of the plotted points are given relative to the distance along the surface profile cross-section from the centre.

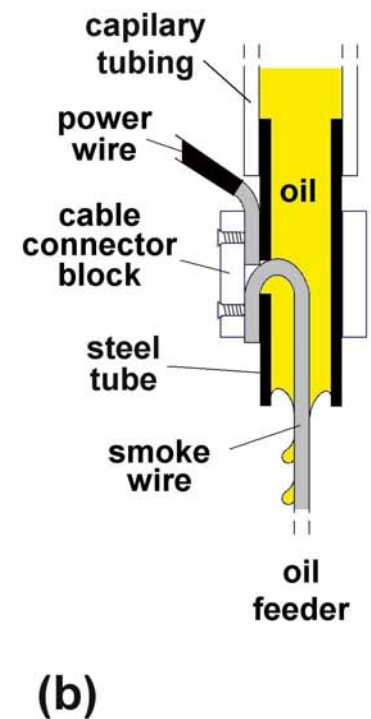
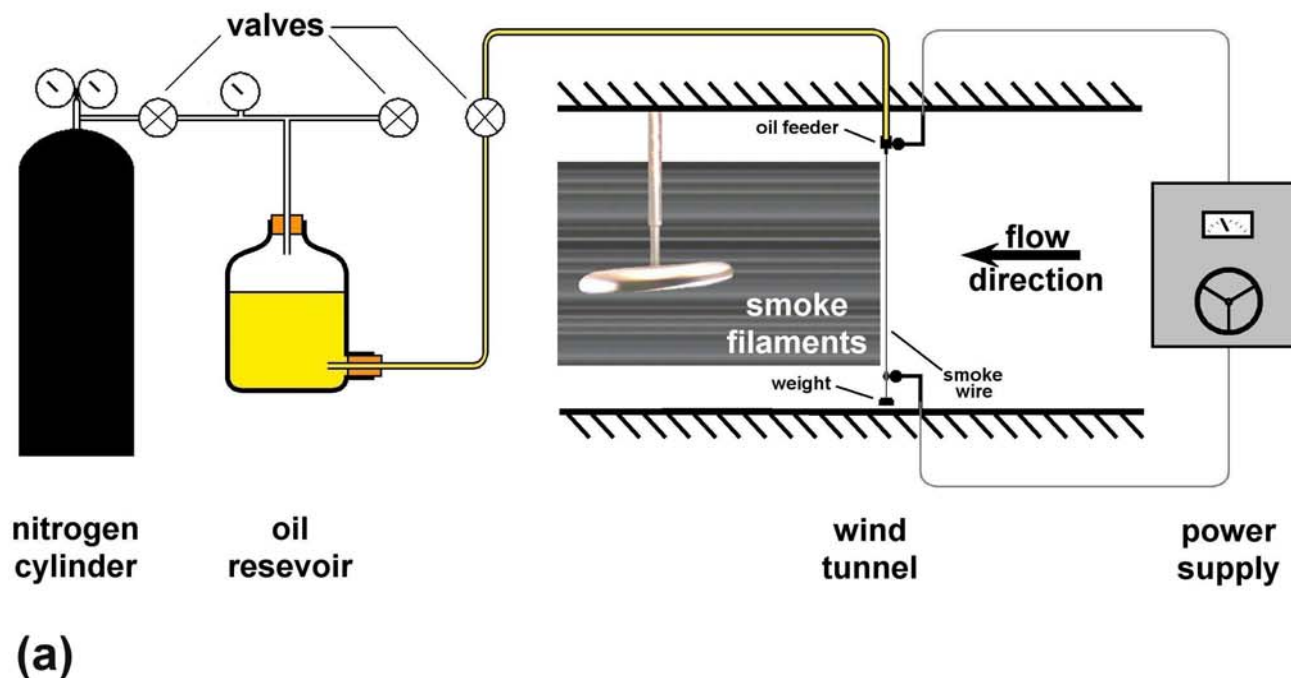
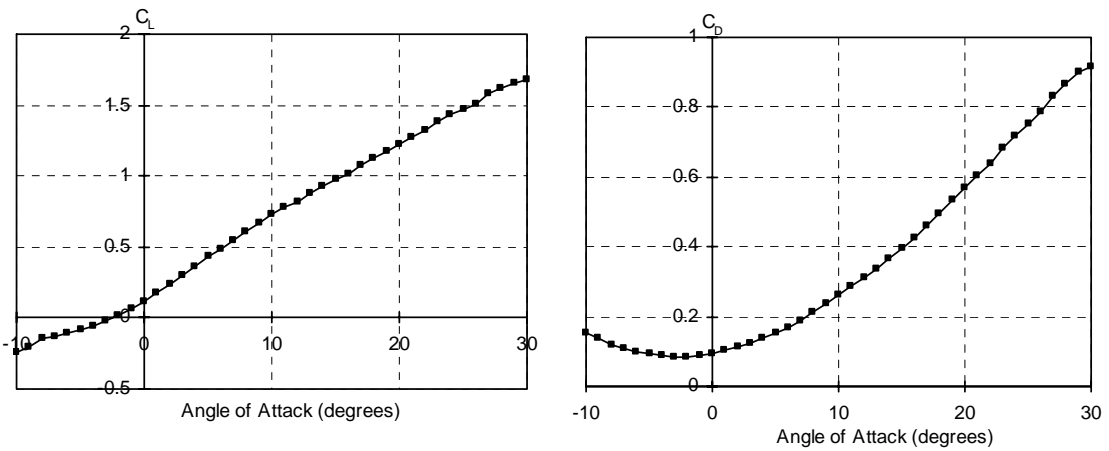
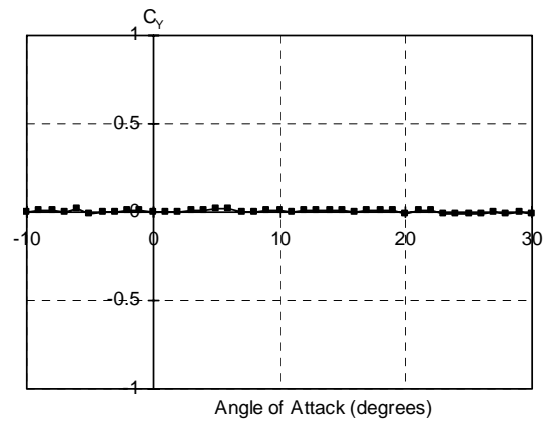


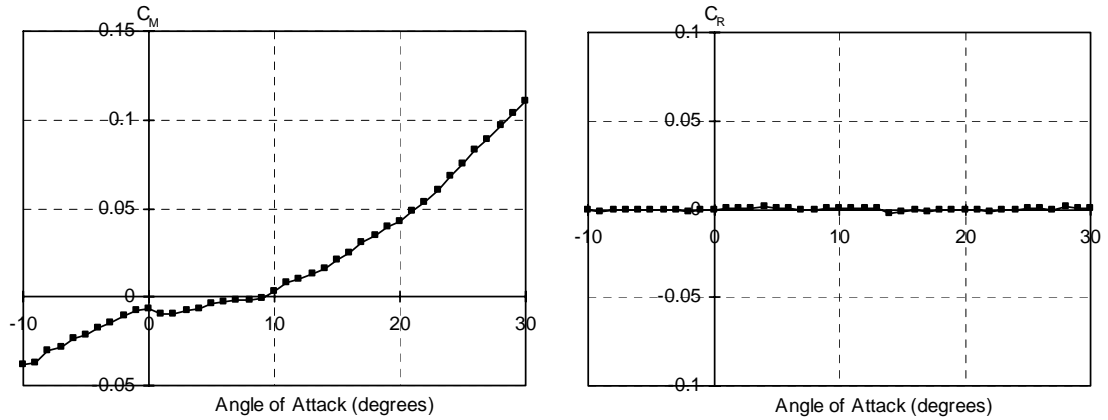
Figure 4.11 Schematic diagram of (a) the smoke wire and oil supply system, (b) the oil feeder device.



(a) Lift coefficient. (b) Drag coefficient.



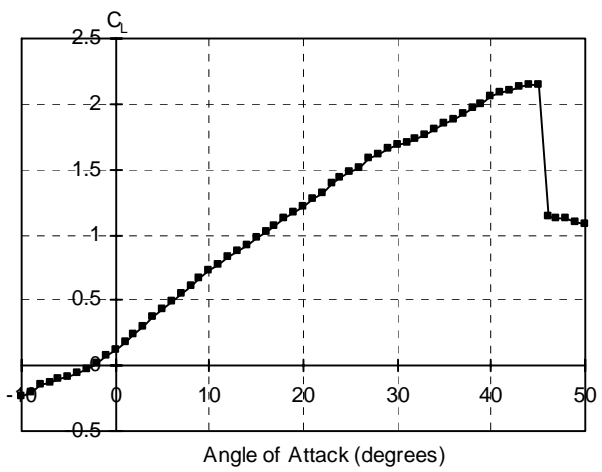
(c) Side force coefficient.



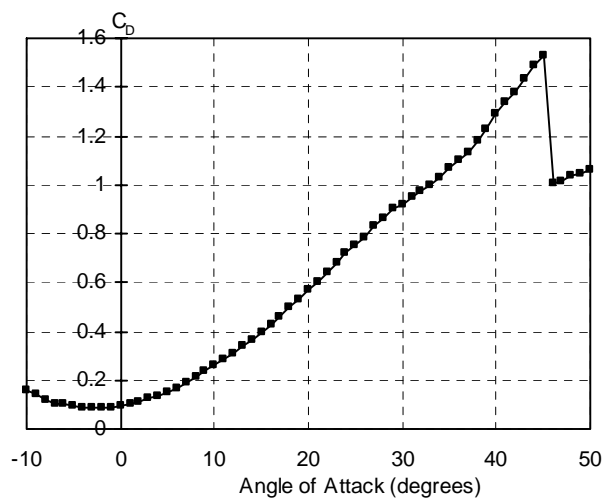
(d) Pitching moment coefficient. (e) Rolling moment coefficient.

Figure 5.1 Load Characteristics at zero spin rate, AoA =  $-10^\circ$  to  $30^\circ$ ,

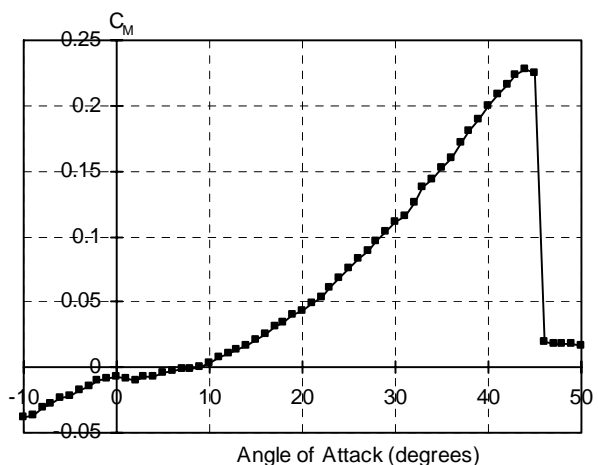
$$V_\infty = 20 \text{ m/s}, \text{Re} = 3.78 \times 10^5.$$



(a) Lift coefficient.



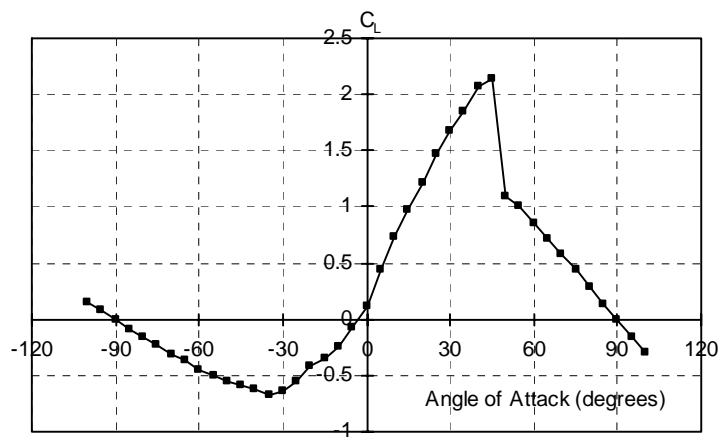
(b) Drag coefficient.



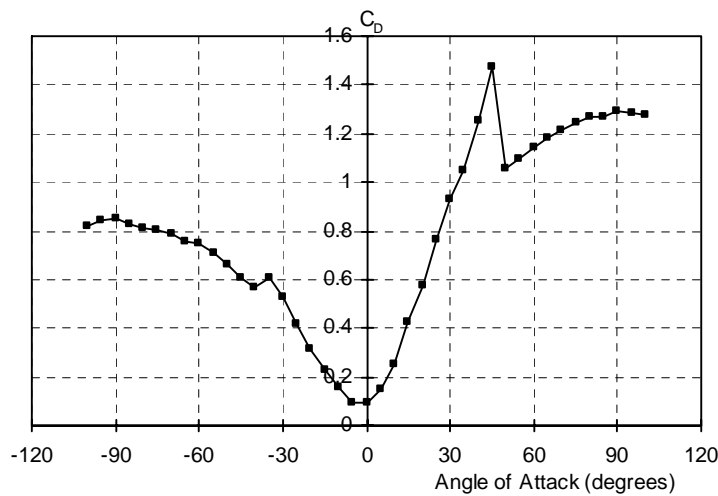
(c) Pitching moment coefficient.

Figure 5.2 Load Characteristics at zero spin rate, AoA =  $-10^\circ$  to  $50^\circ$ ,

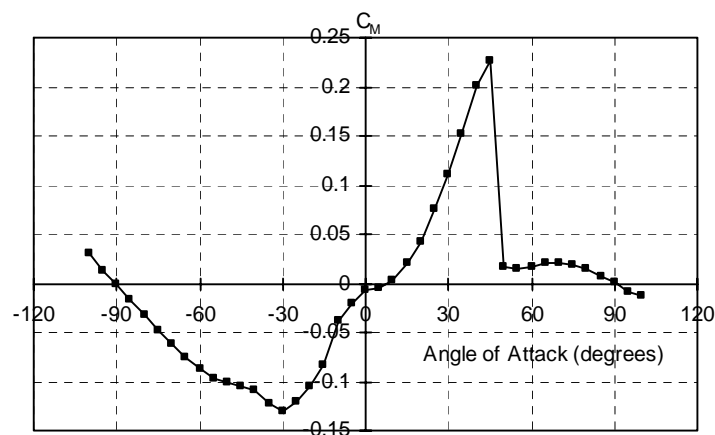
$$V_\infty = 20 \text{ m/s}, \text{Re} = 3.78 \times 10^5.$$



(a) Lift coefficient.



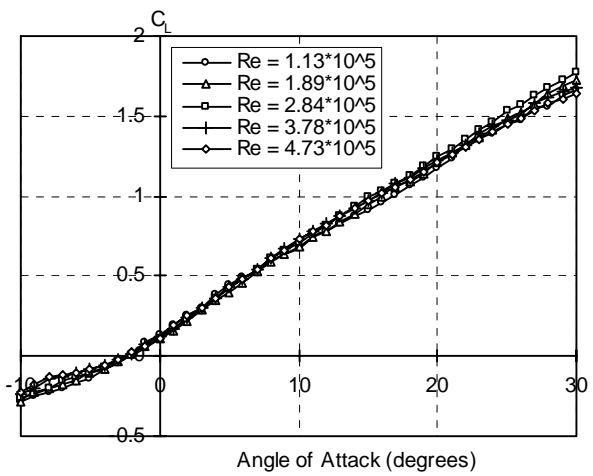
(b) Drag coefficient.



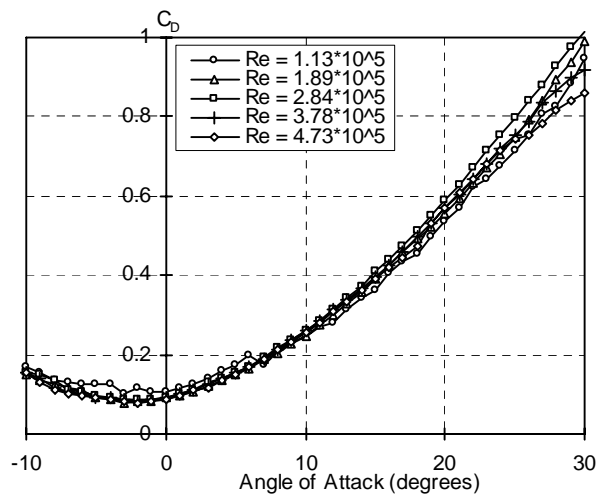
(c) Pitching moment coefficient.

Figure 5.3 Load Characteristics at zero spin rate, AoA =  $-100^\circ$  to  $100^\circ$ ,

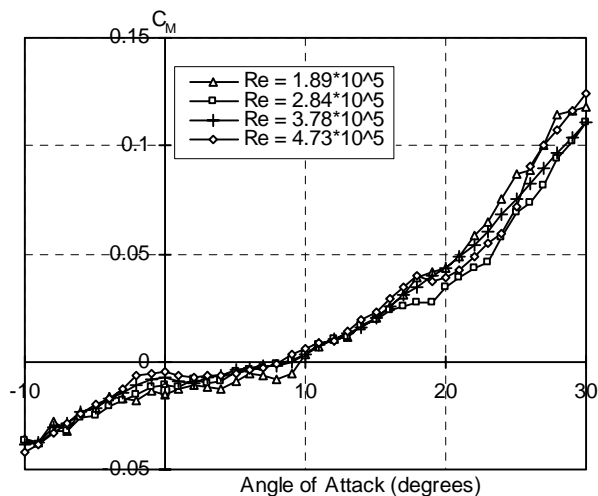
$$V_\infty = 20 \text{ m/s}, \text{Re} = 3.78 \times 10^5.$$



(a) Lift coefficient.



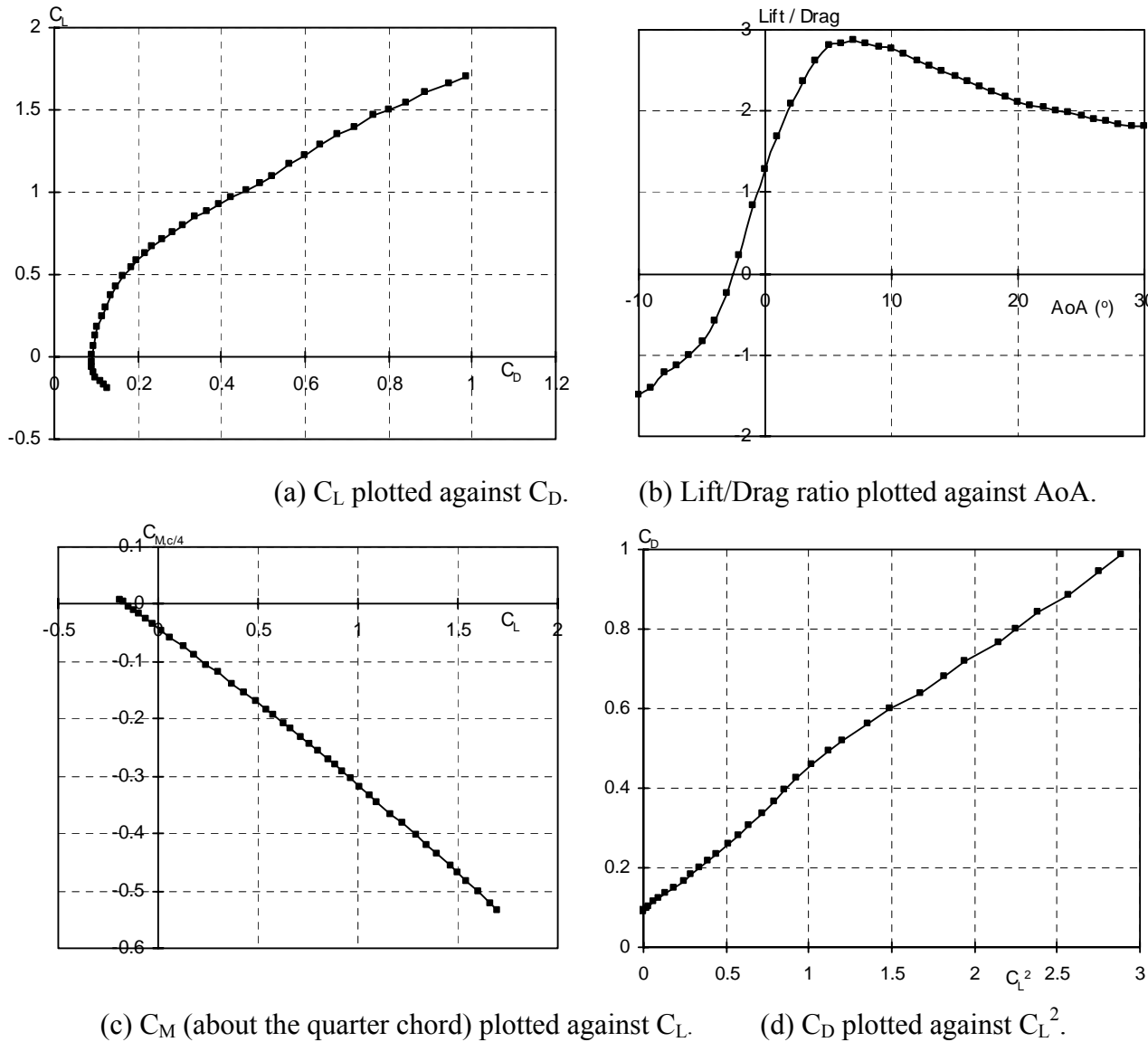
(b) Drag coefficient.

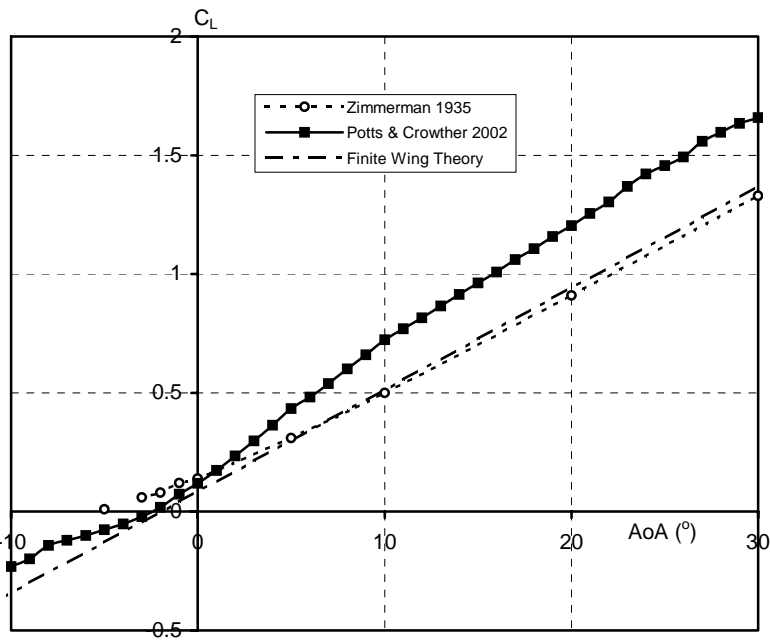


(c) Pitching moment coefficient.

Figure 5.4 Effect of Reynolds number at zero spin rate, AoA =  $-10^\circ$  to  $30^\circ$   
tunnel speed varied to achieve different Re ( $V_\infty = 6, 10, 15, 20, 25 \text{ m/s}$ ).

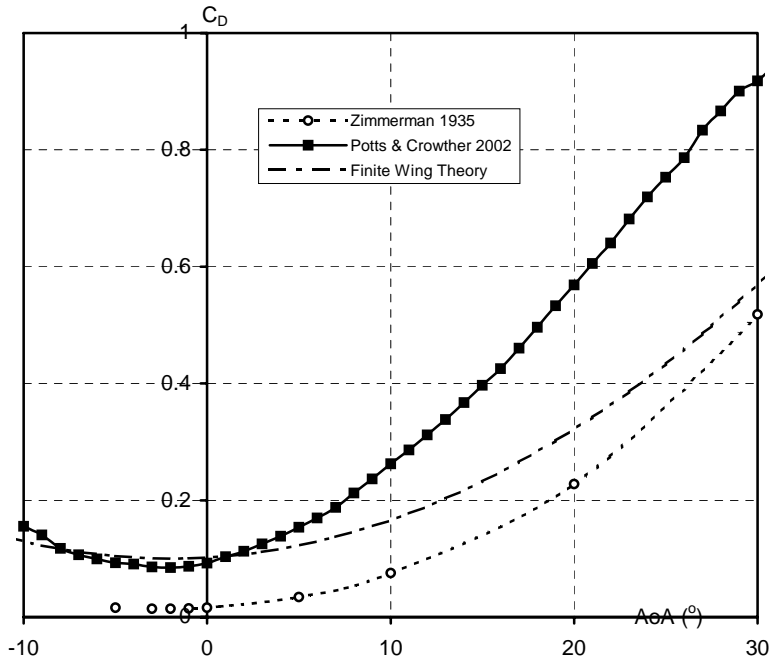
Figure 5.5 Further load characteristics at zero spin rate,  
 $\text{AoA} = -10^\circ \text{ to } 30^\circ$ ,  $V_\infty = 20 \text{ m/s}$ ,  $\text{Re} = 3.78 \times 10^5$ .





(a) Lift coefficient. Finite wing theory governed by the equation,

$$C_L = f_n(AR, e)(\alpha - \alpha_o) , \quad [AR = 4/\pi, e = 1, \alpha_o = -2^\circ].$$

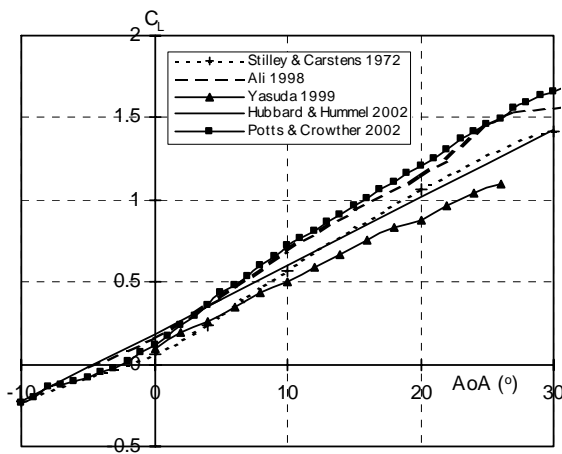


(b) Drag coefficient. Finite wing theory governed by the equation,

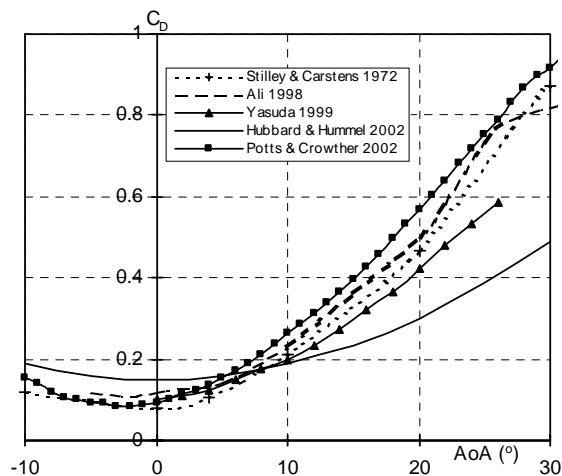
$$C_D = C_{D_0} + \frac{1}{\pi e AR} C_L^2 , \quad [C_{D_0} = 0.1, e = 1, AR = 4/\pi].$$

Figure 5.6 Comparison of the present experimental data to circular planform wings, both theoretical and experimental.

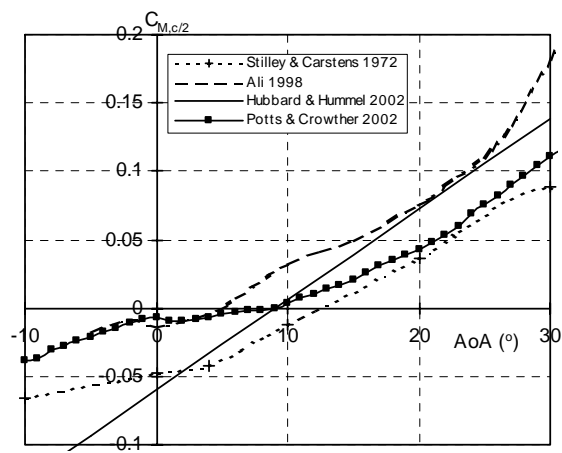




(a) Lift coefficient.



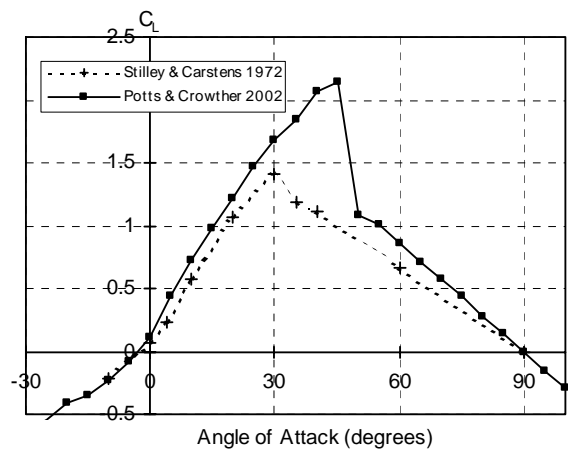
(b) Drag coefficient.



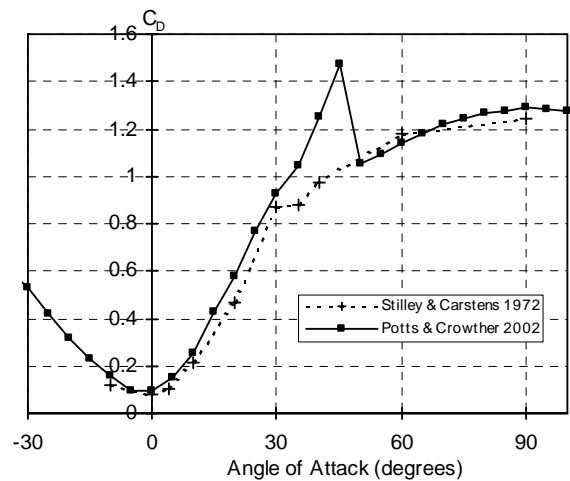
(c) Pitching moment coefficient.

Figure 5.7 Comparison of the present experimental data to Frisbee-like circular planform wings from the literature.

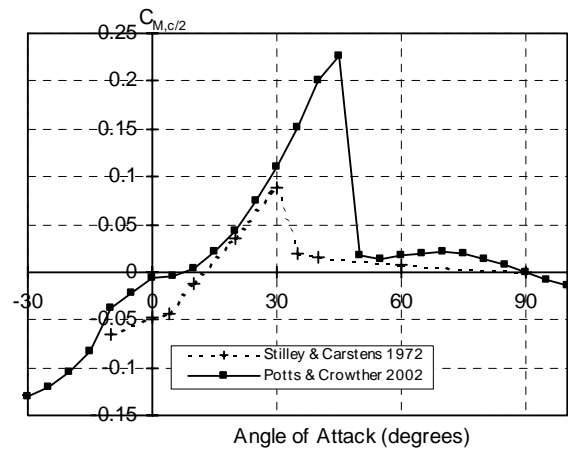




(a) Lift coefficient.



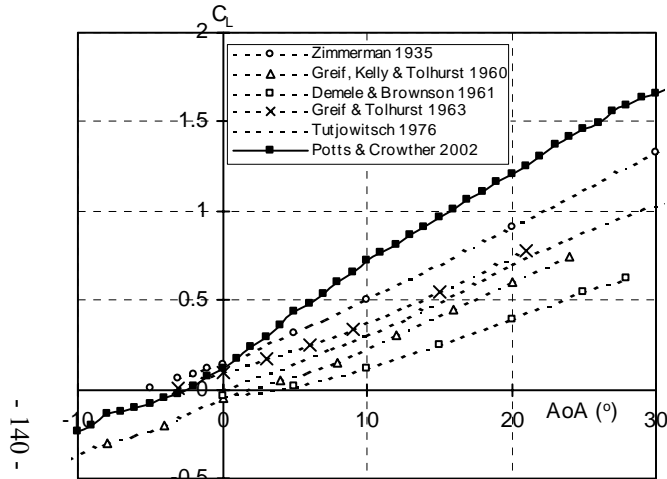
(b) Drag coefficient.



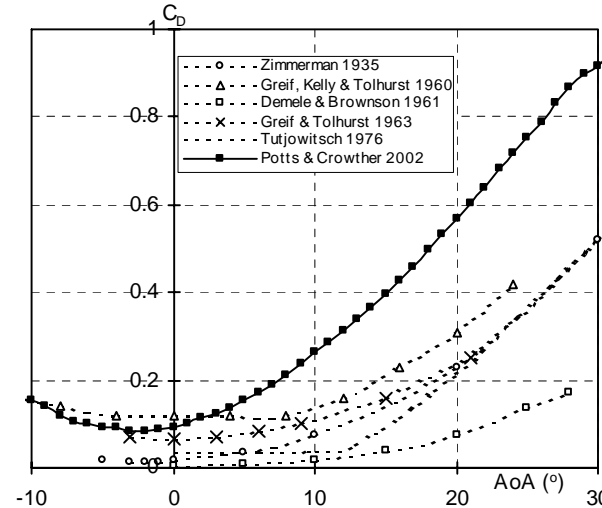
(c) Pitching moment coefficient.

Figure 5.8 Comparison of the present experimental data to a similar Frisbee-like circular planform wing.

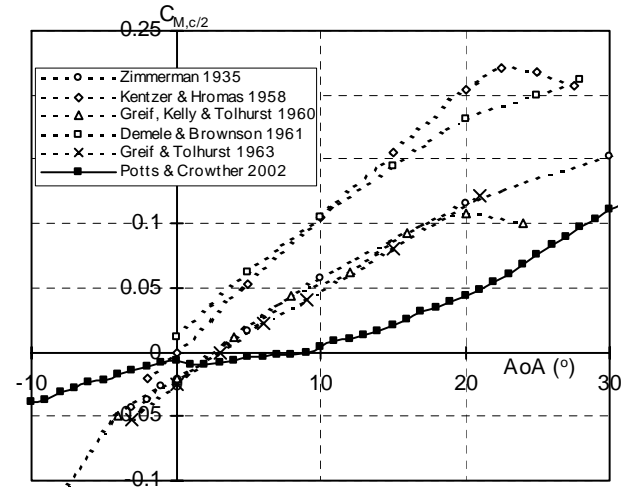




(a) Lift coefficient.

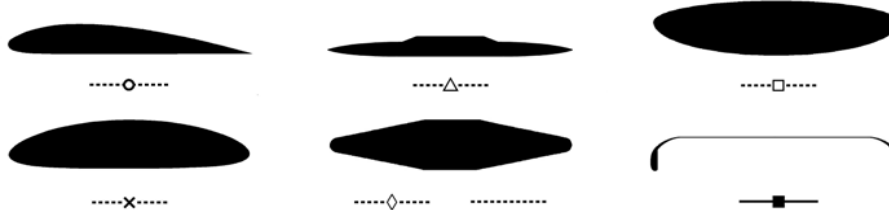


(b) Drag coefficient.



(c) Pitching moment coefficient.

Figure 5.9 Comparison of the present experimental data to a variety of circular planform wings,  
with chordwise cross-sections as seen below.



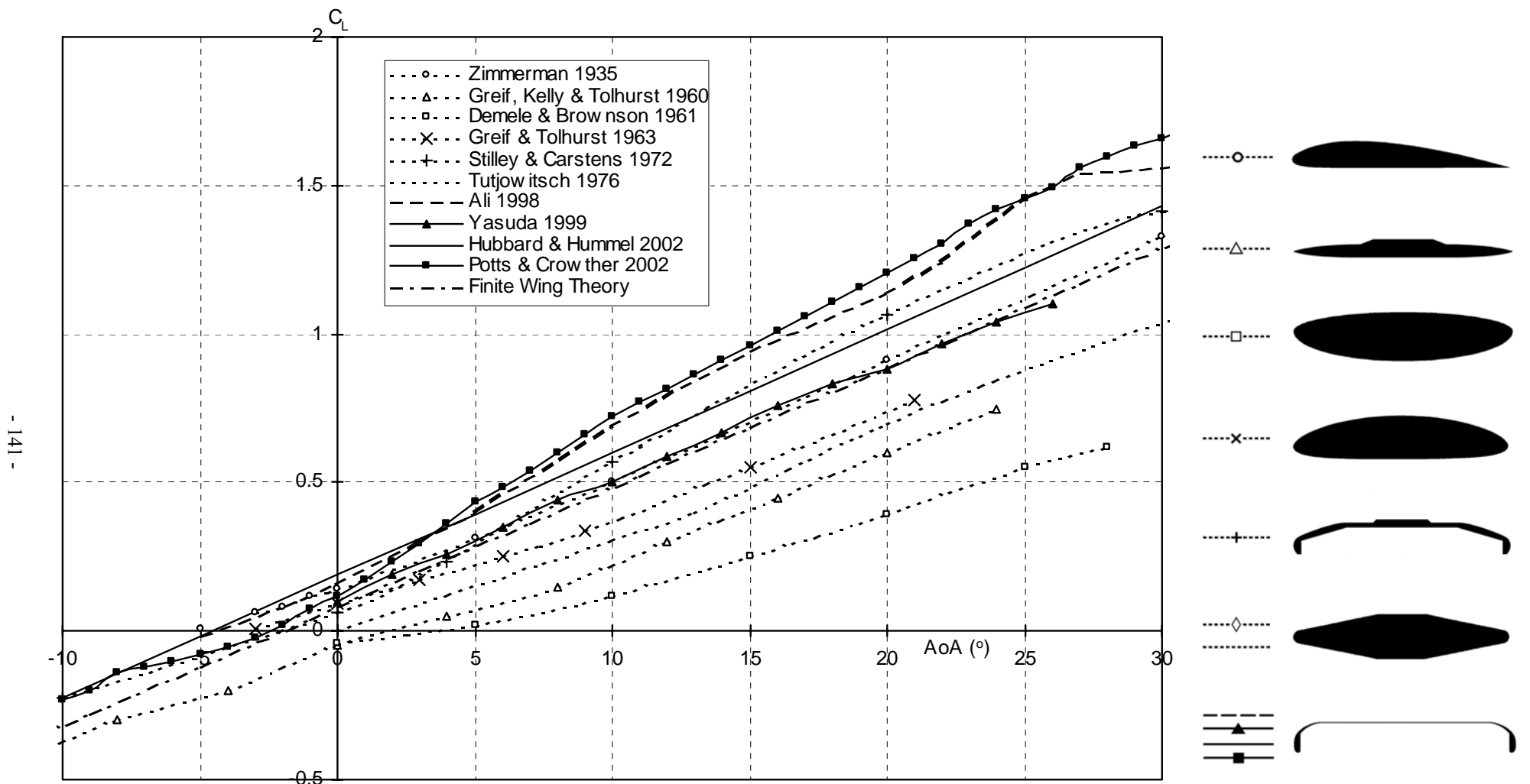


Figure 5.10 Lift coefficient: Comparison of the present experimental data to that found in the literature for similar circular planform wings, with chordwise cross-sections as seen to the right of the figure.

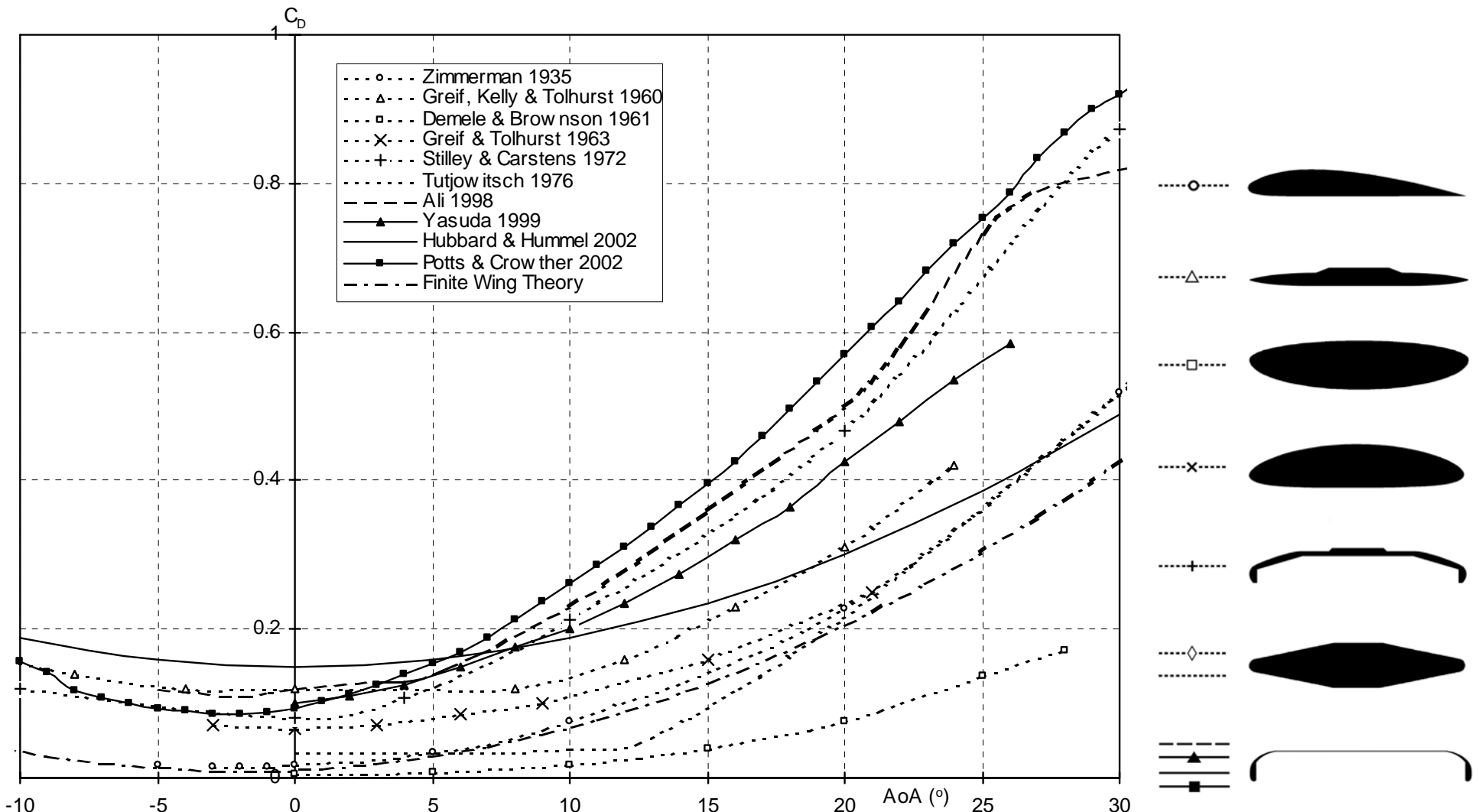


Figure 5.11 Drag coefficient: Comparison of the present experimental data to that found in the literature for similar circular planform wings, with chordwise cross-sections as seen to the right of the figure.

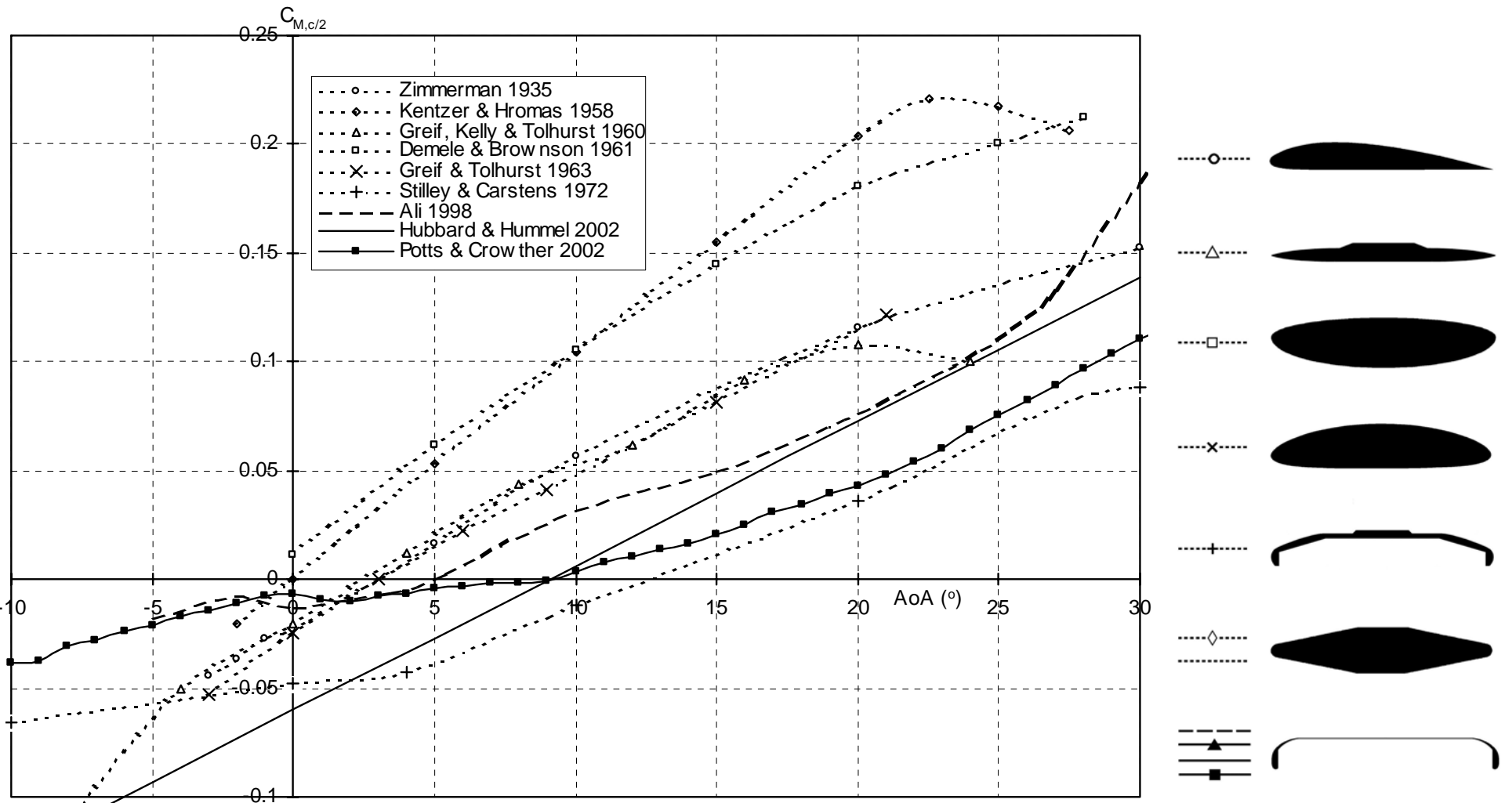
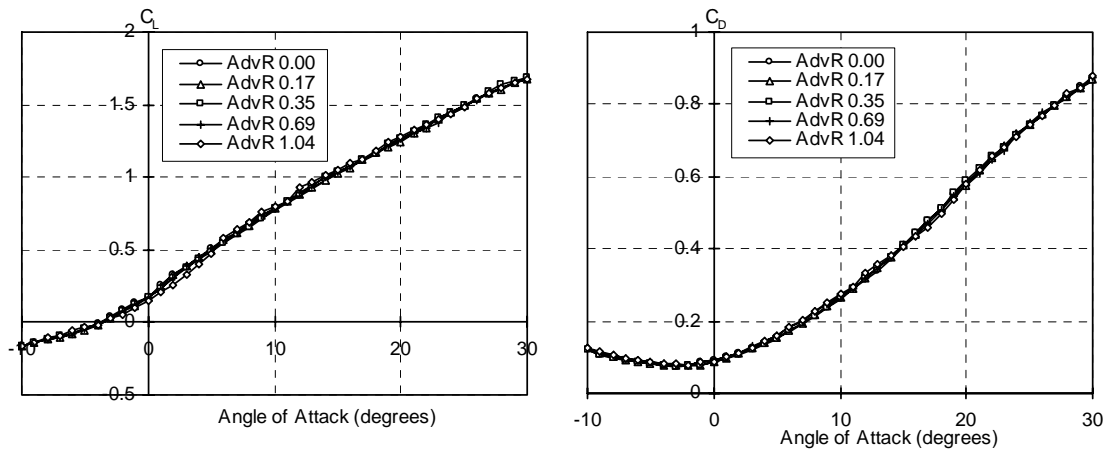
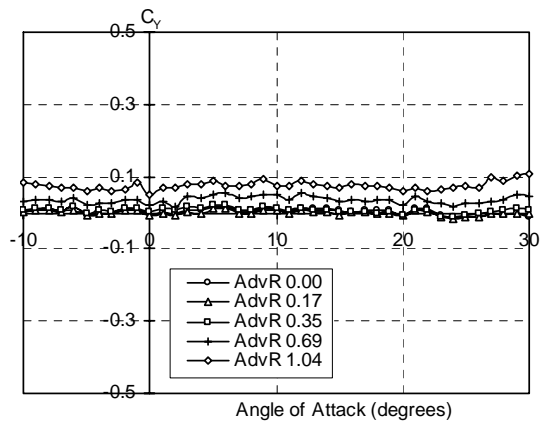


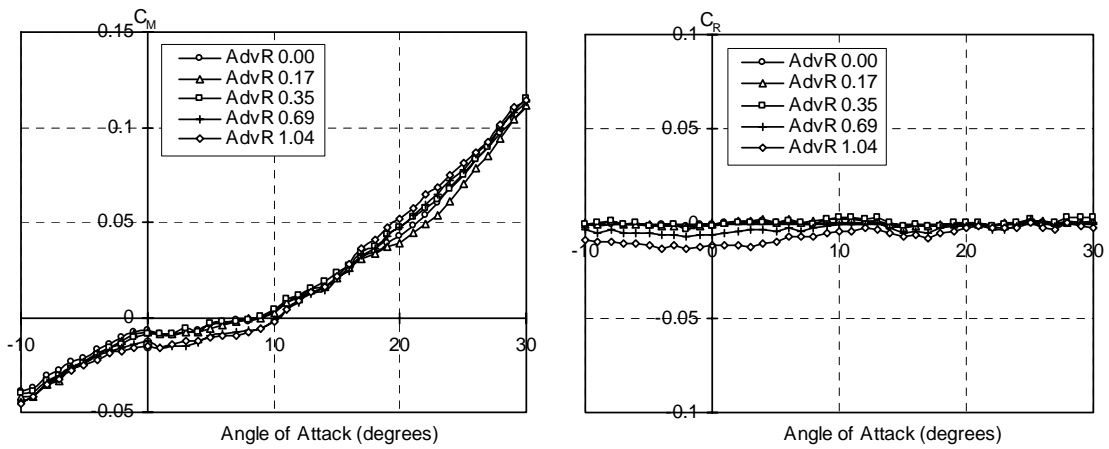
Figure 5.12 Pitching moment coefficient: Comparison of the present experimental data to that found in the literature for similar circular planform wings, with chordwise cross-sections as seen to the right of the figure.



(a) Lift coefficient. (b) Drag coefficient.

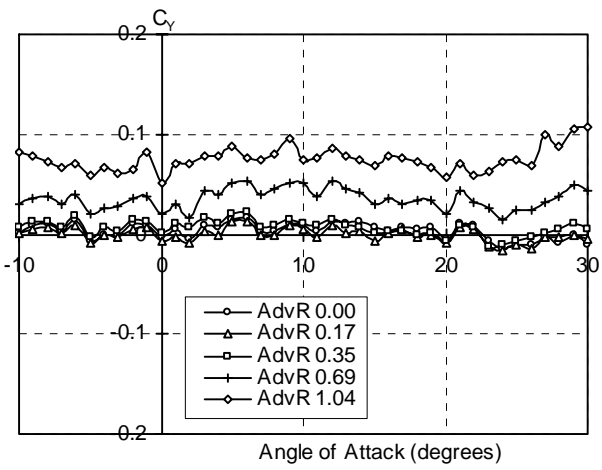


(c) Side force coefficient.

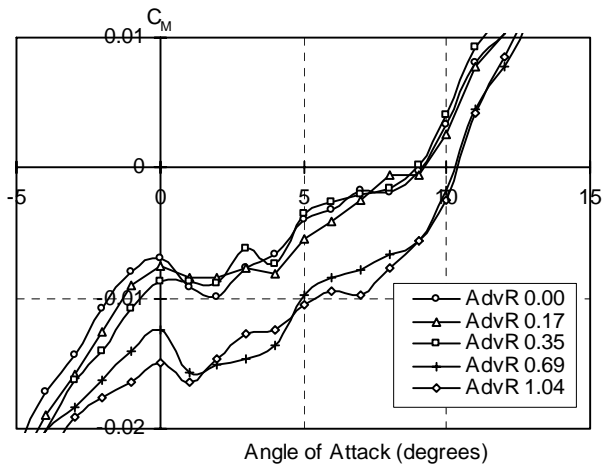


(d) Pitching moment coefficient. (e) Rolling moment coefficient.

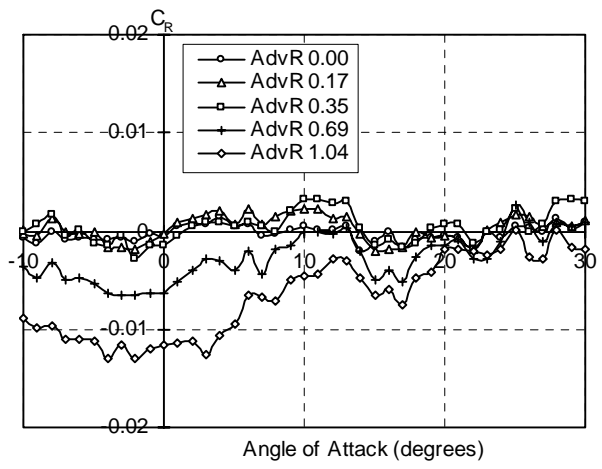
Figure 5.13 Load characteristics at various advance ratios,  
 $\text{AdvR} = 0 \text{ to } 1$ ,  $\text{AoA} = -10^\circ \text{ to } 30^\circ$ ,  $V_\infty = 20 \text{ m/s}$ ,  $\text{Re} = 3.78 \times 10^5$ .



(a) Side force coefficient.



(b) Pitching moment coefficient



(c) Rolling moment coefficient.

Figure 5.14 Load characteristics (detail) at various advance ratios,  
 $\text{AdvR} = 0 \text{ to } 1$ ,  $\text{AoA} = -10^\circ \text{ to } 30^\circ$ ,  $V_\infty = 20 \text{ m/s}$ ,  $\text{Re} = 3.78 \times 10^5$ .

Figure 5.15 Effect of spin on the Lift Coefficient: Comparison set of spin rates (0, 4, 8, 16, 24Hz) tested at various flow speeds ( $V_\infty = 6, 10, 15, 20\text{m/s}$ ),  $\text{AoA} = -10^\circ$  to  $30^\circ$ .

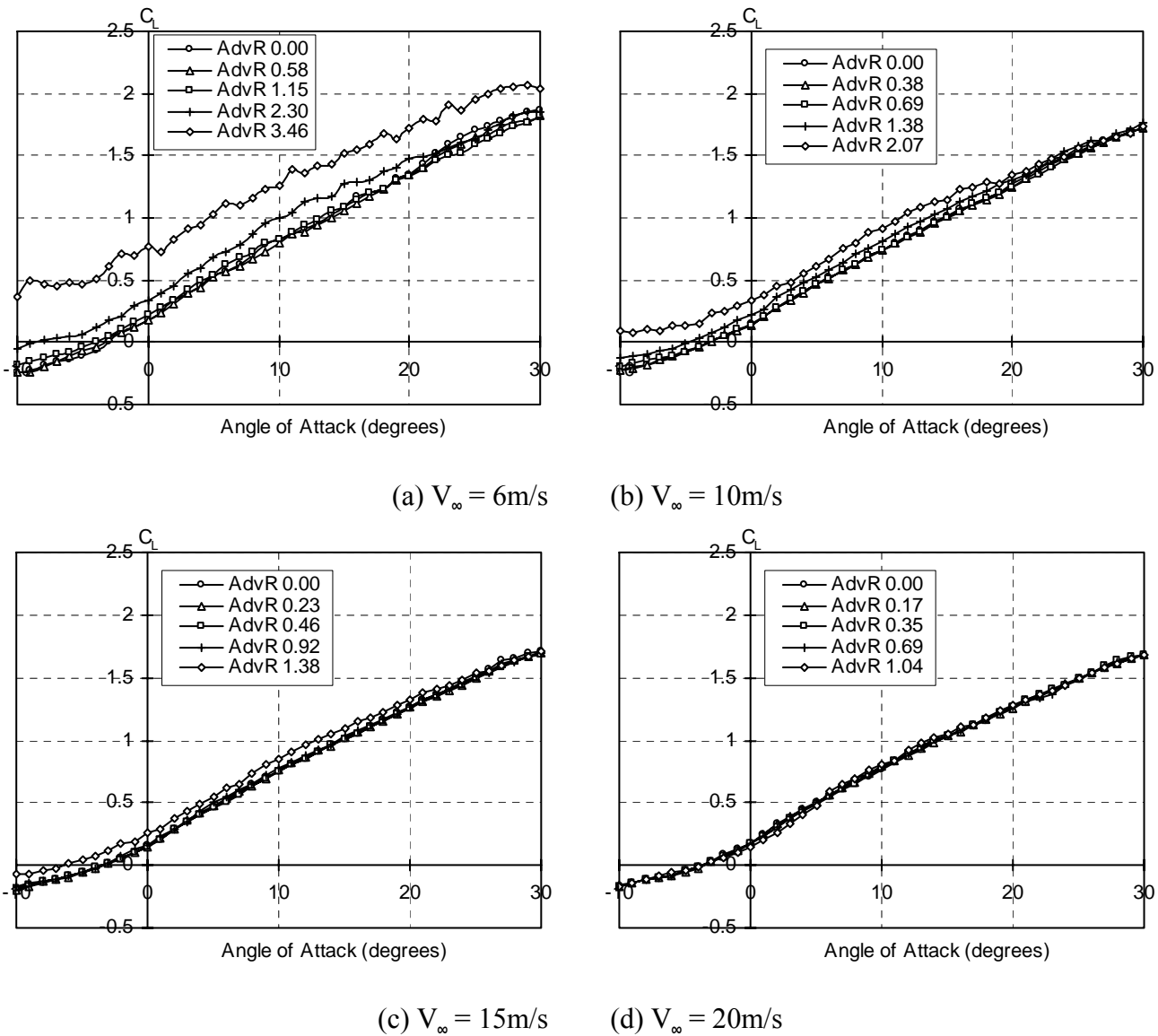


Figure 5.16 Effect of spin on the Drag Coefficient: Comparison set of spin rates (0, 4, 8, 16, 24Hz) tested at various flow speeds ( $V_\infty = 6, 10, 15, 20$ m/s), AoA =  $-10^\circ$  to  $30^\circ$ .

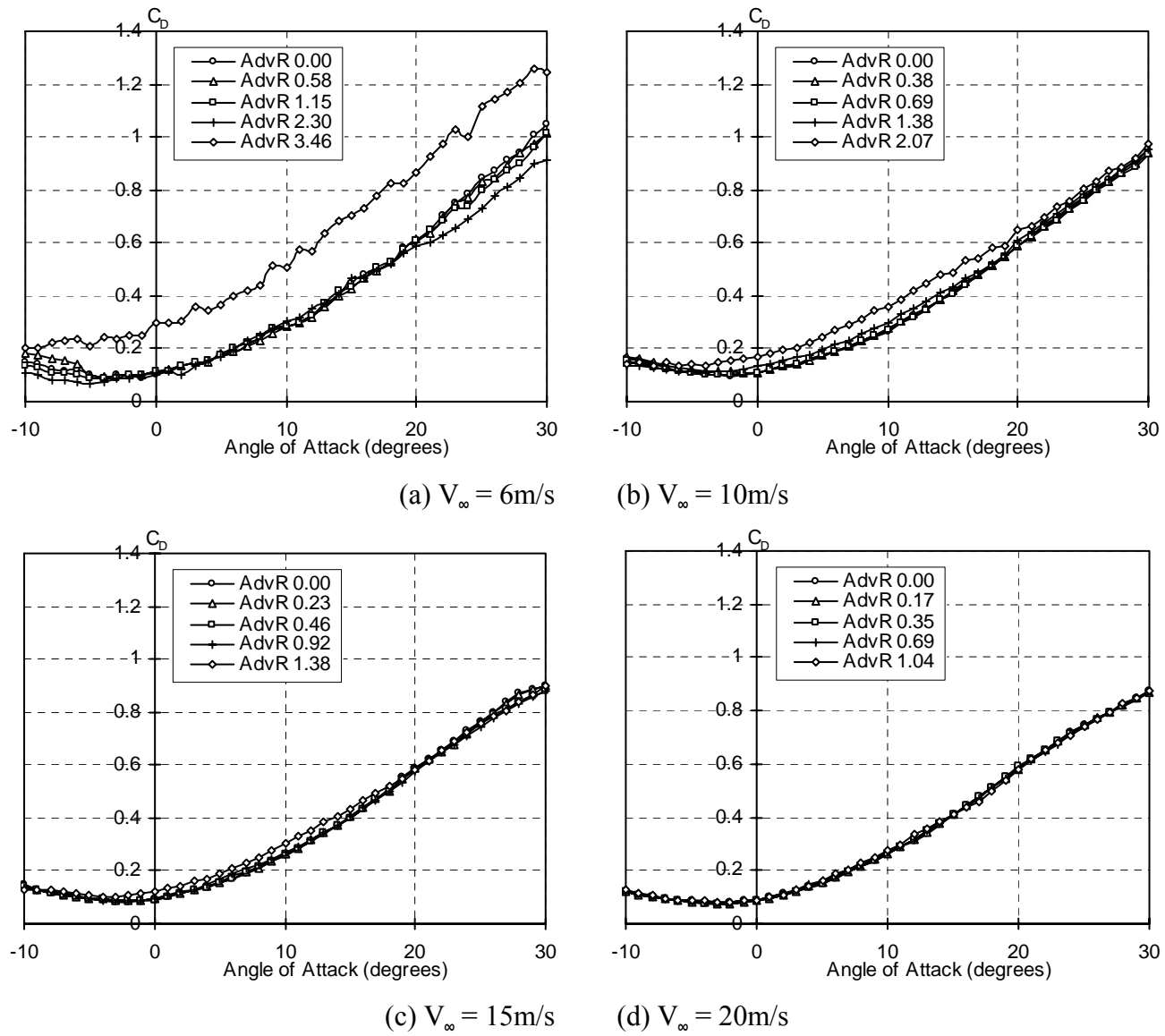


Figure 5.17 Effect of spin on the Side Force Coefficient: Comparison set of spin rates (0, 4, 8, 16, 24Hz) tested at various flow speeds ( $V_\infty = 6, 10, 15, 20$ m/s), AoA =  $-10^\circ$  to  $30^\circ$ .

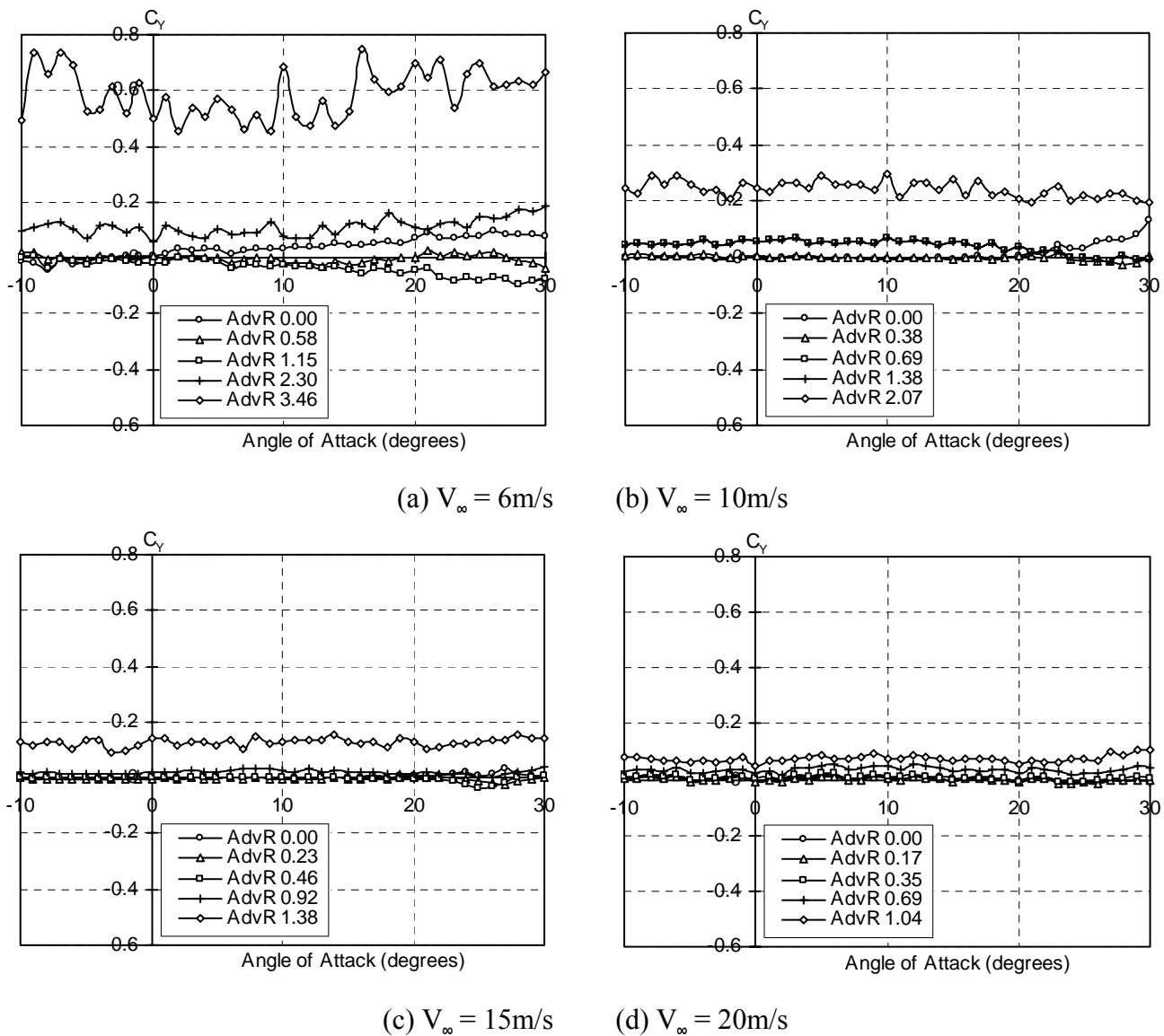


Figure 5.18 Effect of spin on the Pitching Moment Coefficient:  
 Comparison set of spin rates (0, 4, 8, 16, 24Hz) tested at various  
 flow speeds ( $V_\infty = 6, 10, 15, 20$ m/s), AoA =  $-10^\circ$  to  $30^\circ$ .

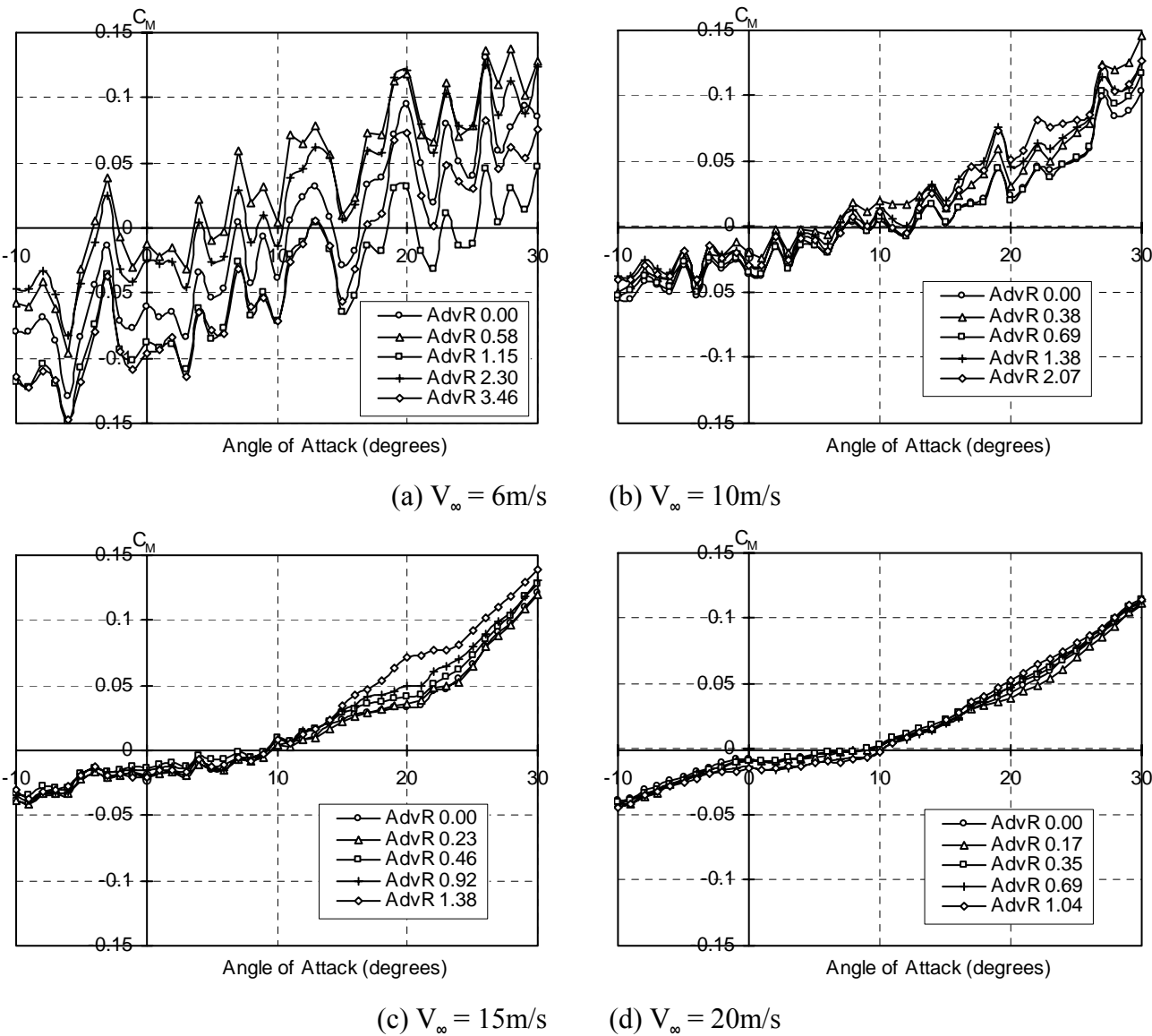
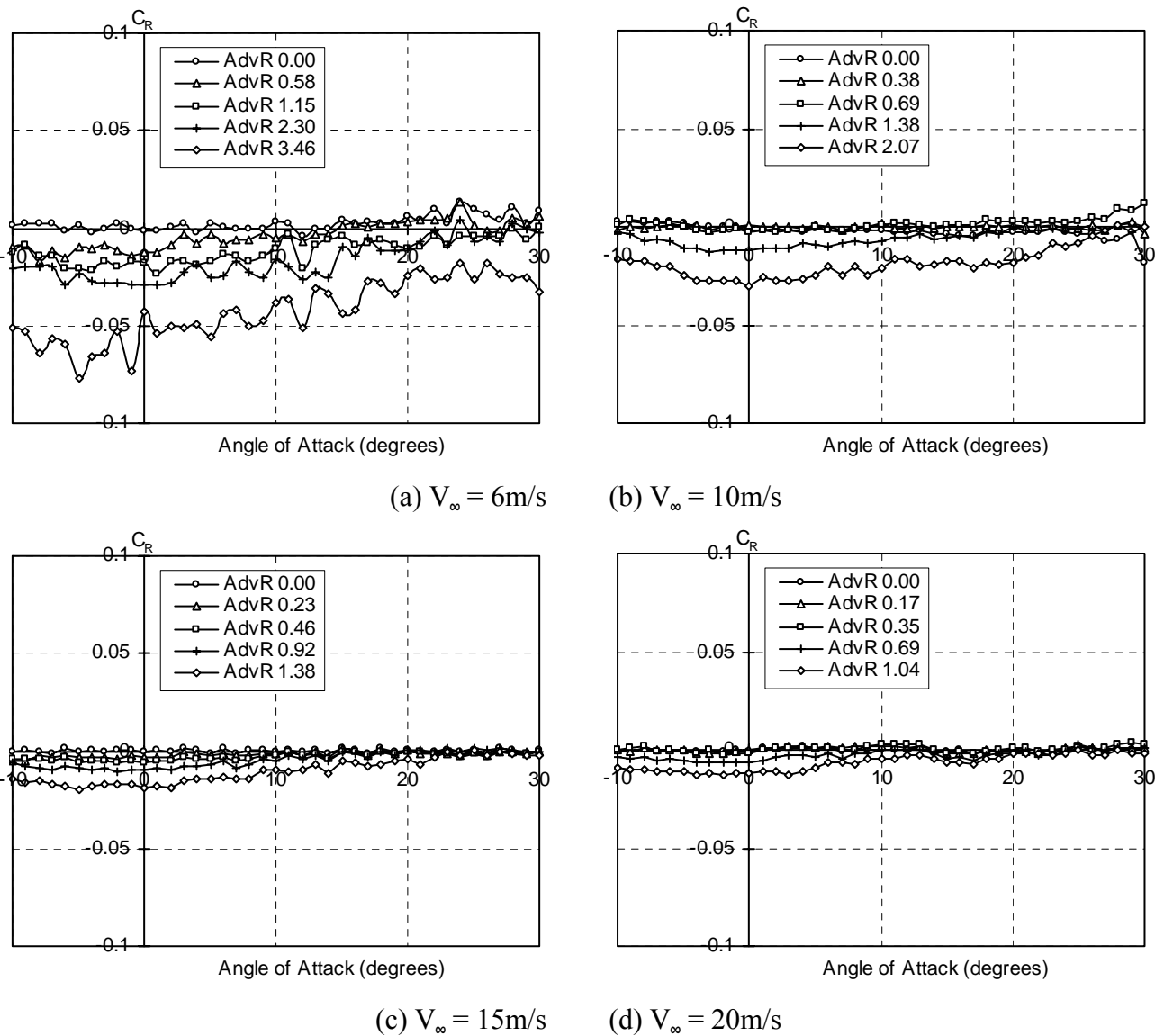


Figure 5.19 Effect of spin on the Rolling Moment Coefficient:  
 Comparison set of spin rates (0, 4, 8, 16, 24Hz) tested at various  
 flow speeds ( $V_{\infty} = 6, 10, 15, 20$ m/s), AoA =  $-10^{\circ}$  to  $30^{\circ}$ .



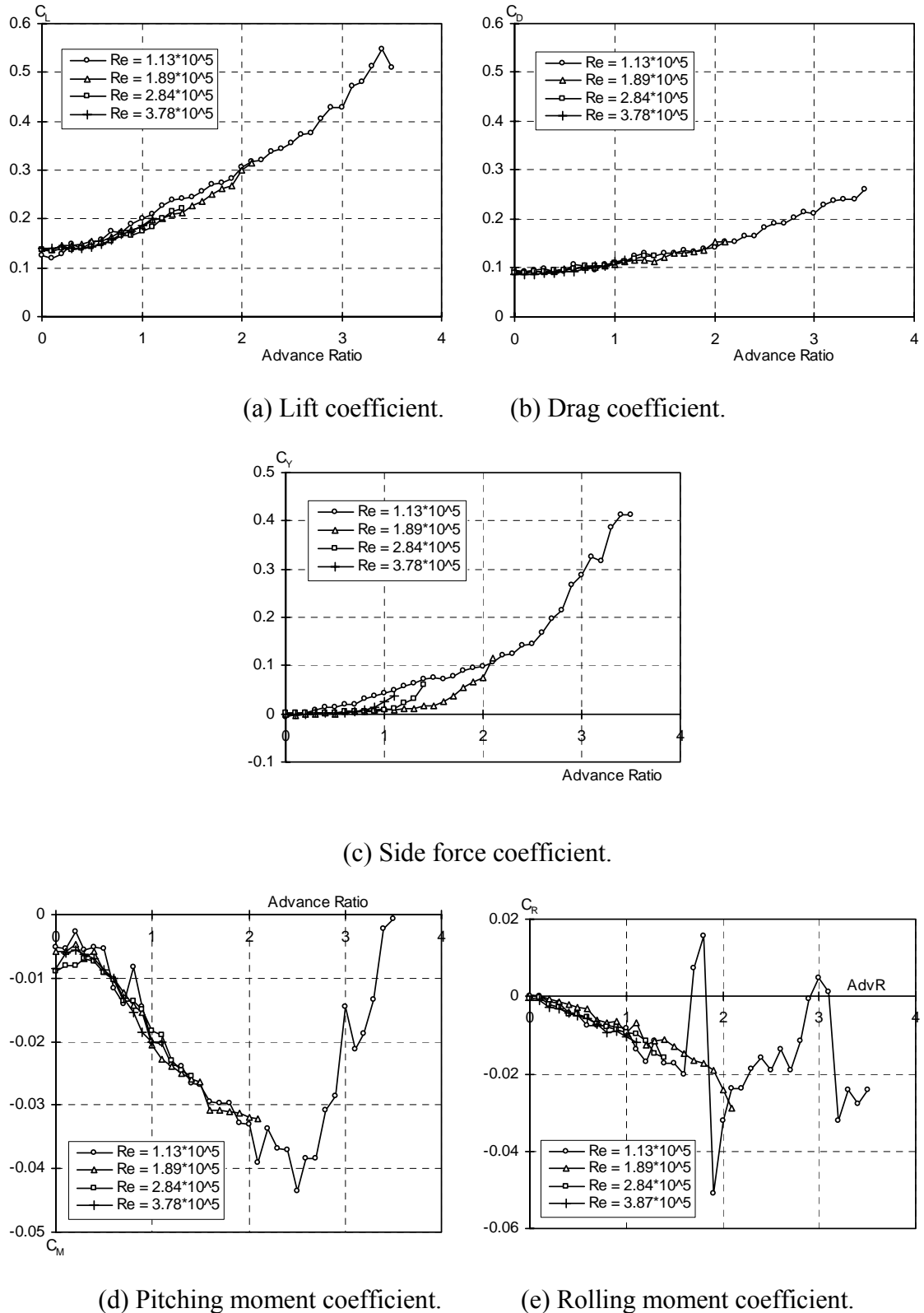
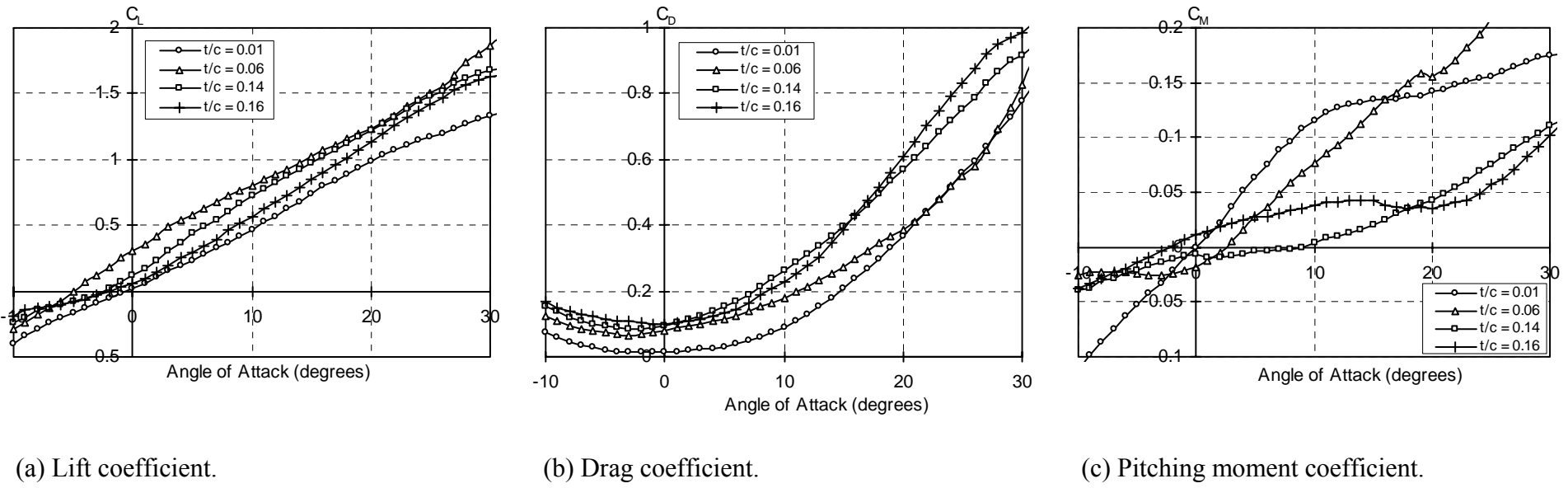


Figure 5.20 Effect of Advance Ratio at  $0^\circ$  AoA for various Reynolds numbers, tunnel speed varied to achieve different  $Re$  ( $V_\infty = 6, 10, 15, 20),  
 AdvR = 0 up to 3.5, each curve utilises a consistent range of spin rates (0 to 31Hz).$

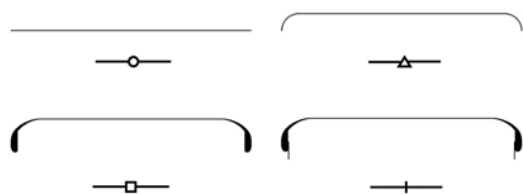


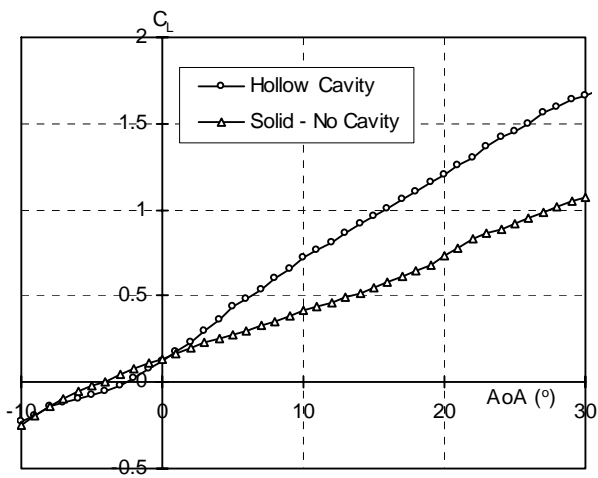
(a) Lift coefficient.

(b) Drag coefficient.

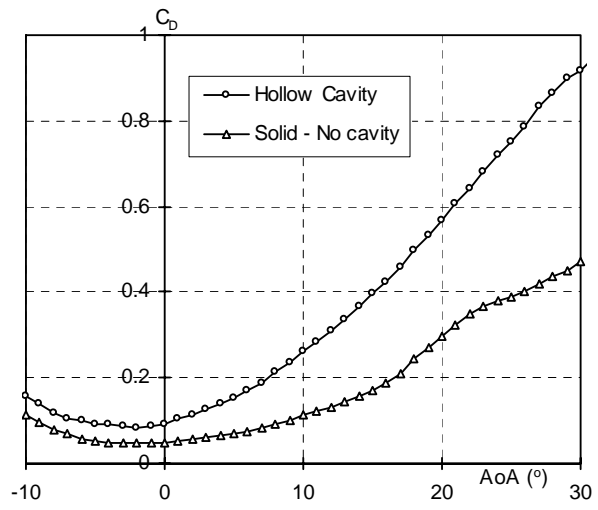
(c) Pitching moment coefficient.

Figure 5.21 Comparison of disc-wings with various thicknesses achieved by modifying the rim height to increase the cavity depth, with chordwise cross-sections as seen below,  $t_h / c = 0.01$  to 0.16.

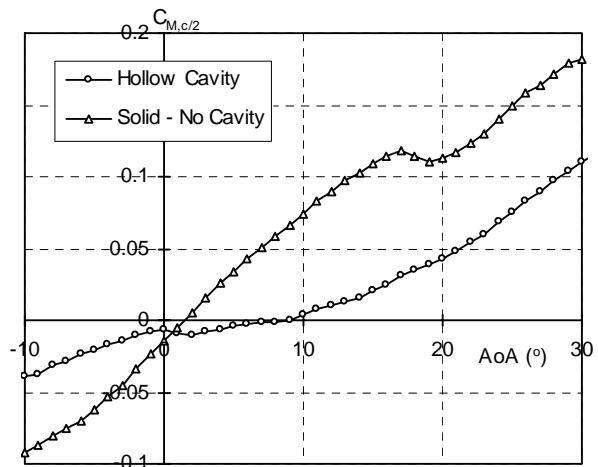




(a) Lift coefficient.



(b) Drag coefficient.



(c) Pitching moment coefficient.

Figure 5.22 Comparison of the baseline (hollow) Frisbee configuration to a cavity filled (solid) disc-wing geometry.



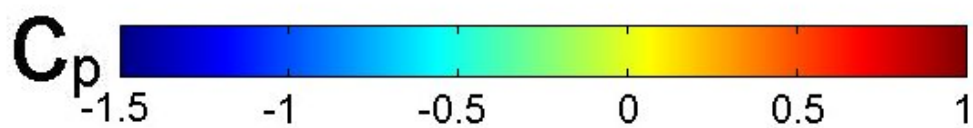
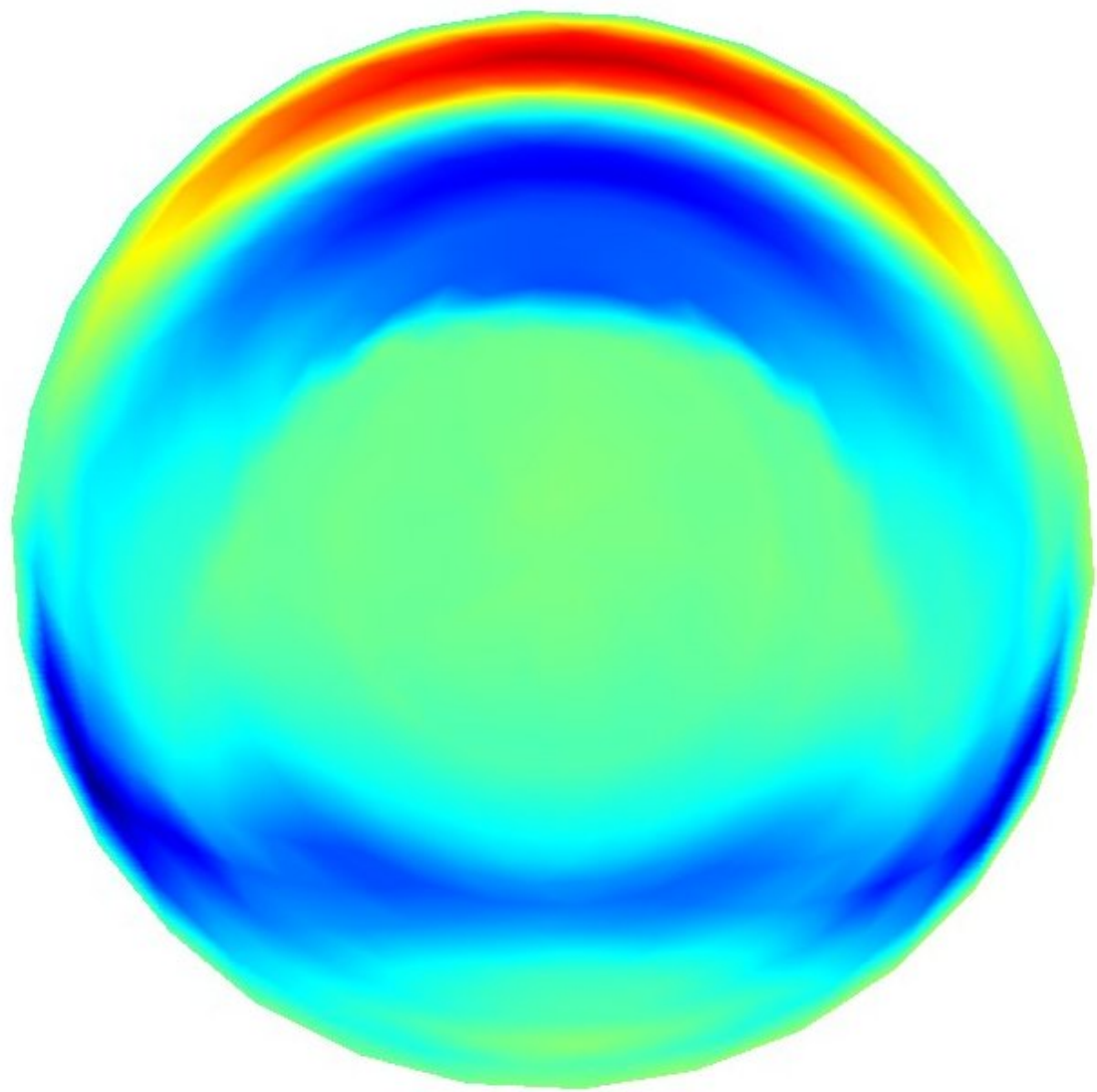


Figure 5.23 2D flat surface colour weighted contour plot of pressure coefficients  $C_p$  derived from measurements of the 3D upper surface pressure distribution of a non-spinning disc-wing, taken over the entire surface, not over half the disc and mirrored to the other side, flow direction from top to bottom,  
 $AoA = 5^\circ$ ,  $V_\infty = 15\text{m/s}$ ,  $Re = 2.84 \times 10^5$ .

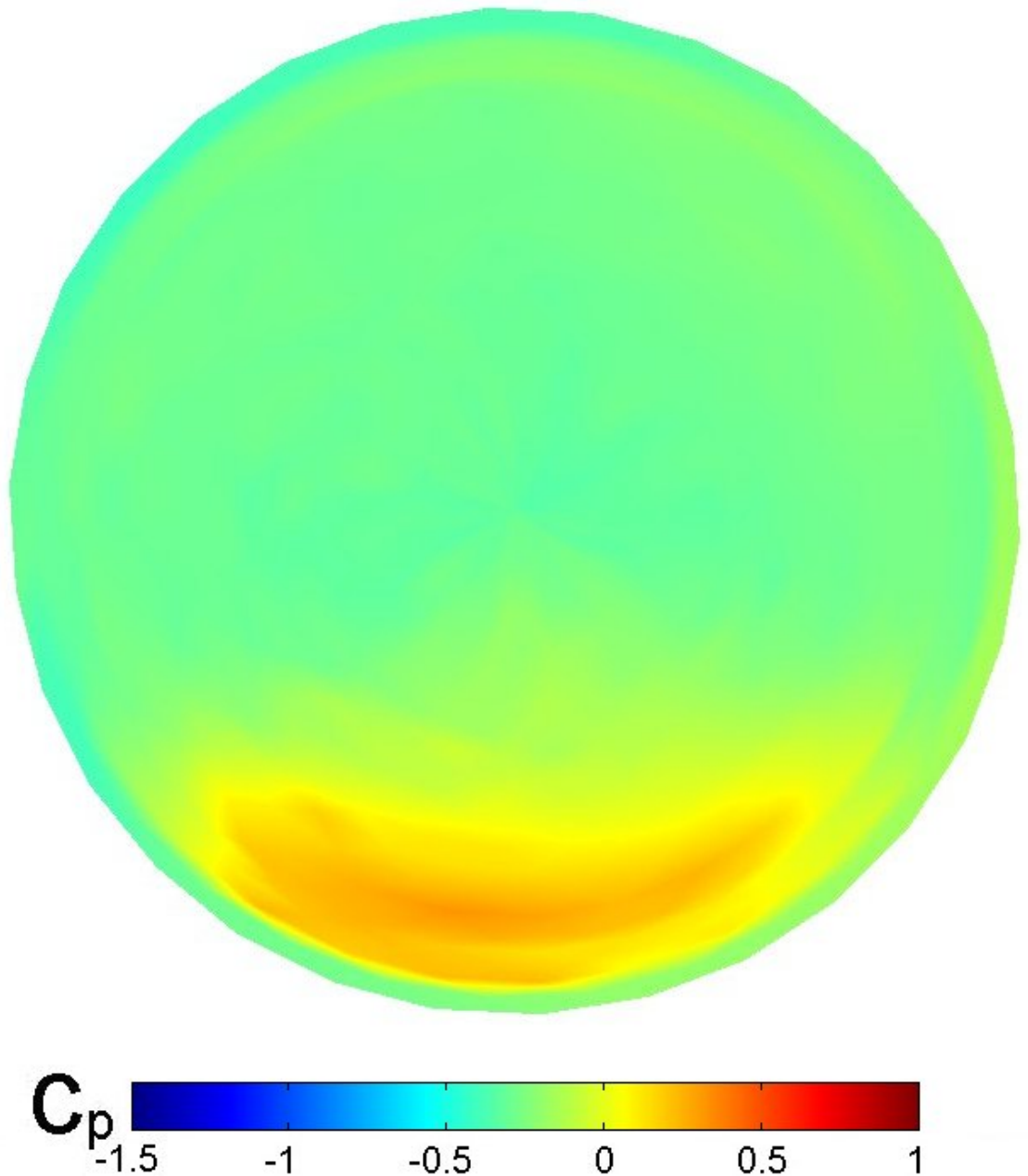


Figure 5.24 2D flat surface colour weighted contour plot of pressure coefficients  $C_p$  derived from measurements of the 3D cavity surface pressure distribution of a non-spinning disc-wing, taken over the entire surface, not over half the disc and mirrored to the other side, flow direction from top to bottom,  $\text{AoA} = 5^\circ$ ,  $V_\infty = 15 \text{ m/s}$ ,  $\text{Re} = 2.84 \times 10^5$ .

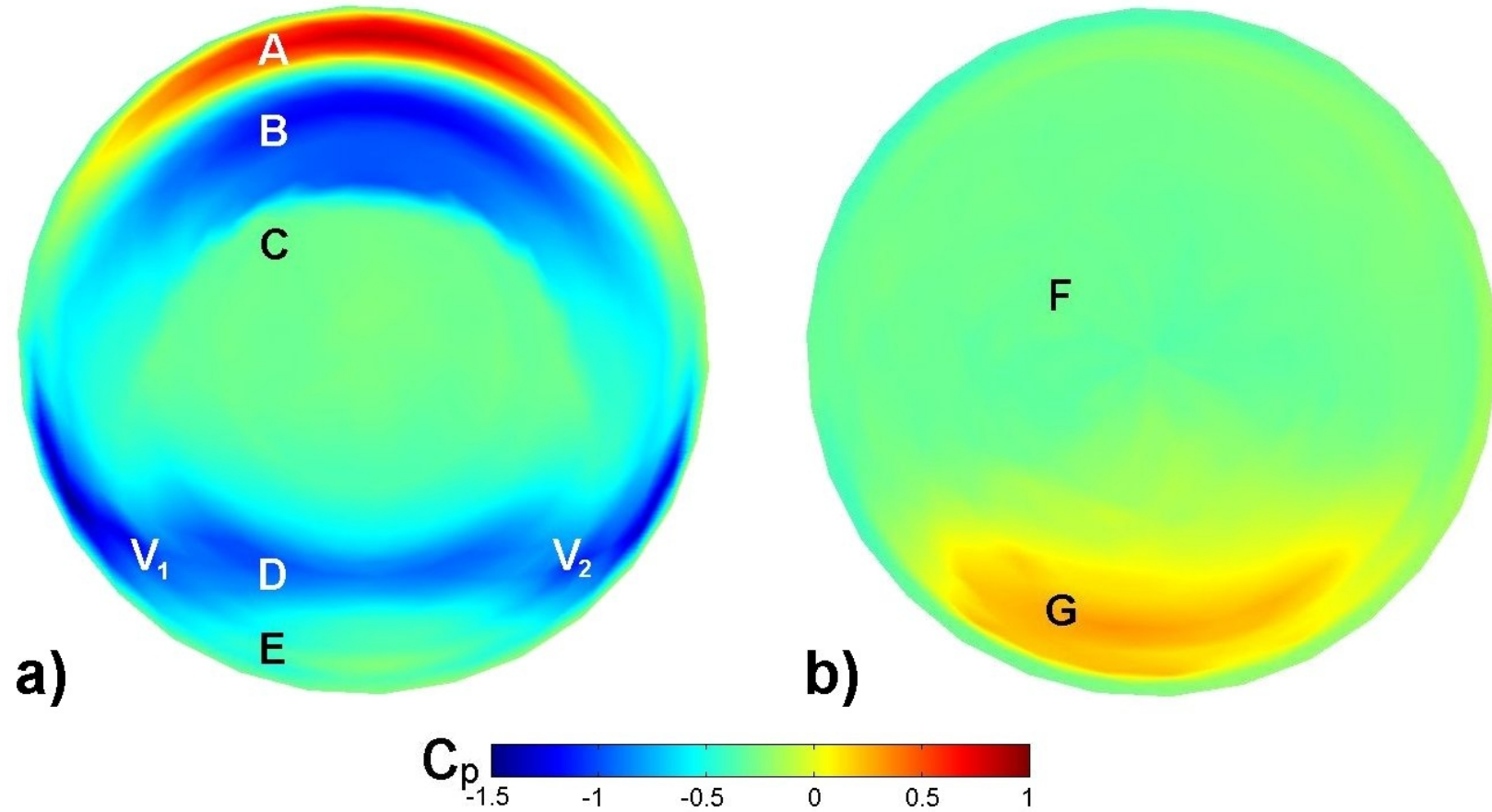


Figure 5.25 2D flat surface colour weighted contour plot of pressure coefficients  $C_p$  derived from measurements of the 3D upper (a) & cavity (b) surface pressure distribution of a non-spinning disc-wing, taken over the entire surface, not over half the disc and mirrored to the other side, flow direction from top to bottom, AoA = 5°,  $V_\infty = 15\text{m/s}$ ,  $\text{Re} = 2.84 \times 10^5$ .

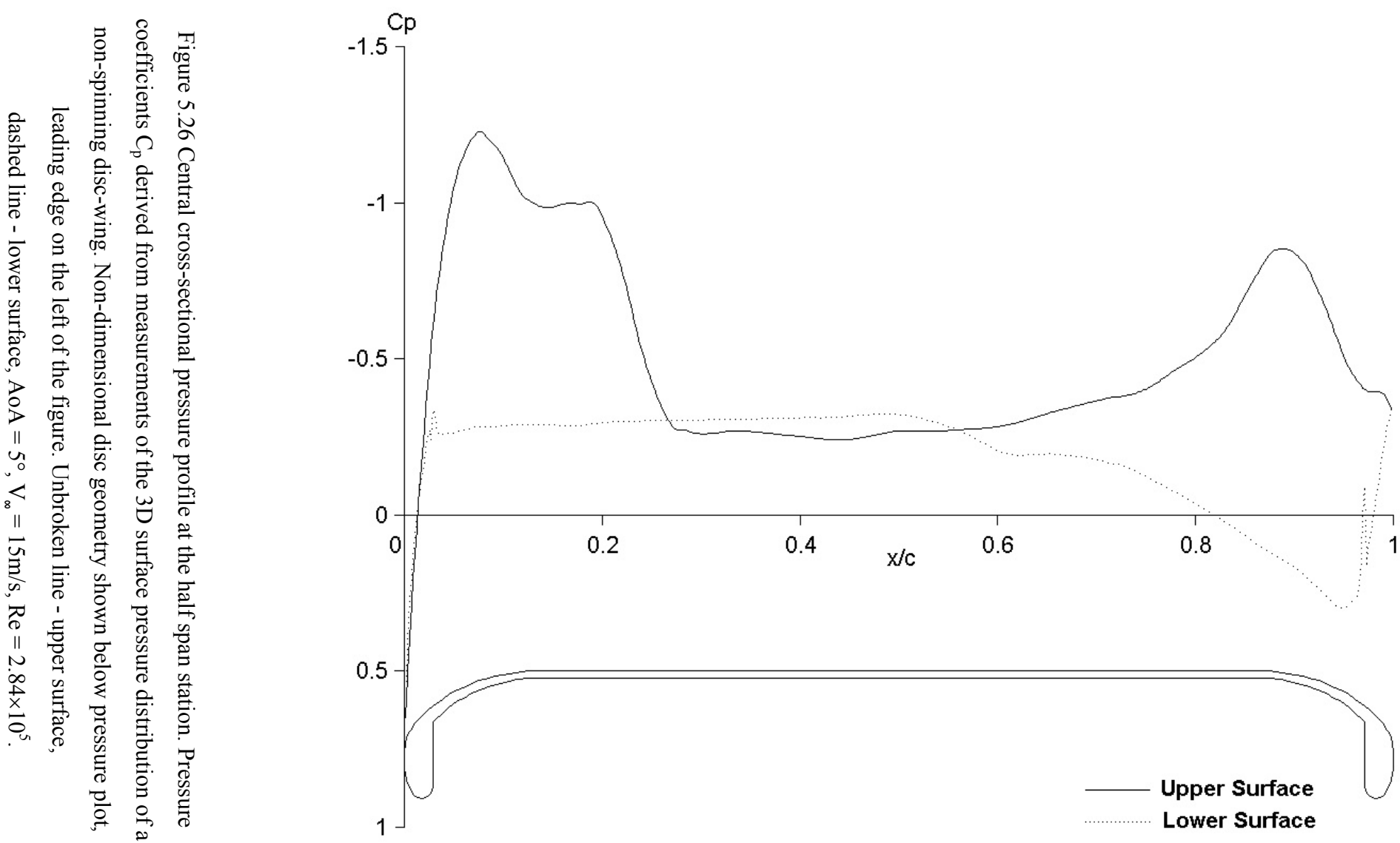


Figure 5.26 Central cross-sectional pressure profile at the half span station. Pressure coefficients  $C_p$  derived from measurements of the 3D surface pressure distribution of a non-spinning disc-wing. Non-dimensional disc geometry shown below pressure plot, leading edge on the left of the figure. Unbroken line - upper surface,

dashed line - lower surface, AoA = 5°,  $V_\infty = 15\text{m/s}$ ,  $\text{Re} = 2.84 \times 10^5$ .

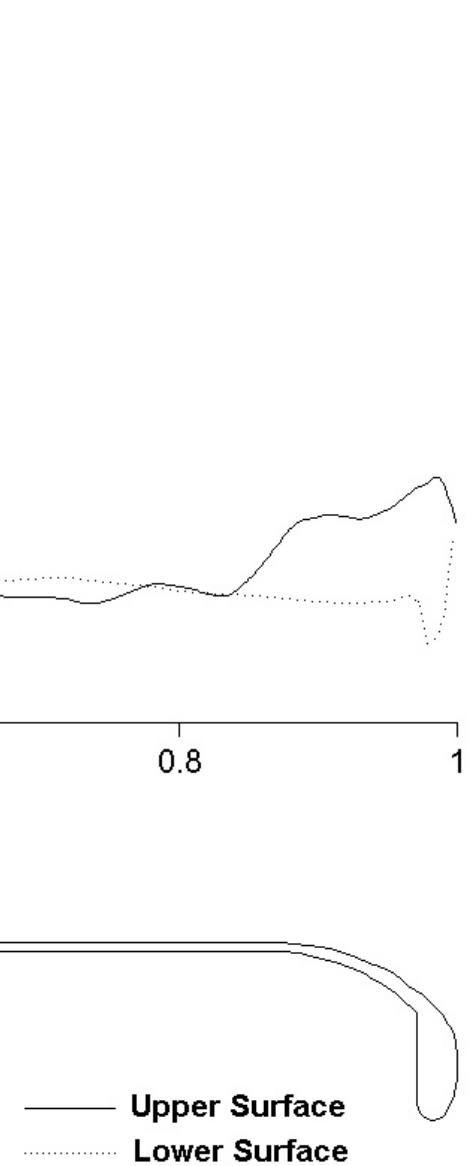


Figure 5.27 Central cross-sectional pressure profile at the half chord station, pressure coefficients  $C_p$  derived from measurements of the 3D surface pressure distribution of a non-spinning disc-wing. Non-dimensional disc geometry shown below pressure plot, port wing tip on the left of the figure. Unbroken line - upper surface,

dashed line - lower surface, AoA = 5°,  $V_\infty = 15\text{m/s}$ ,  $\text{Re} = 2.84 \times 10^5$ .

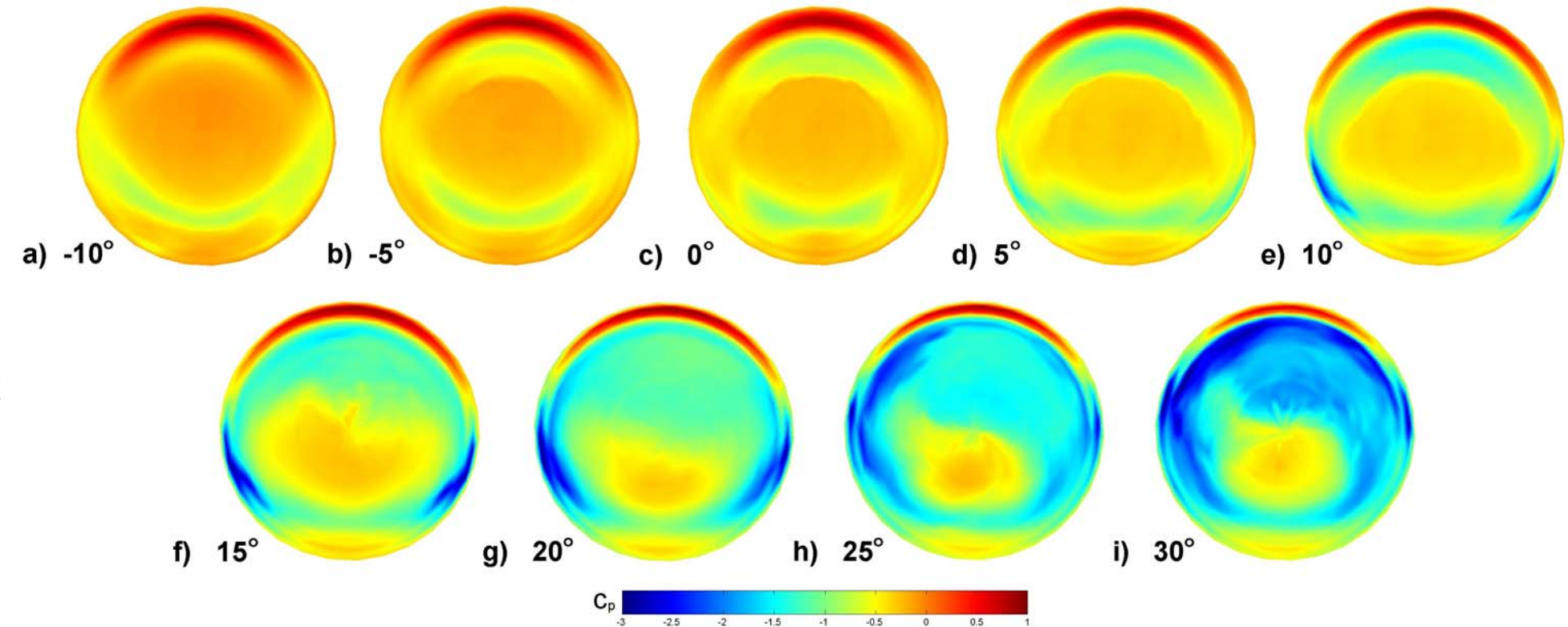


Figure 5.28 2D flat surface colour weighted contour plots of pressure coefficients  $C_p$  for a range of AoA, derived from measurements of the 3D upper surface pressure distribution of a non-spinning disc-wing, taken over the entire surface, not over half the disc and mirrored to the other side, flow direction from top to bottom, AoA =  $-10^\circ$  to  $30^\circ$ ,  $V_\infty = 20\text{m/s}$ ,  $\text{Re} = 3.78 \times 10^5$ .

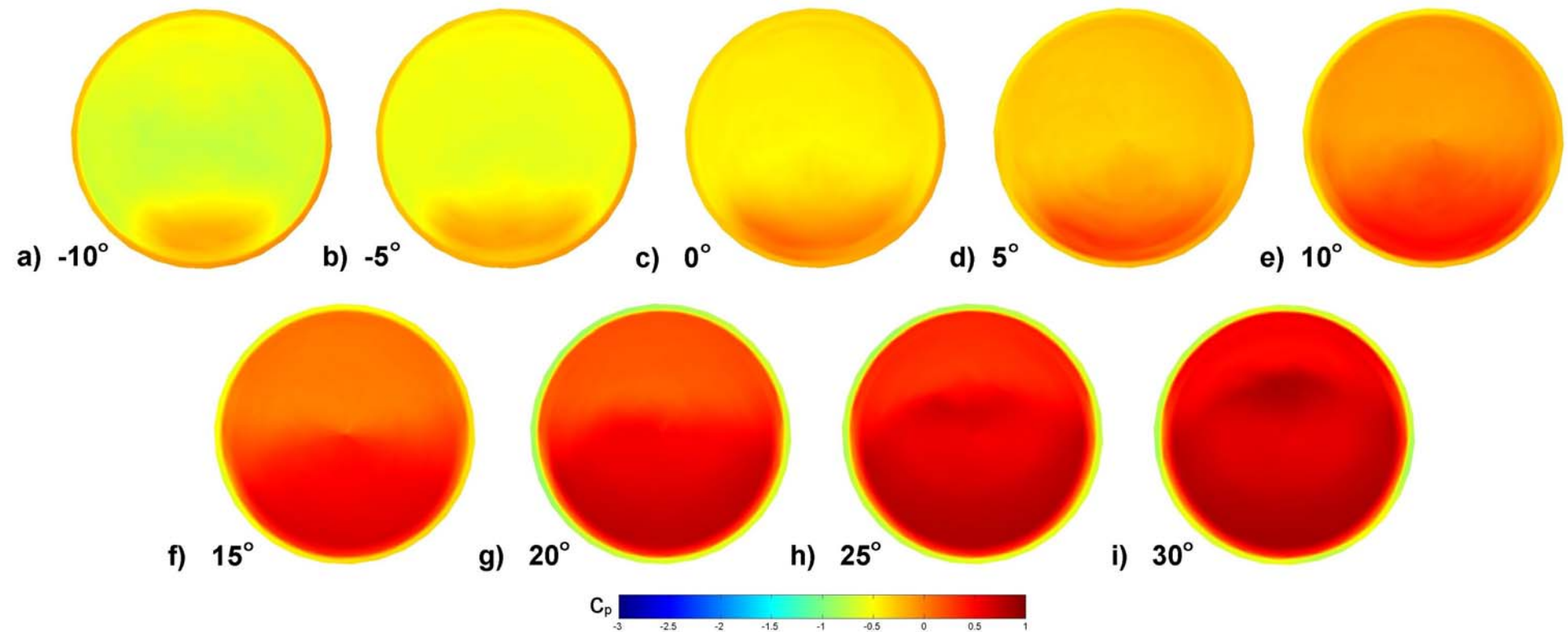


Figure 5.29 2D flat surface colour weighted contour plots of pressure coefficients  $C_p$  for a range of AoA, derived from measurements of the 3D cavity surface pressure distribution of a non-spinning disc-wing, taken over the entire surface, not over half the disc and mirrored to the other side, flow direction from top to bottom, AoA =  $-10^\circ$  to  $30^\circ$ ,  $V_\infty = 20\text{m/s}$ ,  $\text{Re} = 3.78 \times 10^5$ .

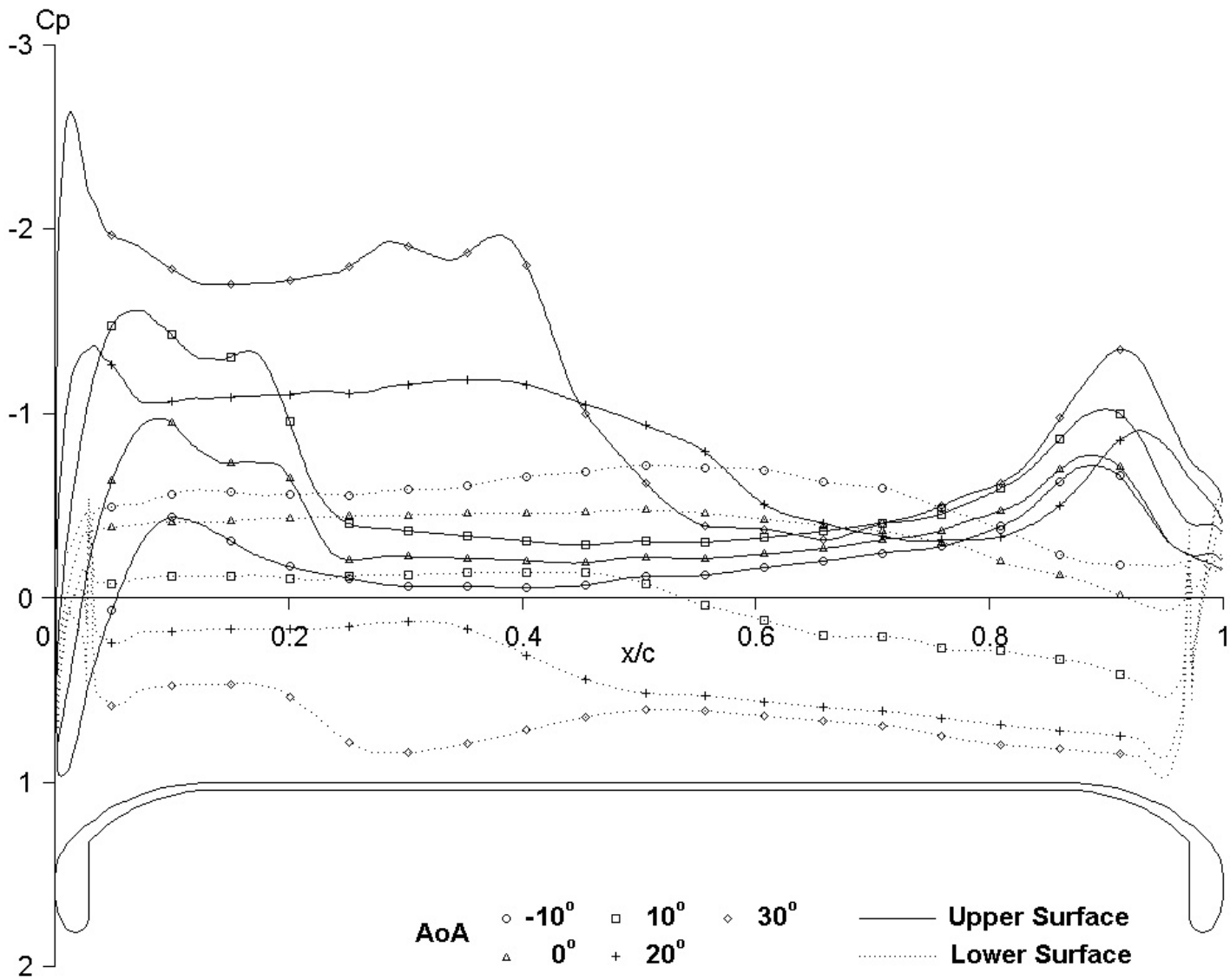


Figure 5.30 Central cross-sectional pressure profiles at the half span station, for a range of AoA. Pressure coefficients  $C_p$  were derived from measurements of the 3D surface pressure distribution of a non-spinning disc-wing. Non-dimensional disc geometry shown below pressure plot, leading edge on the left of the figure. Unbroken line - upper surface, dashed line - lower surface, AoA =  $-10^\circ$  to  $30^\circ$ ,  $V_\infty = 20\text{m/s}$ ,  $\text{Re} = 3.78 \times 10^5$ .

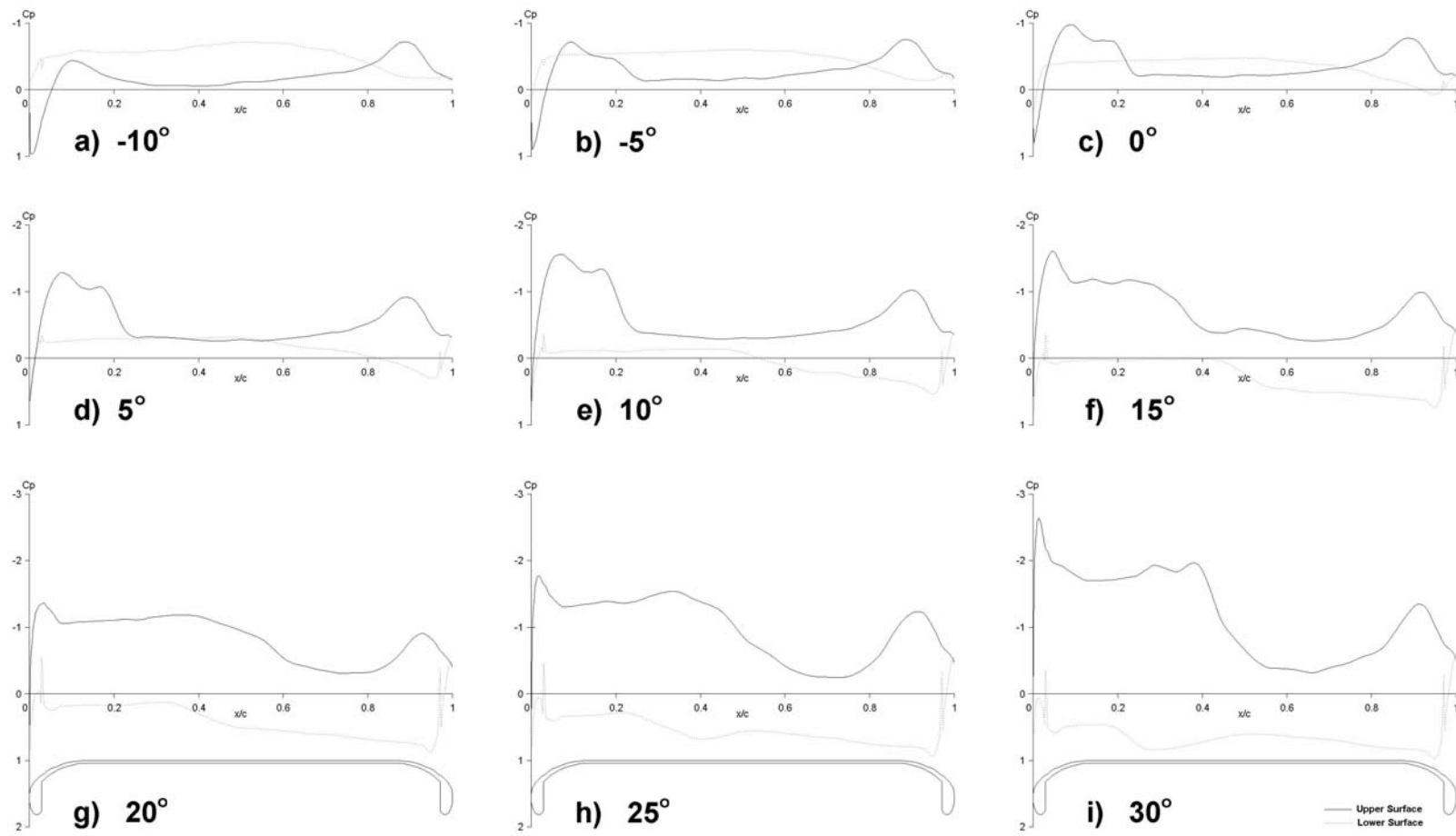
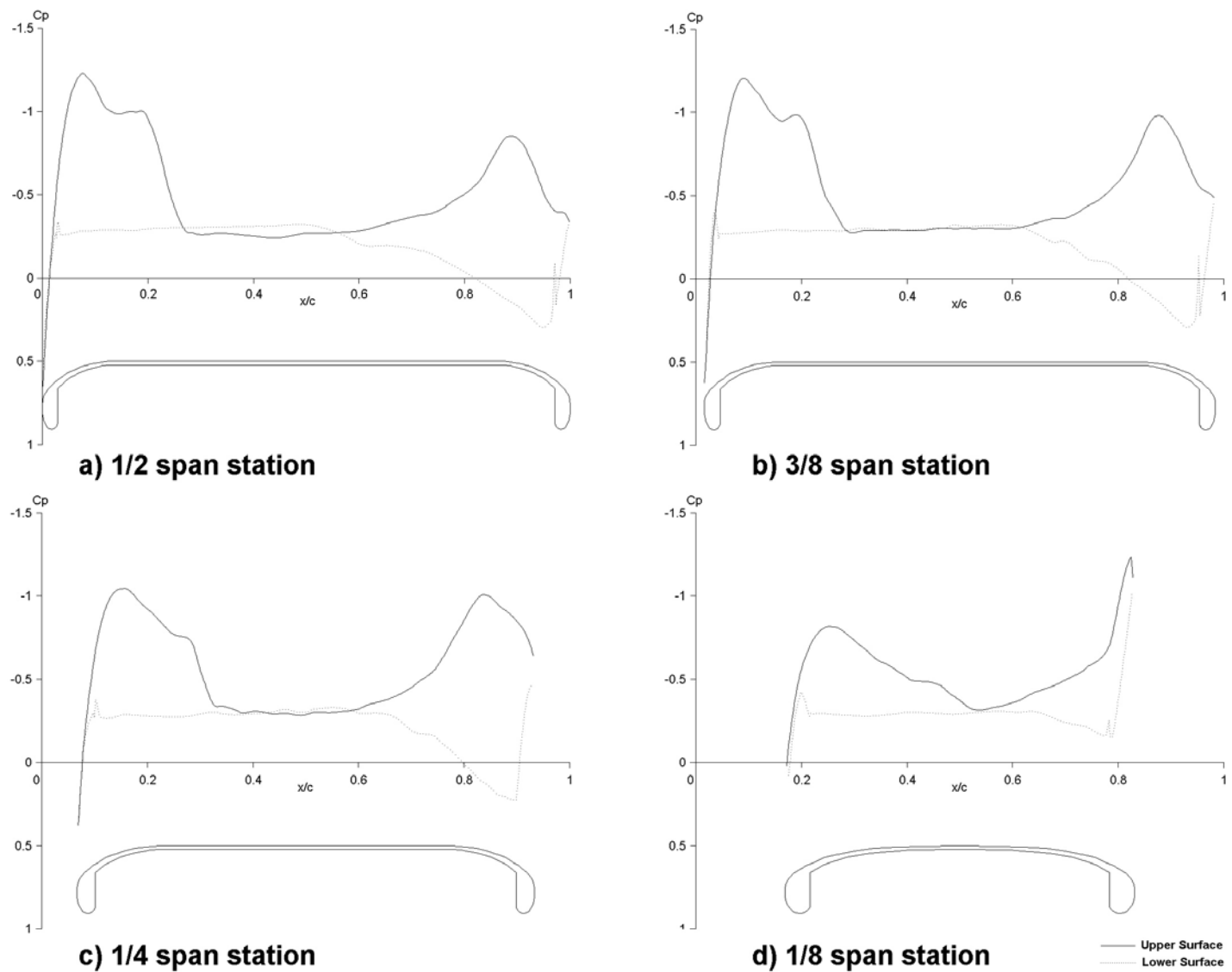


Figure 5.31 Central cross-sectional pressure profiles at the half span station, for a range of AoA. Pressure coefficients  $C_p$  were derived from measurements of the 3D surface pressure distribution of a non-spinning disc-wing. Non-dimensional disc geometry shown below pressure plot, leading edge on the left of the figure. Unbroken line - upper surface, dashed line - lower surface,  $\text{AoA} = -10^\circ$  to  $30^\circ$ ,  $V_\infty = 20\text{m/s}$ ,  $\text{Re} = 3.78 \times 10^5$ .

Figure 5.32 Cross-sectional pressure profiles at various span stations (a) 1/2 b, (b) 3/8 b, (c) 1/4 b (d) 1/8 b. Pressure coefficients  $C_p$  were derived from measurements of the 3D surface pressure distribution of a non-spinning disc-wing. Non-dimensional disc cross-section shown below pressure plot, leading edge on the left of the figure. Unbroken line - upper surface, dashed line - lower surface, AoA =  $5^\circ$ ,  $V_\infty = 15\text{m/s}$ ,  $\text{Re} = 2.84 \times 10^5$ .



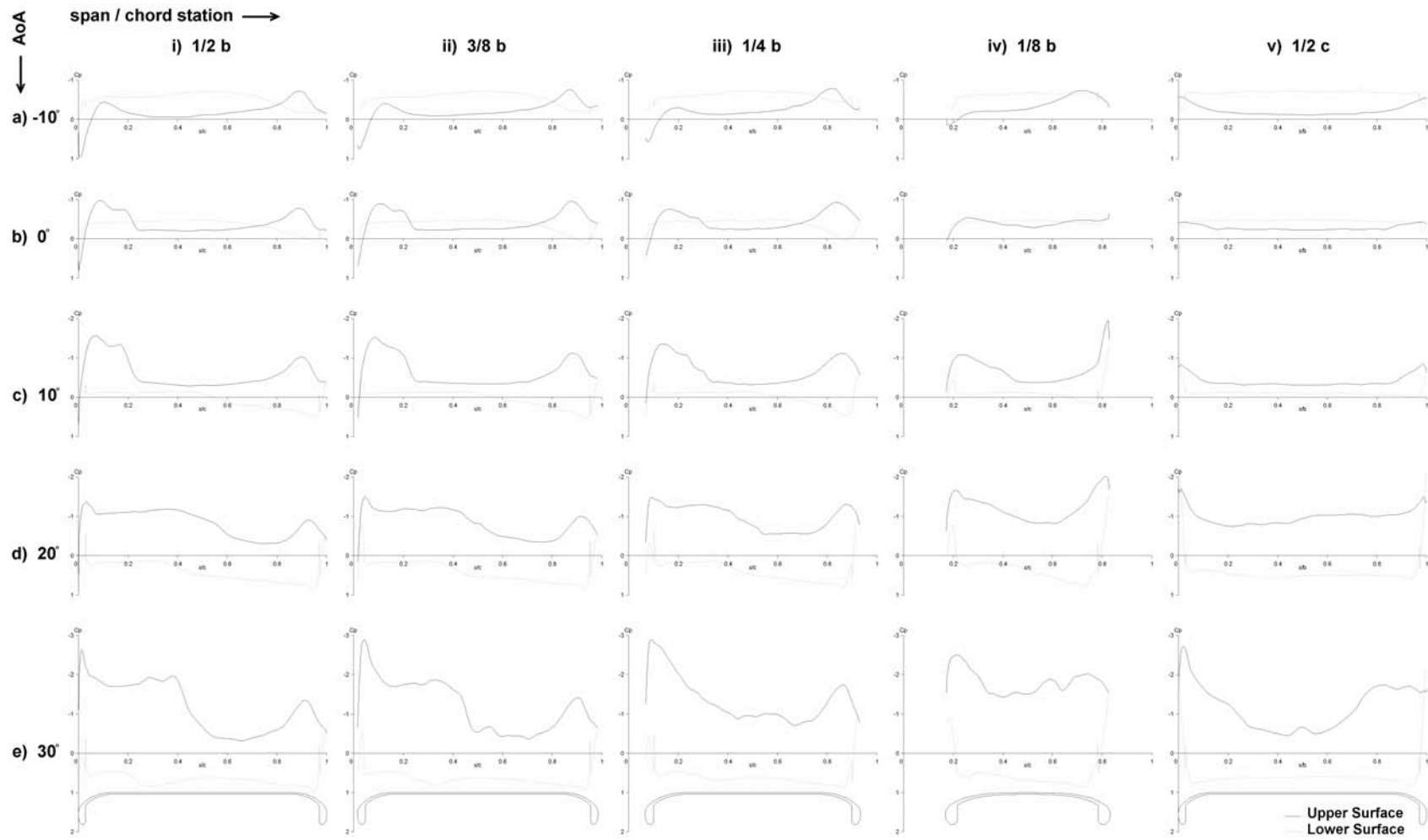
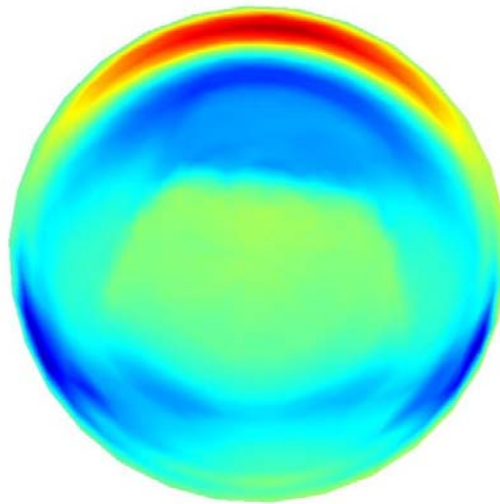
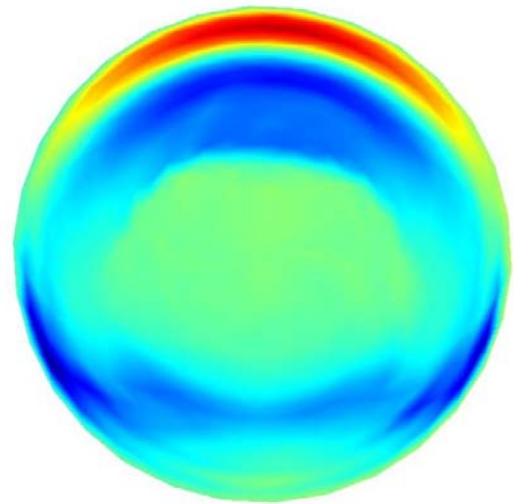


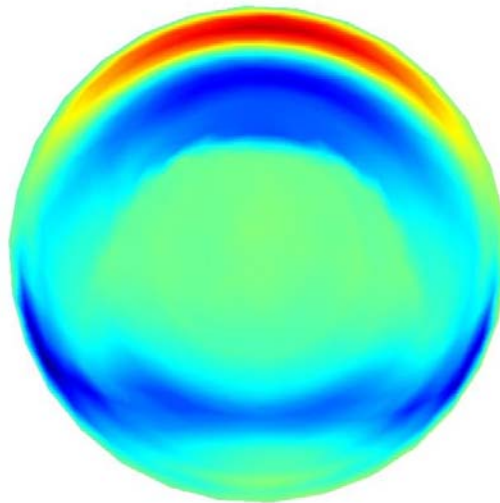
Figure 5.33 Cross-sectional pressure profiles at various span/chord stations (i)  $1/2 b$ , (ii)  $3/8 b$ , (iii)  $1/4 b$ , (iv)  $1/8 b$ , (v)  $1/2 c$  and a range of AoA. Pressure coefficients  $C_p$  were derived from measurements of the 3D surface pressure distribution of a non-spinning disc-wing. Non-dimensional disc cross-section shown below pressure plot (e), leading edge (i, ii, iii, iv) and port wing-tip (v) on the left of each plot. Unbroken line - upper surface, dashed line - lower surface,  $AoA = -10^\circ$  to  $30^\circ$ ,  $V_\infty = 20\text{m/s}$ ,  $Re = 3.78 \times 10^5$ .



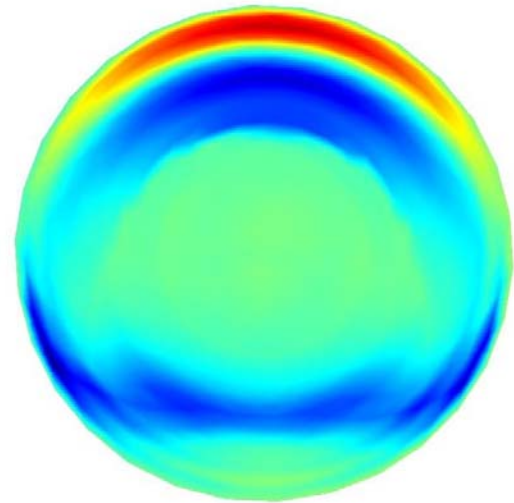
a)  $\text{Re} = 1.13 \times 10^5$



b)  $\text{Re} = 1.89 \times 10^5$



c)  $\text{Re} = 2.84 \times 10^5$



d)  $\text{Re} = 3.78 \times 10^5$

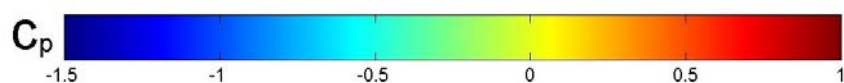
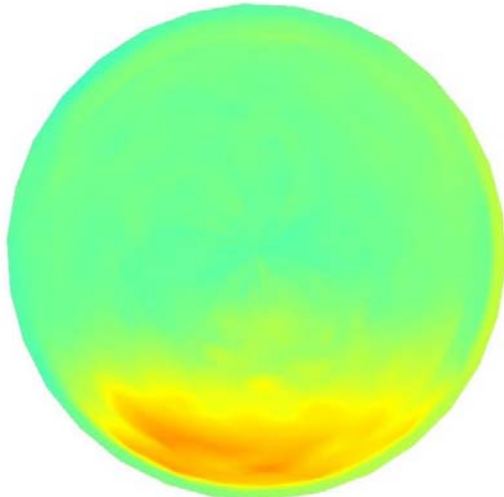
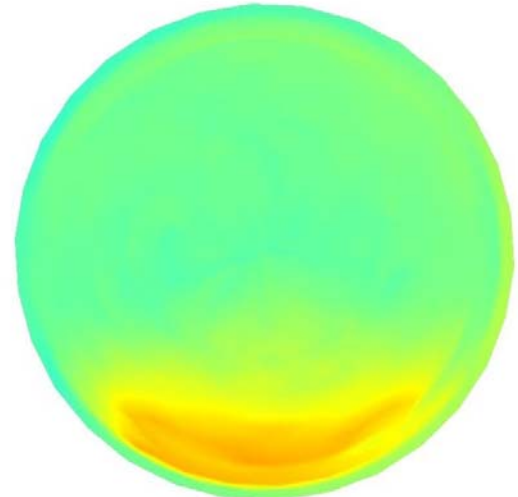


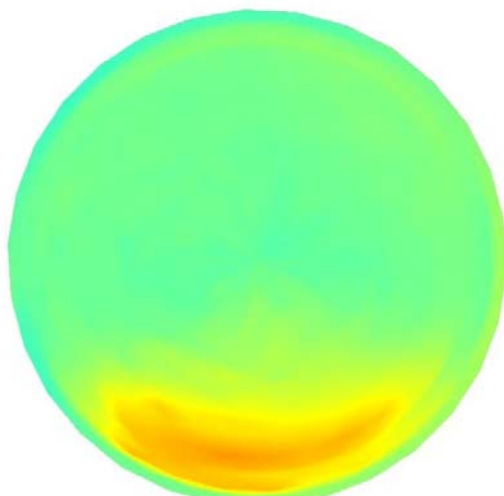
Figure 5.34 2D flat surface colour weighted contour plots of pressure coefficients  $C_p$  for a range of  $\text{Re}$ , derived from measurements of the 3D upper surface pressure distribution of a non-spinning disc-wing, taken over the entire surface, not over half the disc and mirrored to the other side, flow direction from top to bottom,  
AoA = 5°,  $V_\infty$  = 6 to 20 m/s,  $\text{Re} = 1.13$  to  $3.78 \times 10^5$ .



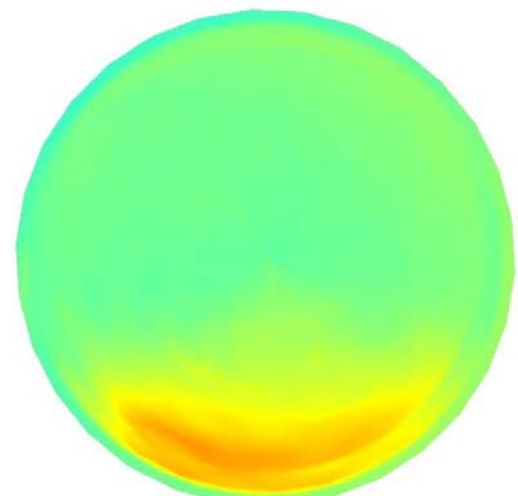
a)  $\text{Re} = 1.13 \times 10^5$



b)  $\text{Re} = 1.89 \times 10^5$



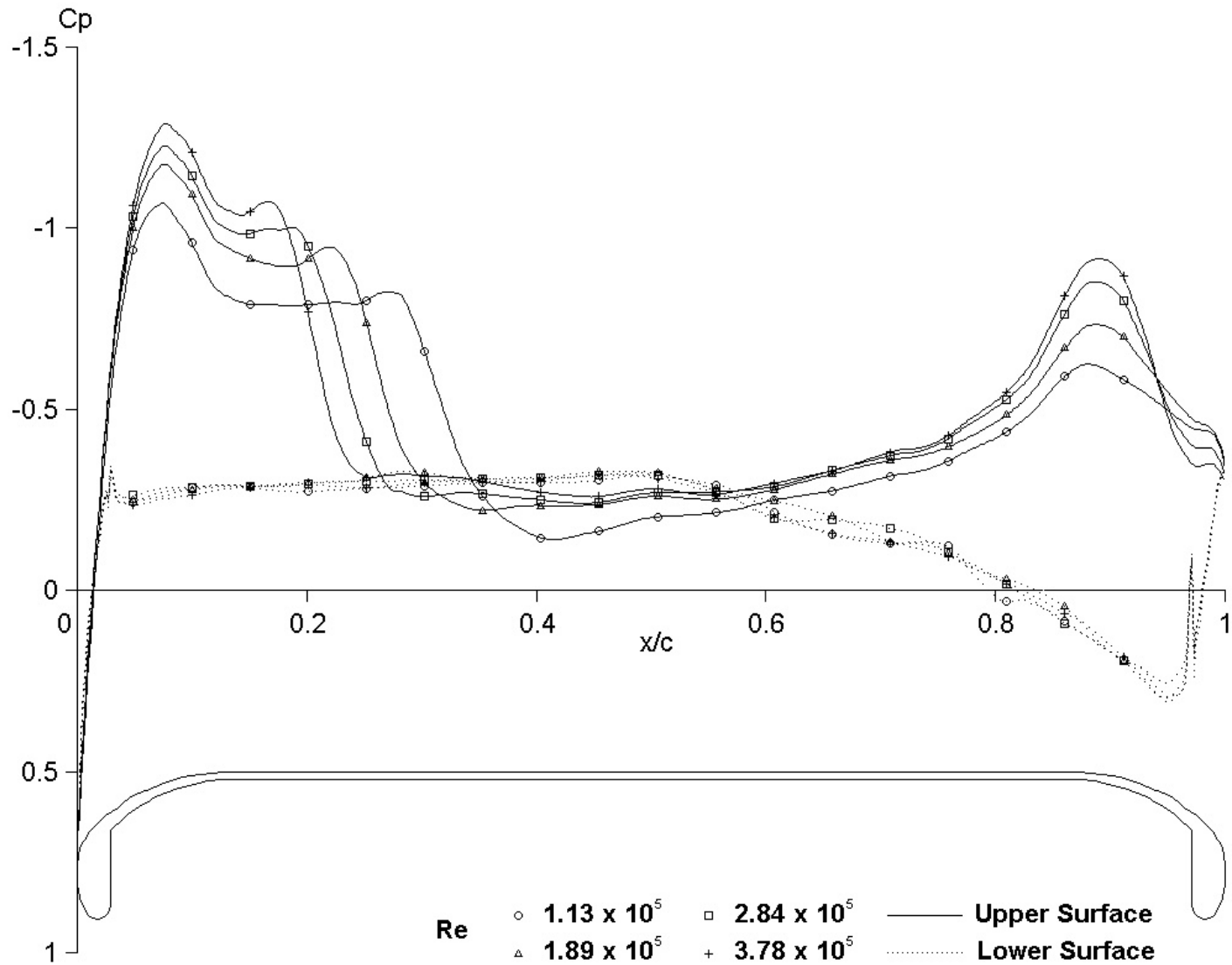
c)  $\text{Re} = 2.84 \times 10^5$

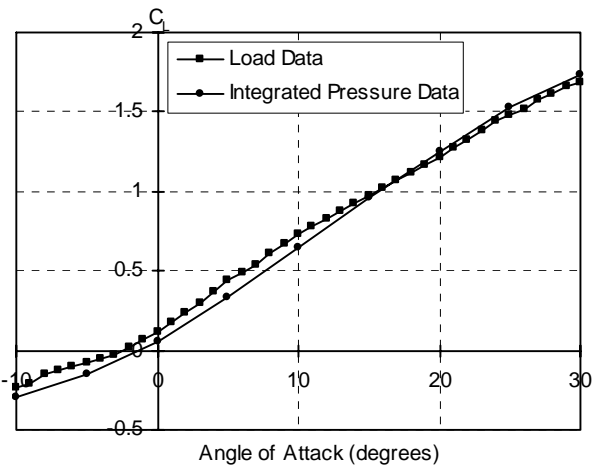


d)  $\text{Re} = 3.78 \times 10^5$

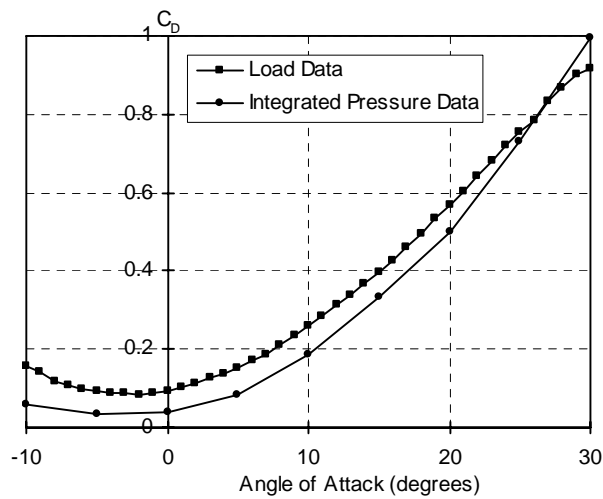


Figure 5.35 2D flat surface colour weighted contour plots of pressure coefficients  $C_p$  for a range of  $\text{Re}$ , derived from measurements of the 3D cavity surface pressure distribution of a non-spinning disc-wing, taken over the entire surface, not over half the disc and mirrored to the other side, flow direction from top to bottom,  
 $\text{AoA} = 5^\circ$ ,  $V_\infty = 6$  to  $20\text{m/s}$ ,  $\text{Re} = 1.13$  to  $3.78 \times 10^5$ .

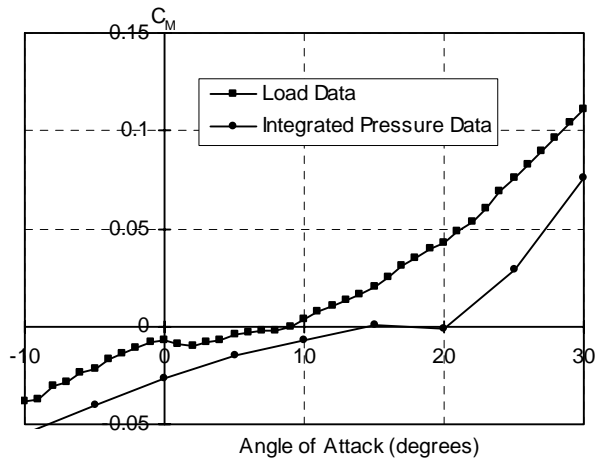




(a) Lift Coefficient.



(b) Drag Coefficient.



(c) Pitching Moment Coefficient.

Figure 5.37 Pressure load characteristics, integrated from the pressure data over the 3D disc-wing geometry, and a comparison to the load measurements, taken from the wind tunnel balance,  $\text{AoA} = -10^\circ$  to  $30^\circ$ ,  $V_\infty = 20\text{m/s}$ ,  $\text{Re} = 3.78 \times 10^5$ .

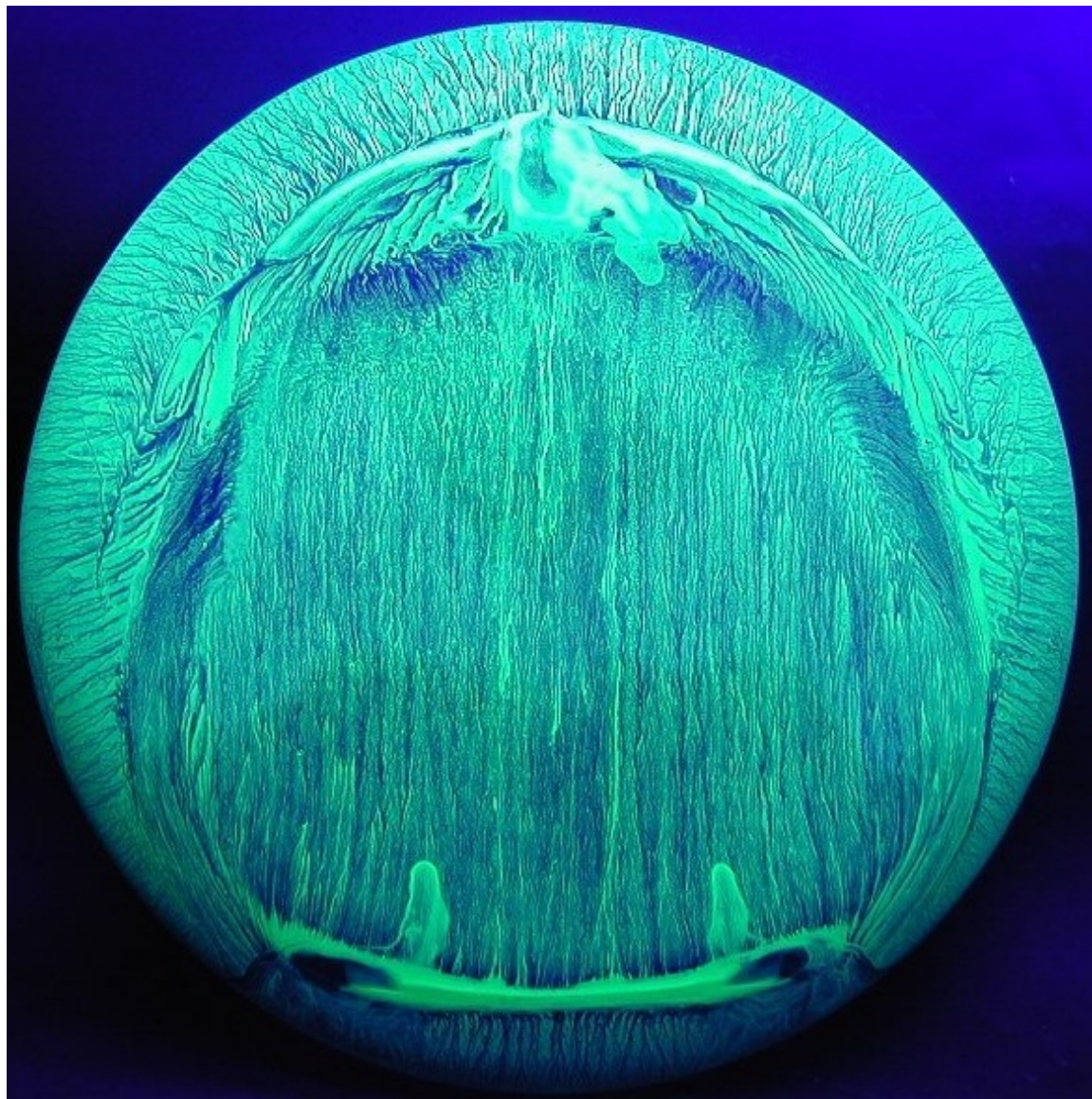


Figure 5.38 Upper surface paint patterns for a non-spinning disc-wing,  
flow direction from top to bottom,  
 $\text{AoA} = 5^\circ$ ,  $V_\infty = 15\text{m/s}$ ,  $\text{Re} = 2.84 \times 10^5$ .

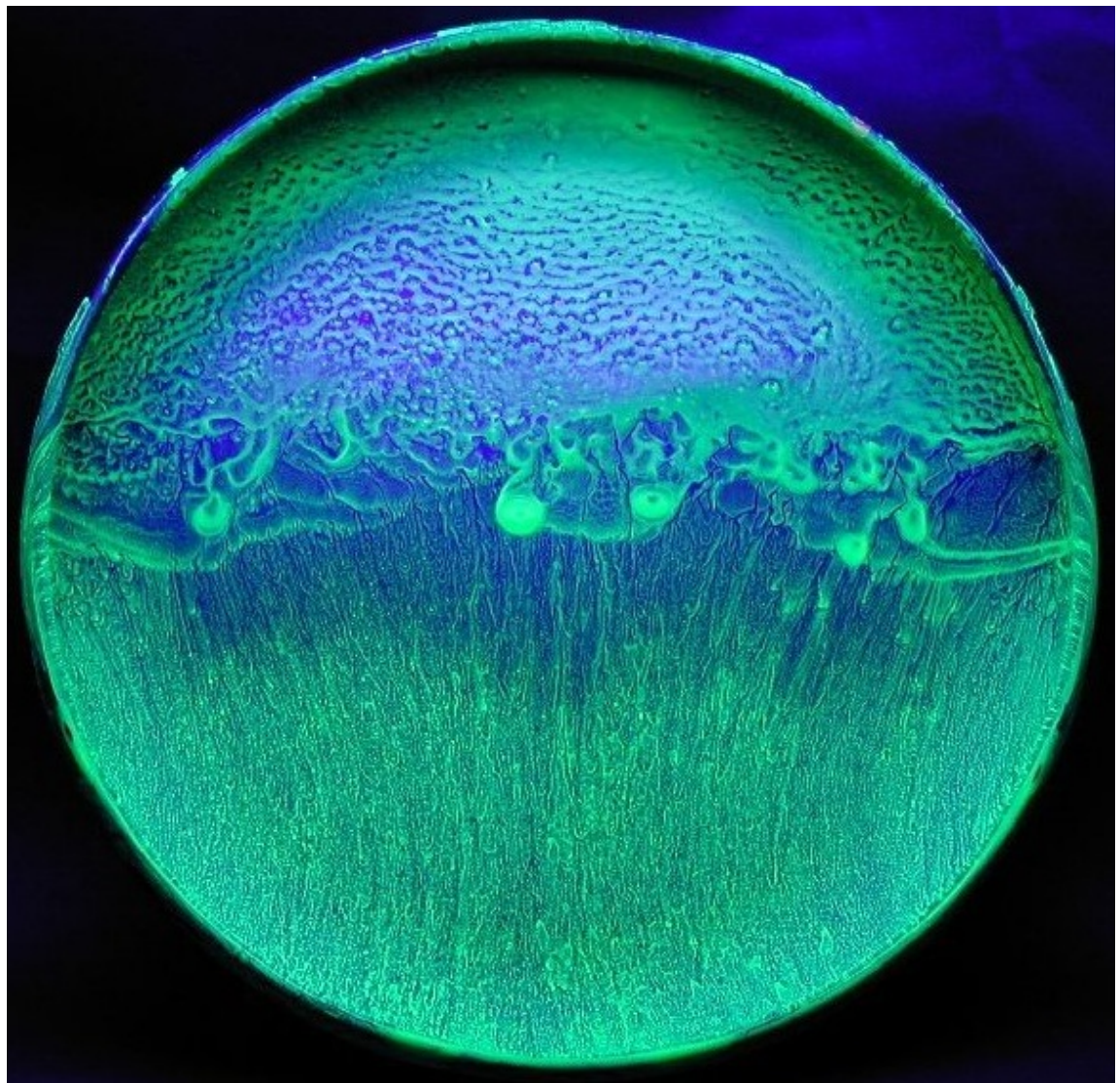


Figure 5.39 Lower (cavity) surface paint patterns for a non-spinning disc-wing,  
flow direction from top to bottom,  
 $\text{AoA} = 5^\circ$ ,  $V_\infty = 15 \text{ m/s}$ ,  $\text{Re} = 2.84 \times 10^5$ .

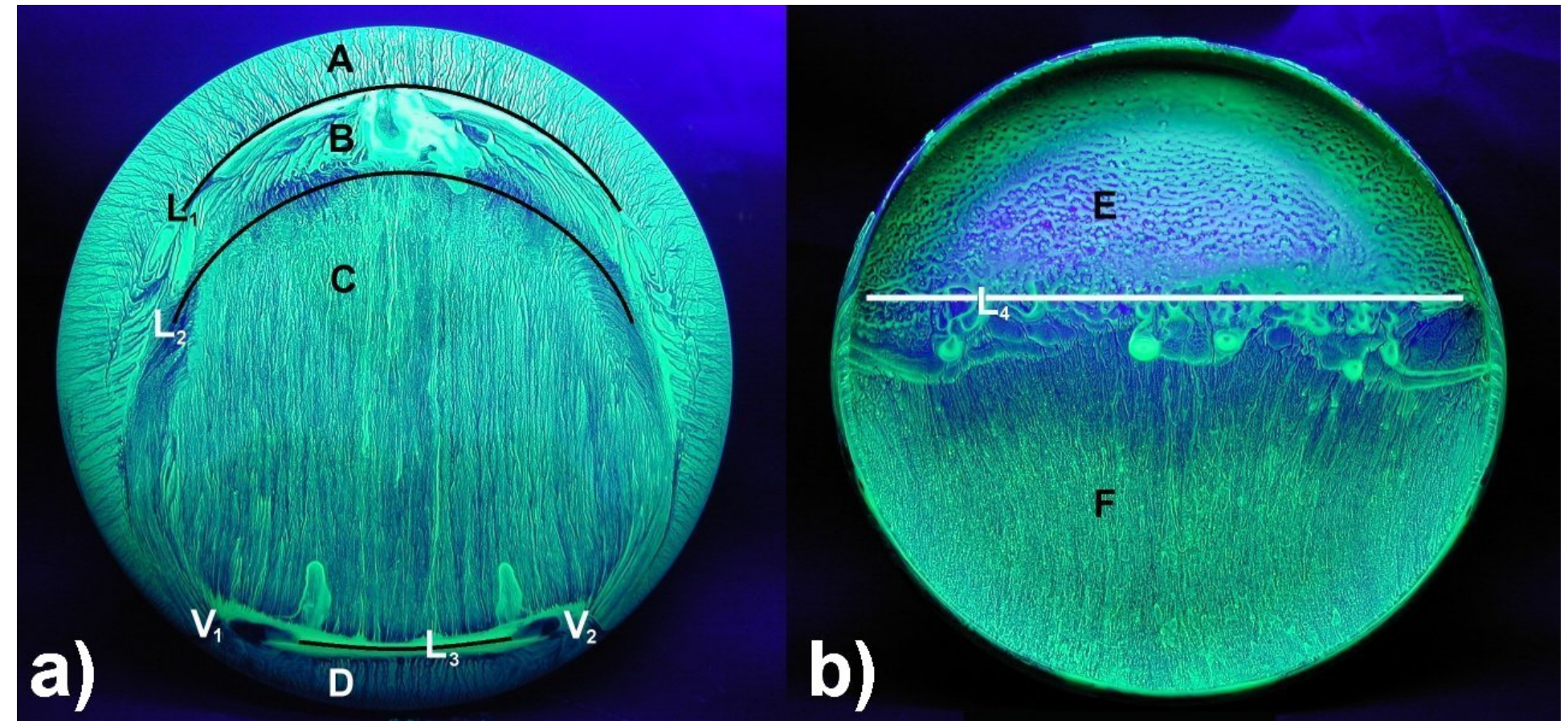


Figure 5.40 Upper (a) and Lower (cavity) (b) surface paint patterns for a non-spinning disc-wing, including superimposed labels to aid the explanation of surface flow features, flow direction from top to bottom,  $\text{AoA} = 5^\circ$ ,  $V_\infty = 15 \text{ m/s}$ ,  $\text{Re} = 2.84 \times 10^5$ .

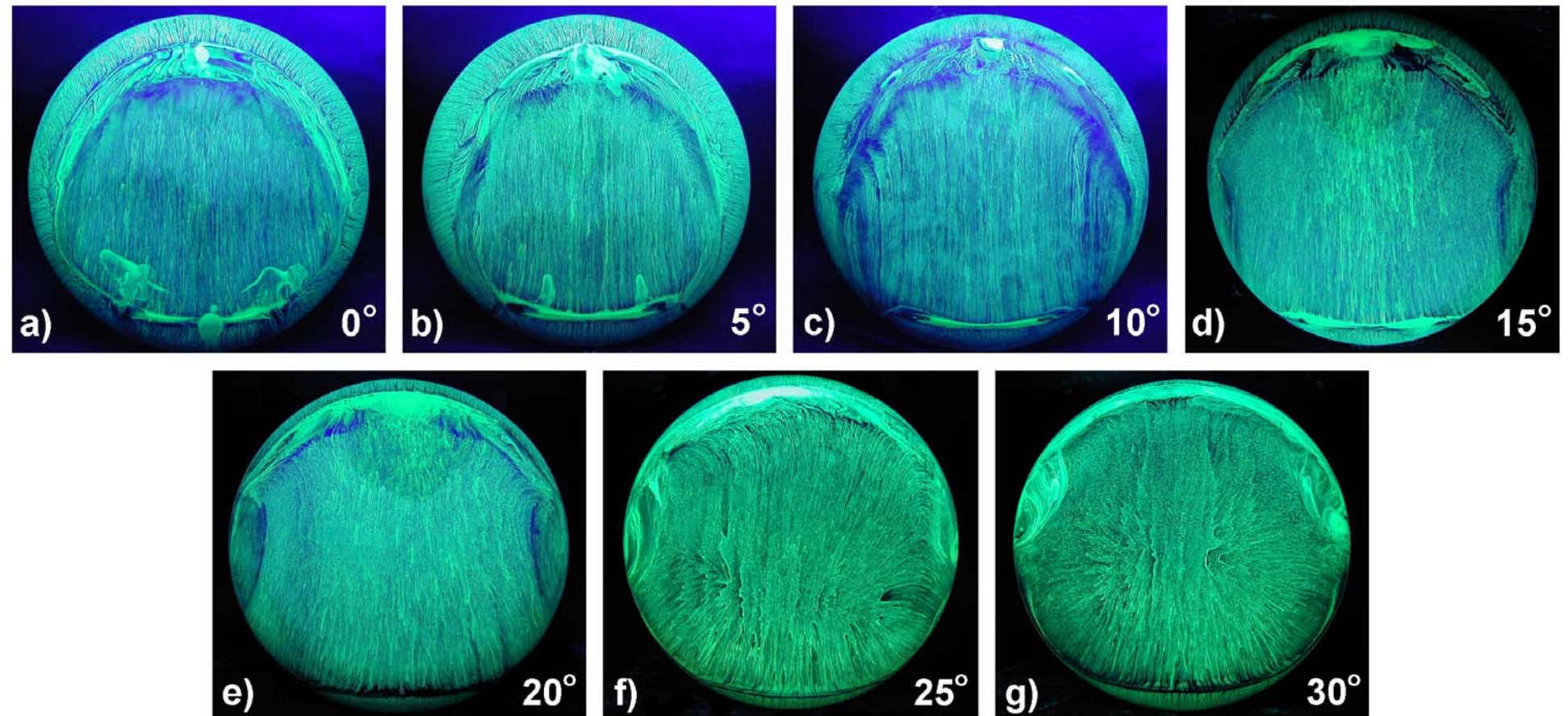


Figure 5.41 Upper surface paint patterns for a non-spinning disc-wing, over a range of AoA,  
flow direction from top to bottom,

AoA =  $0^\circ$  to  $30^\circ$ ,  $V_\infty = 15\text{m/s}$ ,  $\text{Re} = 2.84 \times 10^5$ .

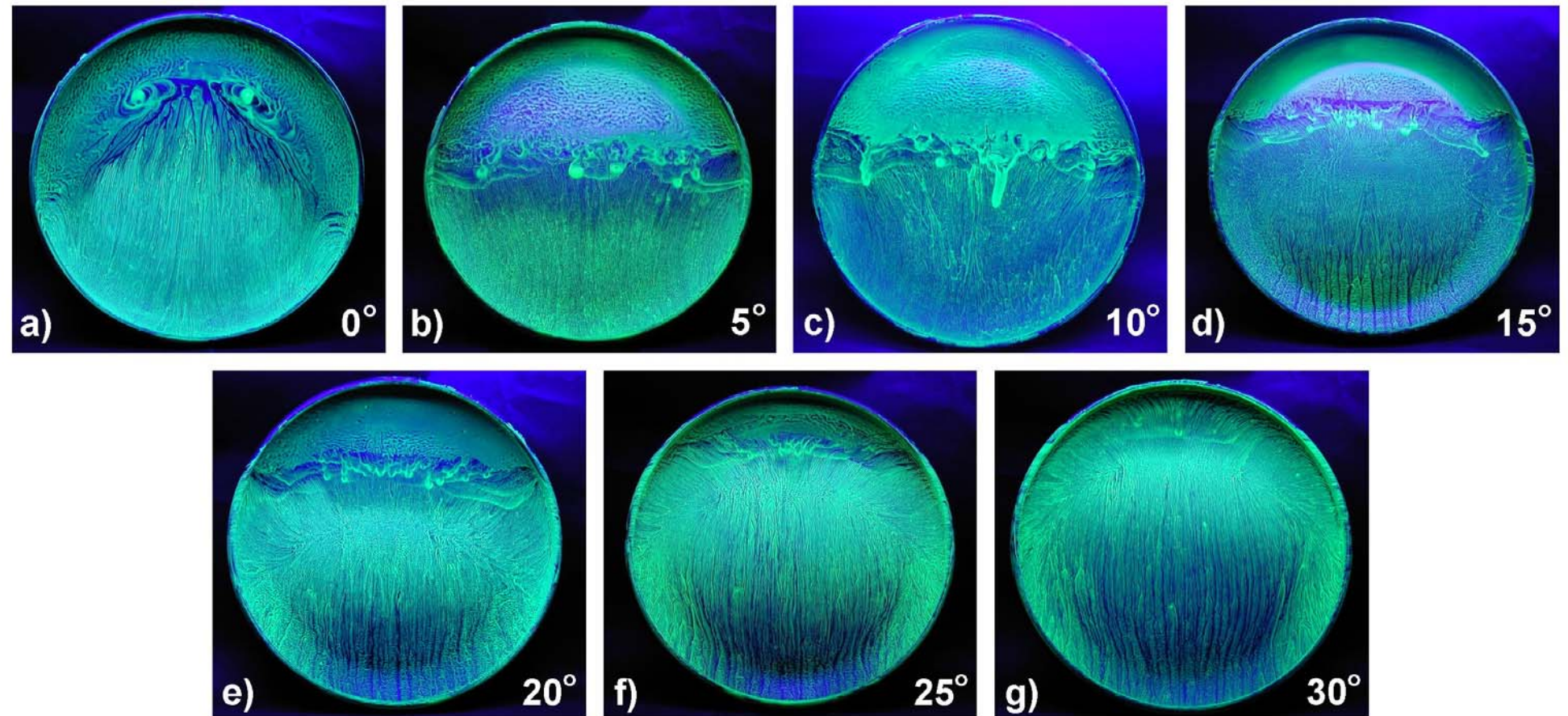


Figure 5.42 Lower (cavity) surface paint patterns for a non-spinning disc-wing, over a range of AoA,  
flow direction from top to bottom,

AoA = 0° to 30°,  $V_\infty = 15\text{m/s}$ ,  $\text{Re} = 2.84 \times 10^5$ .

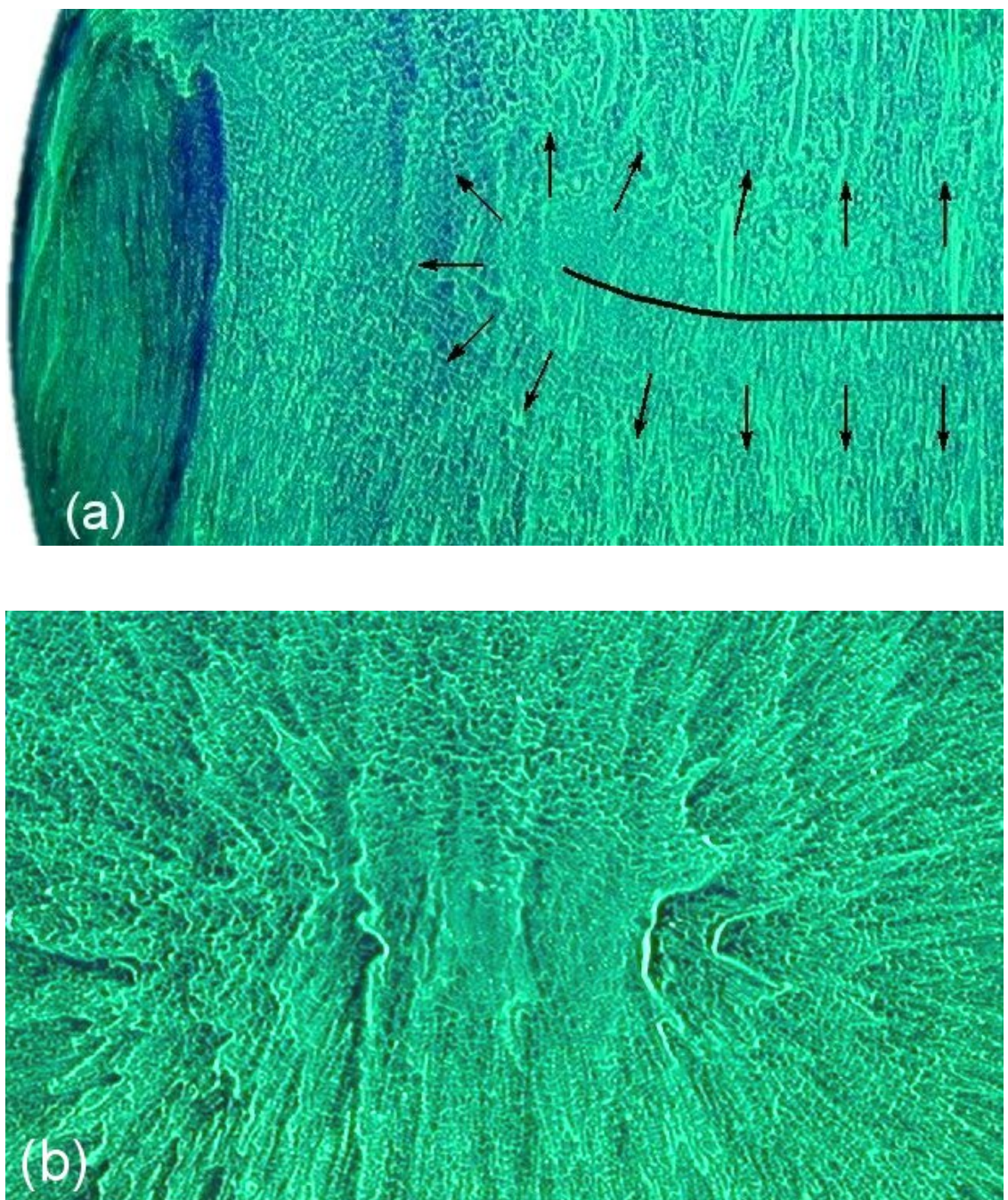


Figure 5.43 Upper surface paint patterns (detail) for a non-spinning disc-wing, depicting boundary layer reattachment features, flow direction from top to bottom,

(a) Straight line reattachment (half disc) at  $20^\circ$  AoA,

(b) Nodal point reattachment at  $30^\circ$  AoA.  $V_\infty = 15\text{m/s}$ ,  $\text{Re} = 2.84 \times 10^5$ .

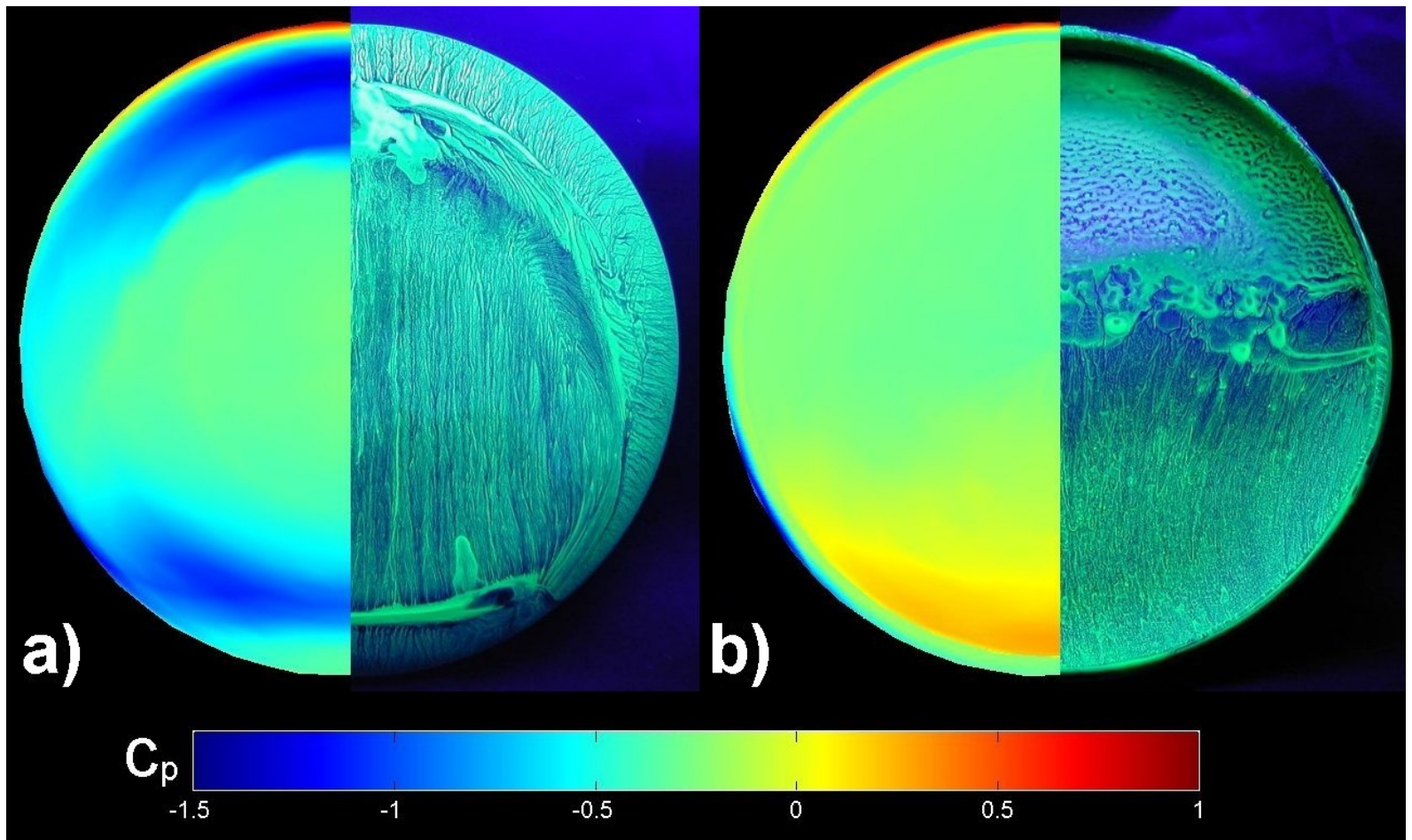


Figure 5.44 Half surface comparison plot: 3D pressure surface colour weighted contour plots of pressure coefficients  $C_p$  derived from measurements of the upper (a) & lower (cavity) (b) surface pressure distribution over a non-spinning disc-wing, superimposed onto the half surface flow visualisation images,

flow direction from top to bottom, AoA =  $5^\circ$ ,  $V_\infty = 15\text{m/s}$ ,  $\text{Re} = 2.84 \times 10^5$ .

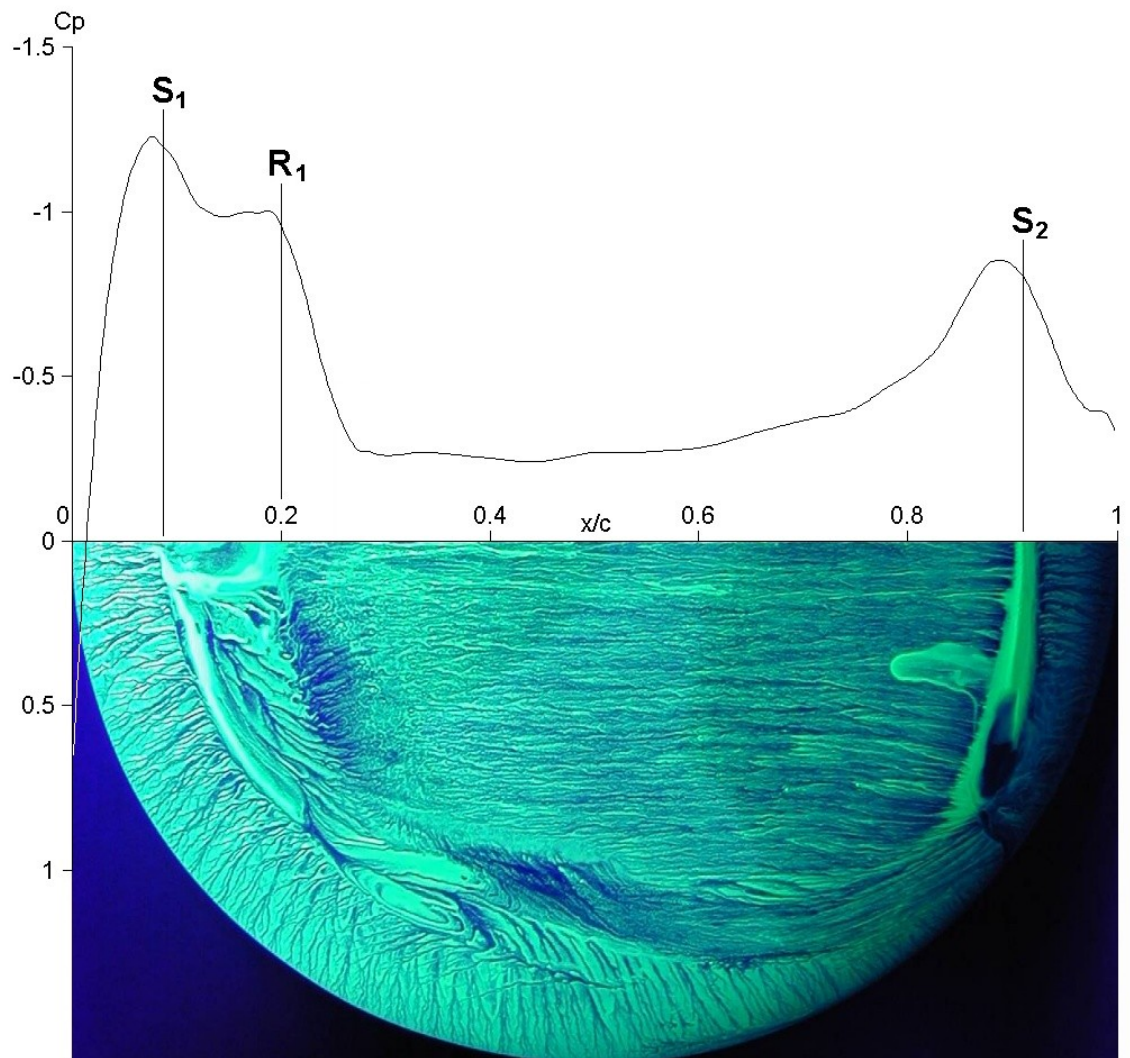


Figure 5.45 Comparison plot: Central cross-sectional, upper surface pressure profile at the half span station, superimposed onto a half surface paint flow visualisation image. Leading edge on the left of the figure. Pressure coefficients  $C_p$  derived from measurements of the upper surface pressure distribution over a non-spinning disc-wing. Separation ( $S_1, S_2$ ) and reattachment ( $R_1$ ) lines are marked on for comparison, flow direction from left to right,

$$\text{AoA} = 5^\circ, V_\infty = 15 \text{ m/s}, \text{Re} = 2.84 \times 10^5.$$

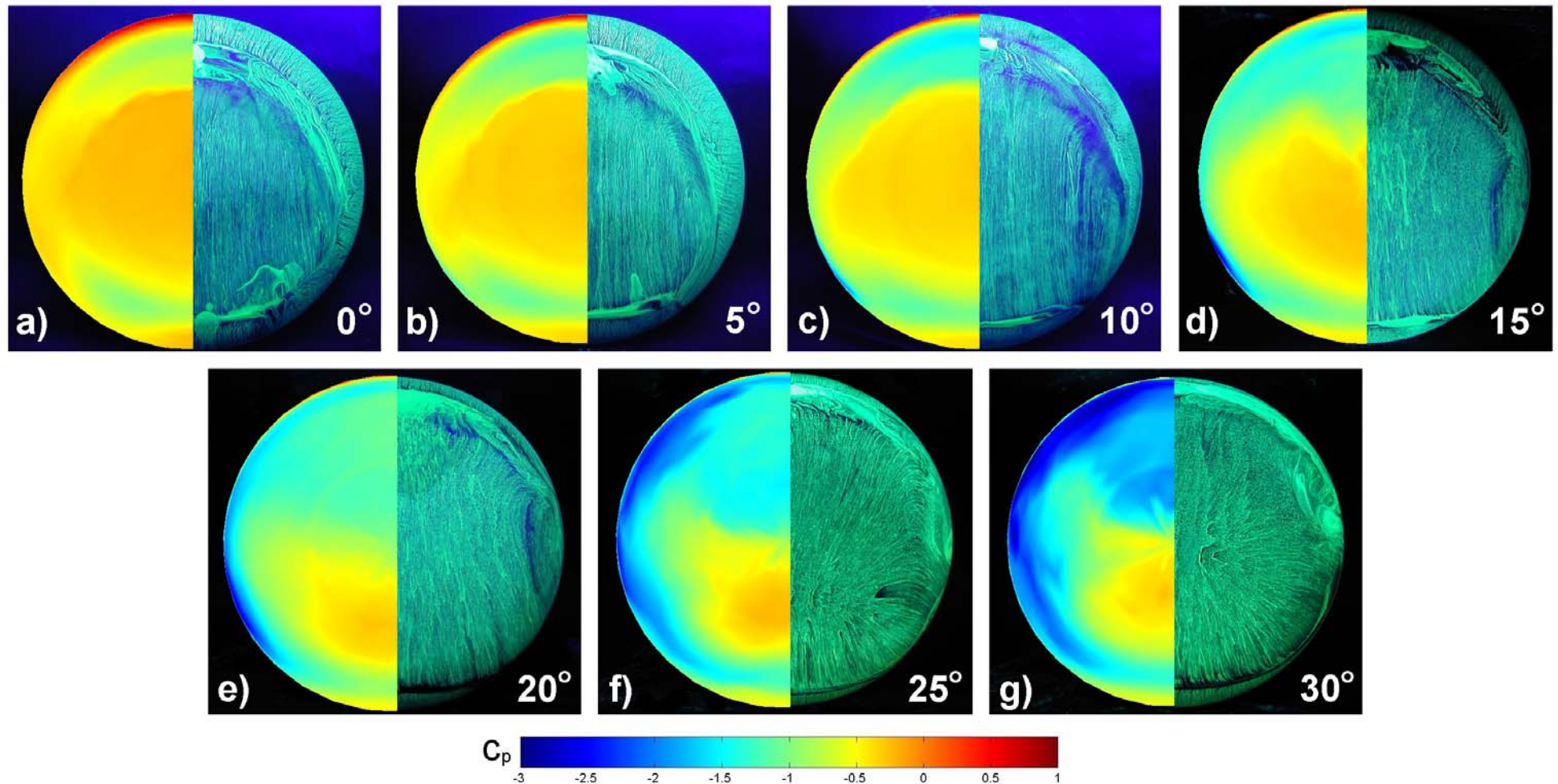


Figure 5.46 Half surface comparison plot: 3D pressure surface colour weighted contour plots of pressure coefficients  $C_p$  derived from measurements of the upper surface pressure distribution over a non-spinning disc-wing, superimposed onto the half surface flow visualisation images, over a range of AoA, flow direction from top to bottom,  $\text{AoA} = 0^\circ$  to  $30^\circ$ ,  $V_\infty = 15\text{m/s}$  (flow vis) &  $20\text{m/s}$  (pressure),  $\text{Re} = 2.84 \times 10^5$  &  $3.78 \times 10^5$ .

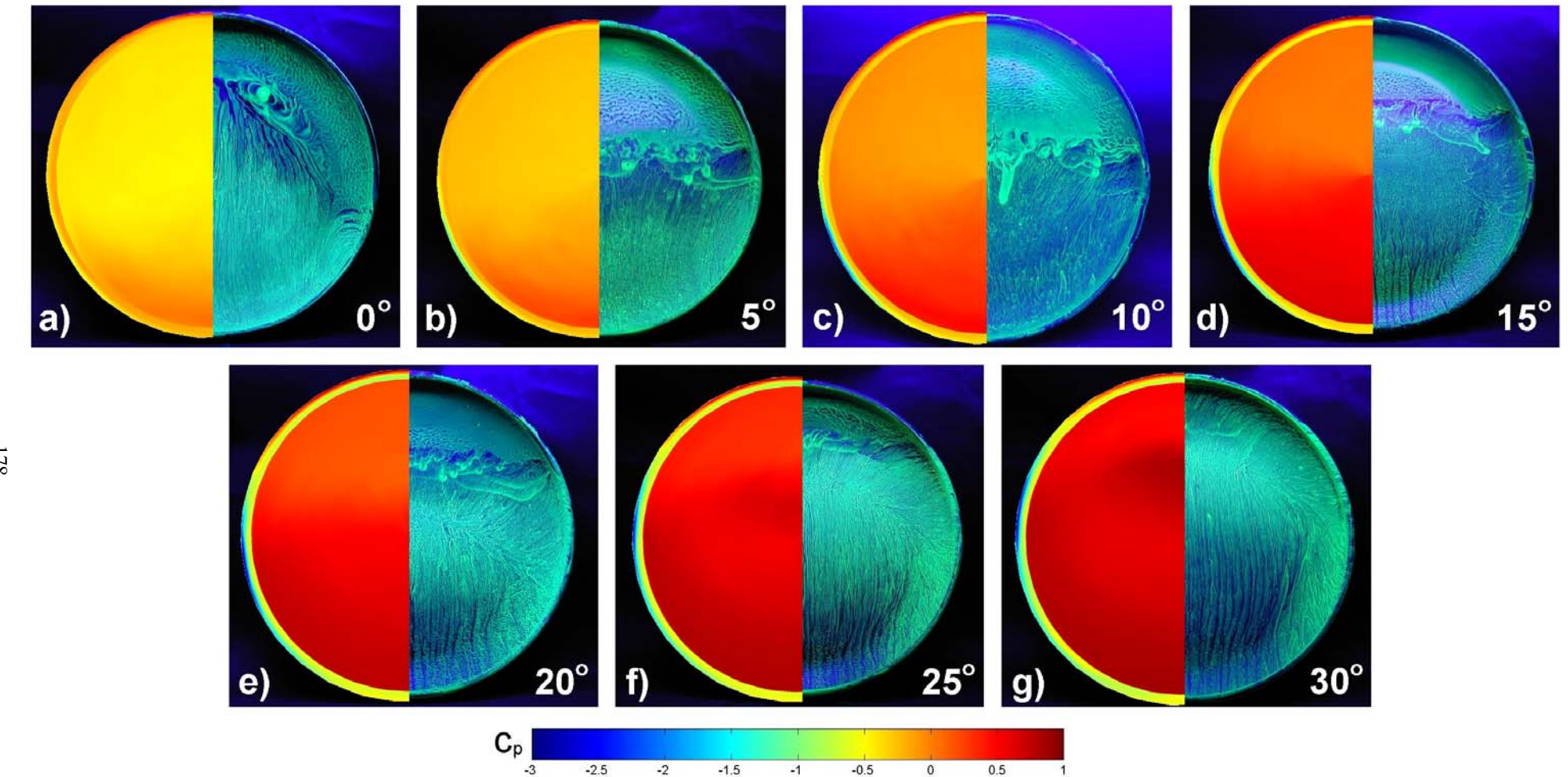


Figure 5.47 Half surface comparison plot: 3D pressure surface colour weighted contour plots of pressure coefficients  $C_p$  derived from measurements of the lower surface pressure distribution over a non-spinning disc-wing, superimposed onto the half surface flow visualisation images, over a range of AoA, flow direction from top to bottom, AoA =  $0^\circ$  to  $30^\circ$ ,  $V_\infty = 15\text{m/s}$  (flow vis) &  $20\text{m/s}$  (pressure),  $\text{Re} = 2.84 \times 10^5$  &  $3.78 \times 10^5$ .

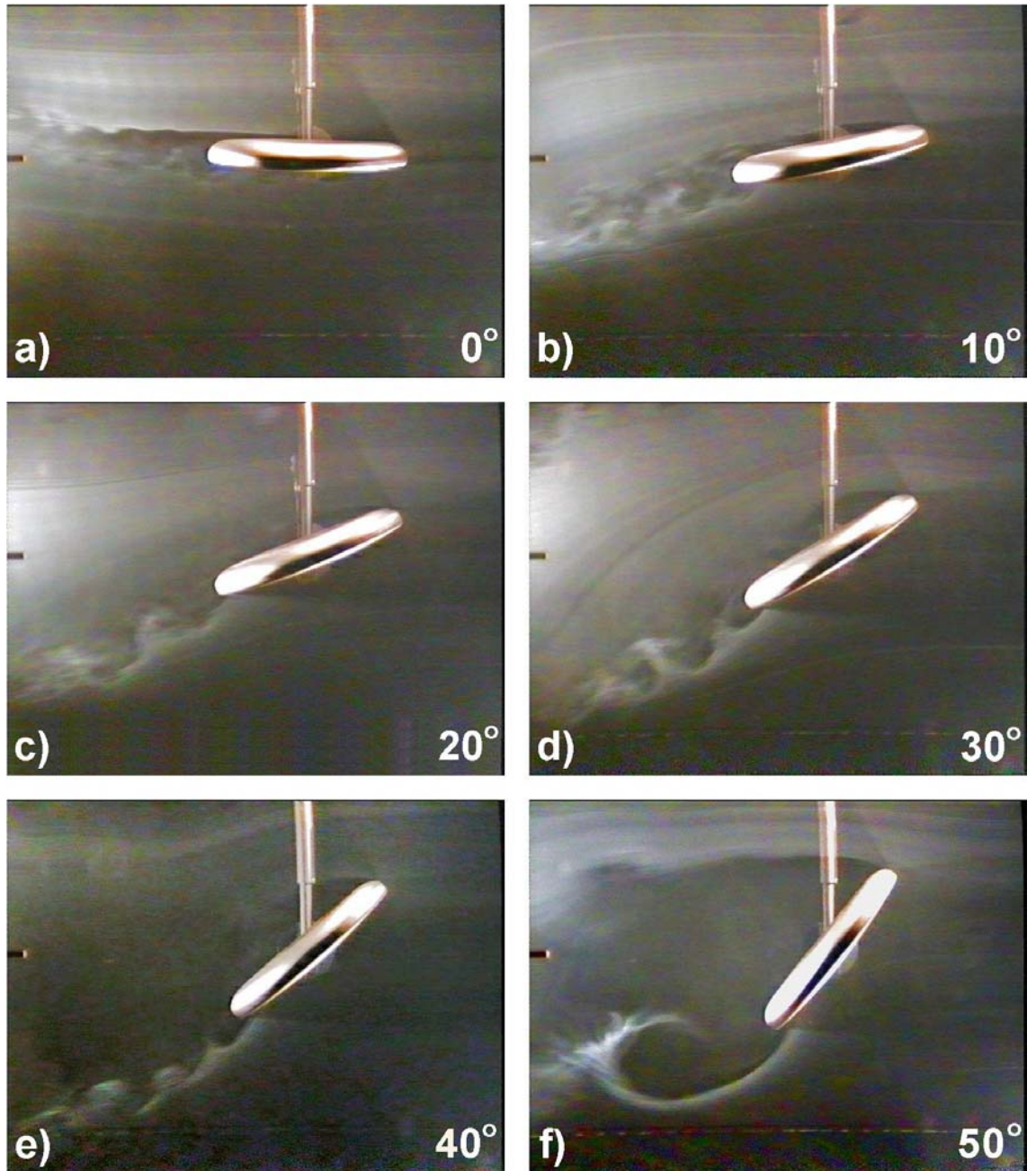


Figure 5.48 Central cross-section of the flow field over a non-spinning disc-wing,  
for a range of AoA, flow direction from right to left.  
An electrically heated wire vaporised oil to create smoke,  
visualising the flow field when illuminated.  
 $\text{AoA} = 0^\circ \text{ to } 50^\circ$ ,  $V_\infty = 3 \text{ m/s}$ ,  $\text{Re} = 5.67 \times 10^4$ .

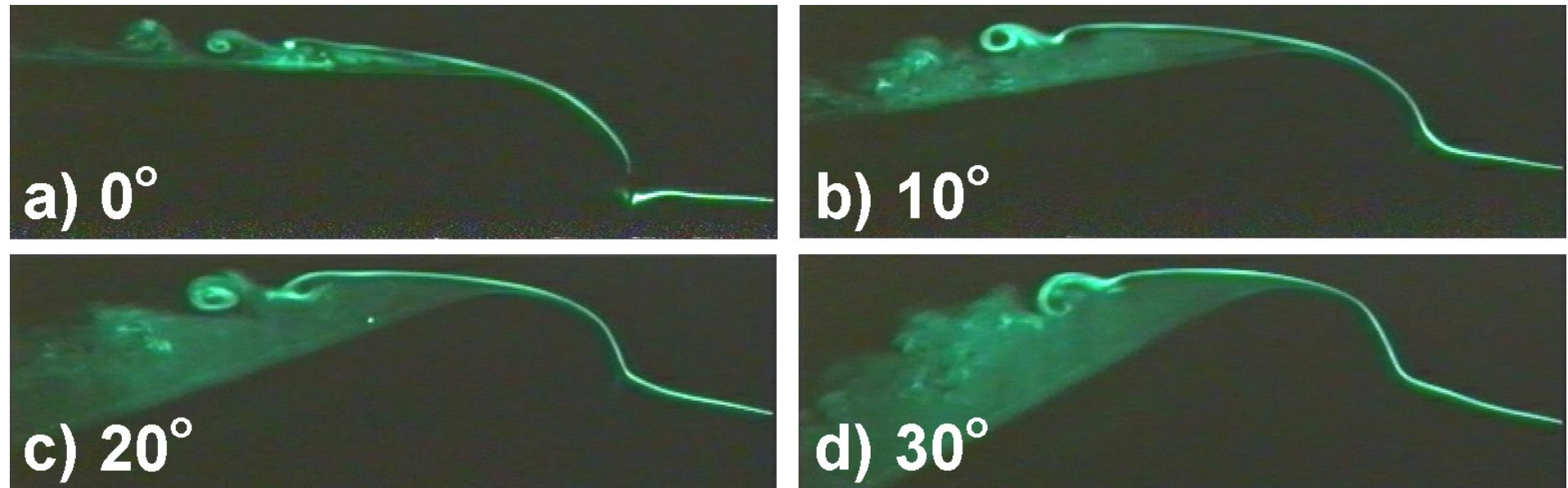


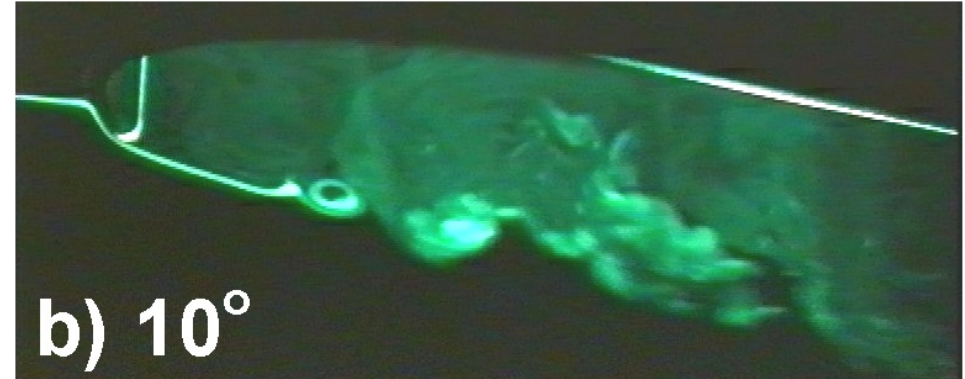
Figure 5.49 Central cross-section of the leading edge separation bubble over a disc-wing, for a range of AoA, flow direction from right to left.

An electrically heated wire vaporised oil to create smoke, visualising the separation bubble when illuminated by a laser light sheet.

$$\text{AoA} = 0^\circ \text{ to } 30^\circ, \text{AdvR} = 0.7, V_\infty = 3 \text{ m/s}, \text{Re} = 5.67 \times 10^4.$$



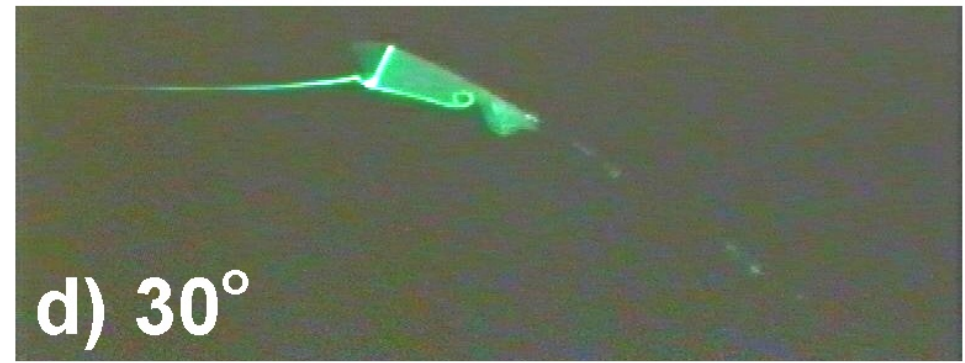
a)  $0^\circ$



b)  $10^\circ$



c)  $20^\circ$



d)  $30^\circ$

Figure 5.50 Central cross-section of the separated shear layer and cavity flow over a non-spinning disc-wing,  
for a range of AoA, flow direction from left to right.

An electrically heated wire vaporised oil to create smoke, visualising the cavity flow when illuminated by a laser light sheet.

$$\text{AoA} = 0^\circ \text{ to } 30^\circ, V_\infty = 3 \text{ m/s}, Re = 5.67 \times 10^4.$$

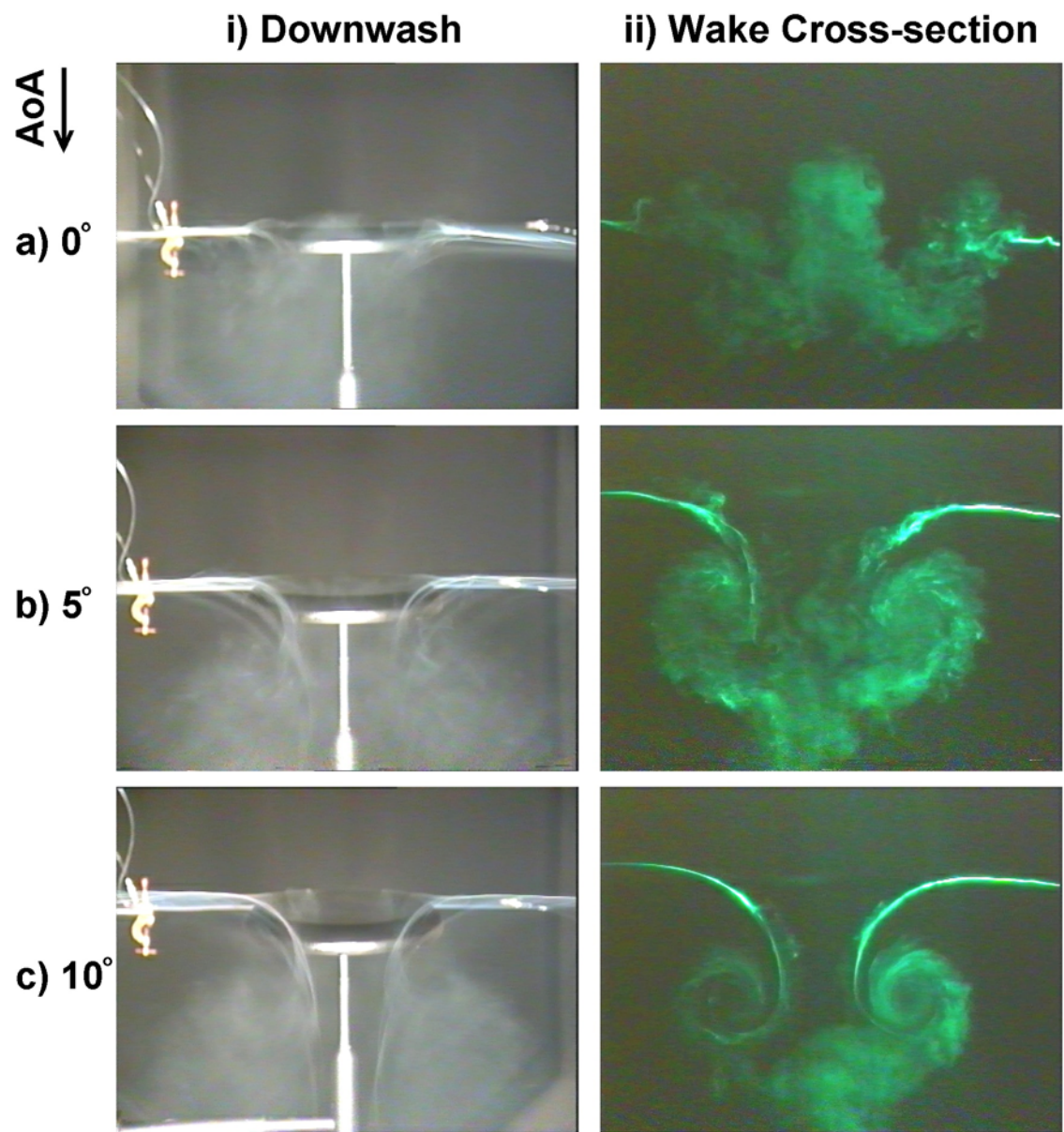


Figure 5.51 Visualisation of the wake, downwash and trailing vortex structures downstream of a non-spinning disc-wing, for a range of AoA. An electrically heated wire vaporised oil to create smoke, visualising the flow field when illuminated by ambient lighting (i) or a laser light sheet (ii). The camera was placed downstream of the disc model, flow direction is out of the page. The wake cross-sections (ii) were taken at a distance of one diameter from the trailing edge,  $\text{AoA} = 0^\circ$  to  $10^\circ$ ,  $V_\infty = 3\text{m/s}$ ,  $\text{Re} = 5.67 \times 10^4$ .

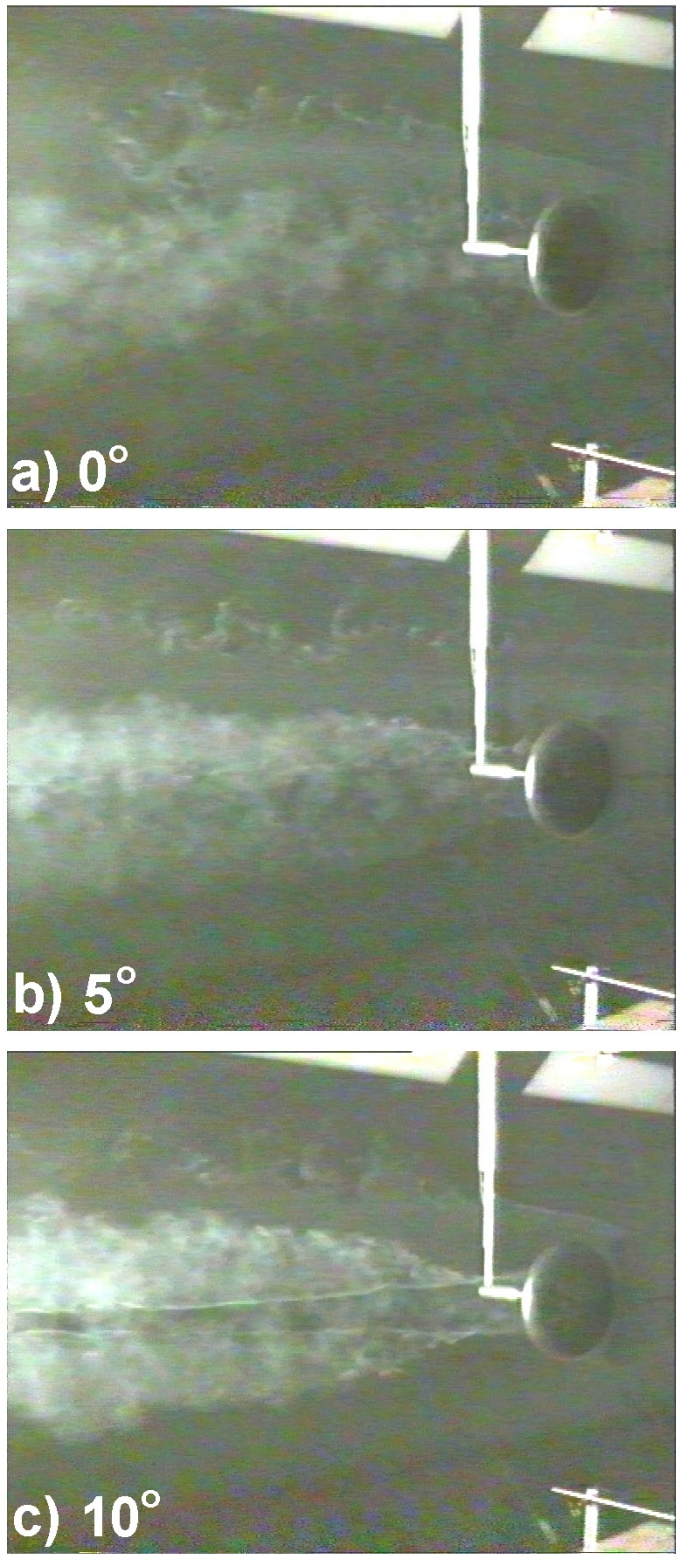


Figure 5.52 Visualisation of the wake, downwash and trailing vortex structures extending to just over five diameters downstream from the trailing edge of a non-spinning disc-wing, for a range of AoA. An electrically heated wire vaporised oil to create smoke, visualising the flow field when illuminated, flow direction from right to left,  
 $\text{AoA} = 0^\circ, 5^\circ \text{ & } 10^\circ$ ,  $V_\infty = 3\text{m/s}$ ,  $\text{Re} = 5.67 \times 10^4$ .

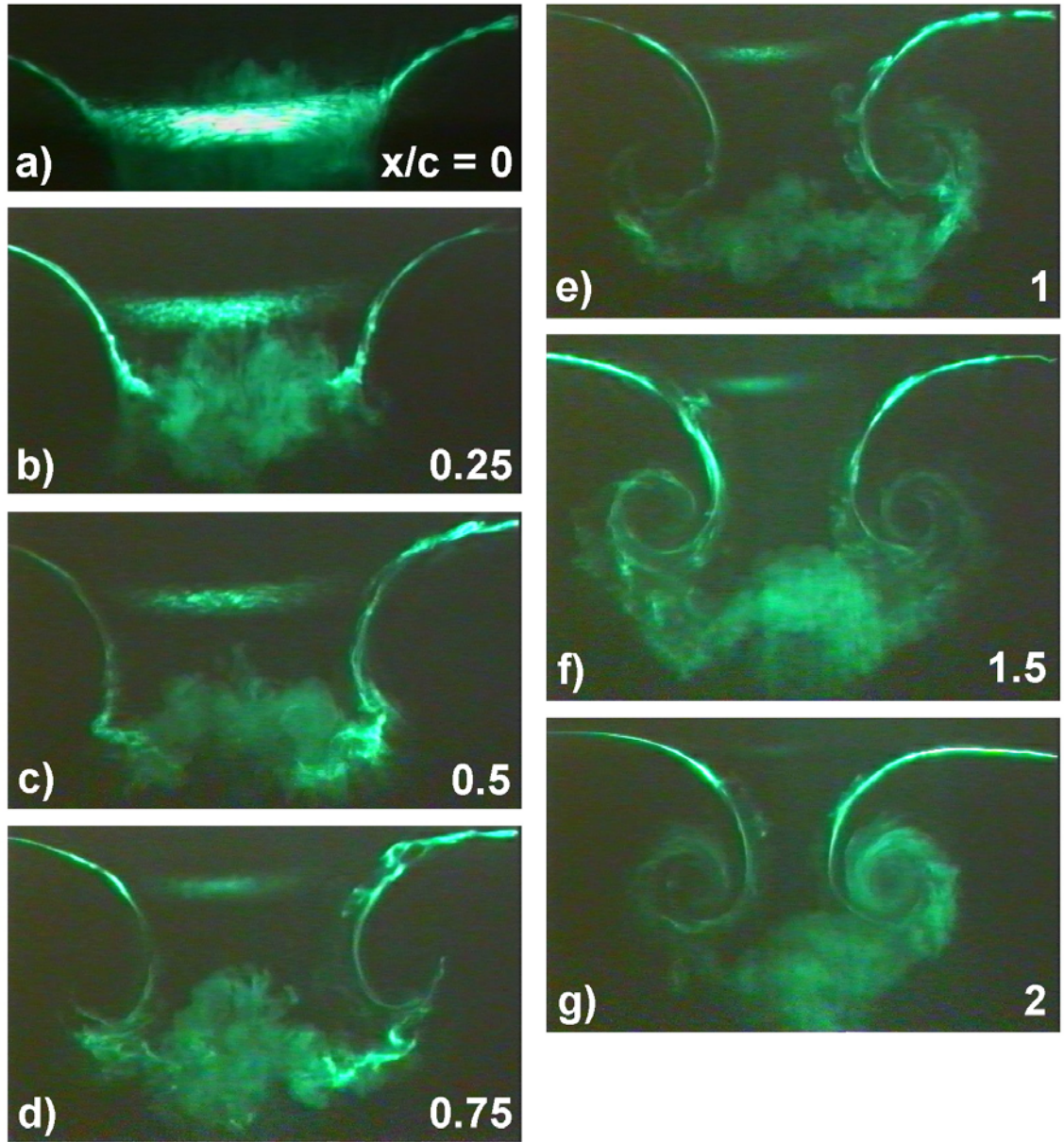


Figure 5.53 Cross-sectional slices through the wake, downwash and trailing vortex structures. Each slice was located aft of a non-spinning disc-wing at a range of positions, up to two chord lengths downstream from the trailing edge. An electrically heated wire vaporised oil to create smoke, visualising the flow field when illuminated by a laser light sheet, flow direction is out of the page.

$$x/c = 0 \text{ to } 2, \text{ AoA} = 10^\circ, V_\infty = 3 \text{ m/s}, \text{ Re} = 5.67 \times 10^4.$$

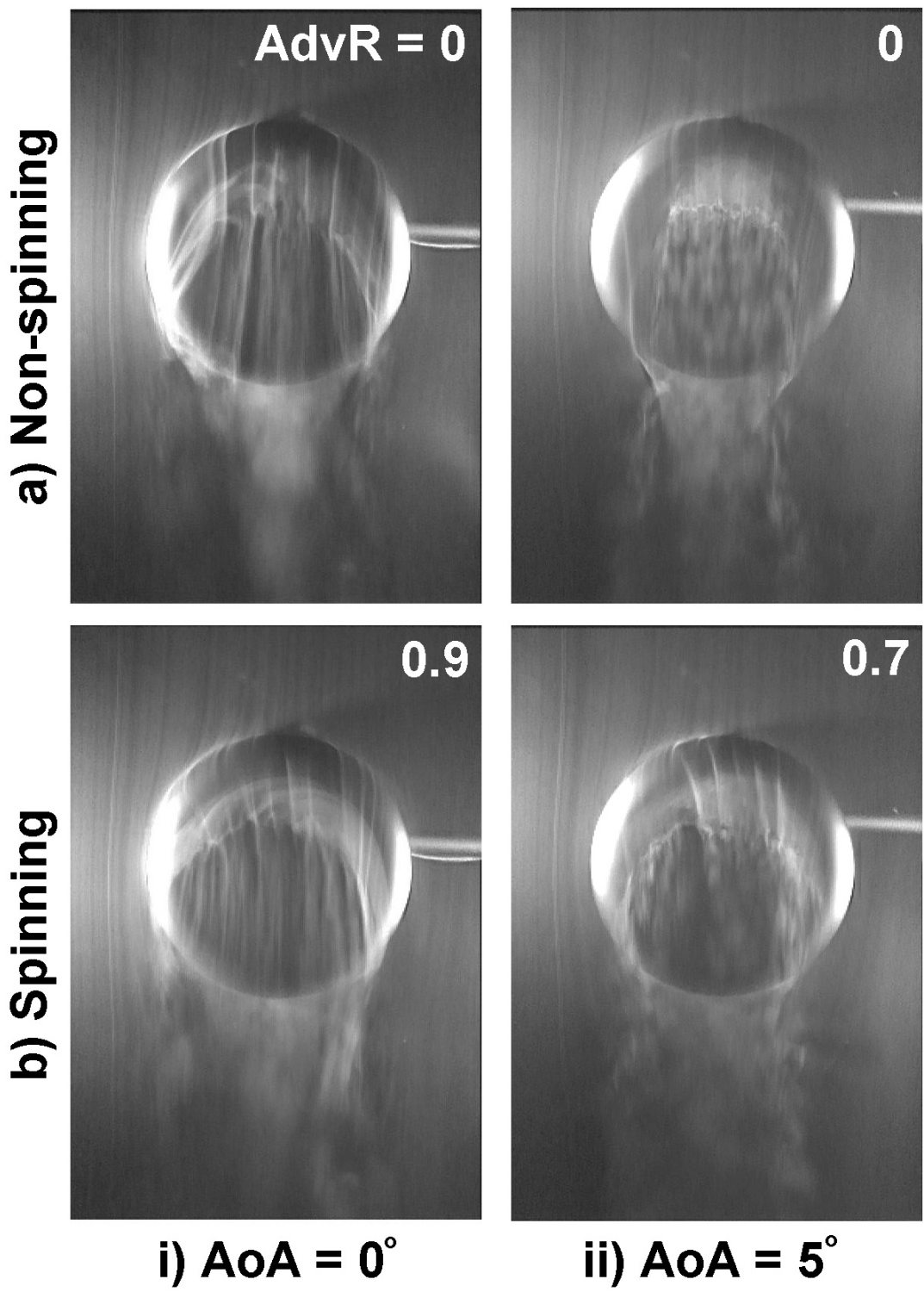


Figure 5.54 Visualisation of flow structures over the upper surface planform including the separation bubble and wake over a disc-wing, for various AoA and advance ratios. An electrically heated wire vaporised oil to create smoke, visualising the flow field when illuminated, flow direction from top to bottom.

i)  $\text{AdvR} = 0 \text{ & } 0.9, \text{AoA} = 0^\circ, V_\infty = 1.5 \text{m/s}, \text{Re} = 2.84 \times 10^4$ ,

ii)  $\text{AdvR} = 0 \text{ & } 0.7, \text{AoA} = 5^\circ, V_\infty = 3 \text{m/s}, \text{Re} = 5.67 \times 10^4$ .

b) Spinning Disc: Advancing side on the left of the figure, retreating side on the right.

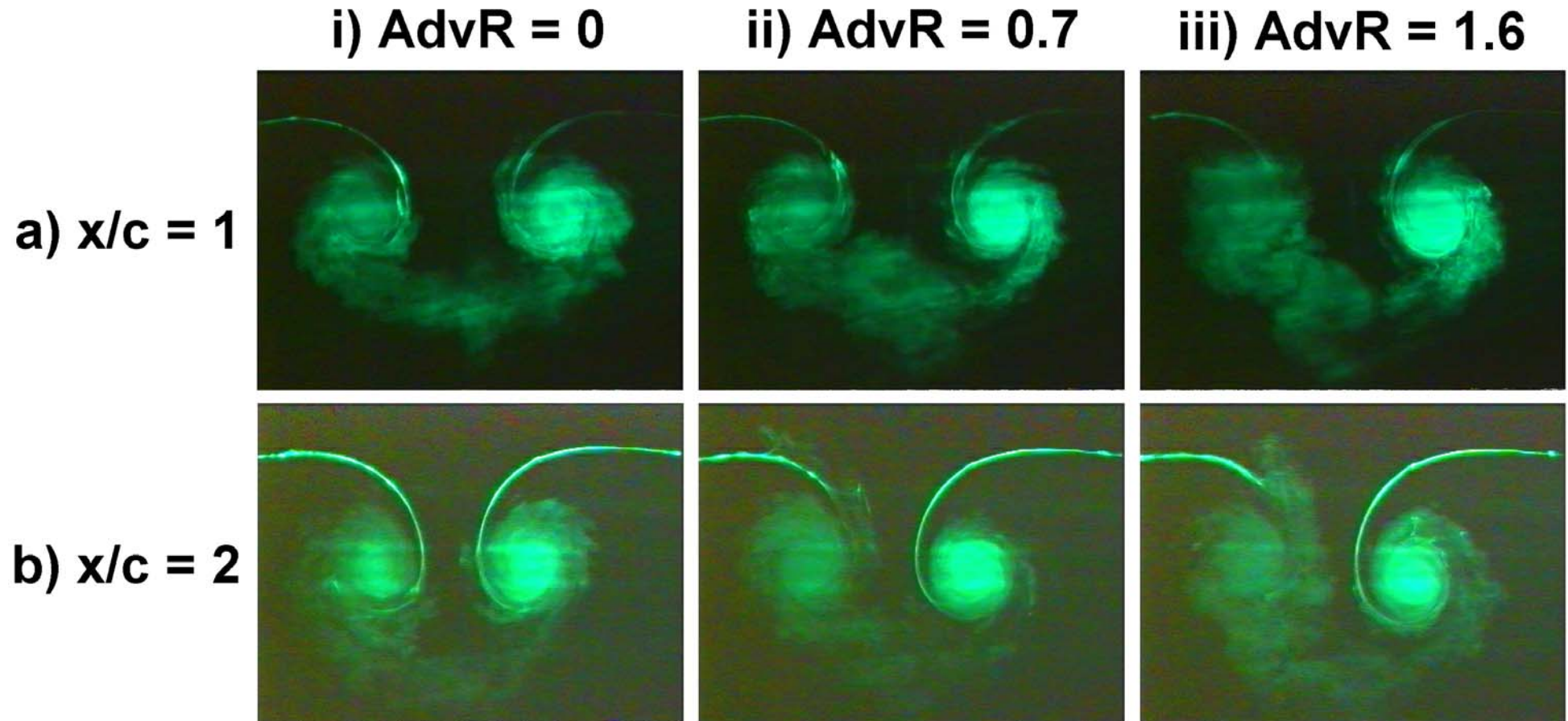


Figure 5.55 Cross-sectional slices through the wake, downwash and trailing vortex structures at various spin rates. Each slice was located aft of a disc-wing model at a couple of positions, up to two chord lengths downstream of the trailing edge. An electrically heated wire vaporised oil to create smoke, visualising the flow field when illuminated by a laser light sheet, flow direction is out of the page.

Advancing side on the left of the figure, retreating side on the right.  $x/c = 1 \& 2$ ,  $\text{AdvR} = 0, 0.7 \& 1.6$ ,  $\text{AoA} = 10^\circ$ ,  $V_\infty = 3\text{m/s}$ ,  $\text{Re} = 5.67 \times 10^4$ .



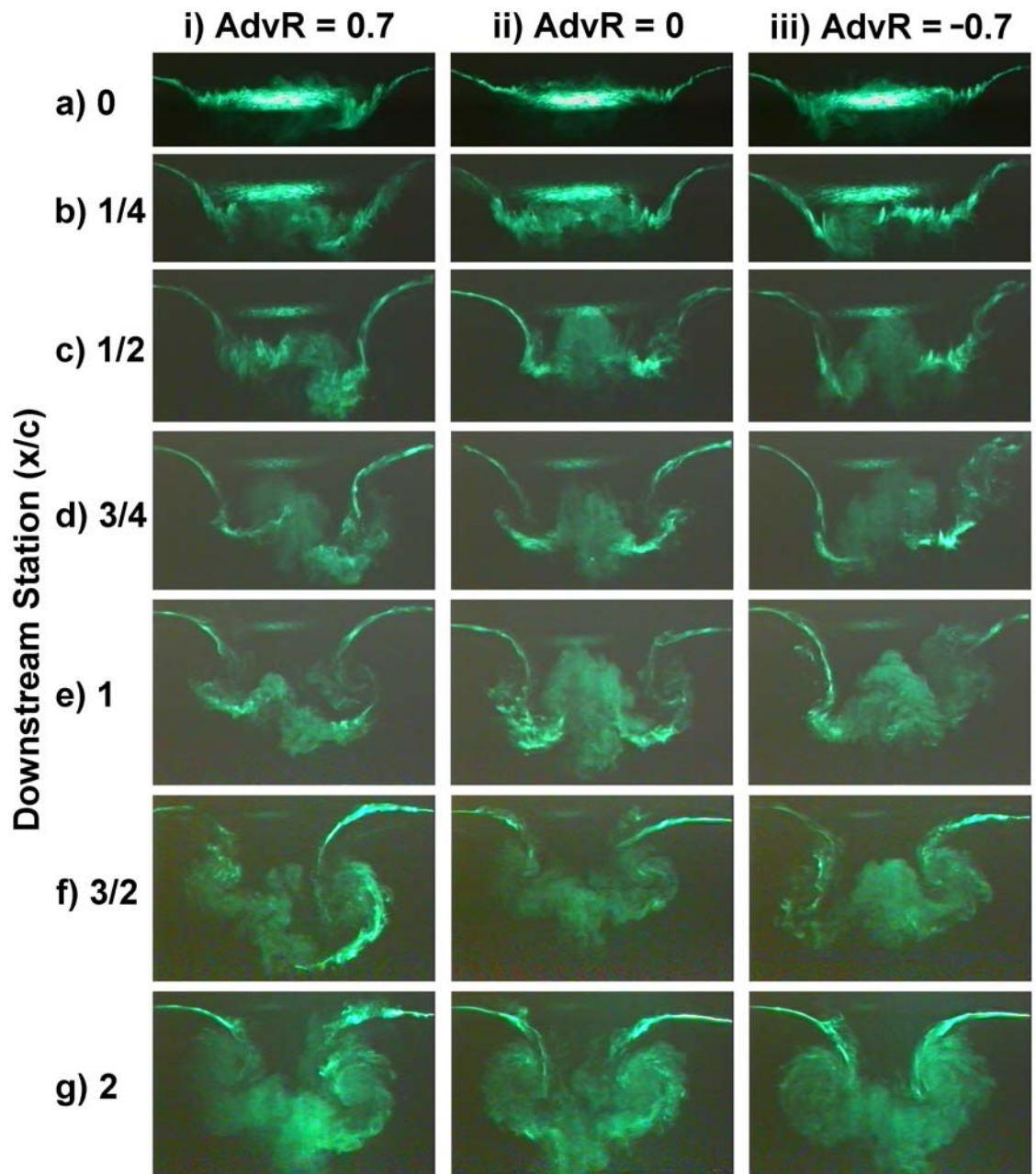
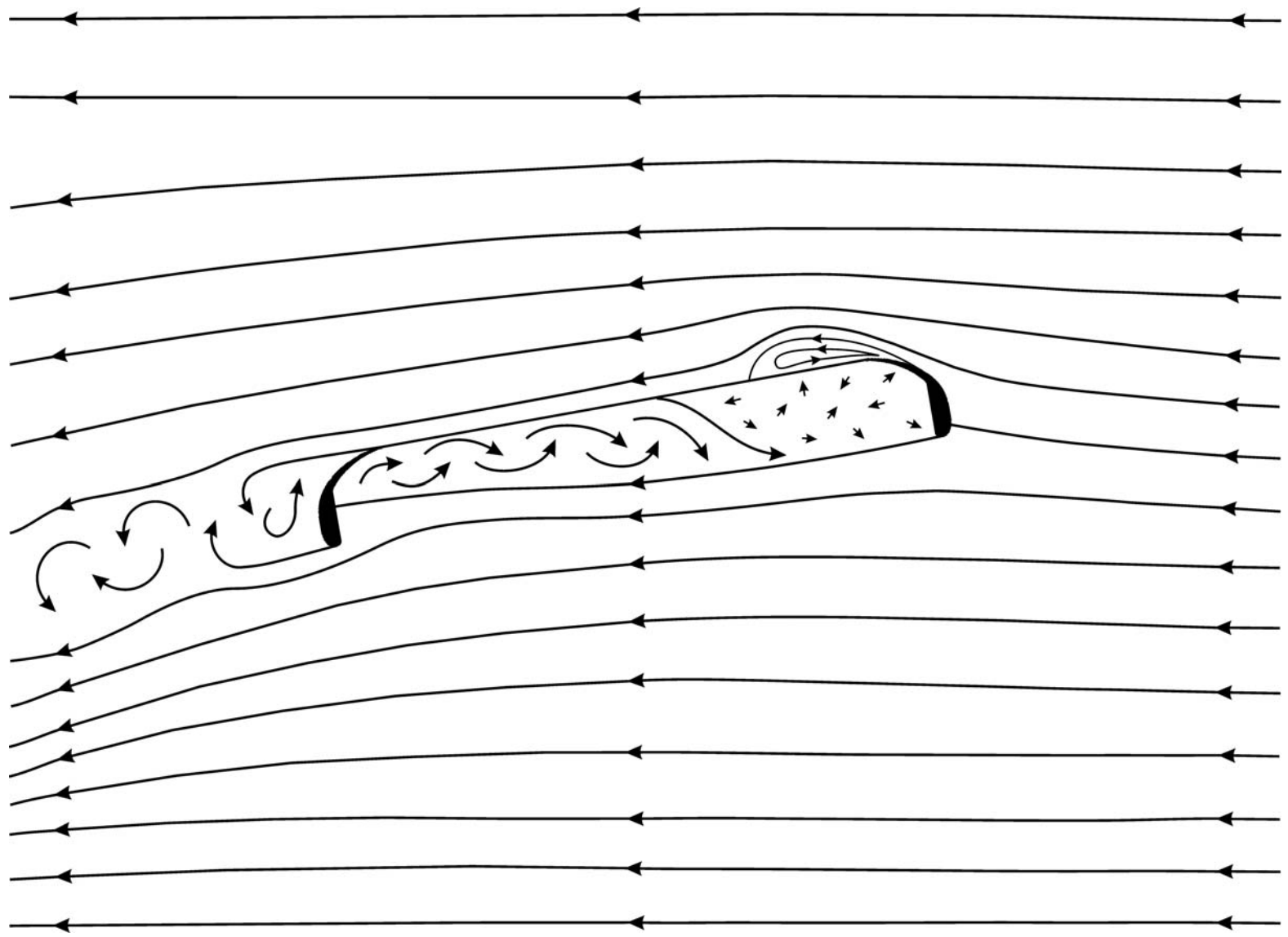


Figure 5.56 Cross-sectional slices through the wake, downwash and trailing vortex structures at various advance ratios including opposite spin directions. Each slice was located aft of a disc-wing model at a range of positions, up to two chord lengths downstream from the trailing edge. An electrically heated wire vaporised oil to create smoke, visualising the flow field using laser light sheet illumination, flow direction is out of the page.  $x/c = 0$  to  $2$ ,  $\text{AdvR} = -0.7, 0 \& 0.7$ ,  $\text{AoA} = 5^\circ$ ,  $V_\infty = 3\text{m/s}$ ,  $\text{Re} = 5.67 \times 10^4$ .

- i) Advancing side on the left of the figure, retreating side on the right.
- iii) Advancing side on the right of the figure, retreating side on the left.

Figure 6.1 Two-dimensional central cross-sectional flow topology for a non-rotating disc-wing at  $10^\circ$  AoA. The proposed topology is based upon the flow visualisation, depicting many of the flow structures, namely the separation bubble, cavity flow and turbulent wake. Flow direction from right to left.



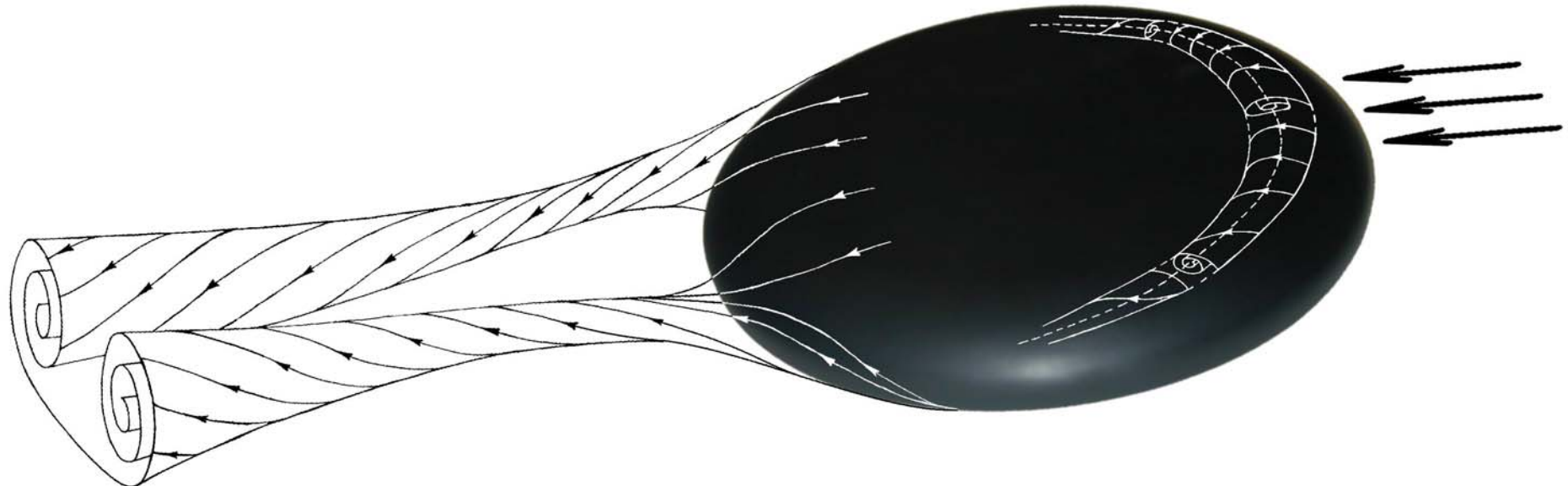
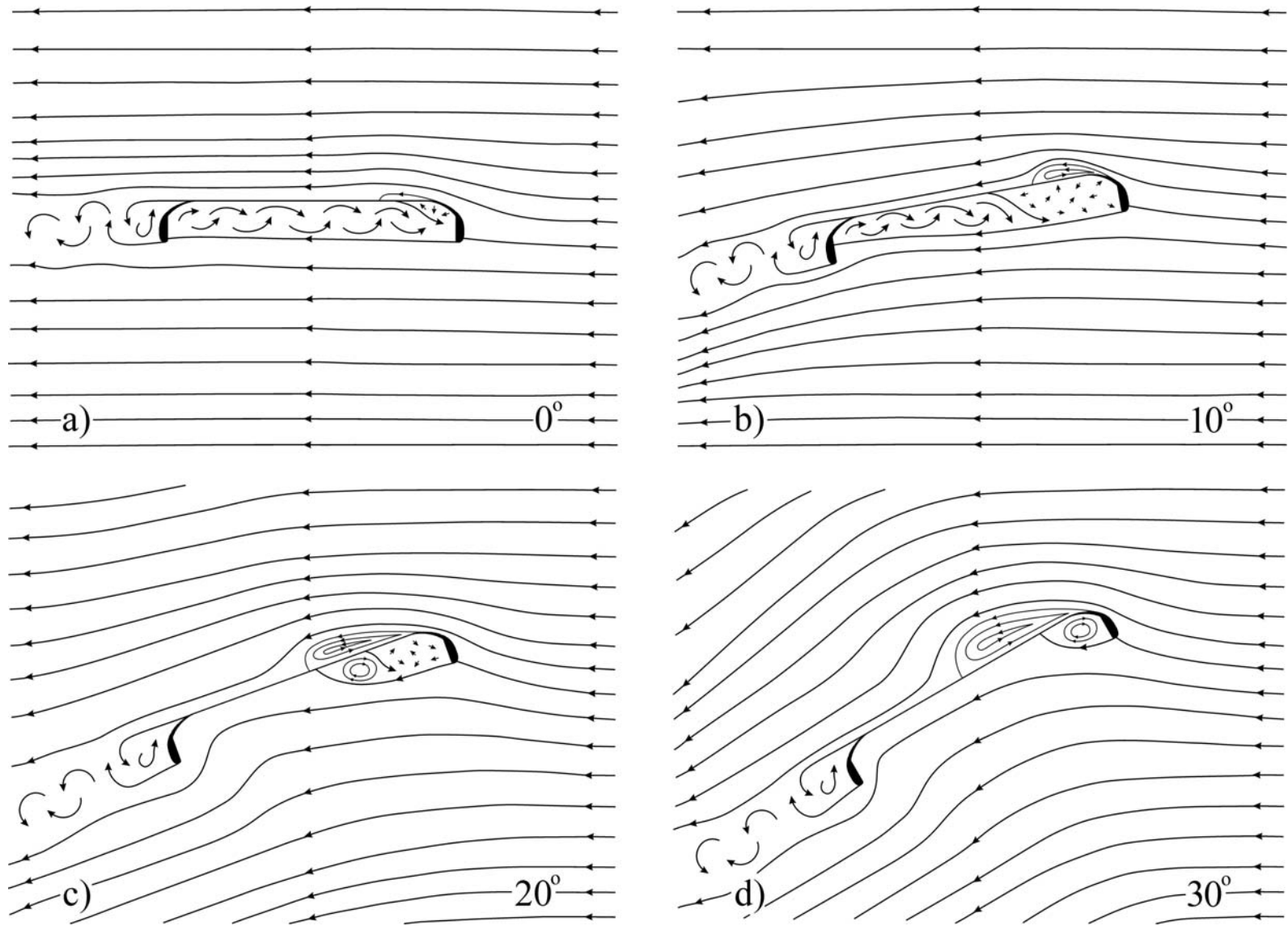


Figure 6.2 Three-dimensional flow topology for a non-rotating disc-wing at 10° AoA.

The proposed topology is based upon the flow visualisation, depicting many of the flow structures, namely the separation bubble and trailing vortices. Flow direction from right to left.

Figure 6.3 Two-dimensional central cross-sectional flow topology for a non-rotating disc-wing for a range of AoA. Each proposed topology is based upon the flow visualisation, depicting many of the flow structures, namely the separation bubble, cavity flow and turbulent wake. Flow direction from right to left, AoA =  $0^\circ$  to  $30^\circ$ .



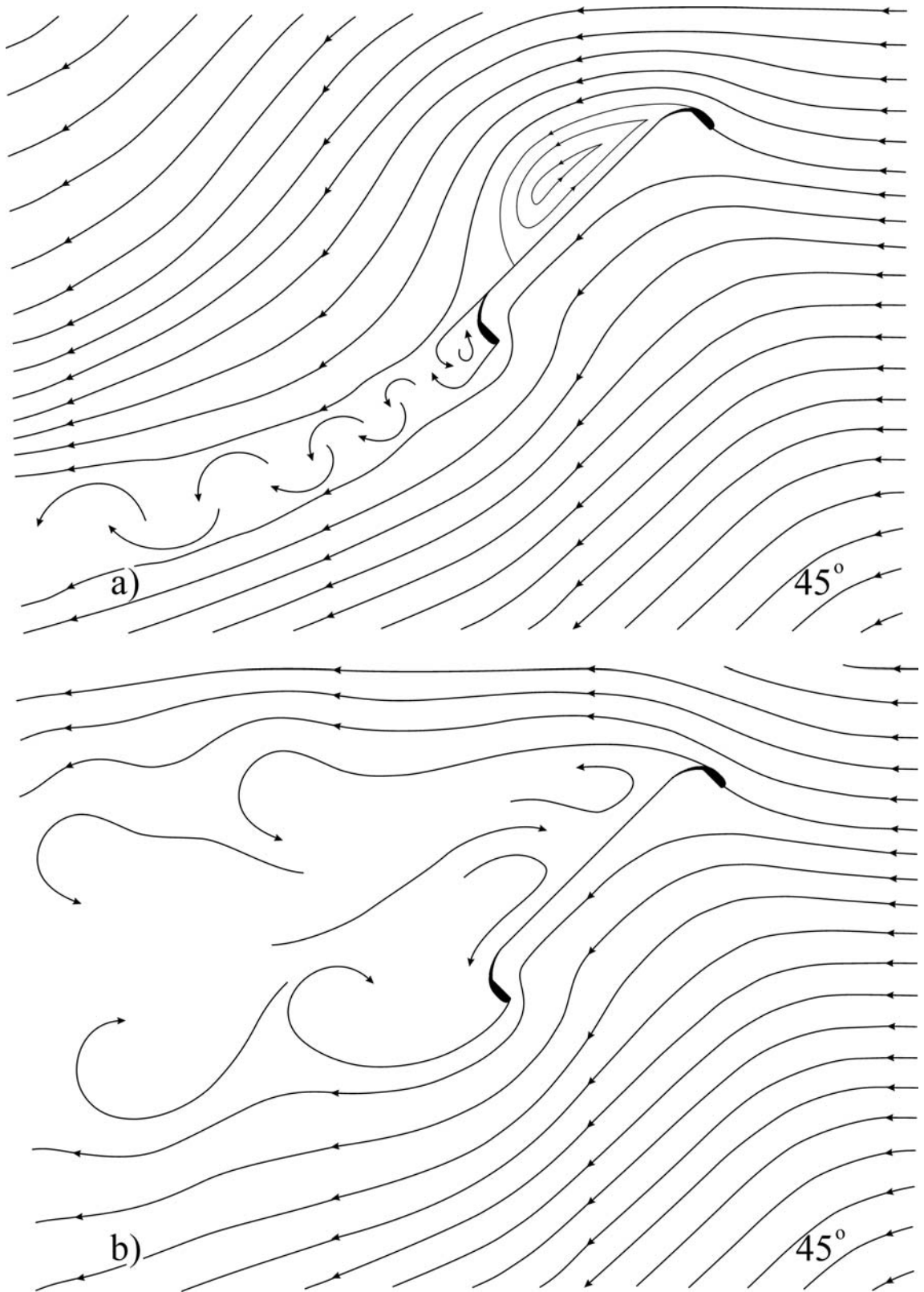
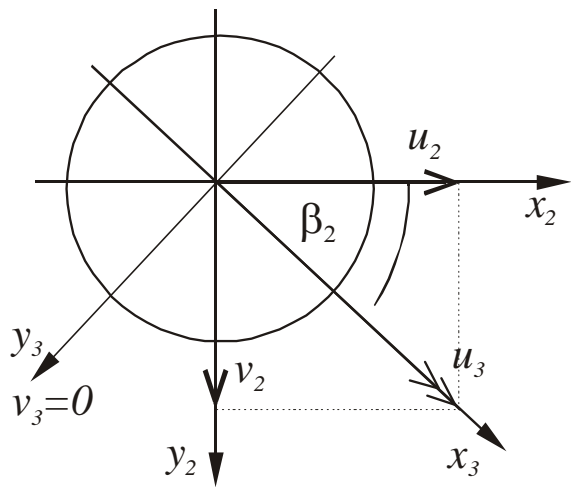
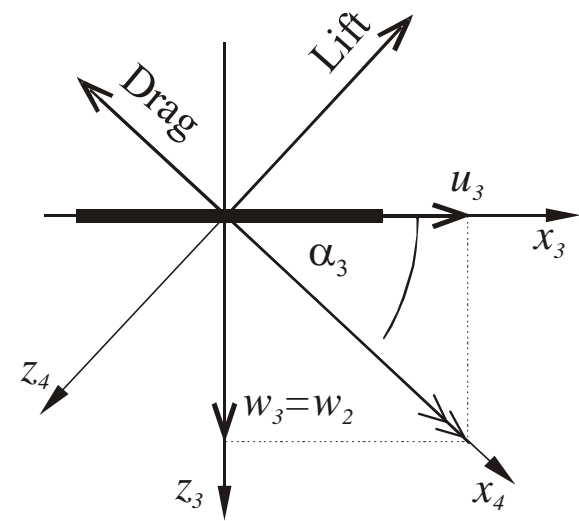


Figure 6.4 Two-dimensional central cross-sectional flow topology for a non-rotating disc-wing at 45° AoA, pre- (a) and post-stall (b). Each proposed topology is based upon the flow visualisation, depicting many of the flow structures, namely the separation bubble and turbulent wake. Flow direction from right to left, AoA = 0° to 30°.



(a) Zero sideslip body axes  $(xyz)_3$ , obtained by rotation of body axes  $(xyz)_2$  through  $-\beta_2$



(b) Relative wind axes  $(xyz)_4$ , obtained by rotation of zero sideslip body axes  $(xyz)_3$  through  $-\alpha_3$

Figure 7.1 Additional axes systems used for the disc-wing simulation.

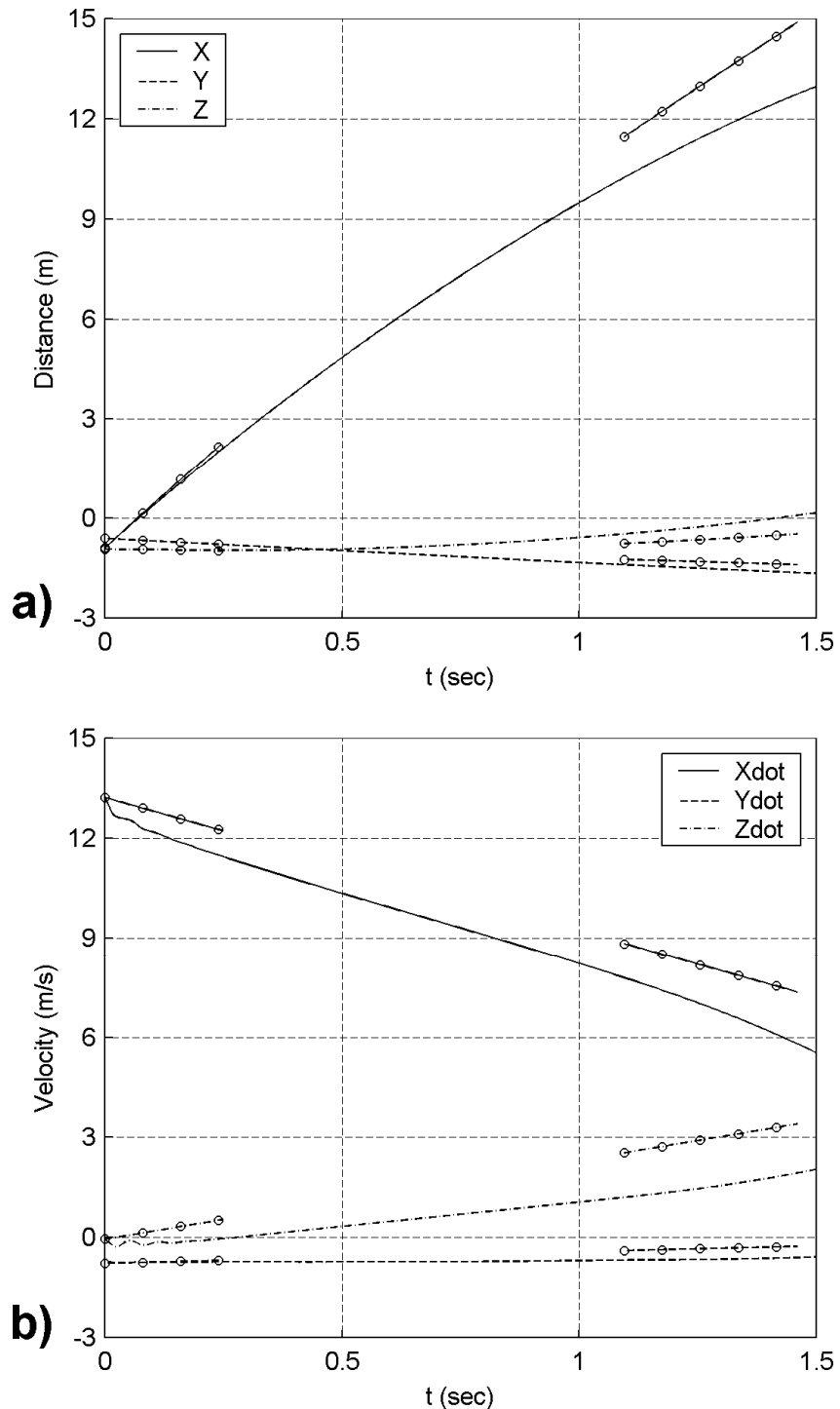
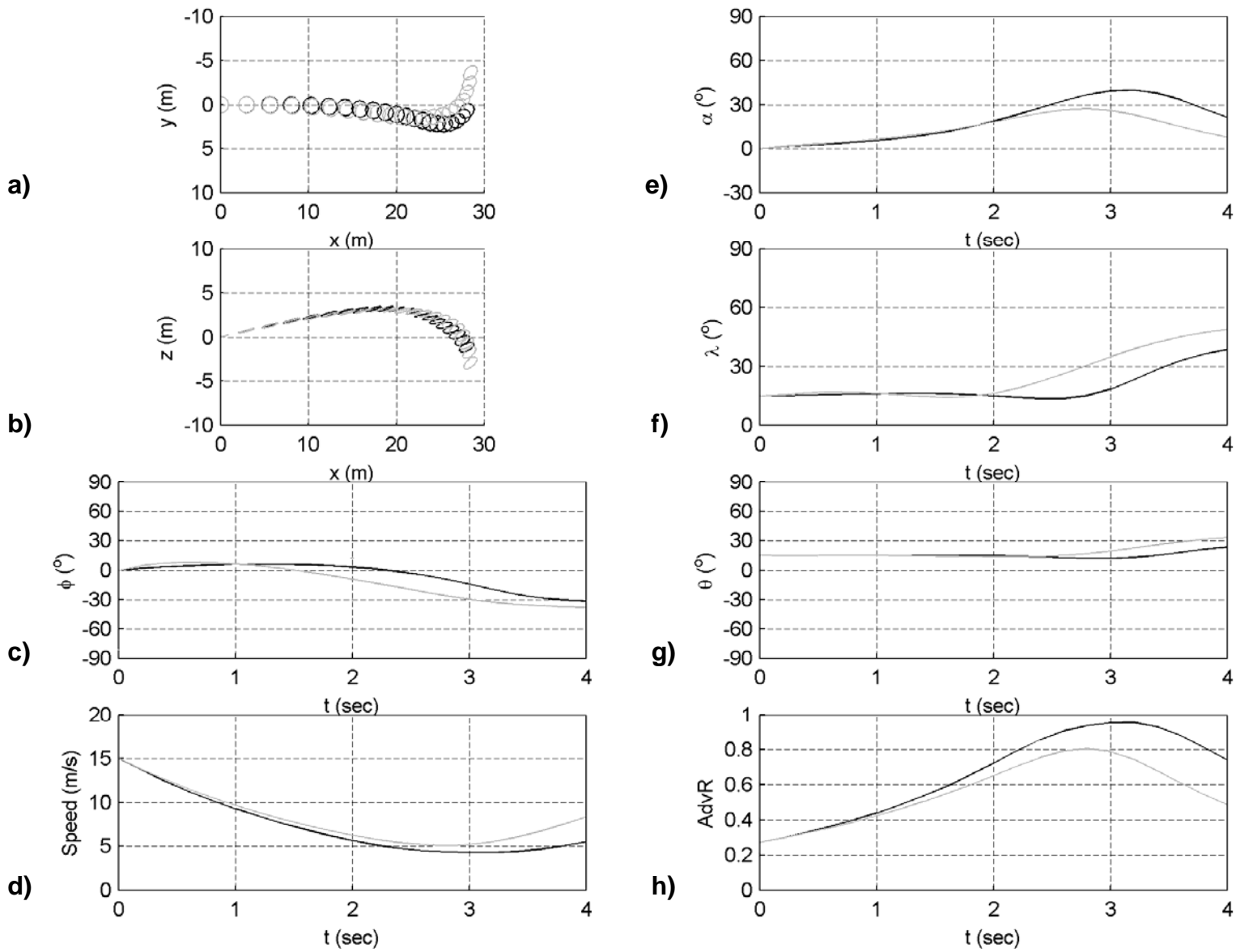
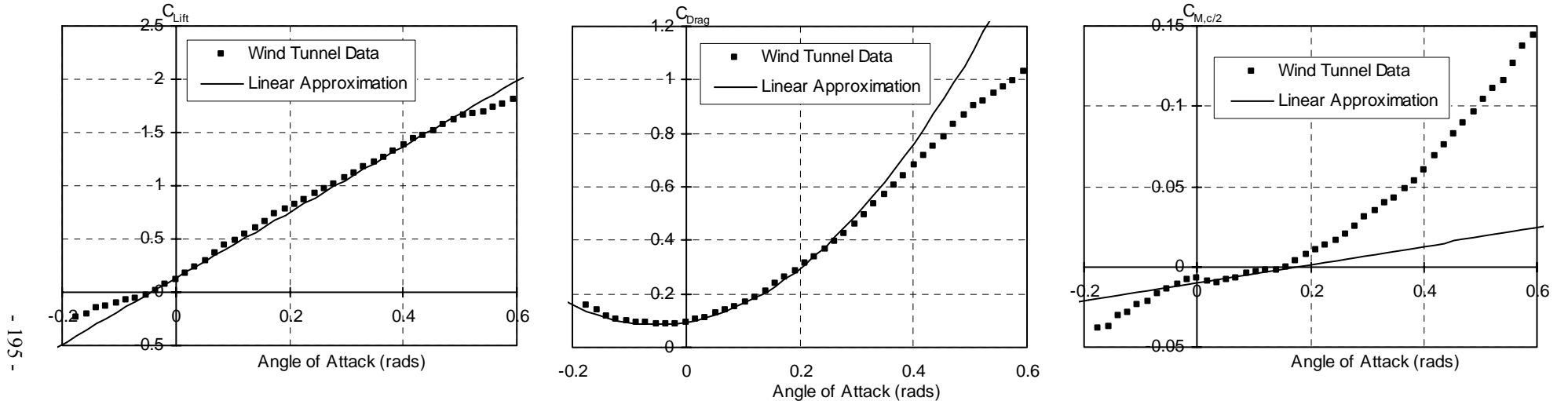


Figure 7.2 Comparison of simulated results (no dots) with experimental time histories (dots) from flight tests (flight f2302; Hummel, 2003), for an identical set of initial conditions, given below.

$Xe_o$	$Ye_o$	$Ze_o$	$u_o$	$v_o$	$w_o$	$\phi_o$	$\theta_o$	$\psi_o$	$p_o$	$q_o$	$r_o$
<i>m</i>	<i>m</i>	<i>m</i>	<i>m/s</i>	<i>m/s</i>	<i>m/s</i>	<i>rad</i>	<i>rad</i>	<i>rad</i>	<i>rad/s</i>	<i>rad/s</i>	<i>rad/s</i>
-0.90	-0.63	-0.91	4.48	12.52	1.84	-0.07	0.21	5.03	-26.3	-5.19	52.85

Figure 7.3 Trajectory plots and parameter time histories for a simulated Frisbee flight path. Solid lines correspond to results from using the full non-linear aerodynamic model. Grey lines correspond to results from using a linear approximation.





(a) Lift coefficient.

$$C_{Lift} = C_{Lift_0} + C_{Lift_\alpha} \alpha$$

$$[C_{Lift_0} = 0.13, \quad C_{Lift_\alpha} = 3.09]$$

(b) Drag coefficient.

$$C_{Drag} = C_{Drag_0} + C_{Drag_\alpha} (\alpha - \alpha_0)^2$$

$$[C_{Drag_0} = 0.085, \quad C_{Drag_\alpha} = 3.30, \quad \alpha_0 = -0.052]$$

(c) Pitching moment coefficient.

$$C_M = C_{M_0} + C_{M_\alpha} \alpha$$

$$[C_{M_0} = -0.01, \quad C_{M_\alpha} = 0.057]$$

Figure 7.4 Comparison of the Frisbee-like disc-wing wind tunnel data to the linear approximations for use in the simulation.

The alpha dependent aerodynamic coefficients are governed by the equations beneath each respective figure, linear derivatives given also. Angle of attack range given in radians, AoA = -0.2 to 0.6 rads.

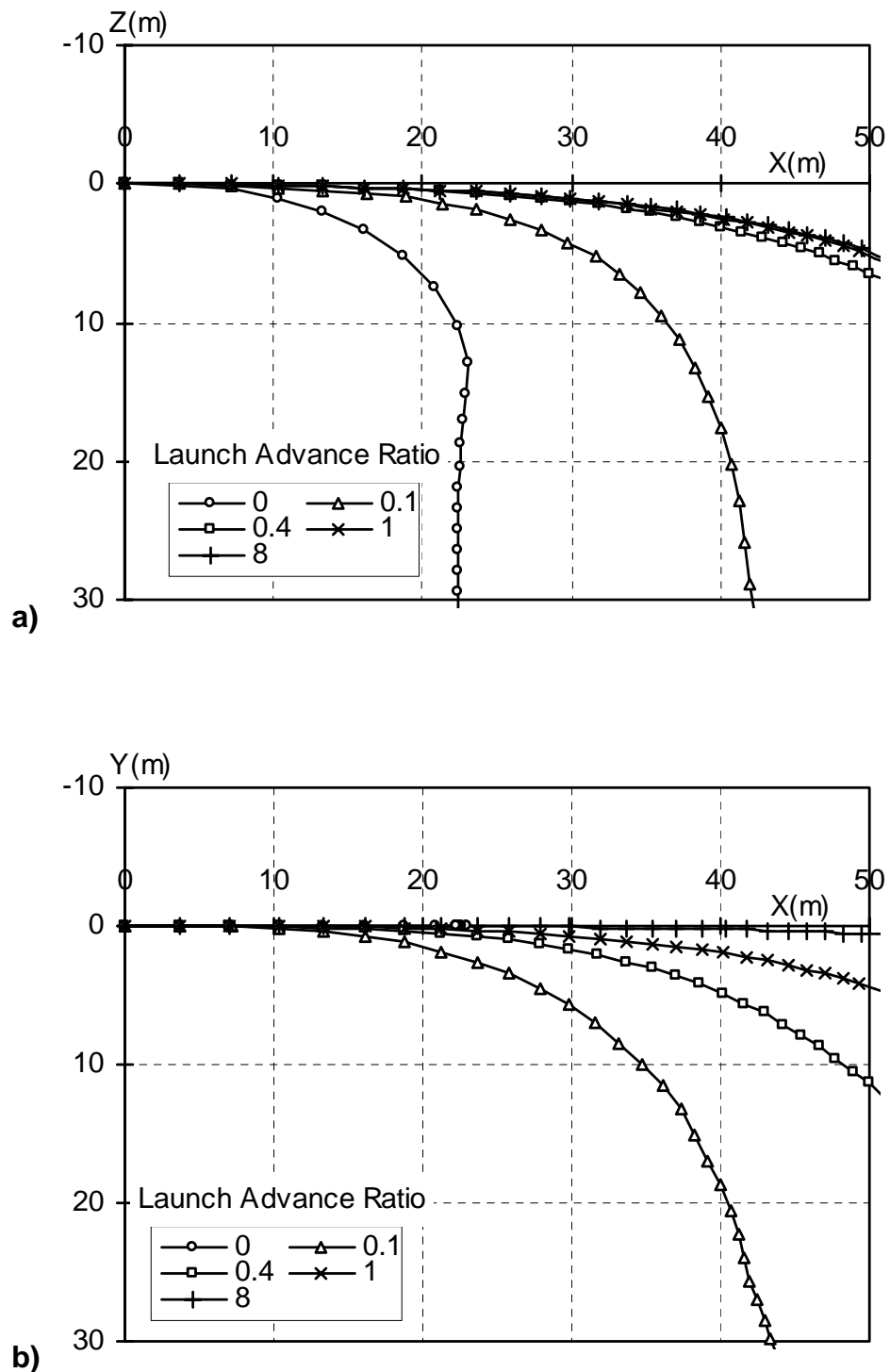


Figure 7.5 Effect of launch conditions (advance ratio) on disc-wing XZ and XY trajectories. The time interval between each data point is 0.2 seconds.

$$\phi_L = 0^\circ, \theta_L = 0^\circ, \psi_L = 0^\circ, \alpha_L = 0^\circ, V_L = 19 \text{ m/s}, \text{AdvR} = 0 \text{ to } 8.$$

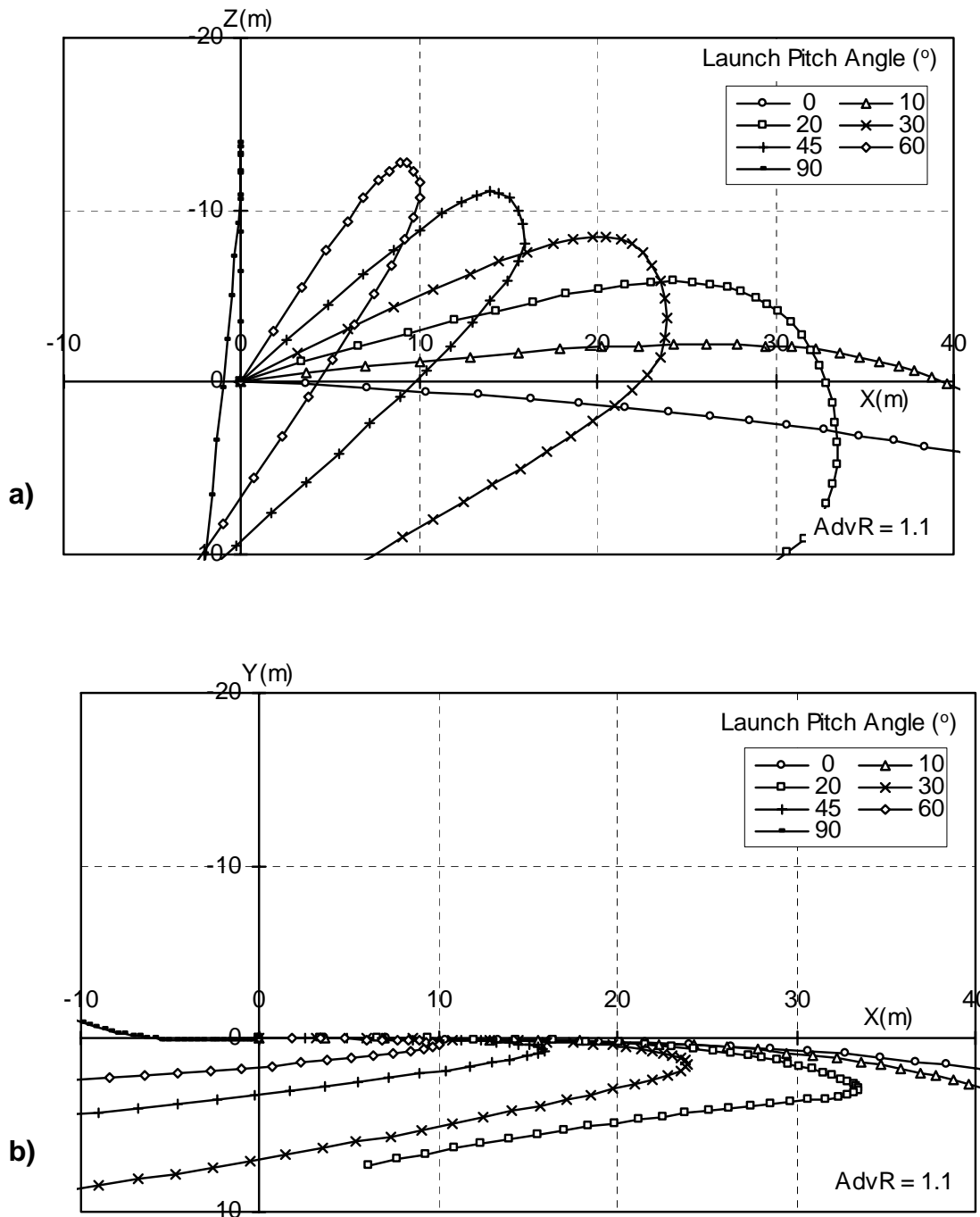


Figure 7.6 Effect of launch conditions (pitch angle) on disc-wing XZ and XY trajectories. The time interval between each data point is 0.2 seconds.

$$\phi_L = 0^\circ, \theta_L = 0^\circ \text{ to } 90^\circ, \psi_L = 0^\circ, \alpha_L = 0^\circ, V_L = 19 \text{ m/s}, AdvR = 1.1.$$

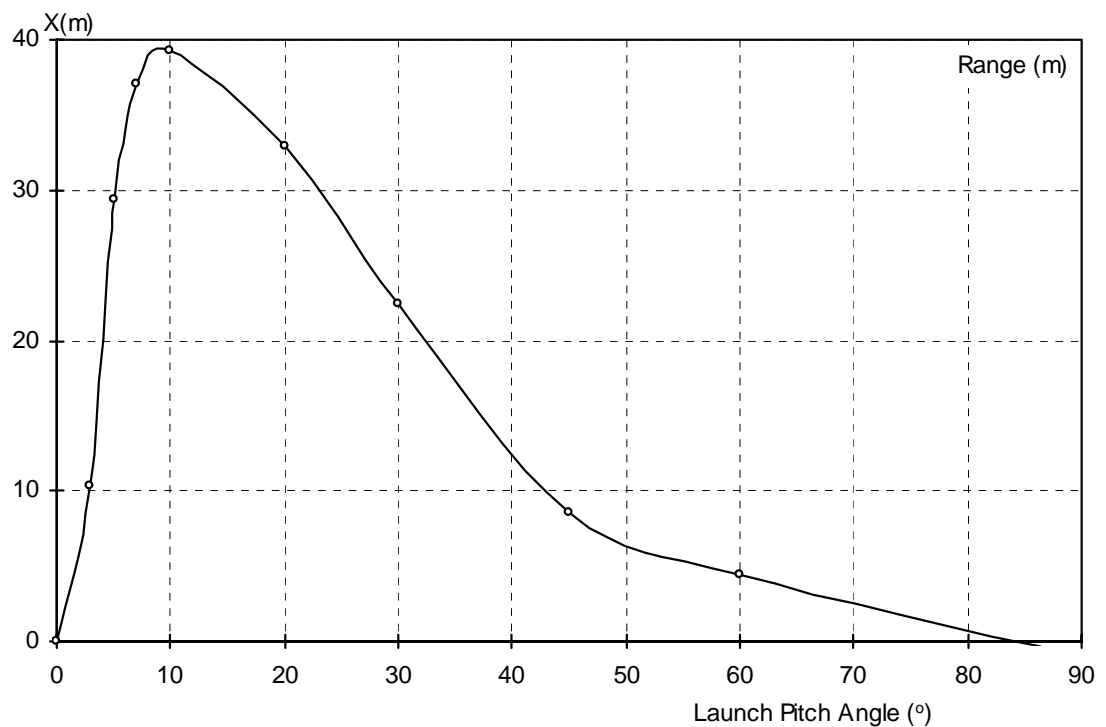


Figure 7.7 Range as a function of launch pitch angle.

Maximum range occurs at  $\theta_L = 10^\circ$ .

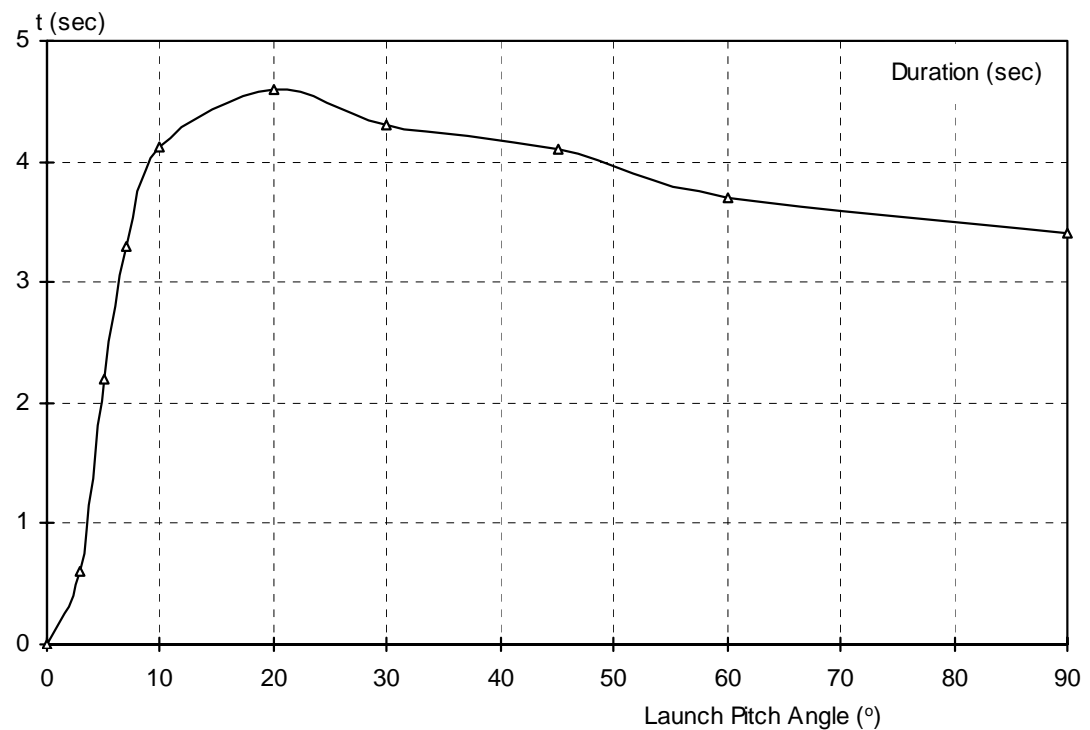


Figure 7.8 Flight duration as a function of launch pitch angle.

Maximum duration occurs at  $\theta_L = 20^\circ$ .

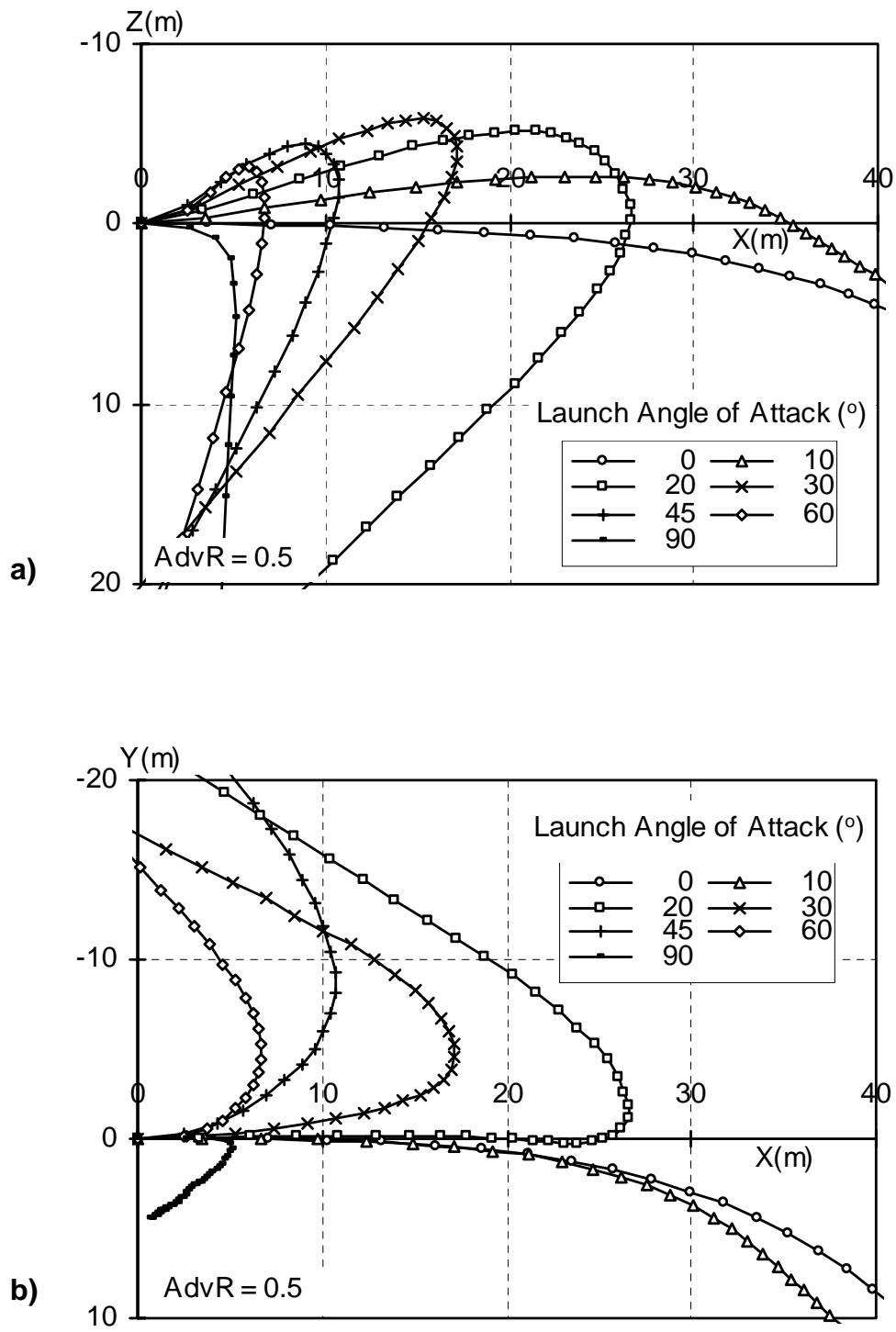


Figure 7.9 Effect of launch conditions (angle of attack) on disc-wing XZ and XY trajectories. The time interval between each data point is 0.2 seconds.

$$\phi_L = 0^\circ, \theta_L = 0^\circ, \psi_L = 0^\circ, \alpha_L = 0^\circ \text{ to } 90^\circ, V_L = 19 \text{ m/s}, AdvR = 0.5.$$

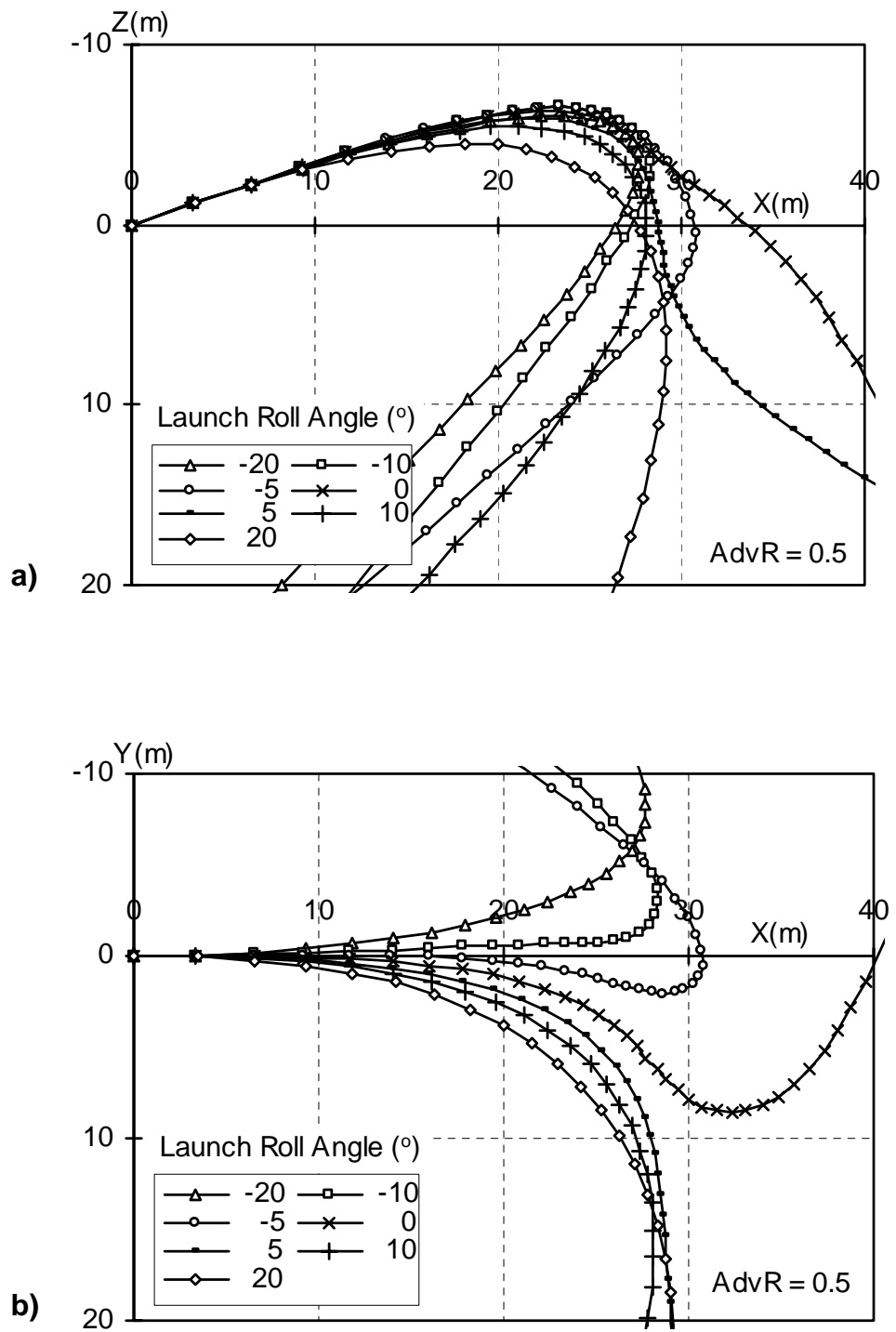


Figure 7.10 Effect of launch conditions (roll angle) on disc-wing XZ and XY trajectories. The time interval between each data point is 0.2 seconds.

$$\phi_L = 0^\circ \text{ to } 90^\circ, \theta_L = 0^\circ, \psi_L = 0^\circ, \alpha_L = 0^\circ, V_L = 19 \text{ m/s}, \text{AdvR} = 0.5.$$

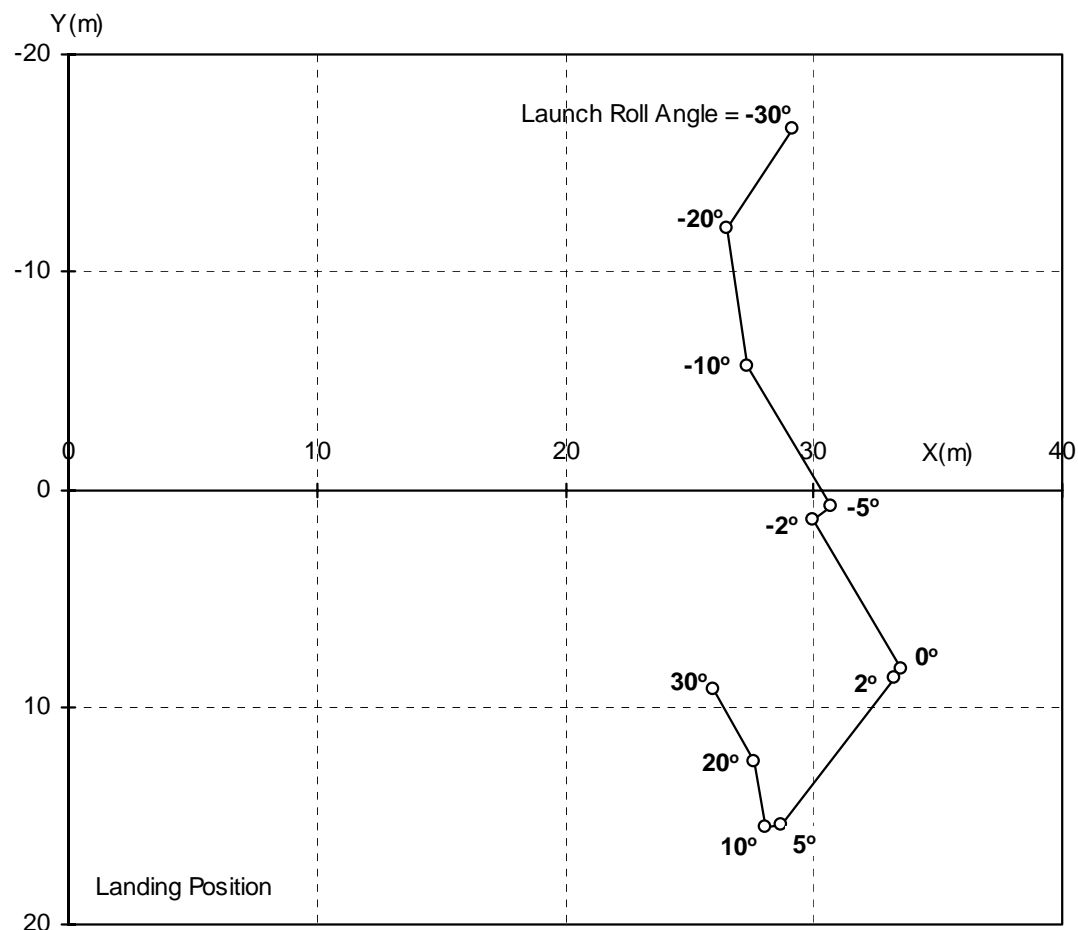


Figure 7.11 Disc landing position (XY location at which Z=0) as a function of launch roll angle. Re-plotted from data in Fig. 57.8a.

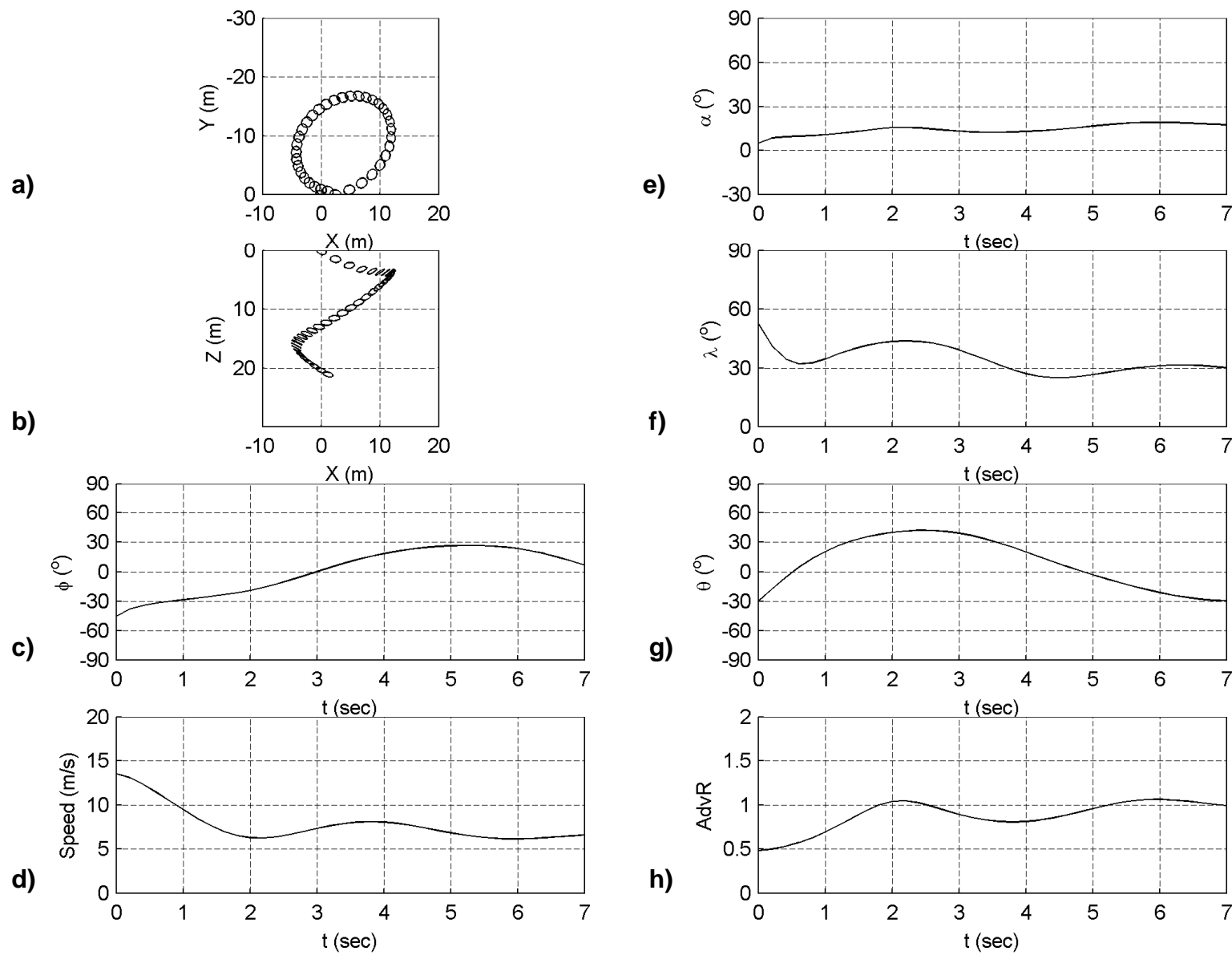
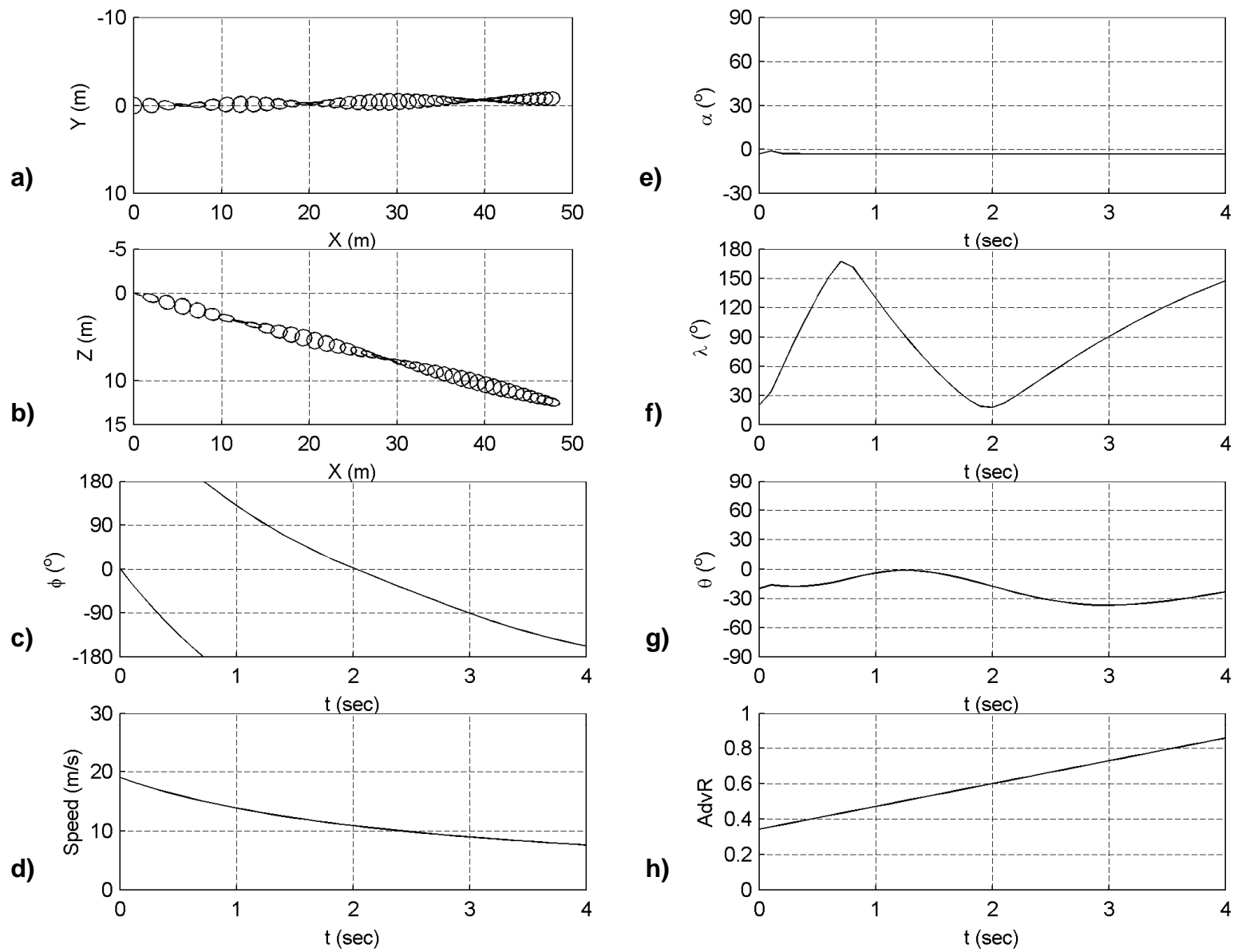
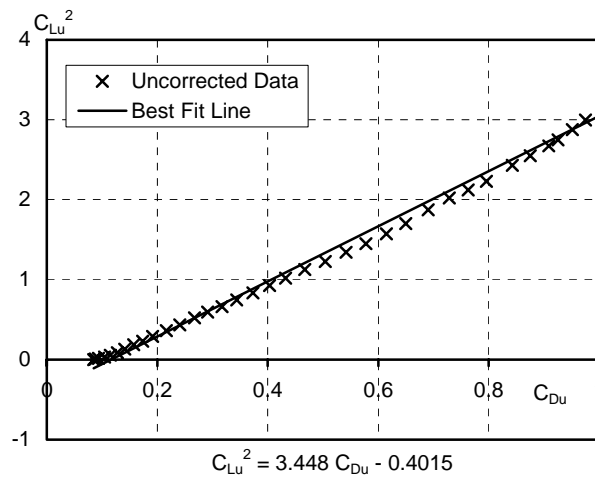


Figure 7.12 Trajectory plots and parameter time histories for a simulated spiral turn manoeuvre obtained using a constant rolling moment control input.

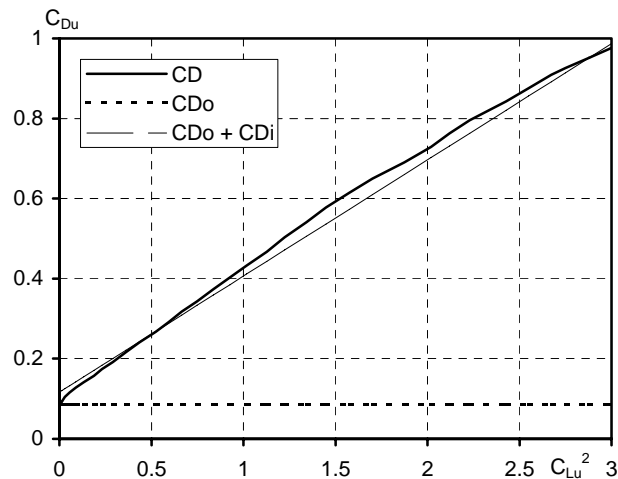
$$\phi_L = -45^\circ, \theta_L = -30^\circ, \psi_L = 0^\circ, \alpha_L = 5^\circ, V_L = 13.5 \text{ m/s}, C_{Lcontrol} = 0.1, AdvR = 0.5.$$

Figure 7.13 Trajectory plots and parameter time histories for a simulated spiral roll manoeuvre obtained using a constant pitching moment control input.  
 $\phi_L = -0^\circ$ ,  $\theta_L = -20^\circ$ ,  $\psi_L = 0^\circ$ ,  $\alpha_L = -3^\circ$ ,  $V_L = 19 \text{ m/s}$ ,  $C_{Mcontrol} = 0.2$ ,  $AdvR = 0.34$ .

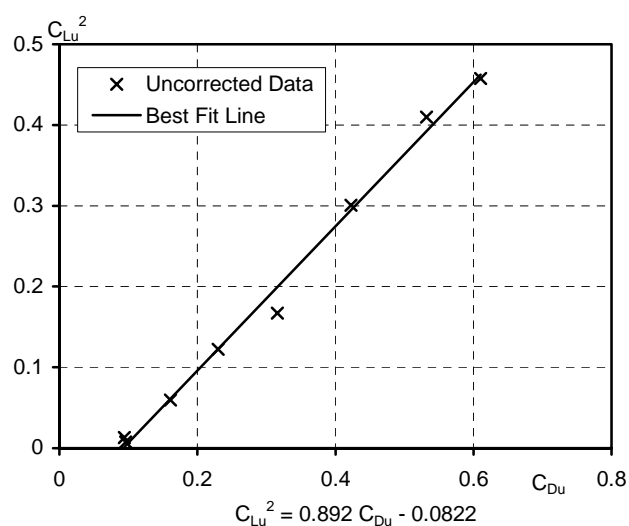




(a) Uncorrected lift data taken in the wind tunnel  $C_{Lu}^2$  plotted against uncorrected drag data  $C_{Du}$ , equation of the best fit line given.

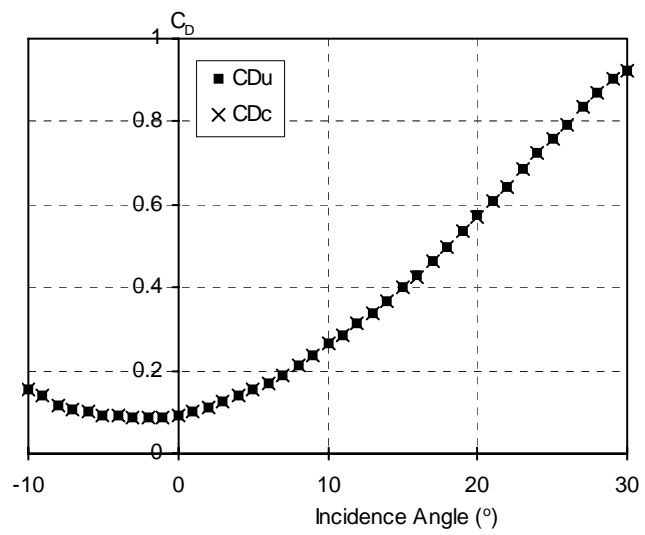


(b) Disc-wing drag analysis for a lifting wing, after Maskell (Fig. 8, 1965).

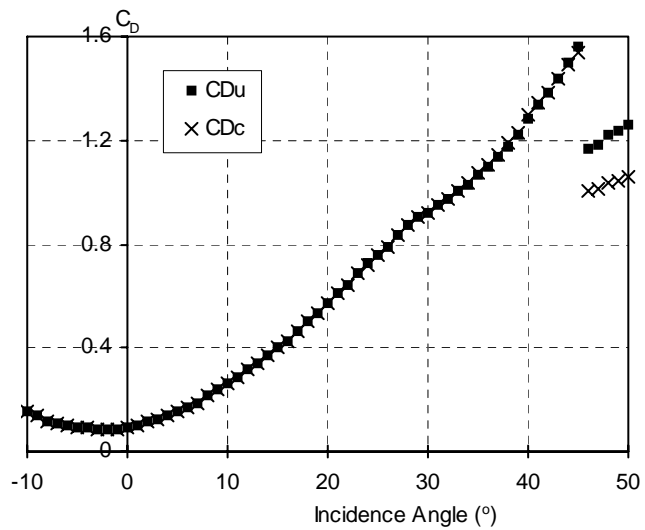


(c) Uncorrected wind tunnel data  $C_{Lu}^2$  plotted against  $C_{Du}$ , for the negative AoA range, equation of the best fit line given.

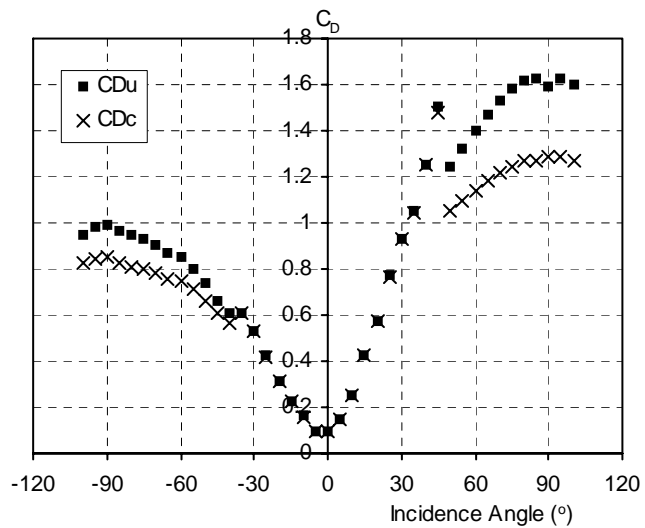
Figure C.1



(a) AoA  $-10^{\circ}$  to  $30^{\circ}$

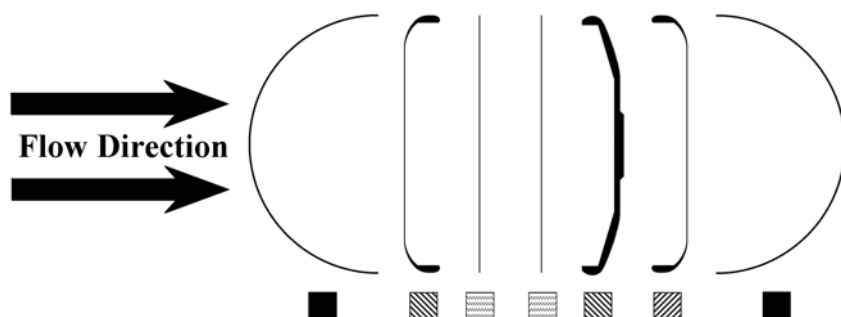
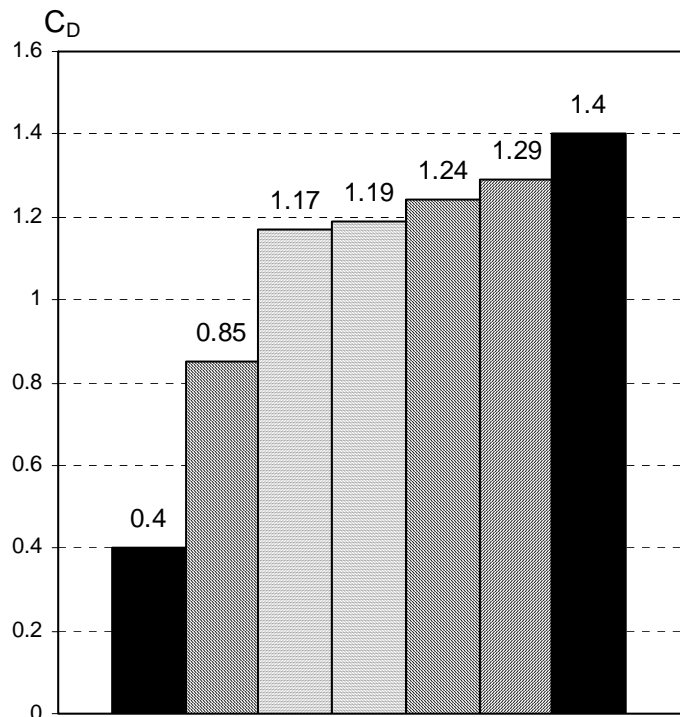


(b) AoA  $-10^{\circ}$  to  $50^{\circ}$



(c) AoA  $-100^{\circ}$  to  $100^{\circ}$ .

Figure C.2 Corrected and uncorrected drag results for various AoA ranges.



- 3D Hemispherical Cup, Rim facing downstream (White 1999)
- ▨ Disc-wing, Rim facing downstream (Potts & Crowther 2002)
- Flat Plate Disc (White 1999)
- Flat Plate Disc (Potts & Crowther 2002)
- ▨ Disc-wing, Rim facing upstream (Stilley & Carstens 1971)
- ▨ Disc-wing, Rim facing upstream (Potts & Crowther 2002)
- 3D Hemispherical Cup, Rim facing upstream (White 1999)

Figure C.3 Experimentally measured open face bluff body drag coefficients for various disc planform configurations (Potts & Crowther, 2002), compared to similar shapes detailed in White (1999) and Stilley & Carstens (1971), AoA = +90° or -90°.

## **Appendices**

## **Appendix A History of the Frisbee**

### **A.1 Introduction**

‘As the sun gleams through the trees, the lingering memory of the stifling oven heat fades away, deeply engrossed in the newly discovered leisure activity. Tracking a flying iron plate as it crosses the grass this way and that, falling over themselves to pluck the low-flyer out of the sky and re-launch onto the next human target.’

This was the scenario outside the Olds Baking Company in Connecticut, USA around the middle of the 20<sup>th</sup> century, workers would toss their deep rimmed backing tins to and fro during lunch breaks. Through some modification to the basic pie tin shape, coupled with the birth of plastics in the 1950s, this small town anomaly was exported to the world as the endearingly familiar form of the Frisbee disc.

### **A.2 Wham-O’s Frisbee™ disc**

William Russell Frisbie moved to Bransford, Connecticut, USA where he began to manage a branch of the Olds Baking Company in 1871. His success led to buying the bakery to form the Frisbie Pie Company, increasing production to supply a number of East Coast shops. It is this humble pie making family from which the Frisbee derives not only its name but the basic shape also. There is some dispute as to whether Cookie-tin lids or Pie-tins were thrown as the first prototype but the commercial value was realised thereafter with the birth of plastic in the 1940’s and growing interest in flying saucers from outer space.

Walter Frederick Morrison of West Coast USA bought an injection mould in the late 1940’s and began production of his first flying disc design. His first design was the somewhat brittle Morrison’s Flyin’ Saucer disc which had a tendency to shatter on impact with a hard surface. His superior design, the Sputnik, flew much more successfully and became the inspiration for all subsequent Frisbee designs.

Rich Knerr and A. K. Melin started a toy company on leaving the University of Southern California in the early 1950’s. They saw Morisson’s Flying Saucers thrown on Californian beaches and targeted Morrison in 1955 making him a proposition to increase production. In 1957 the Wham-O Pluto Platter was sold across the US and

succeeding models became collectively labelled Frisbee after the misspelling of the original Frisbie pie family.

### **A.3 Professional Sport Disc Development**

Many flying disc related sports were developed largely during the 1960's with Wham-O's vice president Ed Headrick driving the development of the Professional Frisbee Model in 1964 and founding the International Frisbee Association. The Guts Frisbee Championship among other events were initiated during this period. Ultimate, probably the most widely played flying disc sport today, was devised in 1969. From small beginnings the flying disc matured from its toy status to become a serious sport implement.

Ed Headrick appears as the inventor of the 'Flying Saucer' on a patent application granted in 1976 (Headrick E, 1976), the first of many flying disc designs protected under law. Disc design also matured driven largely by the increasing popularity of Disc Golf, which is much the same idea as 'ball' Golf. Just as the professional golfer has a variety of clubs, the pro-disc golfer carries a number of discs for various situations. For example, a well designed driver disc has minimum drag for maximum range and little tendency to divert from a straight-line trajectory. The distance record currently stands at 250m held by Christian Sandstrom thrown on 26<sup>th</sup> April 2002 with an Innova<sup>TM</sup> DX Valkyrie disc.

A more detailed history of the Frisbee disc is given by Johnson (1975).

## **Appendix B Disc-wing Aircraft R&D**

### **B.1 Introduction**

Disc-wing based flight vehicles fall into two distinct categories:

1. Non-rotating, non-axisymmetric body.
2. Spin-stabilised, axisymmetric body.

The first type will typically have a conventional airfoil cross-section when viewed from the side with a rounded leading edge and sharp trailing edge and thus defined flight orientation. This type of vehicle has the characteristics of a flying wing aircraft with low aspect ratio and as such is relatively conventional. The second type of flight vehicle by definition has an airfoil section with fore and aft symmetry and a centre of gravity at the centroid of the disc. This configuration will typically be unstable in pitch and for practical purposes must be inertially stabilised by spinning. Such a disc has no predefined flight orientation.

### **B.2 Literature Review: In Brief**

Research and development into circular planform air vehicles has a diverse history. The concept of a circular planform flying wing (XF-5U-1) was developed during the 1930s & 40s based on a family of three dimensional circular wings with cross-sectional profile based on the Clark Y airfoil (Zimmerman, 1935).

In the 1950s a circular VTOL (vertical take off and landing) air-vehicle known as the Avrocar (VZ-9AV) was developed with a central ‘turborotor’ which generated lift and control forces through a combination of annular nozzles and peripheral jets (Frost & Earl, 1959; Greif & Tolhurst, 1963; Murray, 1990).

In the early 1960s, NASA researchers investigated the suitability of disk shapes for reentry vehicles (Demele & Brownson, 1961; Ware, 1962). The proposed lenticular (bi-convex lens-like) shape was part of a preliminary investigation to develop a lifting-body (wingless) reentry vehicle with conventional landing capabilities.

In 1972 the U.S. Navy commissioned a project to further the development of a spin-stabilised self-suspended flare (Stilley & Carstens, 1972; Stilley, 1972), which was essentially a spin-stabilised axi-symmetric cambered wing with circular planform.

The Moller M200X, a disc planform aircraft with distributed engines driving eight individual fans, was the culmination of over thirty years of research and development. Flown in and near hover (1989) the pilot and chief designer, Dr. Paul Moller, furthered this work to develop a personal air vehicle known as the M400 Skycar (Moller, 1998).

In 1996 Imber & Rogers (1996) looked at a low aspect ratio circulation control wing with circular planform, similar to the geometry tested by Demele & Brownson (1961), at zero angle of attack. Annular slots were cut into the rim to allow active tangential blowing over a Coanda surface to modify the near surface flow structures and the global circulatory flow. The tangential blowing, particularly at the trailing edge, favourably modified the lift. The pitching and rolling moments were modified by symmetric and asymmetric blowing, respectively.

With the recent development of such a wide variety of UAV body shapes it is not surprising to find the re-emergence of the disc-wing. The ‘Cypher’ VTOL UAV (Sikorsky Aircraft Corp.) with circular planform encompasses a central rotor and ducted airstream similar to the Avrocar. The Cypher II Marine variant, ‘Dragon Warrior’, adds a conventional wing and another smaller ducted tail fan for longer endurance and range.

The SiMiCon Rotor Craft (SRC) UAV (Glaskin, 2002) has a circular planform fuselage with airfoil cross-section for cruise and retractable rotor blades for VTOL capability.

Slightly smaller was the AeroVironment (DARPA funded, Phase I) Micro Air Vehicle (MAV), a six-inch diameter circular planform wing, remotely piloted with propeller and elevons for control, developed in the mid-1990s. Phase II, a rectangular planform MAV now, due to redefined design criteria, is known as the Black Widow MAV (Grasmeyer & Keenon, 2001).

Smaller still is a silicon wafer integrated MAV under development by Washabaugh et al (2000) at the University of Michigan. It comprises an array of Helmholtz resonators distributed over a thin disc-plate, harnessing synthetic jet technology to provide both lift and control.

Higuchi et al (2000) investigated the flow over a similar disc-wing using smoke wire flow visualisation and PIV (particle image velocimetry) measurements aiming to

provide information for UAV applications.

### **B.3 History of the Circular Planform**

The history of the circular planform for aerospace applications is drawn from sporadic military research and development for various purposes such as signal flares, ground effect research, supersonic cruisers and re-entry vehicles.

#### **B.3.1 Chance-Vought XF-5U-1**

Charles H. Zimmerman conceived the idea for a circular planform aircraft concept in the 1930's, based on a family of three dimensional wings with cross-sectional profile based on the Clark Y airfoil. He won a National Advisory Committee for Aeronautics (NACA) design competition in 1933 with a disc planform concept aircraft capable of flying at high speeds and hovering. NACA chose not to fund the project further but undeterred Zimmerman moved to Chance-Vought in 1937 and began work on an aircraft based upon this disc-wing design. The preliminary stage of the programme to develop a high-speed fighter-bomber for the US Navy, which could operate off small carriers, went ahead. The experimental prototype V-173 was tested in the wind tunnel and test flown from 23 November 1942 proving Zimmerman's circular wing concept practical. It was capable of Short Take Off and Landing (STOL), ideal for carrier missions, but could not quite manage hover with the existing engines. It did however demonstrate remarkable low-speed performance, the circular wing planform design providing the ability to fly at extremely high angles of attack without stalling. The Navy was impressed and ordered the construction of a successor. The XF-5U-1 aircraft was completed but never flown, the programme was cancelled in 1947 as jet engines began to offer greater high-speed advantages.

#### **B.3.2 Avro's Special Projects Group**

In 1947 John Frost, a British aeronautical engineer, joined Avro-Canada to oversee their CF-100 fighter programme. He became chief of Avro's Special Projects Group (SPG) in 1952, formed to develop advanced aircraft for the Canadian Defence Research Board. The board funded start-up studies to develop a Vertical Take Off and Landing (VTOL) fighter aircraft capable of supersonic speeds under the codename 'Project Y'. Frost and his team began design and feasibility studies to meet these criteria and started to build a prototype. Development problems and investment limitations brought the involvement of the US Air Force (USAF) in 1953, who saw great promise in the flying disc concept.

The USAF assigned US scientists to the programme and made US research facilities available to the SPG. The Air Force renamed the programme ‘Project Silver Bug’ continuing research to develop a supersonic disc-shaped aircraft. Frost and his team developed various prototypes over the next five years including supersonic fighters and spy-planes with circular planform. Escalating costs finally halted work on the latest supersonic version (Weapon System 606A) in 1958 and work began on the joint Army-Air Force Avrocar (VZ-9AV) programme. Utilising WS 606A research, Frost built a subsonic Ground Effect Take Off and Landing (GETOL) disc-shaped aircraft, the ‘flying jeep’ concept. The GETOL principle harnessed a circular jet curtain to form an air cushion, similar to a hovercraft. The Avrocar had a central ‘turborotor’ which generated lift and control forces through a combination of annular nozzles and peripheral jets. This enabled the vectoring of air jets to provide lateral thrust but once the vehicle moved forward it became unstable, increasingly so as it lifted out of ground effect (~2m). Modifications to solve the stability problems caused the programme to overrun and in 1960 the Avrocar concept was discontinued.

### **B.3.3 Lenticular Re-entry Vehicle**

In the early 1960s NASA became interested in various geometries conceived for the development of an unpowered, reusable, wingless, lifting body aircraft capable of conventional landing after atmospheric reentry. Three prototypes were investigated as part of a preliminary study (M2-L1, M1-L, L-2C) including the ‘Lenticular Re-entry Vehicle’. Scientists at the NASA research facilities developed various designs, such as the Ames M2-F1 ‘flying bathtub’, the M1-L ‘half-cone’ and the Langley L-2C ‘lenticular body’ which were all variations on the wingless lifting body concept. The lifting body reentry concept had many advantages over non-lifting reentry capsules such as lower peak heating rates and decelerations during atmospheric reentry, conventional horizontal landing, manoeuvrability to a pre-selected landing site and a deeper entry corridor into the atmosphere. The Lenticular body is so called due to the same generic shape as an optical lens i.e. a convex curve on both the upper and lower surfaces with circular planform. Such a vehicle would achieve reentry at high angles of attack (~90°) to utilise the maximum drag exhibited by a disc planform configuration. After reentry a decrease in AoA would allow the generation of lift and aerodynamic control for manoeuvrability to achieve stable glide and horizontal landing. After wind tunnel tests to investigate the feasibility as a practical reentry vehicle, the lenticular lifting body was considered ‘too exotic’ for the programme. The favoured M2-F1 design was constructed

by NASA Dryden in conjunction with a local glider company that incorporating elevons and rudders for control. It was first flown by Milton Thompson in 1963 on-tow from a ground vehicle, enabling a short flight-time of 20 seconds. The prototype was shipped to NASA Ames where it was wind tunnel tested in the 40' by 80' wind tunnel. The data provided important information for aero-tow flight tests, the aircraft released from 12,000 feet descended at 3600 feet/second into smooth landing at 150 mph. This demonstrated the lifting body concept and paved the way for subsequent designs, during the 1960's the HL-10 and X-24A, revisited in the 1990's with the X-33 'VentureStar' and X-38 'Crew Return Vehicle'.

#### **B.3.4 Self-suspended Flare for Special Ordnance**

In the late 1960's the US Navy began development of a self-suspended flare based on the Frisbee flight principle. The spin-stabilised axi-symmetric flare was essentially a cambered wing with circular planform, which would ignite and air-launched to retard the vertical descent of the flare, avoiding the parasitic weight and volume of conventional parachute flares. A self combustible pyrotechnic payload contained within the cavity was ignited providing illumination whilst the flare was held in a horizontal attitude utilising gyroscopic stabilisation. Wind tunnel tests of analogous spin-stabilised projectiles such as the Frisbee, clay pigeon, right circular cylinder (low thickness to chord ratio) were tested to establish the optimum flare configuration and coupled with a computer simulation of flight trajectories the optimum delivery conditions were established also.

## Appendix C Blockage Corrections & Analysis

### C.1 Maskell's Blockage Correction

Consider Maskell's well known dynamic pressure equation,

$$\frac{q_c}{q_u} = 1 + \frac{1}{2} \frac{S_{pf}}{S_{wt}} C_{Do} + \frac{5}{2} \frac{S_{pf}}{S_{wt}} (C_{Du} - C_{Di} - C_{Do}) \quad (\text{C.1})$$

where the third term on the RHS accounts for the contribution of separated flow.  $C_{Do}$  is the profile drag,  $C_{Di}$  is the induced drag,  $C_{Du}$  is the uncorrected drag measured in the wind tunnel,  $S_{pf}$  is the projected frontal area of the model i.e. the area that the flow 'sees',  $S_{wt}$  is the wind tunnel test section area,  $q_c$  the corrected dynamic pressure and  $q_u$  the uncorrected dynamic pressure. The blockage factor 5/2 defined as adequate for most purposes (Maskell, 1965), is adequate in this case.

The ratio of the projected disc area to wind tunnel cross-sectional area is an indicator of the significance of the blockage on the results. At  $0^\circ$  AoA,  $S_{pf}/S_{wt} \sim 0.01$  whereas at  $90^\circ$  AoA,  $S_{pf}/S_{wt} \sim 0.07$ . This suggests that the blockage at typical flight angles of attack the blockage is negligible but at higher AoA and certainly above the stall AoA the blockage will likely cause around 10% error in the wind tunnel results.

Now, the corrected drag coefficient is given by,

$$C_{Dc} = C_{Du} \left/ \frac{q_c}{q_u} \right. . \quad (\text{C.2})$$

So to calculate the dynamic pressure correction (C.1) the profile drag  $C_{Do} = 0.085$  is needed, as is the uncorrected drag  $C_{Du}$  which is dependent on the incidence angle and the induced drag which is given by,

$$C_{Di} = C_{Lu}^2 \frac{dC_{Du}}{dC_{Lu}} + \Delta C_{Du} - C_{Do} \quad (\text{C.3})$$

(Barlow, Rae & Pope, 2001).

Plotting a graph of  $dC_{Lu}^2$  against  $dC_{Du}$  (Fig. C.1a) gives an approximately straight line with gradient  $dC_{Lu}^2/dC_{Du} = 3.4$  and  $C_{Du}$  axis intercept  $\Delta C_{Du} = 0.1$ . The linear nature of the curve suggests that the drag component due to separated flow is minimal and the induced drag dominate over the pre-stall incidence range. This is more evident when plotting the disc-wing case, see Fig. C.1b.

Although the boundary layer separates even at  $0^\circ$  AoA the drag increment due to the separation bubble on the leading edge does not contribute significantly to the total drag, pre-stall the induced drag dominates. Post-stall, separated flow predominates and  $C_{Do}$ ,  $C_{Di}$  are considered much smaller than  $C_{Du}$ . Approximating equation (C.1) by the form,

$$\frac{q_c}{q_u} = 1 + \frac{5}{2} \frac{S_{pf}}{S_{wt}} C_{Du} \quad (\text{C.4})$$

gives the fully separated flow correction valid for bluff bodies with leading edge separation only (Cooper et al, 1996).

The negative AoA range can be treated similarly, correcting the drag measurements using the above analysis, equation (C.1) down to  $-35^\circ$  AoA and equation (C.4) thereafter. However, when calculating the induced drag component equation (C.3),  $dC_{Lu}^2/dC_{Du} = 0.9$  and  $\Delta C_{Du} = 0.1$  based on the drag results for negative AoA, see Fig. C.1c.

Comparing corrected and uncorrected drag results for the various ranges of AoA. The blockage has little effect on the pre-stall drag (Fig. C.2a) with the corrected drag curve largely unchanged. However post-stall the fully separated wake creates a large closed fluidic recirculating separation bubble obstruction, which causes a large error in uncorrected drag (Fig C.2b). A similar situation occurs for the negative AoA range, minimal error in pre-stall ( $0^\circ$  to  $-35^\circ$ ) drag, whereas post-stall ( $-40^\circ$  to  $-100^\circ$ ) the blockage is much greater requiring a significant blockage correction, although the error is not nearly as much as for the high positive AoA range (Fig. C.2c).

## C.2 Analysis

The defining factor for the difference in drag at  $+/-90^\circ$  is the rim, which points upstream at  $90^\circ$  AoA and downstream at  $-90^\circ$ . The recirculating bubble aft of the post-stall disc has maximum diameter equal to or larger than the disc diameter itself, for a flat plate disc the separation bubble diameter is 1.3 diameters (Fail et al, 1957). For the disc-wing model at  $90^\circ$  there will be more spillage due to the cavity and rim which enlarges the separation bubble diameter and increases the blockage in the working section, which provides a large error in the drag. The validity of the blockage correction is reinforced by values for the drag coefficients of similar disc shapes found in the literature with planform normal to the airstream i.e. at  $+/-90^\circ$  AoA. Fig. C.3 shows experimentally measured and corrected drag coefficients for a disc-wing and flat plate disc compared to those quoted in White (1999) for a 3D hemispherical cup and a flat plate disc.

The wind tunnel measured and corrected drag results (Potts & Crowther 2002) for the disc-wing are a  $C_D$  of 1.29 with the rim pointing upstream and 0.85 when the rim points downstream. The maximum measured  $C_D$ , 1.29, for a disc-wing at  $90^\circ$  compares well with that of Stilley & Carstens (1971, 1972), 1.24, for a similarly shaped disc-wing (Fig. C.3). The measured disc-wing results lie within the comparable upper and lower values quoted in White (1999) for a 3D hemispherical cup or shell (Fig. C.3). The cup shape has a  $C_D$  of 1.4 with the rim pointing upstream and 0.4 when the rim points downstream (White, 1999).

Now the disc-wing shape is somewhere in between the hemispherical shell and the flat plate disc and the measured drag results agree accordingly (Fig. C.3). For a definitive comparison, the drag coefficient for a flat plate disc (with identical diameter) was measured in the wind tunnel alongside the disc-wing. The measured and corrected  $C_D$  for the flat plate disc was 1.20 which compares well with the quoted values in the literature namely, 1.17 (White, 1999), 1.18 (Soong, 1976), 1.12 (Fail et al, 1957). So using Maskells blockage correction for separated flows, the measured  $C_D$  for the flat plate disc agrees very well with that quoted recently in the literature (White, 1999). This provides a good degree of confidence in the blockage correction applied to the disc-wing also, which was the same method as for the flat plate disc.